

Report No.
CVEEN-25/01

**SEISMICALLY RESILIENT BRIDGE BENTS
WITH STRETCH LENGTH ANCHORS AS
ENERGY DISSIPATORS**

**SUMAN NEUPANE
CHRIS P. PANTELIDES**

June 2025

**Civil & Environmental Engineering
College of Engineering
University of Utah
Salt Lake City, UT 84112
USA**

TECHNICAL REPORT DOCUMENTATION PAGE

1. Report No. 25/01	2. Government Accession No. N/A	3. Recipient's Catalog No. N/A	
4. Title and Subtitle SEISMICALLY RESILIENT BRIDGE BENTS WITH STRETCH LENGTH ANCHORS AS ENERGY DISSIPATORS		5. Report Date July 2025	
		6. Performing Organization Code	
7. Author(s) Suman Neupane and Chris P. Pantelides https://orcid.org/0000-0003-3309-3488		8. Performing Organization Report No.	
9. Performing Organization Name and Address Department of Civil and Environmental Engineering University of Utah 110 Central Campus Drive Room 2115 Salt Lake City, UT 84112		10. Work Unit No. (TRAIS)	
		11. Contract or Grant No. 693JJ321C000033	
12. Sponsoring Agency Name and Address Federal Highway Administration Office of Bridges and Structures 1200 New Jersey Ave SE Washington, DC 20590		13. Type of Report and Period Covered Final Report	
		14. Sponsoring Agency Code	
15. Supplementary Notes			
<p>16. Abstract</p> <p>Accelerated bridge construction (ABC) using precast concrete bents has substantial potential to improve construction time and seismic performance in earthquake-prone regions. This study investigates the seismic performance of hybrid self-centering bridge bents that employ unbonded post-tensioning (PT) bars for self-centering and replaceable stretch length anchors (SLAs) as external energy-dissipation devices. Experimental cyclic loading tests were performed on a 42% scale, two-column bridge bent to assess its self-centering capability and hysteretic energy dissipation. The study included four test configurations: two with combined PT bars and SLAs and two with PT bars only, the variables included shear key details at the footings and cap beam.</p> <p>In addition to physical testing, a three-dimensional finite element model (FEM) of the hybrid bridge bent was developed to simulate and predict the cyclic envelope, peak load, and initial stiffness, which showed strong agreement with experimental results. These findings support the reliability of the model for predicting the seismic response of hybrid bridge bents. Further analytical modeling, using empirical equations validated against the scaled specimens, enabled response predictions for the full-scale Riverdale Bridge.</p> <p>The seismic demand was investigated using simplified models. It was determined that the Riverdale Bridge would be able to resist the maximum considered earthquake without any damage. These experimental and analytical results underscore the effectiveness of this hybrid approach for improving seismic resilience and post-earthquake reparability in precast bridge bents, demonstrating its viability for broader applications in seismic bridge design.</p>			
17. Key Words Analysis; Hybrid bridge bent; Hysteretic energy; Post-tensioning; Seismic; Self-centering; Stretch length anchors.		18. Distribution Statement No restrictions.	
19. Security Classif.(of this report) Unclassified	20. Security Classif.(of this page) Unclassified	21. No. of Pages 156	22. Price N/A

SI* (MODERN METRIC) CONVERSION FACTORS				
APPROXIMATE CONVERSIONS TO SI UNITS				
Symbol	When You Know	Multiply By	To Find	Symbol
LENGTH				
in	inches	25.4	millimeters	mm
ft	feet	0.305	meters	m
yd	yards	0.914	meters	m
mi	miles	1.61	kilometers	km
AREA				
in ²	square inches	645.2	square millimeters	mm ²
ft ²	square feet	0.093	square meters	m ²
yd ²	square yard	0.836	square meters	m ²
ac	acres	0.405	hectares	ha
mi ²	square miles	2.59	square kilometers	km ²
VOLUME				
fl oz	fluid ounces	29.57	milliliters	mL
gal	gallons	3.785	liters	L
ft ³	cubic feet	0.028	cubic meters	m ³
yd ³	cubic yards	0.765	cubic meters	m ³
NOTE: volumes greater than 1000 L shall be shown in m ³				
MASS				
oz	ounces	28.35	grams	g
lb	pounds	0.454	kilograms	kg
T	short tons (2000 lb)	0.907	megagrams (or "metric ton")	Mg (or "t")
TEMPERATURE (exact degrees)				
°F	Fahrenheit	5 (F-32)/9 or (F-32)/1.8	Celsius	°C
ILLUMINATION				
fc	foot-candles	10.76	lux	lx
fl	foot-Lamberts	3.426	candela/m ²	cd/m ²
FORCE and PRESSURE or STRESS				
lbf	poundforce	4.45	newtons	N
lbf/in ²	poundforce per square inch	6.89	kilopascals	kPa
APPROXIMATE CONVERSIONS FROM SI UNITS				
Symbol	When You Know	Multiply By	To Find	Symbol
LENGTH				
mm	millimeters	0.039	inches	in
m	meters	3.28	feet	ft
m	meters	1.09	yards	yd
km	kilometers	0.621	miles	mi
AREA				
mm ²	square millimeters	0.0016	square inches	in ²
m ²	square meters	10.764	square feet	ft ²
m ²	square meters	1.195	square yards	yd ²
ha	hectares	2.47	acres	ac
km ²	square kilometers	0.386	square miles	mi ²
VOLUME				
mL	milliliters	0.034	fluid ounces	fl oz
L	liters	0.264	gallons	gal
m ³	cubic meters	35.314	cubic feet	ft ³
m ³	cubic meters	1.307	cubic yards	yd ³
MASS				
g	grams	0.035	ounces	oz
kg	kilograms	2.202	pounds	lb
Mg (or "t")	megagrams (or "metric ton")	1.103	short tons (2000 lb)	T
TEMPERATURE (exact degrees)				
°C	Celsius	1.8C+32	Fahrenheit	°F
ILLUMINATION				
lx	lux	0.0929	foot-candles	fc
cd/m ²	candela/m ²	0.2919	foot-Lamberts	fl
FORCE and PRESSURE or STRESS				
N	newtons	0.225	poundforce	lbf
kPa	kilopascals	0.145	poundforce per square inch	lbf/in ²

*SI is the symbol for the International System of Units. Appropriate rounding should be made to comply with Section 4 of ASTM E380.
(Revised March 2003)

TABLE OF CONTENTS

Chapter 1. Introduction.....	15
1.1 Previous Research on Hybrid Bridge Bents	17
1.2 Previous Research on Energy Dissipators.....	17
Chapter 2. Proposed research.....	19
2.1 Phase I: Cyclic test of self-centering bridge bent with 4PT bars and energy dissipators with shear keys in the footings (4FA and 4F).....	19
2.2 Phase II: Cyclic test of self-centering bridge bent with 4PT bars, energy dissipators and shear keys in the footings and cap-beam (4FBA and 4FB)	20
2.3 Phase III: Computational model of self-centering bridge bent with 4PT bars and energy dissipators and proposed design guideline for hybrid bents	20
Chapter 3. Experimental Setup and Specimen Construction	21
3.1 Four PT bars in each column with SLAs and shear keyS in the footings (Test 4FA)	21
3.2 Four PT bars in each column with shear key in the footings (4F)	23
3.3 Four PT bars in each column with SLAs and shear key in the footing and cap beam (4FBA)	23
3.4 Four PT bars in each column with shear keys in the footings and cap beam (4FB)	24
3.5 Specimen Construction.....	25
3.5.1 Column Details	25
3.5.2 Cap Beam Details	27
3.5.3 Footing Details.....	29
3.5.4 Computation of Number of PT bars and SLAs.....	29
3.5.5 Steel Collar Thickness, Length, and Stud Count Calculation.....	31
3.5.6 Installation of SLAs	31
3.5.7 Post-tensioning Bars	33
3.6 Loading Protocol and Gravity Load	33
3.7 Measured Material Properties Used in the Study.....	34
Chapter 4. Experimental Results for bents with Stretch Length Anchors (SLAS)	35
4.1 Hysteretic Performance of Bent 4FA and 4FBA.....	35
4.2 Post tensioning forces of bents with SLAs.....	36
4.3 Residual drift and re-centering performance of bents with SLAs.....	36
4.4 Backbone curve and stiffness degradation of bents with SLAs	37
4.5 Hysteretic energy dissipation of bents with SLAs	38
Chapter 5. Experimental Results for PT-only bents.....	40
5.1 Hysteretic performance of PT-only bents	40
5.2 Post-tensioning force of PT-only bents	41
5.3 Residual drift and re-centering performance of PT-only bents	42
5.4 Backbone curve and stiffness degradation of PT-only bents	42
5.5 Hysteretic energy dissipation of PT-only bents	43
Chapter 6. Comparison of Bridge Bents with and without Stretch length anchors	44
6.1 Hysteretic performance comparison.....	44
6.2 Hysteretic performance of stretch length anchors	45
6.3 Joint Gap Opening comparison	47

Chapter 7. Experiments and Analysis of Steel Collar Plate with Shear Studs in Concrete Column Stubs under Eccentric Load	48
7.1 Introduction	48
7.1.1 Previous Research	50
7.1.2 Research Objectives	51
7.2 Experimental Methods and Results	52
7.2.1 Concrete Column Stub Specimen Details and Setup	52
7.2.2 Test Results	54
7.2.3 Failure Modes	57
7.3 Analysis Techniques	60
7.3.1 Yield-pullout-tensile fracture failure mode I	61
7.3.2 Weld-shear stud fracture mode II	62
7.4 Numerical Finite Element Analysis	64
7.4.1 Element type and mesh density	64
7.4.2 Material modeling and interaction properties	65
7.4.3 Boundary and loading conditions	66
7.4.4 Model validation	66
7.5 Conclusions from small scale subassemblies and parametric study	68
Chapter 8. Capacity Calculation Using Finite Element Method	70
8.1 Finite Element Model of Bent 4FA and 4F	70
8.1.1 Model Layout	70
8.1.2 FEM Results and Comparison with Experiments	73
8.2 Parametric Study with Studs and Rims	74
8.3 Concrete damage propagation	76
8.4 Design of shear Rims	77
8.5 Conclusions based on fem study	78
Chapter 9. Pushover Capacity Estimation of Rocking Bridge Bent using Analysis Method	80
9.1 Pre-rocking or decompression stage	80
9.2 Rocking stage	81
9.2.1 Rocking bridge bent with post-tensioning and external energy dissipators	82
9.3 Computation of Neutral Axis Depth (c)	84
9.4 Validation of analysis method results	84
9.5 Design Steps	86
9.5.1 Initial Design	86
9.5.2 Selection of initial PT force (Rigid body analogy with neutral axis depth)	88
9.5.3 Pushover capacity prediction	90
9.5.4 Additional recommendations:	92
Chapter 10. Pushover Capacity Estimation of Existing and Modified Riverdale Bridge Bent Using Analysis Method	93
10.1 Pushover capacity of existing and modified Riverdale Bridge Bents	95
10.2 Calculation of number of SLAs	96
10.3 Calculation of steel collar thickness (t_s) and height (h_s)	98

Chapter 11. Capacity Estimation using Conventional Structural Modeling in SAP 2000	99
11.1 Numerical Model Details for Specimen Bent.....	99
11.1.1 Material and Element Properties.....	99
11.1.2 Boundary Conditions and Loading	99
11.1.3 Modeling Approach	99
11.1.4 Calibration and Validation.....	100
11.1.5 Results.....	101
11.2 Numerical Model Details for Riverdale Bridge.....	102
11.2.1 Simplified model of the Riverdale Bridge Bent:	102
11.2.2 Simplified Model of the Riverdale Bridge (3D-model):.....	105
Chapter 12. Conventional Structural Demand Analysis in SAP2000	108
12.1 Selection of Response Spectra	108
Chapter 13. Conclusions.....	112
Chapter 14. References	114
Chapter 15. Appendix.....	121
15.1 Experimental Construction Highlights	121
15.2 Cap-beam Modification	129
15.3 Specimen set up and instrumentation	130
15.4 Experimental Results	133
15.5 Step by step analysis procedure for specimen bent	136
15.6 Step by Step Analysis Procedure for Riverdale Bridge Bent	147

LIST OF FIGURES

Figure 1. Bridge bent and their hysteretic curves: (a) Monolithic bent; (b) PT-only bent; and (c) Hybrid bent with PT-bars and external energy dissipators.....	16
Figure 2. Test setup of scaled bridge bent 4FA.	22
Figure 3. Test setup of scaled bridge bent 4F.	23
Figure 4. Test setup of scaled bridge bent 4FBA.....	24
Figure 5. Test setup of scaled bridge bent 4FB.	24
Figure 6. Column details: (a) elevation; (b) connection at footing; (c) connection at cap beam; (d) collar cross-section at footing; (e) collar cross section at cap beam; (f) steel plate at column base; (g) steel collar and studs at cap beam; and (h) steel collar, studs and bottom plate at footing.	26
Figure 7. Cap beam details: (a) elevation and reinforcement; and (b) anchor bolt connection details and bottom view.	27
Figure 8. Cap-beam detail with shear-keys: (a) elevation; and (b) plan.	28
Figure 9. Footing details: (a) footing plan; (b) footing section in longitudinal direction; (c) section at E-E; and (d) 25 mm thick steel base plate for anchorage of PT bars.	29
Figure 10. Variation of PT force for various levels of initial PT force using rigid body analogy.....	30
Figure 11. Stretch length anchor details: (a) L-shaped anchor; (b) SLA for footing; (c) SLA for cap beam; (d) hexagonal nut; (e) coupler; (f) connection at footing; (g) connection at cap beam 4F and 4FA; (h) installation at footing; and (i) connection at cap beam 4FB and 4FBA.	32
Figure 12. Applied lateral and axial load: (a) Cyclic loading protocol; and (b) Axial load.	34
Figure 13. Hysteretic response comparison of bents with SLAs: (a) Bent 4FA; (b) Bent 4FBA; (c) comparison between 4FA and 4FBA; and (d) deflected shape of 4FA at the end of the test.	35
Figure 14. Recentering efficiency of bents with SLAs: (a) residual displacement; and (b) relative self-centering index.....	37
Figure 15. Performance envelope for bents with SLAs: (a) backbone curve; and (b) stiffness degradation.	37
Figure 16. Energy response for bents with SLAs: (a) hysteretic energy; and (b) equivalent viscous damping ratio.	38
Figure 17. Hysteretic response of bent 4FA and 4FBA: (a and c) At 2.0% drift ratio; and (b and d) At 3.0% drift ratio.....	39
Figure 18. Hysteretic response comparison of bents with SLAs: (a) Bent 4F; (b) Bent; (c) comparison between 4F and 4FB; and (d) deflected shape of 4F at the end of the test (pull cycle).....	40
Figure 19. PT force distribution experiment: (a) Specimen bent 4FB and 4F; and (b) Specimen bent 4FBA and 4FA.	41
Figure 20. Recentering efficiency of bents without SLAs: (a) residual displacement; and (b) relative self-centering index.	42
Figure 21. Performance envelope of bents without SLAs: (a) backbone curve; and (b) stiffness degradation.	42
Figure 22. Energy response for bents without SLAs: (a) hysteretic energy; and (b) equivalent viscous damping ratio.....	43

Figure 23. Hysteresis and hysteretic energy: (a, b) Bent 4FA and 4F; and (c, d) Bent 4FBA and 4FB.	44
Figure 24. Hysteresis from energy dissipation mechanisms: (a) SLA hysteresis for Bent 4FA; (b) SLA hysteresis for Bent 4FBA; (c) SLA after the experiment for Bent 4FA; and (d) elongated SLAs for test 4FBA.	45
Figure 25. Elongation of 19 mm diameter SLAs at end of experiment: (a) footing SLAs; (b) cap beam SLAs; (c) SLAs attached to west footing (test 4FA); (d) SLAs attached to east footing (test 4FA); and (e) elongated SLA with nut compared to original SLA.....	46
Figure 26. Maximum joint gap opening: (a) bents with SLAs; and (b) bents without SLAs.	47
Figure 27. Bridge column with SLAs: (a) exterior; (b) interior; (c) section at SLAs; (d) rocking.	49
Figure 28. Specimen details: (a) column stub reinforcement cage; (b) column stub, steel collar plate, HSS tube, load cell, load and LVDTs; (c) elevation; (d) side view; (e) plan view; (f) column stub cross-section; and (g) elevation showing reinforcement.	53
Figure 29. Shear force comparison at failure for 12.7 mm vs. 9.5 mm collar plates across varying stud numbers and diameters.....	56
Figure 30. Total shear force versus actuator displacement comparison for: (a) 12.7 mm steel collar plate specimens (<i>Specimen 12.7-1-12.7, Specimen 12.7-2-12.7, Specimen 12.7-1-25.4, and Specimen 12.7-2-25.4</i>); and (b) 9.5 mm steel collar plate specimens (<i>Specimen 9.5-1-12.7, Specimen 9.5-2-12.7, Specimen 9.5-1-25.4, and Specimen 9.5-2-25.4</i>).	56
Figure 31. Total shear force versus actuator displacement: (a) 12.7 mm studs (<i>Specimen 12.7-1-12.7, Specimen 12.7-2-12.7, Specimen 9.5-1-12.7, and Specimen 9.5-2-12.7</i>) failure mode I; (b) 25.4 mm diameter studs (<i>Specimen 12.7-1-25.4 and Specimen 9.5-1-25.4</i>) failure mode II; and (c) 25.4 mm diameter studs (<i>Specimen 12.7-2-25.4 and Specimen 9.5-2-25.4</i>) failure mode III.	58
Figure 32. Failure modes: (a) yield-pullout-tensile fracture mode I; (b) shear stud shear fracture mode II; and (c) concrete cracking-shear stud pullout failure mode III.	58
Figure 33. Schematic of experimental failure modes: (a) yield-pullout-tensile fracture mode I; (b) shear stud shear fracture mode II; and (c) concrete cracking-shear stud pullout failure mode III.	62
Figure 34. Finite element model used in analysis: (a) mesh density of the specimen; and (b) encastre boundary conditions applied to top and bottom of the specimen.....	65
Figure 35. Comparison between experiment and finite element model results for total shear force versus actuator displacement: (a) Test 1; (b) Test 2; (c) Test 3; (d) Test 4; (e) Test 5; (f) Test 7; (g) Test 6; and (h) Test 8.....	67
Figure 36. Meshed structures: (a) Column; (b) Cap beam; (c) Footing; and (d) Steel collar and studs.....	71
Figure 37. Schematic of the FEM model: (a) 4F; (b) 4FA; and (c) Whole bent as represented by ABAQUS	72
Figure 38. FEM Results: (a) Deflected shape; (b) Hysteresis vs Pushover test 4F; (c) Deflected shape test 4FA; and (d) Hysteresis vs Pushover test 4FA.....	73

Figure 39. Experimental cyclic envelope vs pushover response from FEM model: (a) bent 4FBA; and (b) bent 4FB.	74
Figure 40. Parametric study of bent specimen with rims: (a) FEM model layout, (b) Deflected shape showing concrete damage with studs (4.0% drift ratio), (c) Deflected shape with rims (2.75% drift ratio), (d) Steel collar detail with rims and studs, and (e) Pushover response comparison of studs vs. rims.	75
Figure 41. Concrete compressive damage propagation at different lateral displacement for column with shear rim: (a) Initial state; (b) 1.5 % drift ratio; (c) 2.5% drift ratio; and (d) Concrete compressive strain distribution inside the steel collar.	77
Figure 42. Schematic of shear rim force distribution at 4.0% drift ratio.	78
Figure 43. Two-column bridge bent at decompression stage with or without SLAs.	81
Figure 44. Two-column bridge bent at rocking stage with SLAs.	82
Figure 45. Comparison of analysis method to experiments: (a) normalized neutral axis depth for 4F and 4FA; (b) pushover capacity for bent 4FA (c) pushover capacity for bent 4F; (d) pushover capacity for bent 4FB; and (e) pushover capacity for bent 4FBA.	85
Figure 46. Contribution of PT bars and SLAs in Lateral Load capacity.	86
Figure 47. Flow chart for initial design.	88
Figure 48. Flow chart for PT force distribution.	89
Figure 49. Flowchart for pushover capacity.	91
Figure 50. Existing and modified Riverdale Bridge bents: (a) existing bent; (b) modified bent; (c) section A-A; (d) section C-C without SLAs; (e) section C-C with SLAs; (f) footing details; and (g) cap beam details.	95
Figure 51. Post-tensioning force at various drift ratios for different initial post-tensioning stress.	95
Figure 52. Analytical pushover capacity for existing and modified Riverdale bridge bent with and without SLAs.	96
Figure 53. Schematic of Specimen Bent SAP 2000 model.	101
Figure 54. Pushover response obtained from SAP 2000 while using various values of <i>M_{joint}</i> and comparison with analytical equation.	102
Figure 55. Pushover Response Comparison for Bent 4FA: (a) Experimental vs Analytical Equations; and (b) Experimental vs SAP 2000.	102
Figure 56. Schematic of SAP 2000 model: (a) 3D model of the Riverdale Bent; and (b) 2D model of bent in consideration.	103
Figure 57. Riverdale Bridge bent Model SAP 2000: (a) Rotational Spring used in SAP 2000; and (b) Pushover response comparison analytical equation vs SAP 2000.	104
Figure 58. Mode shape of the 2D-model in SAP 2000.	105
Figure 59. 3D SAP 2000 model of the bent showing soil springs.	106
Figure 60. Pushover Response from 3D model: (a) Whole Riverdale Bridge; and (b) Riverdale bent only (2D-model) and response of the bent only from Riverdale Bridge (3D-model).	106
Figure 61. Mode shapes; (a) 1 st mode response; and (b) 2 nd mode response.	107
Figure 62. Design base and maximum credible response spectra used for demand calculation.	108
Figure 63. Flow chart showing the seismic demand calculation procedure once the trilinear curve is determined.	109

Figure 64. Demand Calculation: (a) Effective stiffness calculation; and (b) Demand obtained from the tri-linear and linear responses for a Riverdale Bent only from Riverdale Bridge Model.....	110
---	-----

LIST OF TABLES

Table 1. Test specimen terminology.....	21
Table 2. Test specimen experimental details.	21
Table 3. Stretch length and steel chair gap with concrete surface.	33
Table 4. Material properties used in the experiments.	34
Table 5. Post-tensioning force variation for bents with SLAs.....	36
Table 6. Post-tensioning force variation for bents without SLAs.....	41
Table 7. Maximum joint opening for specimen bents.	47
Table 8. Test matrix for stub column tests.....	54
Table 9. Material properties used in the experiment.....	55
Table 10. Experimental results	59
Table 11. Experimental tensile force in shear studs at stud fracture	62
Table 12. Comparison of experimental result to code predictions	64
Table 13. Concrete damage plasticity values used in finite element model	66
Table 14. Parts with their respective elements.....	71
Table 15. Parts and their respective contact properties.....	73
Table 16. Details of the existing and modified Riverdale Bridge bents.	93
Table 17. Rotational Spring Properties	100
Table 18. Calculation of Rotational Spring Properties for Riverdale Bridge bent	104
Table 19. Analytical calculation for PT force distribution for specimen bent.....	142
Table 20. Analytical response for specimen bent 4FA and 4FBA.	145
Table 21. Analytical response for specimen bent 4F and 4FB.	146
Table 22. Analytical calculation for PT force distribution for Riverdale bent	152
Table 23. Analytical pushover response calculation for Modified Riverdale with SLAs.	154
Table 24. Analytical pushover response calculation for Modified Riverdale with PT bars only.	155
Table 25. Analytical pushover response calculation for Existing Riverdale with PT bars only.	155

LIST OF ABBREVIATIONS AND SYMBOLS

Abbreviations

AASHTO	American Association of State Highway and Transportation Officials
ABC	accelerated bridge construction
ACI	American Concrete Institute
ASTM	American Society of Testing and Materials
CFT	concrete filled tube
DCR	damaged controlled rocking
FHWA	Federal Highway Administration
LVDT	linear variable differential transducer
OpenSees	Open System for Earthquake Engineering Simulation
FEM	finite element method
PBES	prefabricated bridge element and systems
PRESSS	precast seismic structural system
PT	post-tensioning
SLA	stretch length anchor

Symbols

T_{ult}	= total ultimate tensile strength
A_g	= gross area of the column cross-section
f_u	= ultimate tensile strength
$F_{PT,y}$	= total PT force at yield of all PT bars in each column (measured for single column)
F_{SLA}	= total force dissipated by all the external dissipators in each column
Λ_D	= energy dissipation coefficient
P_u	= total gravity load
$F_{PT,i}$	= initial PT load for all the PT bars in one column
n_{SLA}	= the number of SLAs in one column
$F_{y,SLA}$	= the yield strength of SLAs
A_{SLA}	= cross-sectional area of each SLA
d_b	= diameter of SLAs
f'_c	= concrete compressive strength
f_y	= yield strength
RSE	= relative self-centering efficiency
u_{res}^+, u_{res}^-	= positive and negative residual displacement for the given cycle
u_m^+, u_m^-	= maximum positive and negative displacement for the given cycle
E_s	= strain energy
u_o	= maximum displacement
K	= stiffness
ξ_{eq}	= equivalent viscous damping ratio
E_D	= hysteretic energy
C	= compressive force in the concrete
T	= total tensile force
M_{ext}	= external bending moment
P	= applied load
e	= eccentricity
jd	= lever arm
y	= connection arm from the bottom of the steel collar plate to the center of the shear stud
V_{tot}	= the total shear force
$A_s = A_{sc}$	= shear stud cross-sectional area
σ_u	= shear stud ultimate strength
E_c	= modulus of elasticity of concrete
Q_n	= stud nominal shear strength
K_c	= flexural stiffness of the fixed column before rocking
I_{eff}	= effective moment of inertia of the column

I_g	= gross moment of inertia of the column
H_c	= column height
n_c	= number of columns
M_{dec}	= decompression moment
W	= total axial gravity load of the system
P_u	= total axial gravity load on each column
n_{PT}	= number of PT bars on each column
D	= diameter of the equivalent section
A_c	= cross-sectional area of the column
F_{dec}	= Decompression force
F_{PT}	= tensile force in a PT bar at a given drift ratio
A_{PT}	= area of a PT bar
E_{PT}	= modulus of elasticity of the PT bars
Δ_{rot}	= lateral displacement due to rotation only
Δ_{Tot}	= lateral displacement due to rotation and elastic deformation
$\Delta_{elastic}$	= elastic deformation of the rocking system
Δ_{decc}	= elastic decompression displacement due to decompression force
DR	= rotation only drift ratio
DR_T	= total drift ratio (includes rotational and elastic displacement)
θ	= total joint rotation
L_T	= total unbonded length of the PT bars
ε_0	= the initial strain due to initial post tensioning
DR	= drift ratio expressed as a percentage
$f_{PT,i}$	= initial post tensioning stress
F_{rot}	= lateral force due to rocking
F_{Tot}	= total lateral force due to rocking and horizontal component of PT force
$F_{PT,horizontal}$	= horizontal component of PT force contributing to lateral load
c	= neutral axis depth
ε_{SLA}	= strain in SLAs
D_i	= the distance of the SLA from the extreme compressive fiber
L_{SLA}	= SLA stretch length
$\sigma_{T,i}$	= corresponding tensile stress in SLAs
$F_{T,i}$	= tensile force in an SLA during rocking
A_{SLA}	= area of SLAs
n_{SLA}	= number of SLAs
h_s^*	= unfactored height of the steel collar
λ_s	= factor of safety
h_s	= factored height of steel collar
t_s	= thickness of the steel collar

CHAPTER 1. INTRODUCTION

Accelerated bridge construction (ABC) has emerged as a popular alternative to traditional cast-in-place methods. ABC prioritizes speed, efficiency, and safety by using prefabricated bridge elements and systems (PBES). This approach allows much of the construction—such as reinforcing steel installation, formwork preparation, and casting—to be completed off-site, significantly reducing on-site construction time and traffic disruption (Culmo et al. 2011; FHWA 2011). Recent advancements in bridge design have focused on improving seismic resilience through innovative construction techniques. In this research, stretch length anchors (SLAs) are used as external energy dissipators. SLAs have been found to significantly enhance the ductility and energy absorption of structures during earthquakes, offering a cost-effective and simple solution. These anchors operate under tensile forces, eliminating the need for buckling protection, and are designed to stretch over a length at least eight times the anchor diameter ($8d_b$). This stretch length allows controlled plastic deformation, helping the structure withstand seismic forces while minimizing damage (Soules et al. 2016; Trautner et al. 2017; Parks et al. 2018).

In seismic regions, the connections between precast elements in ABC are critical. These connections must provide adequate ductility, reparability, and lateral load capacity to ensure superior seismic performance. Research has focused on various connection types, including grouted reinforcing splice couplers, grouted ducts, and post-tensioning systems, as well as hybrid connections that combine unbonded post-tensioning (PT) with mild steel reinforcement at joint interfaces (Ameli and Pantelides 2017; Marsh 2011). Hybrid connections also integrate energy dissipating elements, such as viscous dampers, or buckling restrained braces, which contribute to managing seismic forces and enhancing structural resilience (Mashal and Palermo 2019a; Sideris et al. 2014).

One of the key innovations in bridge design utilizing ABC is the use of PT bars for self-centering of bridge bents. These systems utilize PT bars to minimize residual displacements after seismic events. The concept of self-centering is crucial in earthquake-prone areas, since it allows the structure to return to its original position after experiencing lateral loads, due to the elastic restoring forces generated by PT systems (Guerrini et al. 2015a; Sideris 2012). Hybrid systems using SLAs and other energy dissipators have shown great potential for achieving hysteretic energy dissipation, low residual drift, maintaining structural integrity, and allowing easier post-earthquake repair (Thapa and Pantelides 2021). Several experimental studies have demonstrated the effectiveness of hybrid bridge bents in seismic conditions. Mander and Cheng (1997) tested precast post-tensioned bridge piers, demonstrating bilinear behavior with minimal permanent damage. Marriott et al. (2009), and Ou et al. (2010) explored the use of unbonded PT bars and internal energy dissipators, which provided excellent self-centering capabilities and reduced residual drift. More recent studies, such as Thonstad et al. (2016), confirmed that pre-tensioning columns with partially unbonded tendons could significantly reduce post-earthquake residual displacements.

Figure 1(a) shows the typical hysteretic response of the cast in place or monolithic bridge bent in which longitudinal reinforcing bars passing through the column-to-footing and column-to-cap beam dissipate hysteretic energy. **Figure 1(b)** shows the typical hysteretic response of a bridge bent with only PT-bars connecting the column with the footing and cap beam. Such bridges with only PT bars connecting structural elements do not dissipate hysteretic energy as suggested by the linear hysteretic curve. PT-only bridge bents have minimal residual displacement since PT-bars come back to their original position when stressed within their elastic limit. **Figure 1(c)** shows the hysteretic response of a hybrid bridge bent with PT bars and replaceable energy dissipators.

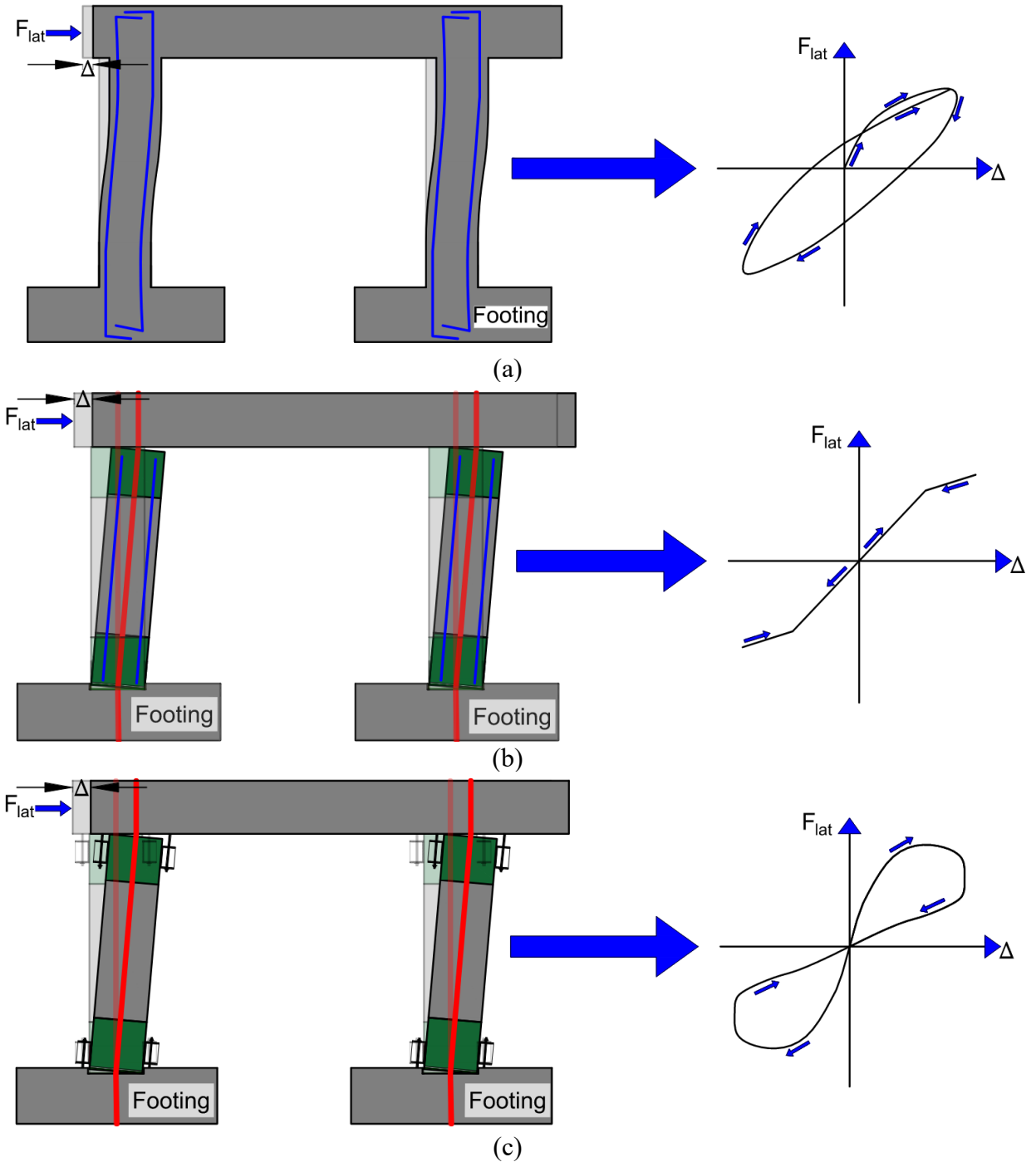


Figure 1. Bridge bent and their hysteretic curves: (a) Monolithic bent; (b) PT-only bent; and (c) Hybrid bent with PT-bars and external energy dissipators.

In addition to PT-bars, external replaceable energy dissipators are used at column-to-footing or column-to-cap beam interfaces; these devices dissipate hysteretic energy forming flag shaped hysteresis curves. The PT-bars assist in re-centering the bridge bent since the initial PT-forces enable the bridge bent to come to its original position.

To protect against concrete damage in self-centering hybrid bridge bents, particularly at the base of the columns, steel jackets are often used. These jackets prevent spalling and toe crushing, ensuring that PT forces remain intact during seismic loading. However, the steel jacket height is important since stresses above the jacket can lead to concrete spalling and toe crushing (Hewes 2007; Thapa and Pantelides 2021).

1.1 PREVIOUS RESEARCH ON HYBRID BRIDGE BENTS

Hybrid techniques include combining unbonded post-tensioning elements with mild steel reinforcement at joint interfaces, often incorporating other energy-dissipating elements which can be external as well as internal (Guerrini et al. 2015b; Mashal et al. 2019; Sideris 2012). Utilizing post-tensioning and external energy dissipators can reduce residual displacement and enhance energy dissipation in hybrid bridges. When subjected to seismic loads, joints between precast members exhibit rocking behavior, allowing for the absorption of member displacement without causing plastic deformation (Marsh 2011; Zhang et al. 2020). This rocking behavior enables unbonded tendons to stretch evenly causing the elastic stretching of the post-tensioning element; the elastic restoring force facilitates self-centering behavior, assisting the structure to return to its original position (Bu et al. 2016a; b; Dangol and Pantelides 2022; Sideris 2012; Trono et al. 2015; White and Palermo 2016).

In general, hybrid bridge bent systems using post-tensioning rely on their inherent self-centering attributes and internal mild steel bars for energy dissipation. Recent developments have seen the incorporation of external, replaceable energy dissipators into these systems. Extensive testing, including the evaluation of nearly full-scale precast post-tensioned bridge piers, has resulted in their ability to exhibit bilinear elastic behavior without causing permanent damage (Mander and Cheng 1997). Research efforts, such as those undertaken by Marriott et al. (2009), have explored hybrid piers that combine unbonded post-tensioning with external replaceable dissipators, demonstrating stable hysteretic responses with minimal residual displacement and substantial energy dissipation. These external dissipators offer the advantage of easy replacement after seismic events. It is worth noting that while the use of energy dissipation bars enhances hysteretic energy dissipation, excessive lateral displacement can result in premature failure, a concern that can be addressed through techniques such as intentional debonding (Barton et al. 2022). Experiments conducted by Ou et al. (2010) on precast segmental concrete columns connected by post-tensioning bars and internal energy dissipators confirmed their ability to self-center, effectively dissipate energy, and exhibit minimal residual drift. These findings highlight the benefits of designing bridge bents with the capability to self-center and dissipate hysteretic energy without causing structural damage in seismic regions. Shi et al. (2022) performed a study on a seismic design procedure for a self-centering pier on soil-structure-interaction and used data from 12 ground motions to perform nonlinear time history analysis.

1.2 PREVIOUS RESEARCH ON ENERGY DISSIPATORS

The inclusion of high-performance energy dissipators has resulted in enhanced capacity for drift resistance, increased energy dissipation, and improved lateral strength (Dangol and Pantelides 2022; ElGawady and Sha'Lan 2011; Routledge et al. 2020; Wang et al. 2019). Xue et al. (2021) proposed using slip friction braces for enhancing self-centering capabilities and were able to obtain a flag shaped hysteresis with significant energy dissipation. In a study conducted by Zhong et al. (2022), rocking mechanical hinges were used at the joint to protect the concrete from damage

during rocking action and analytical equations were proposed to obtain hysteretic performance of such a self-centering bridge bent. New technologies such as shape memory alloys, buckling restraint brace fuses or viscous dampers have also been used as external and internal energy dissipators that were able to produce self-centering behavior of the bent (Wang et al. 2018; Mashal and Palermo 2019; Raza et al. 2023). In a study conducted by Thapa and Pantelides (2021), tests were carried out to combine stretch length anchors (SLAs) with PT bars to establish a hybrid bridge structure capable of self-centering. While PT bars contribute to self-centering, prior experiments have uncovered instances of residual displacement and damage to column areas (Thapa and Pantelides 2021). It is important to emphasize that self-centering capability depends on factors such as the number of PT bars, initial PT forces, protection of column base in the plastic hinge region to restrict concrete damage during rocking of the bridge piers and the energy dissipating system used.

This research builds on previous work by examining four different experiments involving hybrid self-centering bridge bents. Variables such as the arrangement of shear keys, and the presence or absence of SLAs as external energy dissipators are explored. The goal is to optimize these parameters to enhance the bridge's seismic performance by reducing residual drift, dissipating hysteretic energy efficiently, and ensuring the structure's ability to self-center after an earthquake.

In conclusion, the combination of ABC techniques and hybrid self-centering systems, including post-tensioning and external energy dissipators (SLAs), represents a significant advancement in bridge construction for seismic regions. These methods not only improve the resilience and durability of bridges but also reduce construction time and cost, making them an ideal solution for modern infrastructure projects.

CHAPTER 2. PROPOSED RESEARCH

The proposed research is concerned with the study of self-centering and energy dissipation of a hybrid bridge bent with and without energy dissipation devices in terms of SLAs. The number of PT bars has been increased compared to previous research to enhance the self-centering system, and the steel collar length extended to provide better protection for the plastic hinge region. The initial post-tensioning force plays an important role in maintaining post tensioning forces below the yield limit of the PT-bars; this research uses rigid body analogy to predict the evolution of post tensioning force at various drift ratios. Elevating the steel chairs above the footing or cap beam surface allows for free rocking of the bridge bent. Experimental results indicate that this approach effectively reduces the residual drift ratio to less than 0.5% while protecting the concrete columns, footings, and cap beam from damage. The following are the specific objectives of the study which will be achieved in three phases:

Phase I: Evaluate experimentally the seismic performance of a two-column bridge bent with shear-keys at the footings only and four post-tensioning bars in each column with external energy dissipators (SLA) and subsequently the seismic performance of the bridge bent without external energy dissipators.

Phase II: Evaluate experimentally the seismic performance of a two-column bridge bent with shear-keys in the footings and the cap-beam and four post-tensioning bars in each column with external energy dissipators (SLA) and subsequently the seismic performance of the bridge bent without external energy dissipators.

Phase III: Perform finite element modeling of the experiments with and without SLAs using a detailed FEM model (ABAQUS) to predict the pushover response and use analytical equations to obtain the pushover response and compare it with the experimental results. Finally, propose design guidelines for self-centering bridge piers with external energy dissipators (SLA) using the experimental results, analytical calculations and FEM model response. This study presents a simplified numerical modeling approach using SAP2000, a conventional engineering software, to predict the pushover response of rocking bridge bents. This methodology offers practitioners a straightforward tool for modeling and evaluating self-centering bridge bents without requiring complex finite element modeling. The proposed framework guides users through step-by-step procedures for developing a SAP2000 model of a rocking bridge bent, determining demand and capacity, and designing key components, including steel collars, PT bars, and anchors. The capacity calculations integrate analytical formulations to facilitate the practical design of self-centering bridge bents.

2.1 PHASE I: CYCLIC TEST OF SELF-CENTERING BRIDGE BENT WITH 4PT BARS AND ENERGY DISSIPATORS WITH SHEAR KEYS IN THE FOOTINGS (4FA AND 4F)

The first phase of the research includes the initial design, construction, and quasi-static cyclic testing of the specimen with post-tensioning bars. This phase includes two tests: (1) testing of the hybrid bridge bent with external energy dissipators (tension only stretch length anchors), and (2) testing of the hybrid bridge bent without external energy dissipators i.e., bridge bent with

only post-tensioning bars. This experiment shows the difference in performance of the bridge bent with the use of external dissipators compared to when they are not used.

2.2 PHASE II: CYCLIC TEST OF SELF-CENTERING BRIDGE BENT WITH 4PT BARS, ENERGY DISSIPATORS AND SHEAR KEYS IN THE FOOTINGS AND CAP-BEAM (4FBA AND 4FB)

The second phase includes the addition of shear-keys in the cap-beam of the bridge bent and quasi-static cyclic testing of the specimen with post-tensioning bars. This phase includes two tests: (1) testing of the hybrid bridge bent with external energy dissipators (tension only stretch length anchors), and (2) testing of the hybrid bridge bent without external energy dissipators i.e., only with post-tensioning bars. This experiment shows the difference in performance of the bridge bent when shear-keys are provided in the both-cap beam and footings compared to Phase I where shear-keys were only provided in the footings.

2.3 PHASE III: COMPUTATIONAL MODEL OF SELF-CENTERING BRIDGE BENT WITH 4PT BARS AND ENERGY DISSIPATORS AND PROPOSED DESIGN GUIDELINE FOR HYBRID BENTS

In this phase of the study, numerical models for all four tests will be developed and validated with experimental results using finite element models (FEM). Theoretical analytical equations are used to compute the pushover response of the bents, based on the normalized neutral axis depth, and compare with the experimental and FEM results. Moreover, design equations for calculating the number of PT bars and number of stretch length anchors (SLAs) are developed based on the desired self-centering ratio using seismic design principles for design of conventional cast-in-place bridges.

The simplified numerical approach uses SAP2000, a widely used engineering software, to model the pushover response of self-centering rocking bridge bents. The method avoids complex finite element modeling (FEM), providing engineers with a practical tool to analyze and design these systems. The framework outlines a step-by-step process to: (1) develop SAP2000 models of rocking bents, (2) evaluate seismic demand and structural capacity, and (3) design critical elements including the steel collar, post-tensioned (PT) bars, and anchorage systems. It incorporates analytical equations to calculate key capacity metrics, such as decompression force, PT recentering capacity, and energy dissipation, directly within the software environment. By aligning the theoretical model with accessible software, this approach enables efficient, code-compliant design of rocking systems, empowering practitioners to design self-centering bridge bents using conventional tools.

CHAPTER 3. EXPERIMENTAL SETUP AND SPECIMEN CONSTRUCTION

The specimen was scaled to 42% of the prototype bridge bent. Mild steel reinforcing bars were used to reinforce the cap beam, columns and footings. A target 3.5% drift ratio was considered adequate since it surpassed the expected demand of 2.0% drift ratio, as determined by non-linear time history analysis of the prototype bridge for the maximum credible earthquake (Upadhyay and Pantelides 2022). All other mild steel reinforcement details comply with the AASHTO Guide Specifications for LRFD Seismic Bridge Design (AASHTO 2011). The residual drift ratio was expected to remain below 1.0% which is acceptable for monolithic bridge bents (Kawashima 1997).

The first experiment, labeled 4FA, had four post-tensioning (PT) bars in each column along with 28 SLAs serving as external energy dissipators. In the second experiment, labeled 4F, four PT bars were used in each column without any energy dissipation devices. The third experiment, 4FBA, incorporated four PT bars per column, 28 SLAs across the entire system, and shear keys in both the footing and cap beam. Lastly, the fourth experiment, 4FB, consisted of four PT bars per column and shear keys in both the footing and cap beam. **Table 1** presents the experimental details, and the components used in each test. For all experiments, a consistent vertical axial load was applied to the cap beam to simulate gravity effects. **Table 2** shows the details of the experimental setup including steel collar length and surface interaction at column ends.

Table 1. Test specimen terminology.

Bent	Description
4FA	Four PT bars in each column with SLAs and shear keys in the footings
4FBA	Four PT bars in each column with SLAs and shear keys in the footings and cap beam
4F	Four PT bars in each column with shear keys in the footings
4FB	Four PT bars in each column with shear keys in the footings and cap beam

3.1 FOUR PT BARS IN EACH COLUMN WITH SLAS AND SHEAR KEYS IN THE FOOTINGS (TEST 4FA)

The precast concrete footings, columns, and cap beam were connected using 14 SLAs (6 SLAs at the cap beam and 8 SLAs at the footing) and four unbonded post-tensioned bars in each column, as shown in **Figure 2** and **Figure 6(a-e)**. An octagonal steel plate was placed in the octagonal shear key inside the footing to mitigate concrete crushing, as shown in **Figure 2** and **Figure 6(f)**. HSS steel tube segments were welded to steel collars at the top and bottom of each column to attach the SLAs from the footings and cap beam, as shown in **Figure 2**; this detail eliminates construction of specialized steel chairs (Parks et al. 2018; Thapa and Pantelides 2021).

Table 2. Test specimen experimental details.

Specimen	No. of PT bars per column	Initial PT force	Column-to-cap beam surface interaction	Column-to-footing surface interaction	Steel jacket height	Steel chair interaction
----------	---------------------------	------------------	--	---------------------------------------	---------------------	-------------------------

						with concrete
	(No.)	(kN)	-	-	(mm)	-
4FA	4	1420	Concrete-to- concrete	Steel-to-steel	457	NO
4FBA	4	1420	Steel-to- concrete	Steel-to- concrete	457	NO
4F	4	1420	Concrete-to- concrete	Steel-to-steel	457	NO
4FB	4	1420	Steel-to- concrete	Steel-to- concrete	457	NO

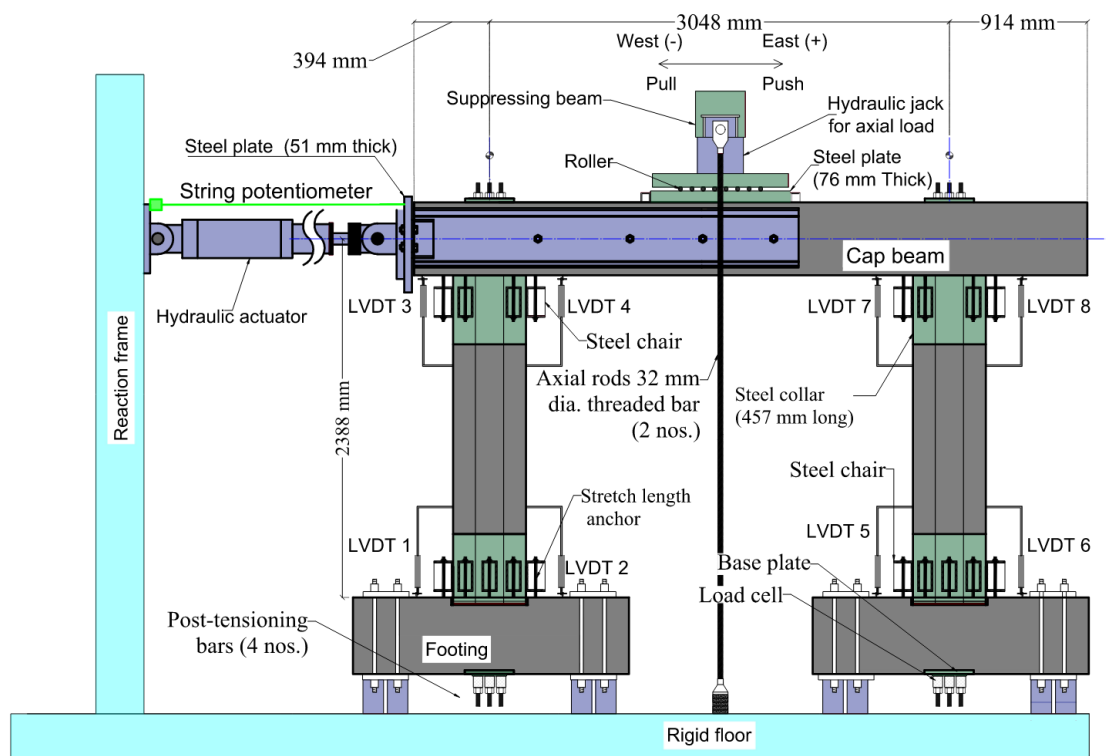


Figure 2. Test setup of scaled bridge bent 4FA.

Using rigid body analogy as detailed in the precast seismic structural system (PRESSS) Handbook (Pampanin et al. 2010) and self-centering considerations as shown subsequently, it was determined that the desired level of initial post-tensioning force for each of the four PT bars was 178 kN. In the experiment, every PT bar was initially post-tensioned to a force of 178 kN so that the total post-tensioning force per column was 712 kN. A constant 605 kN axial load was applied to the cap beam using a hydraulic jack, as shown in **Figure 2** using two 32 mm diameter threaded bars connected to a suppressing beam to simulate gravity. More details on the number of PT-bars, initial PT-force and number of SLAs are discussed in the following sections. The cyclic quasi-static load was applied horizontally at mid-height of the cap beam using a hydraulic actuator and two steel channels, as shown in **Figure 2**. Strain gauges were attached to the column longitudinal steel bars and spirals, as well as to the SLAs. Linear variable differential transformers (LVDTs)

were placed on both sides of the column top and bottom to measure column rotation; a string potentiometer was attached to the top of the cap beam to measure lateral displacement, as shown in **Figure 2**. Load cells were used to measure the applied lateral load and post-tensioning force in each PT bar, as shown in **Figure 2**.

3.2 FOUR PT BARS IN EACH COLUMN WITH SHEAR KEY IN THE FOOTINGS (4F)

The setup for test 4F was similar to 4FA, except that the SLAs were removed, and the specimen was tested with four PT bars in each column. Each column had a total PT force of 712 kN; a 605 kN axial load was applied to the cap beam, as for test 4FA to simulate gravity. **Figure 3** shows the experimental setup of bent 4F, without any SLAs or shear keys in the cap beam. PT-bars were the only element passing through the column to the cap-beam and footings. The only contributing elements to the system's hysteretic energy were the friction existing between the surfaces of the column and cap beam, as well as the footing, along with the friction occurring between the PT bars and the PVC pipe surface, observed during the application of the quasi-static cyclic load.

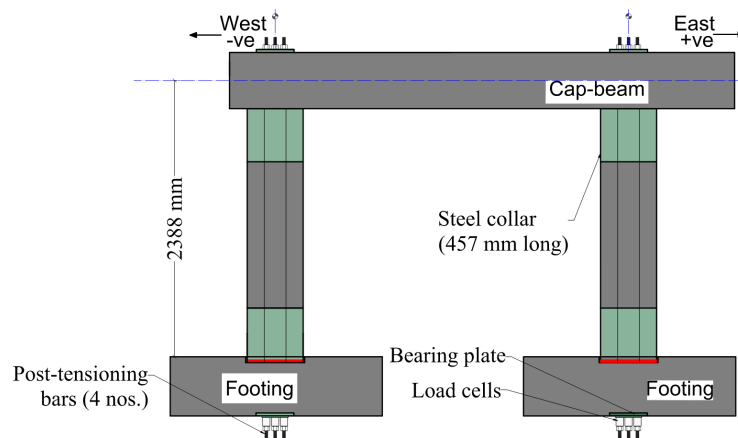


Figure 3. Test setup of scaled bridge bent 4F.

3.3 FOUR PT BARS IN EACH COLUMN WITH SLAS AND SHEAR KEY IN THE FOOTING AND CAP BEAM (4FBA)

The experimental setup was similar to 4FA, with the same SLAs, PT bars, initial PT forces, and gravity load. The only difference was the addition of shear keys in both the footings and cap beam. **Figure 4** shows the schematic of the experimental setup for bent 4FBA, with SLAs and shear keys in both the cap beam and footings. To address out-of-plane movement during lateral cyclic loading, the cap-beam underwent modifications after the initial tests to accommodate these shear-keys.

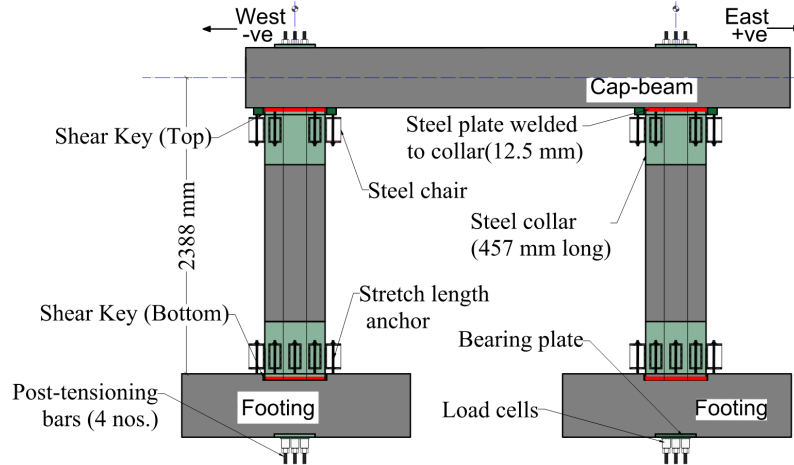


Figure 4. Test setup of scaled bridge bent 4FBA.

3.4 FOUR PT BARS IN EACH COLUMN WITH SHEAR KEYS IN THE FOOTINGS AND CAP BEAM (4FB)

The setup for test 4FB was similar to 4FBA, except that the SLAs were removed, and the specimen was tested with only four PT bars in each column. Each column had a total PT force of 712 kN; a 605 kN axial load was applied to the cap beam, as was done in test 4FBA. **Figure 5** shows the schematic of the experimental setup for bent 4FB, with shear keys in the cap beam and footings without any external energy dissipators. Specimen 4FB lacked any external energy dissipation system, the only contributing elements to hysteretic energy dissipation were the friction existing between the surfaces of the column and cap beam, as well as the footing, along with the friction occurring between the PT bars and the PVC pipe surface. In this test, a steel plate was welded to the top of the column, effectively reducing the friction generated by the contact between concrete surfaces. The presence of the steel plate, shown in **Figure 5** modified the contact of the column to the cap beam from a concrete-to-concrete contact to a concrete-to-steel contact, resulting in reduction of frictional forces.

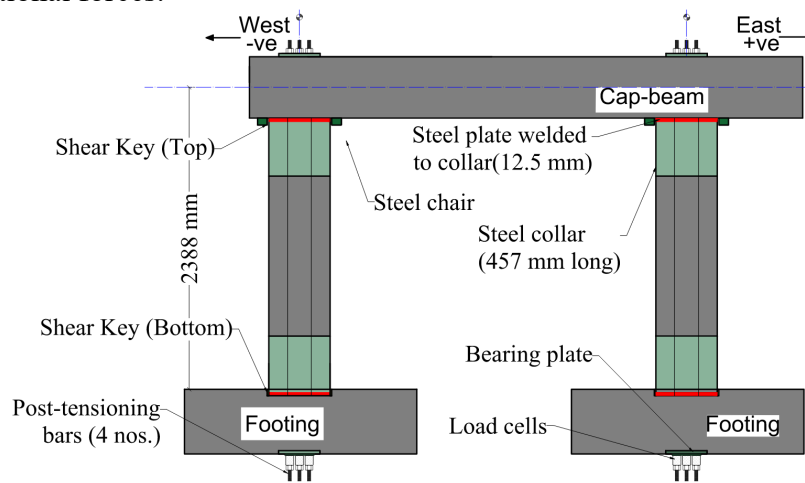


Figure 5. Test setup of scaled bridge bent 4FB.

3.5 SPECIMEN CONSTRUCTION

3.5.1 Column Details

The columns were 483 mm wide, with an octagonal cross-section and 2184 mm high, as shown in **Figure 6(a)**; were reinforced with twelve 16 mm diameter longitudinal bars with a reinforcement ratio of 1.2%; a 381 mm diameter spiral with a 16 mm bar at a 64 mm pitch with a transverse reinforcement ratio of 3.3% was used to confine the concrete. A 13 mm thick octagonal steel collar that was 457 mm high was used at the column top and bottom to attach the HSS steel chairs, as shown in **Figure 6 (a-e)**. The mild steel reinforcement, which was terminated at the column top and bottom, had a tensile yield strength of 469 MPa. The concrete compressive strength was 86 MPa on the day of testing.

In the prototype bridge bent, six 32 mm PT bars were used in each 1067 mm diameter column; only two 25 mm PT bars were used in previous tests which resulted in yielding of the PT bars at high drift ratios (Thapa and Pantelides 2021). Four 25 mm diameter 1035 MPa threaded PT bars, positioned 76 mm apart from the centerline of the column on either side, were used, as shown in **Figure 6 (d, e)**. This arrangement of four PT bars is advantageous for self-centering since two of the PT bars are located at the neutral axis; the PT reinforcement ratio was 1.2%. The 25 mm PT bars were unbonded and placed in 51 mm inner diameter PVC pipes, which left a 13 mm space on each side of the PT bar. The column base plate had four 25 mm diameter studs, as shown in **Figure 6(a, b, and f)**. The steel collar had three 25 mm diameter studs on each sides; details of mild steel cages and stud placement on the steel collar are shown in **Figure 6 (g)** for the column top and **Figure 6 (h)** for the column bottom. The columns were recessed 51 mm in the footing; the recess accommodated a free moving 13 mm steel plate, as shown in **Figure 6 (b)**. The recess worked as a shear key that transfers the shear force from the columns to the footings and prevents sliding. Similarly, for bents 4FBA and 4FB shear key was also provided on the cap beam by adding additional steel plates for the shear key. A steel plate was welded to the top of the column with steel collar, effectively reducing the friction generated by the contact between concrete surfaces. This welding of steel plate with the steel jacket protected column toe crushing due to the interaction of column surface with the cap-beam surface. The presence of the steel plate, shown in **Figure 5** modified the contact of the column to the cap beam from a concrete-to-concrete contact to a concrete-to-steel contact, resulting in reduction of frictional forces. All tests have steel plate welded to the steel jacket at the bottom of the column protecting column base while it interacts with the footing and only test 4FBA and 4FB have steel plate welded to the steel jacket while the test 4FA and 4F had concrete-concrete interaction.

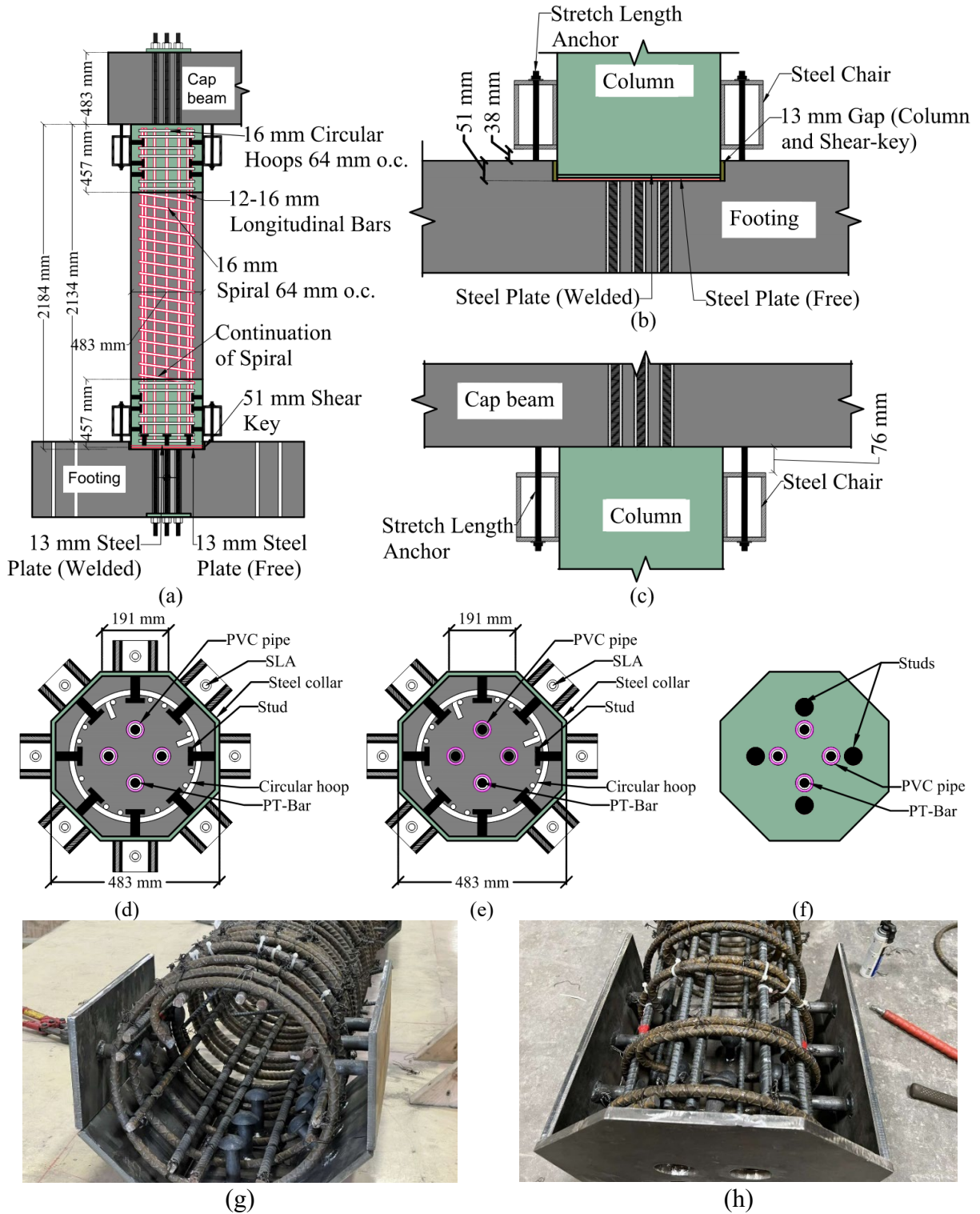


Figure 6. Column details: (a) elevation; (b) connection at footing; (c) connection at cap beam; (d) collar cross-section at footing; (e) collar cross section at cap beam; (f) steel plate at column base; (g) steel collar and studs at cap beam; and (h) steel collar, studs and bottom plate at footing.

3.5.2 Cap Beam Details

The cap beam was 4356 mm long and was connected to two octagonal columns spaced 3048 mm apart, as shown in **Figure 7**; the cap beam was 559 mm wide and 483 mm high with 38 mm clear cover. The cap beam was reinforced with 36 longitudinal bars, 16 mm in diameter that were bent at both ends to meet anchorage and development length requirements. The longitudinal bar reinforcing ratio was 2.5%. The longitudinal steel bars at the corners and edges of the beam cross-section were confined with rectangular stirrups, while the inner layers were confined with hooks of two successive cross ties engaging the same longitudinal bar. A standard hook extension of 76 mm was used to meet ACI 318 seismic hook provisions (ACI 2019). Additional spirals. The 10 mm diameter stirrups were spaced 152 mm apart; they had 90° hooks on one end and 135° hooks

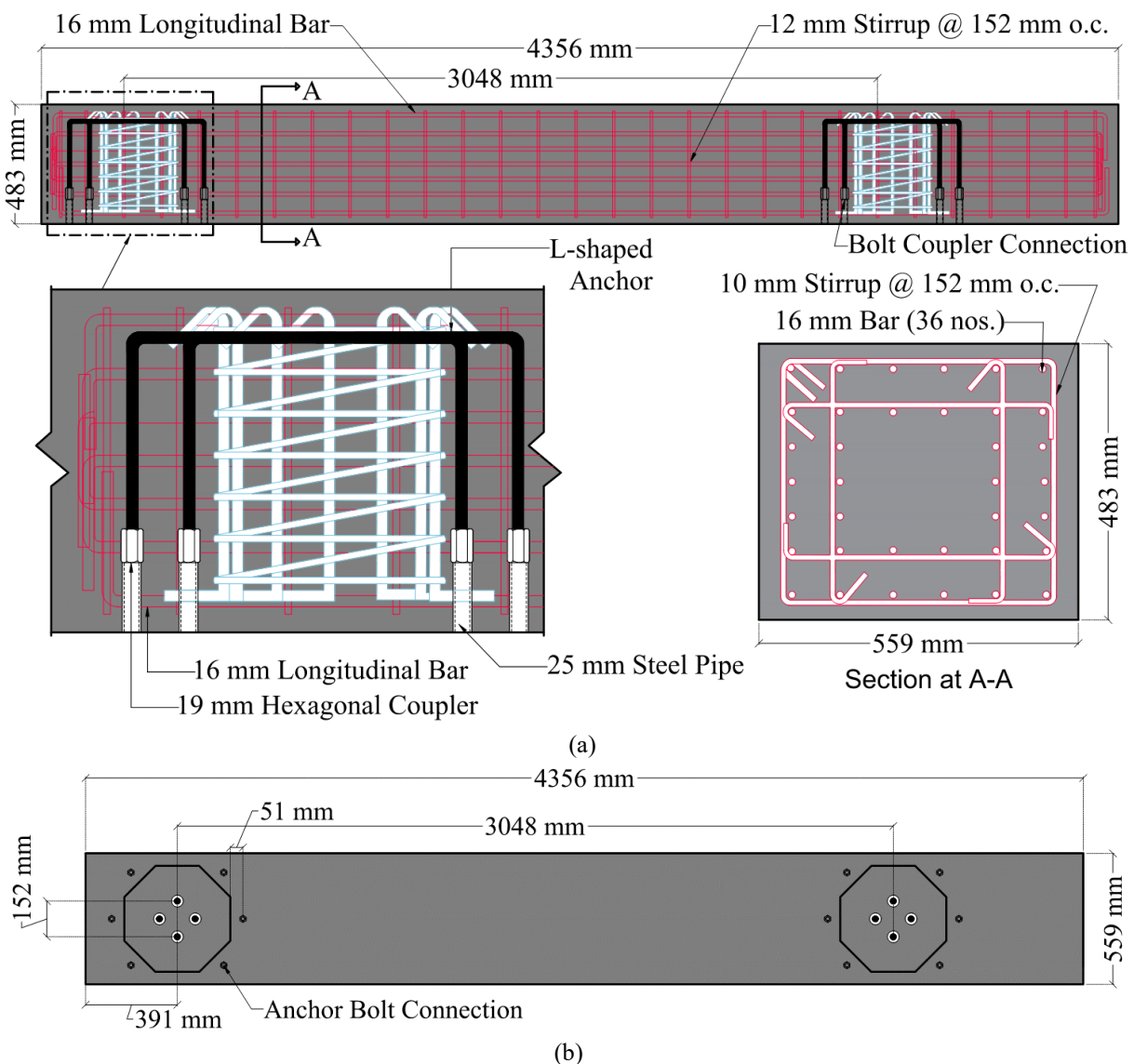


Figure 7. Cap beam details: (a) elevation and reinforcement; and (b) anchor bolt connection details and bottom view.

3.5.3 Footing Details

The footings had a size of 1829 mm x 914 mm x 508 mm, as shown in **Figure 9**. Each footing had eight 25 mm diameter longitudinal bars at the top and bottom. The shear key was 508 mm octagonal and 51 mm deep. All longitudinal bars were bent 90° to satisfy anchorage and development length. All top and bottom longitudinal bars were enclosed with 12 mm diameter double hoops spaced 102 mm on center **Figure 9(c)**. Additional confinement was provided below the octagonal recess; twelve 16 mm diameter vertical bars with 90° hooks on one end and 135° hooks on the other end were tied with 10 mm diameter spiral hoops at a 63 mm pitch. Eight anchors were embedded in the footing as shown in **Figure 9(a, b)**; L-shaped anchors were connected to 51 mm long couplers 127 mm below the footing top, as shown in **Figure 9(b)**. The coupler was welded to a 25 mm inside diameter hollow steel pipe to prevent concrete from entering the coupler and for installation of SLAs. The 25 mm thick steel base plates used for anchoring the PT bars were located at the bottom of the footings and the base plate dimensions are shown in **Figure 9(b, d)**.

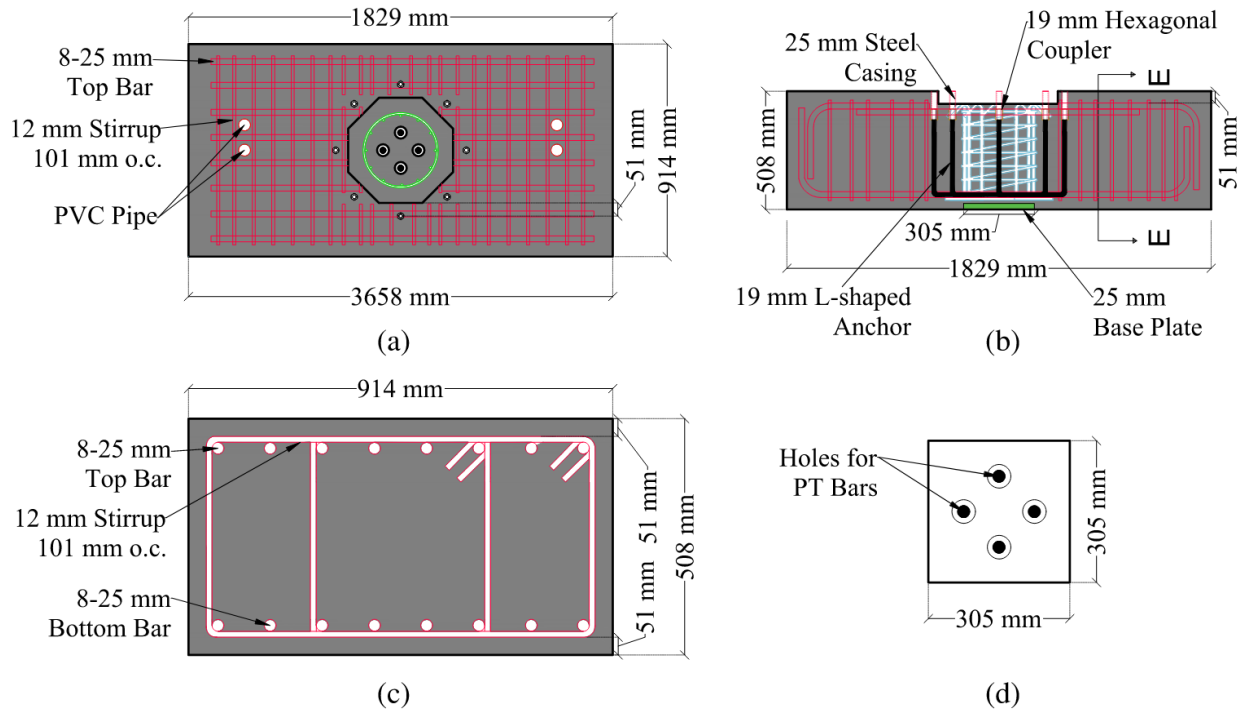


Figure 9. Footing details: (a) footing plan; (b) footing section in longitudinal direction; (c) section at E-E; and (d) 25 mm thick steel base plate for anchorage of PT bars.

3.5.4 Computation of Number of PT bars and SLAs

Optimization of the number of PT bars and SLAs is necessary to meet self-centering requirements. For each column, the total ultimate tensile strength at the rocking joint is determined based on the assumption of a force generated by a 1.0% to 2.0% column longitudinal steel reinforcing ratio (Guerrini et al. 2015a). For the experimental study 2.0% was used as a longitudinal reinforcing ratio. Eq. (3.1) can be used to compute the ultimate tensile strength (T_{ult}) for each column:

$$T_{ult} = 0.02 * A_g * f_u \quad (3.1)$$

where A_g is gross area of the column cross-section, and f_u is the ultimate tensile stress of the reinforcing bars. Once the value of T_{ult} is computed, it is distributed between the post-tensioning force and the external energy dissipators attached to the column. This distribution is given as (Guerrini et al. 2015b):

$$T_{ult} = F_{PT,y} + F_{SLA} \quad (3.2)$$

where $F_{PT,y}$ is the total PT force at yield of all bars in tension for each column and F_{SLA} is the total force dissipated by all the external dissipators in one column.

Self-centering of the rocking system can be verified using self-centering efficiency (Λ_c) which is recommended to be less than 1.0 to ensure self-centering, however when uncertainties on post-tensioning losses and debris formation in gaps are considered a value for Λ_c limit of 0.6 is used. The energy dissipation coefficient (Λ_D) should be higher than 0.1 to satisfy energy dissipation (Guerrini et al. 2015a) which is given as:

$$\Lambda_c = \frac{F_{SLA,y}}{P_u + F_{PT,i}} \leq 1.0 \quad (3.3a)$$

$$\Lambda_D = \frac{F_{SLA,u}}{P_u + F_{PT,i} + F_{SLA,u}} \geq 0.1 \quad (3.3b)$$

where P_u is the gravity load in one column and $F_{PT,i}$ is the initial PT load for all the PT bars in one column. From Eq. (3.1) T_{ult} is equal to 2332 kN; for a bent with four PT bars in each column, based on manufacturer data, $F_{PT,y}$ for four PT bars is equal to 1816 kN; from Eq. (3.2) this leaves a tensile force F_{SLA} equal to 516 kN to be dissipated by the SLAs.

The initial PT force was determined using rigid body analogy principles as provided in the PRESSS Handbook (Pampanin et al. 2010). Various initial PT force values were considered for the experimental study: the change in PT force was determined by computing the PT bar strain at

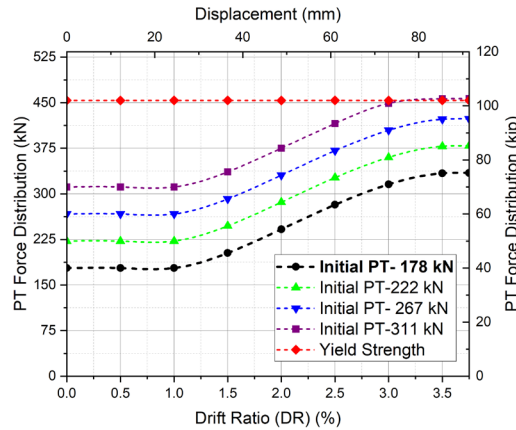


Figure 10. Variation of PT force for various levels of initial PT force using rigid body analogy.

a certain drift ratio; this strain was transformed to stress and the trajectory of the PT force was evaluated (**Figure 10**). Based on **Figure 10**, an initial PT force value of 178 kN was chosen for each PT bar to avoid yielding of the PT bars; thus, the total initial PT force $F_{PT,i}$ in each column was 712 kN. A gravity loads P_u equal to 303 kN was applied to each column. Eq. (3.3) gives an energy dissipation coefficient Λ_D equal to 0.48, greater than 0.1 and a self-centering coefficient Λ_c equal to 0.91, less than 1.0; this shows good self-centering performance and energy dissipation. Apart from the use of forces obtained from the structure, calculations based on the moment capacity of the column and axial load capacity of the collar can be used for a better estimate of the self-centering coefficient. Once the required tensile force dissipated by the SLA (F_{SLA}) is determined, the number of SLAs can be found based on the yield strength of SLAs ($F_{y,SLA}$) and the cross-sectional area of each SLA (A_{SLA}) as:

$$F_{SLA} = n * F_{y,SLA} * A_{SLA} \quad (3.4)$$

where, n is the number of SLAs. The number of 19 mm ASTM F1554 Grade 36 SLAs required to distribute the 516 kN force is calculated by assuming that each SLA experiences a force equivalent to the yield force, or 69 kN; from Eq. (3.4), eight SLAs are required. In the 4FA experiment, there are eight SLAs at the bottom and six SLAs on the top, of which only five are activated in tension at the bottom and three are activated in tension on the top.

3.5.5 Steel Collar Thickness, Length, and Stud Count Calculation

The rocking column with an external energy dissipator must be protected from crushing, as the concrete toe experiences high compressive loads during rocking, potentially causing damage. To prevent this, steel collars or jackets are used to safeguard the concrete at the column ends. Without sufficient collar height, the concrete just above the surface may be damaged. Therefore, designing the appropriate thickness and length of the steel collar is crucial to protect the rocking toe and high-stress zones. Roh and Reinhorn (2009) provided equations to calculate the steel collar length based on the neutral axis depth and column's equivalent diameter, which was then adjusted by an overstrength factor recommended by AASHTO (2015). The steel collar thickness was determined using the equation by Guerrini et al. (2015a). The resulting collar length was 457 mm, and the thickness was 13 mm. Additionally, steel plates must be placed on both ends of the column and welded to the steel jacket to prevent concrete crushing during rocking.

Beyond protection, the steel collar also transfers forces generated in the steel chairs when SLAs elongate. To prevent the jacket from being pulled out, force dissipation methods are necessary. In the experimental study, three 25 mm diameter studs were welded to the jackets on each side of the column to transfer the forces caused by SLA elongation as shown in **Figure 6(d-h)**. Detailed computations of stud numbers and diameters are covered in subsequent sections.

3.5.6 Installation of SLAs

L-shaped anchors in the footings and cap beam were used to connect the precast concrete elements. At each location, there were eight 19 mm ASTM F1554 Grade 36 L-anchors embedded in the footing and six L-anchors in the cap beam (ASTM 2018). At the end of each L-anchor, a hexagonal coupler was attached with threads inside, as shown in **Figure 11**. In the footing and cap beam, the bottom part of the 19 mm (d_b) diameter L-anchor bolt has a minimum bent diameter of 114 mm ($6d_b$) and a development length of 381 mm ($20d_b$), as shown in **Figure 11(a)**; this development length is sufficient to transfer the load transmitted by the couplers (ACI 314-18). Straight SLAs

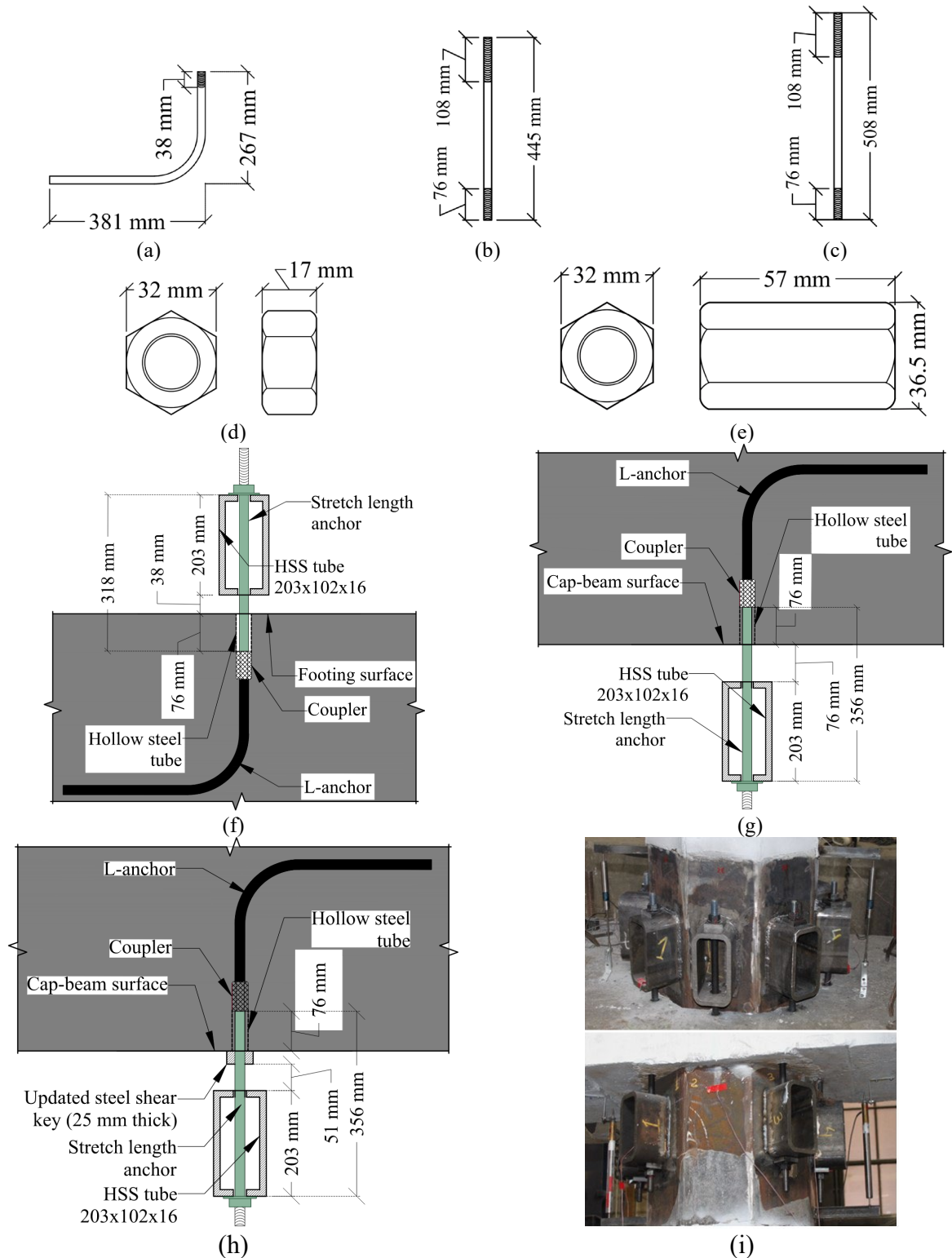


Figure 11. Stretch length anchor details: (a) L-shaped anchor; (b) SLA for footing; (c) SLA for cap beam; (d) hexagonal nut; (e) coupler; (f) connection at footing; (g) connection at cap beam 4F and 4FA; (h) installation at footing; and (i) connection at cap beam 4FB and 4FBA.

with threaded ends attached to hexagonal couplers. The 19 mm diameter SLAs had a length of 445 mm at the footing (**Figure 11(b)**) and 508 mm at the cap beam (**Figure 11(c)**). The SLA had threads at both ends, with 76 mm of thread at the end fastened to the coupler and 108 mm at the end fastened to the HSS steel tube. The dimensions of the hexagonal nut used to attach the SLA to the steel chair are shown in **Figure 11(d)**. **Figure 11(e)** shows the dimensions of the coupler used to connect the SLAs to the footing (**Figure 11(f)**, **Fig. 4(b)**), and the cap beam (**Figure 11(g, h)**).

The SLAs pass through 102 mm x 203 mm x 16 mm HSS steel tube used as a steel chair; this simplifies construction of SLAs compared to previous details (Parks et al. 2019; Thapa and Pantelides 2021). There was a 38 mm gap between the HSS tube and footing top (**Figure 11(f)**) and a 76 mm gap between the HSS tube and cap beam bottom (**Figure 11(g)**) for bent with shear key only in the footing and gap between HSS tube and cap beam base for the bents 4FBA and 4FB was; maintaining a minimum 38 mm gap from the concrete surface prevented contact of the HSS tube and concrete surface thereby eliminating damage and allowing free rocking action. Gap calculations were based on rigid body column rotation at maximum drift.

The stretch length from coupler to nut at the footing was 318 mm ($17d_b$) (**Figure 11(f)**), and 356 mm ($19d_b$) for the cap beam (**Figure 11(g, h)**) that are greater than the recommended stretch length of $8d_b$ (ACI 314-18; Soules et al. 2016; Trautner et al. 2017; Parks et al. 2018; Parks et al. 2020). A nut is used on one side of the HSS tube horizontal plate (top plate for footing in **Figure 11(f)** and bottom plate for cap beam in **Figure 11(g, h)**) so that SLAs work only under tension. A 13 mm thick washer was used to secure the SLAs, as shown in **Figure 11(f-i)**. **Table 3** shows the stretch length and gap between steel chair base and cap beam and footing surface.

Table 3. Stretch length and steel chair gap with concrete surface.

Specimen	Stretch length		Gap with steel chair	
	Footing (mm)	Cap beam (mm)	Footing (mm)	Cap Beam (mm)
4FA	318	356	38	76
4FBA	318	356	38	51

3.5.7 Post-tensioning Bars

PT bars meeting ASTM A722 and AASHTO M 275 were used (AASHTO 2011; ASTM 2018). The 1034 MPa all-threaded bars were smooth, hot rolled, high strength steel that are effective when used for self-centering due to their elastic behavior up to 80% of the ultimate tensile strength. Four 25 mm diameter, 3404 mm long PT bars were used in each column.

3.6 LOADING PROTOCOL AND GRAVITY LOAD

A displacement-based lateral quasi-static cyclic load was applied using a hydraulic servo actuator up to 3.5% drift ratio. The load was applied horizontally at the cap beam mid-height, located 2388 mm from the footing top (**Figure 2**), at a rate of 30 mm/min. The time history for the quasi-static displacement-controlled load applied to the cap beam using a hydraulic jack is shown in **Figure 12(a)**. The axial load system using rollers was effective in keeping the axial load variation limited. **Figure 12(b)** shows the axial load variation with drift ratio for both tests.

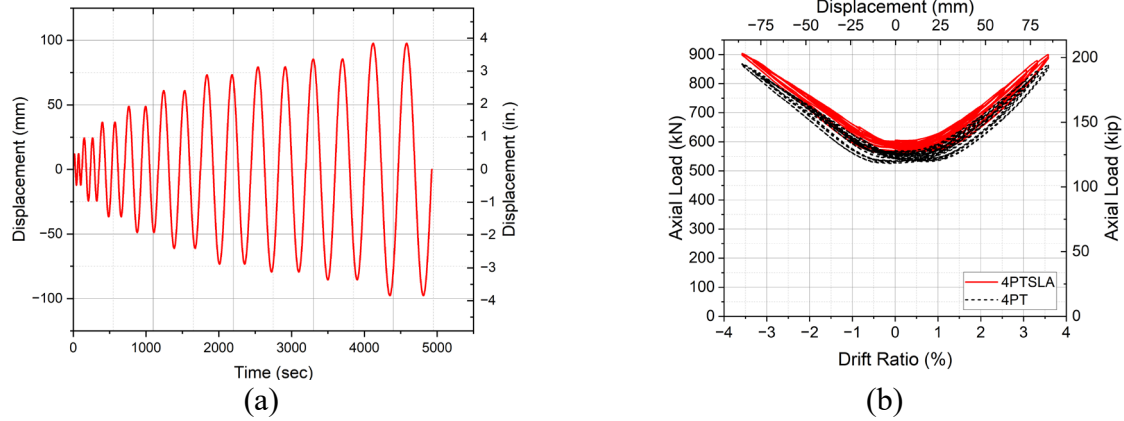


Figure 12. Applied lateral and axial load: (a) Cyclic loading protocol; and (b) Axial load.

3.7 MEASURED MATERIAL PROPERTIES USED IN THE STUDY

Various materials, including concrete, steel plates, steel collars, SLAs, and PT bars, were used in the experimental study, and their properties were crucial for evaluating the results. The compressive strength of high-strength self-settling concrete was 86 MPa for specimens 4FA and 4F, and 93 MPa for 4FBA and 4FB on the test day. Other properties, such as those of steel plates and PT bars, were as determined by the manufacturer as shown in **Table 4**.

Table 4. Material properties used in the experiments.

Components		Material Properties
Concrete	f'_c	86 MPa - Bents 4FA/4F
		93 MPa - Bents 4FBA/4FB
Stretch Length Anchors	f_y	272 MPa
	f_u	399 MPa
Studs	f_y	301 MPa
	f_u	426 MPa
Steel Plates	f_y	345 MPa
	f_u	455 MPa
PT bars	f_y	827 MPa
	f_u	1034 MPa
Mild Steel Bars	f_y	469 MPa (expected)
	f_u	641 MPa

Note: f'_c = compressive strength on test day; f_y = yield strength; and f_u = ultimate strength.

CHAPTER 4. EXPERIMENTAL RESULTS FOR BENTS WITH STRETCH LENGTH ANCHORS (SLAS)

4.1 HYSTERETIC PERFORMANCE OF BENT 4FA AND 4FBA

The hysteretic response of the specimen with SLAs (4FA and 4FBA) under lateral quasi-static cyclic loading was evaluated; the displaced shape during the maximum pull and push at 3.5% drift ratio for specimen 4FA and 4.0% drift ratio for specimen 4FBA is shown in **Figure 13(a, b)**. The hysteresis curves for 4FA in Fig. 9(a) show that the force-displacement performance was governed by yielding and elongation of SLAs; symmetric and stable behavior with efficient hysteretic energy dissipation and self-centering was observed. The hysteretic response of both bents with external dissipators are compared in **Figure 13(c)**. For most of the loading protocol the bents showed symmetric hysteretic performance; during the test of Bent 4FBA the columns reacted against the shear keys in the cap beam resulting in unsymmetric hysteresis loops (**Figure 13(b)**). The highest peak load was 660 kN for Bent 4FA at 3.5% drift ratio, and 705 kN for Bent 4FBA at 4.0% drift ratio. No lateral load reduction or unreparable damage was observed in any of the experiments.

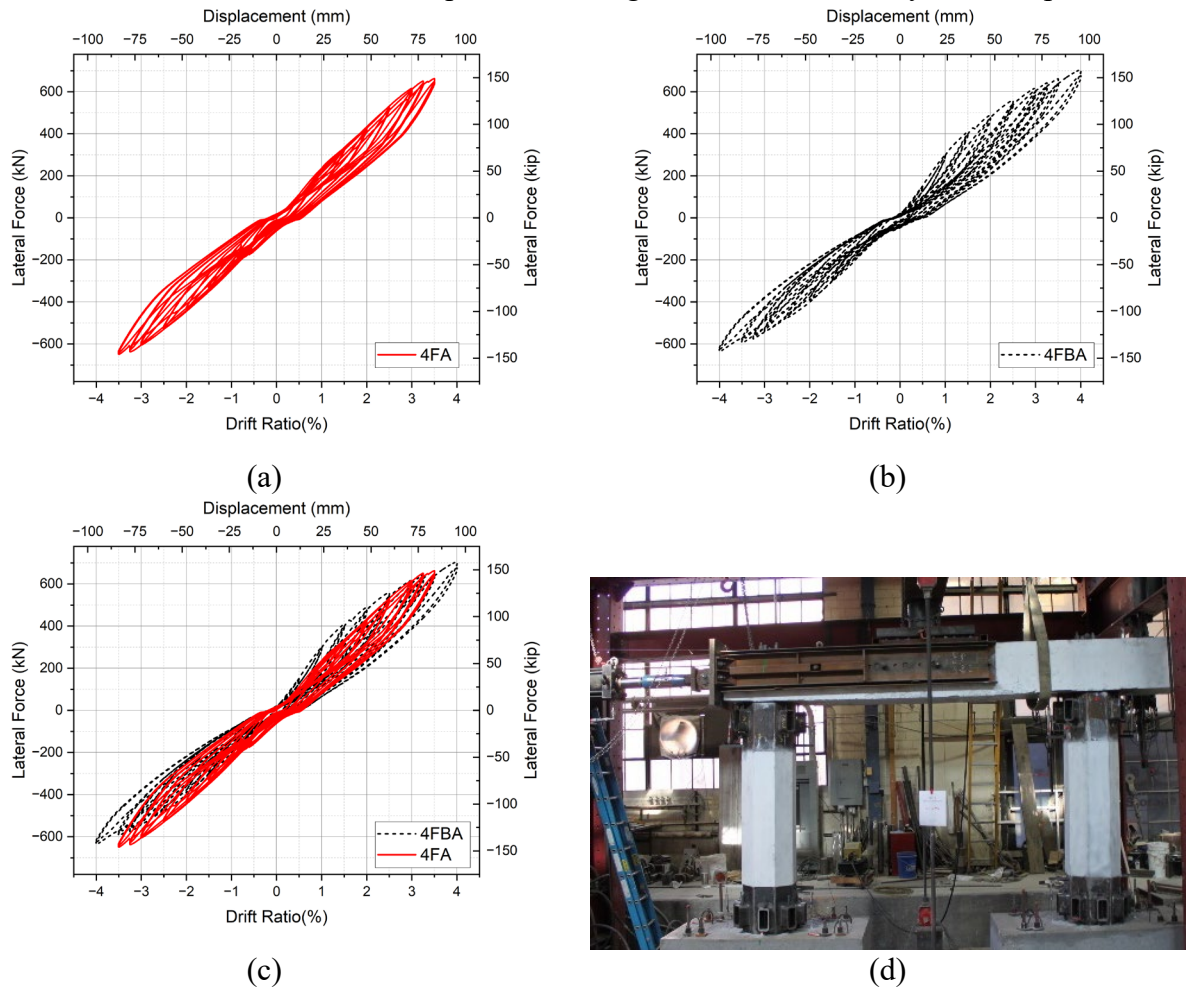


Figure 13. Hysteretic response comparison of bents with SLAs: (a) Bent 4FA; (b) Bent 4FBA; (c) comparison between 4FA and 4FBA; and (d) deflected shape of 4FA at the end of the test.

There was no yielding of PT bars while the SLAs started yielding at 1.0% drift ratio for both 4FA and 4FBA specimen. The SLAs elongated up to an amount equal to the anchor diameter but none of them fractured. **Figure 13(d)** shows the deflected shape of bent 4FA during the 3.5% drift ratio. There was no permanent deformation of the PT bars in the experiments involving SLAs; this is attributed to the fact that SLAs were able to resist a portion of the lateral force.

4.2 POST TENSIONING FORCES OF BENTS WITH SLAS

The initial post-tensioning force was determined using rigid body analogy. A similar initial PT force was used for both specimens to maintain self-centering coefficient. As lateral displacement increased, the PT bars elongated and increased the post-tensioning forces. **Table 5** shows the initial, maximum, final, and maximum variation in post-tensioning forces. All PT bars remained elastic thus improving self-centering. The maximum force in each PT bar for all specimens remained nearly identical for a given drift ratio since PT bars elongated by a similar amount based on rigid body rotation.

Table 5. Post-tensioning force variation for bents with SLAs.

Specimen	Initial force per PT bar	Maximum force per PT bar	Final force per PT bar	Percentage variation
	kN	kN	kN	%
4FA (up to 3.5%)	178	325	153	15
4FBA	178	383	129	28

4.3 RESIDUAL DRIFT AND RE-CENTERING PERFORMANCE OF BENTS WITH SLAS

Post-tensioned bridge bents are designed to self-center after an earthquake. Post-tensioning bars must remain elastic and the re-centering bending moment from the superstructure weight and column post-tensioning forces must exceed the dissipative moment. Prompt restoration of the bent to its original position after an earthquake eliminates the need for retrofit. It has been proposed that the residual drift ratio after an earthquake should not exceed 1.0% (Kawashima 1997). The two bents with SLAs had a residual drift ratio below 1.0% drift ratio. Bent 4FBA had a residual drift ratio of 0.5% at the end of 4.0% drift ratio, and Bent 4FA had a residual drift ratio of 0.4% at the end of 3.5% drift ratio. The residual displacement for the three bents is shown in **Figure 14(a)**. Self-centering efficiency is another method for evaluating residual displacements. The relative self-centering efficiency (RSE) is found by computing the portion of the peak deformation which can be recovered as (Sideris et al. 2014):

$$RSE = 1 - \frac{u_{res}^+ - u_{res}^-}{u_m^+ - u_m^-} \quad (5)$$

where u_{res}^+ , u_{res}^- = positive and negative residual displacement for the given cycle; and u_m^+ , u_m^- = maximum positive and negative displacement for the given cycle. In **Figure 14(b)** it is evident that the RSE for the bents with four PT bars per column reaches 0.91 for both bents at the end of the test and does not fall in the region with residual drift ratio greater than 1.0%. Without the shear key, the steel plate dug into the concrete at zero displacement without any sliding and reduced the

relative self-centering and residual displacement in the case of a bent with shear-keys in both footings and cap-beam.

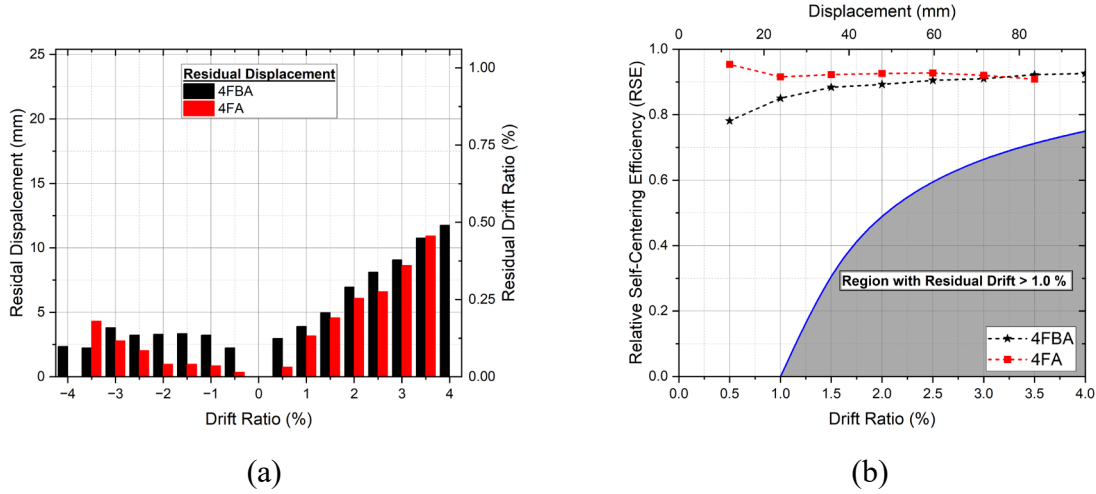


Figure 14. Recentering efficiency of bents with SLAs: (a) residual displacement; and (b) relative self-centering index.

4.4 BACKBONE CURVE AND STIFFNESS DEGRADATION OF BENTS WITH SLAS

The backbone curve for each bent was computed by selecting the peak force at maximum displacement for each drift ratio, as shown in **Figure 15(a)**. Bent 4FBA had a peak load of 702 kN compared to 663 kN at 3.5% drift ratio for bent 4FA. **Figure 15(b)** shows the secant stiffness in both push and pull directions. The bents with external energy dissipators experienced a rapid degradation in stiffness; this is attributed to the continuous strength degradation of the external dissipators, since they yielded at a relatively small drift ratio of 1.0%. Bents 4FA and 4FBA rocked freely since there was no interaction between steel chairs and concrete surface.

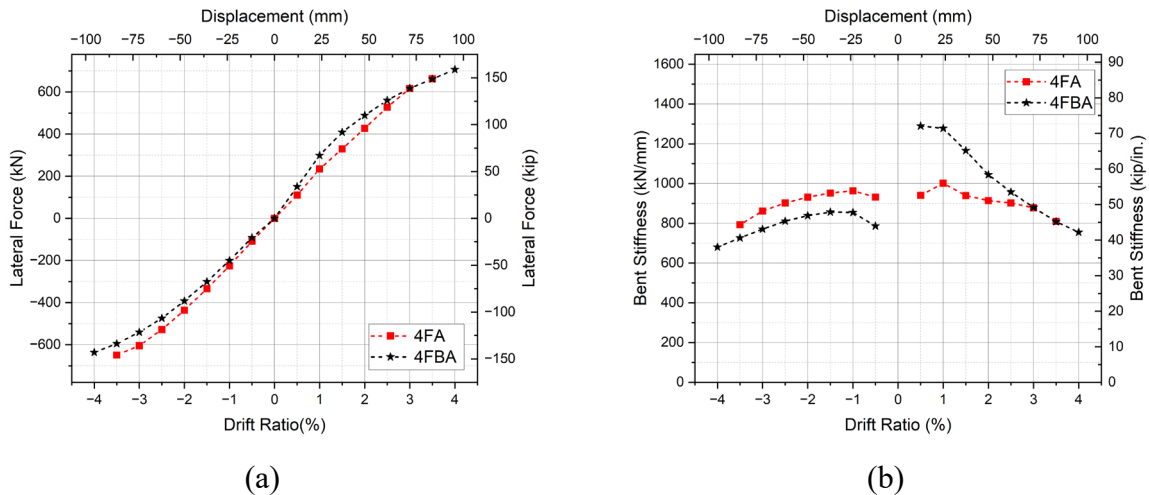


Figure 15. Performance envelope for bents with SLAs: (a) backbone curve; and (b) stiffness degradation.

Figure 15(b) shows continuous stiffness degradation after the SLAs yielded at 1.0% drift ratio. The asymmetric behavior observed in Bent 4FBA can be attributed to two factors. First,

during the push cycle, the initial stiffness was higher due to the fact that the post-tensioning steel bearing plate wedged against the top surface of the cap beam; this effect diminished once the steel bearing plate returned to its final position. Second, the two columns came into contact with the shear keys at 2.0% drift ratio, resulting in a change in stiffness during the push cycle compared to the pull cycle, where no shear key and column interaction occurred.

4.5 HYSTERETIC ENERGY DISSIPATION OF BENTS WITH SLAS

Hysteretic energy is calculated as the area enclosed by the force-displacement curves. The hysteretic energy dissipation in the case of bent 4FA is attributed to the SLAs, yielding of reinforcing bars, and friction between contact surfaces. Bent 4FA dissipated slightly higher hysteretic energy compared to Bent 4FBA at 3.5% drift ratio since concrete-to-concrete interaction between the cap beam and column top surface in Bent 4FA was replaced by steel-to-concrete interaction in Bent 4FBA (**Figure 16a**).

Equivalent viscous damping is used to assess relative energy dissipation capacity; it incorporates both hysteretic and strain energy. In each cycle, with known stiffness (K) and maximum displacement (u_o), the strain energy (E_s) can be obtained as (Chopra 2007):

$$E_s = \frac{1}{2} K u_o^2 \quad (4.1)$$

The equivalent viscous damping ratio (ξ_{eq}) is expressed as the ratio of hysteretic energy (E_D) to energy of the equivalent viscous system as:

$$\xi_{eq} = \frac{E_D}{4\pi E_s} \quad (4.2)$$

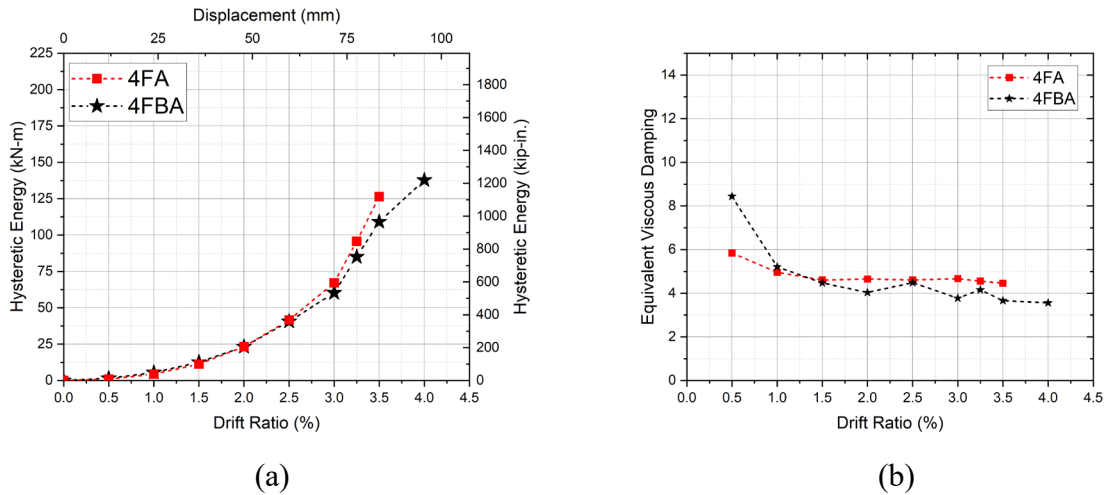


Figure 16. Energy response for bents with SLAs: (a) hysteretic energy; and (b) equivalent viscous damping ratio.

The equivalent viscous damping ratio for each specimen was determined using Eq. (4.2). The experimental results for Bents 4FA, and 4FBA indicate a consistent equivalent viscous damping ratio, with values of 4.5%, and 3.5%, respectively at the end of the tests in **(Figure 16b)**. This behavior shows proportional rise in hysteretic energy compared to strain energy. The value of strain energy and hysteretic energy was calculated based on experimental hysteretic curves and the area under each loop. The hysteretic loops at 2.0% drift ratio and 3.0% drift ratio for bents 4FA and 4FBA are plotted as shown in **Figure 17**. In the first loop the curve shows wider area while in the second loop there is a lower energy dissipation. This was due to the fact that SLAs on the extreme face of the column yielded first, while others towards the center did not yield suggesting some energy dissipation in the second loop.

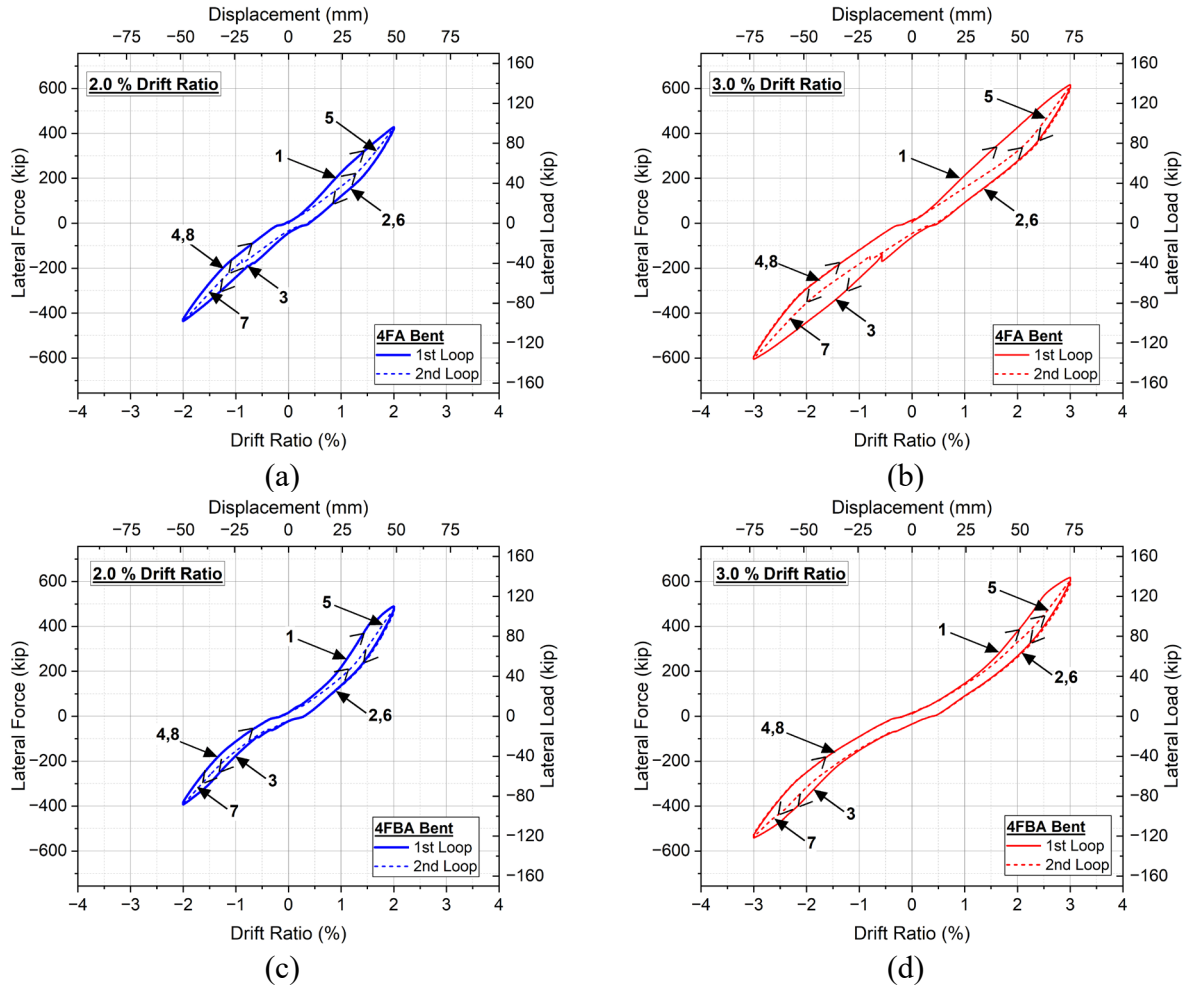


Figure 17. Hysteretic response of bent 4FA and 4FBA: (a and c) At 2.0% drift ratio; and (b and d) At 3.0% drift ratio.

CHAPTER 5. EXPERIMENTAL RESULTS FOR PT-ONLY BENTS

Bents 4F and 4FB shared similar geometry and axial load, both featuring four PT bars per column. Bent 4FB had shear-keys in both the footings and cap beam, engaging steel-to-concrete interaction at both column ends. Bent 4F had shear keys only in the footings, with steel-to-steel interaction at the column base and concrete-to-concrete interaction at the column top. SLAs were removed from the experiments with external energy dissipators for both cases when there is shear key only in the footing and when shear key is in both footing and cap beam. The schematic details of the bents without external dissipators are shown in **Figure 3** and **Figure 5**.

5.1 HYSTERETIC PERFORMANCE OF PT-ONLY BENTS

Both 4F and 4FB bents exhibited primarily linear response. The lateral force capacity of Bents 4F and 4FB was similar, up to a 3.5% drift ratio. The maximum lateral force was 550 kN for Bent 4F at a 3.5% drift ratio, and 650 kN for Bent 4FB at a 4.0% drift ratio. No lateral force

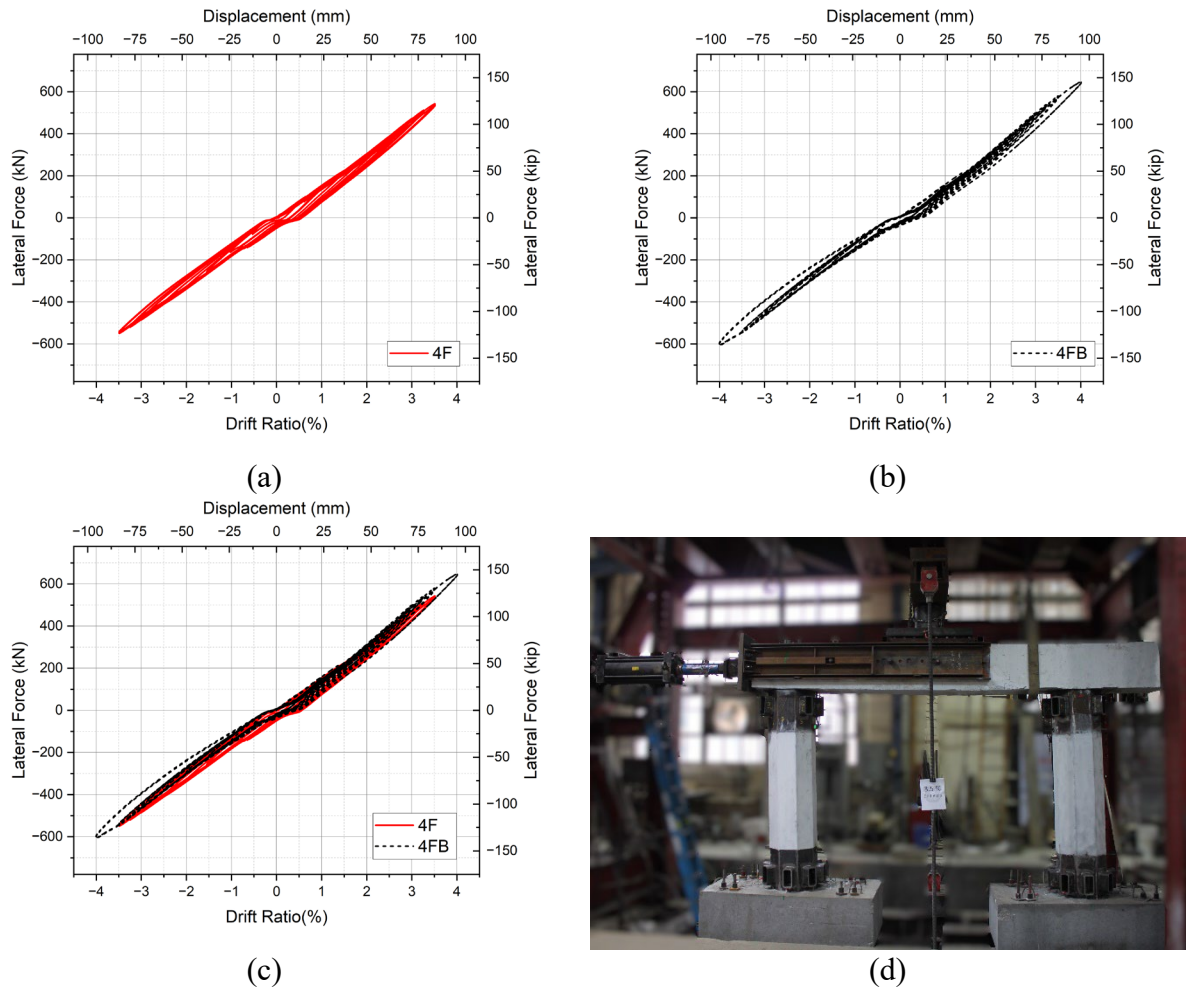


Figure 18. Hysteretic response comparison of bents with SLAs: (a) Bent 4F; (b) Bent; (c) comparison between 4F and 4FB; and (d) deflected shape of 4F at the end of the test (pull cycle).

reduction was observed in any experiment. There was no yielding of column longitudinal steel bars or PT bars in any of the bridge bents up to 4.0% drift ratio. There was no concrete damage observed in the bents with four PT bars per column. Despite the almost entirely linear behavior and excellent self-centering performance, the hysteretic energy dissipated was relatively low, since there was no external energy dissipation mechanism. The hysteretic energy dissipated during the test was due to friction between the contact surfaces. **Figure 18(a)** shows the hysteretic response of bent 4F, **Figure 18(b)** shows the hysteretic response of bent 4FB and **Figure 18(c)** shows the comparison of the hysteretic response between bent 4F and 4FB. **Figure 18(d)** shows the deflected shape of the bent 4F during pull cycle at 3.5% drift ratio.

5.2 POST-TENSIONING FORCE OF PT-ONLY BENTS

The axial post-tensioning force in the PT bars was recorded using load cells. Table 6 shows the initial, overall maximum, and final post-tensioning force, and its variation at the end of the test. All PT bars exhibited elastic behavior. Bents 4F and 4FB experienced post-tensioning force loss below 18%; this loss was due to interaction of PT bars with PVC pipe in the column and elastic bending of the PT bars in the column to cap-beam or footing interface during lateral load application. The axial gravity load did not remain constant during the experiment and as the axial gravity load increased, shown in Figure 12(b), the PT forces decreased. Four PT bars in each column contributed to similar maximum post-tensioning force distribution among East and West PT bars and a similar PT force between North and South PT bars as shown in Figure 19.

Table 6. Post-tensioning force variation for bents without SLAs.

Specimen	Initial load per PT bar	Maximum force per PT bar	Final force per PT bar	Percentage variation
	(kN)	(kN)	(kN)	(%)
4F (up to 3.5%)	178	356	152	15
4FB	178	409	147	18

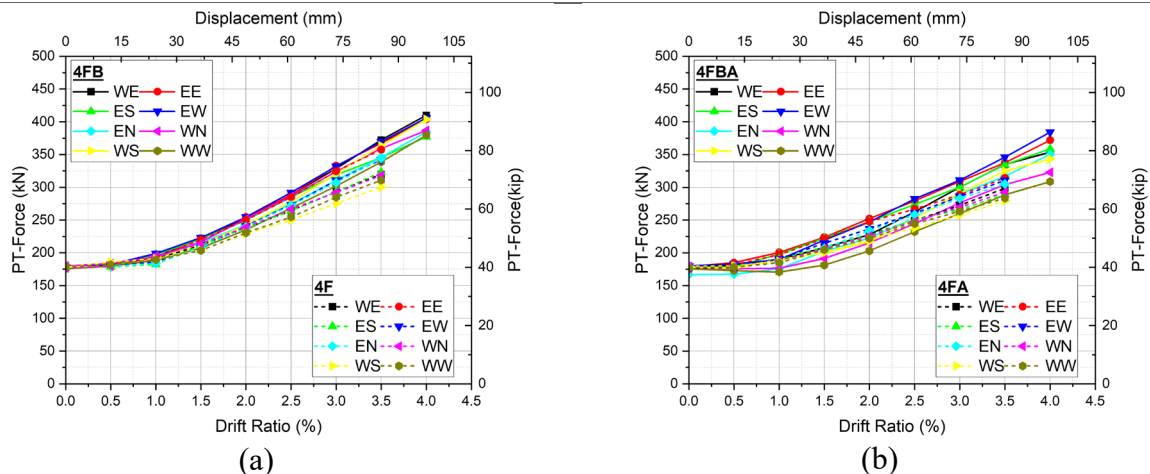


Figure 19. PT force distribution experiment: (a) Specimen bent 4FB and 4F; and (b) Specimen bent 4FBA and 4FA.

5.3 RESIDUAL DRIFT AND RE-CENTERING PERFORMANCE OF PT-ONLY BENTS

All bents without SLAs performed well, and the residual drift ratio remained below 1.0%. The residual displacement for bents 4F and 4FB is shown in **Figure 20(a)**. Bent 4FB had a maximum residual drift ratio equal 0.42% at 4.0% drift ratio; Bent 4F had a residual drift ratio of 0.32% at 3.5% drift ratio. **Figure 20(b)** shows that the relative self-centering efficiency for bents with four PT bars per column is higher, reaching 0.94 and also shows none of the bent lie in the region of residual drift ratio more than 1.0%.

5.4 BACKBONE CURVE AND STIFFNESS DEGRADATION OF PT-ONLY BENTS

The backbone curve for each bent is shown in **Figure 21(a)**. Bent 4FB exhibited a peak lateral force of 649 kN; Bent 4F reached a peak lateral force equal to 552 kN at the end of the 3.5% drift ratio. **Figure 21(b)** shows stiffness degradation of the three bents. Since all PT bars remained within the elastic limit and no external dissipators were present, the stiffness remained relatively constant throughout the tests. The increase in initial stiffness of Bents 4F and 4FB is due to the steel bearing plate at the column top being wedged into the concrete.

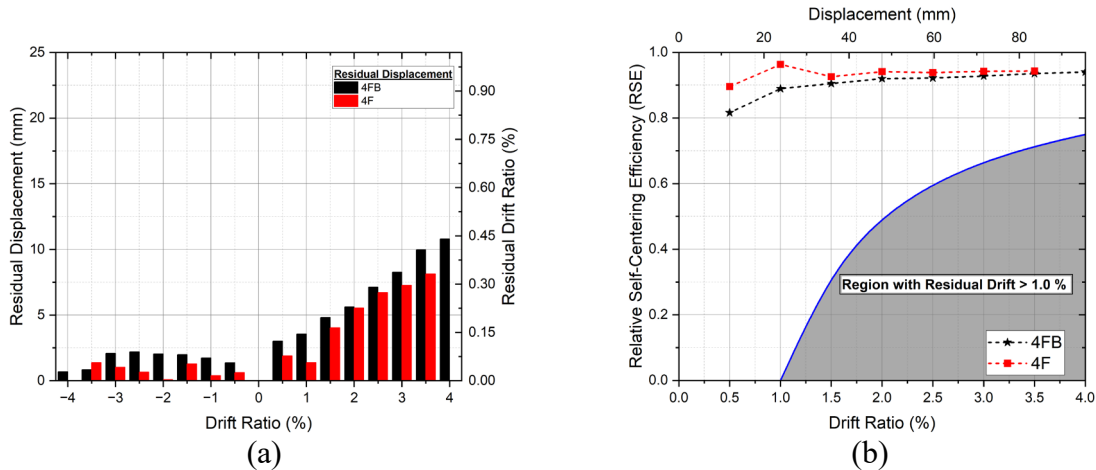


Figure 20. Recentering efficiency of bents without SLAs: (a) residual displacement; and (b) relative self-centering index.

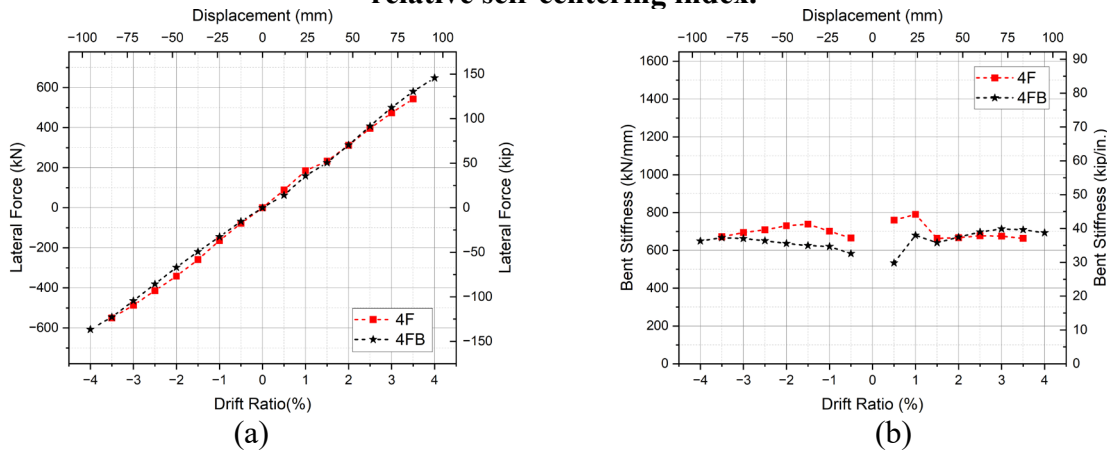


Figure 21. Performance envelope of bents without SLAs: (a) backbone curve; and (b) stiffness degradation.

5.5 HYSTERETIC ENERGY DISSIPATION OF PT-ONLY BENTS

The primary source of hysteretic energy dissipation for bents without SLAs arises from friction between components. Friction occurs at the cap beam surface, footing surface, and interaction of PT bars with PVC pipes. The increased energy dissipation of Bent 4F is attributed to concrete-to-concrete interaction between the cap beam and column surface and steel-to-steel interaction at the footing **Figure 22(a)**. In contrast bent 4FB had steel-to-concrete interaction, resulting in lower frictional resistance and lower hysteretic energy dissipation. The variation of viscous damping is shown in **Figure 22(b)**. Evaluation of equivalent viscous damping shows that the damping ratio gradually decreases, with Bent 4F having the highest viscous damping ratio. The viscous damping ratio was 5.5% for Bent 4F and 2.6% for Bent 4FB at the end of the test. The increased viscous damping of Bent 4F is attributed to concrete-to-concrete interaction between the cap beam and column surface and steel-to-steel interaction at the footing.

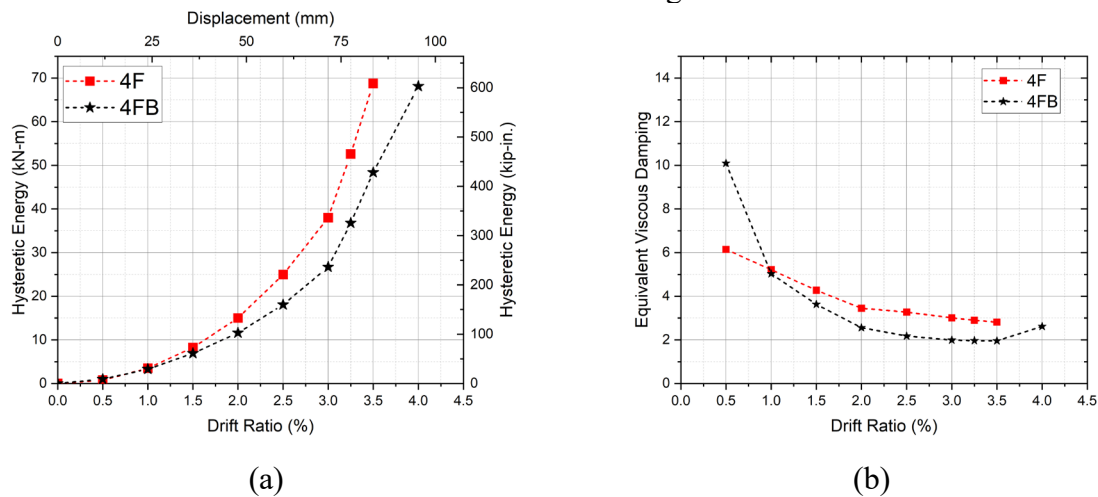


Figure 22. Energy response for bents without SLAs: (a) hysteretic energy; and (b) equivalent viscous damping ratio.

CHAPTER 6. COMPARISON OF BRIDGE BENTS WITH AND WITHOUT STRETCH LENGTH ANCHORS

This section presents a comparison of the hysteretic performance of bents with similar shear key details to determine the hysteretic energy provided by the SLAs. To enhance performance, the bents with four PT bars had a steel jacket height of 457 mm, a large gap between steel chair and concrete surface, and the steel plate at the column base was welded to the steel jacket, which protected the concrete column toe from crushing. As the lateral force increased, the gap between the column and footing, and the gap between column and cap beam increased which allowed damage-free rocking with larger rotations.

6.1 HYSTERETIC PERFORMANCE COMPARISON

Hysteretic response was compared between bents of similar geometry and similar shear key configuration with the difference being the inclusion of SLAs. In **Figure 23(a)**, comparison of Bent 4FA and Bent 4F shows that the initial stiffness of Bent 4FA is 1.4 times that of Bent 4F,

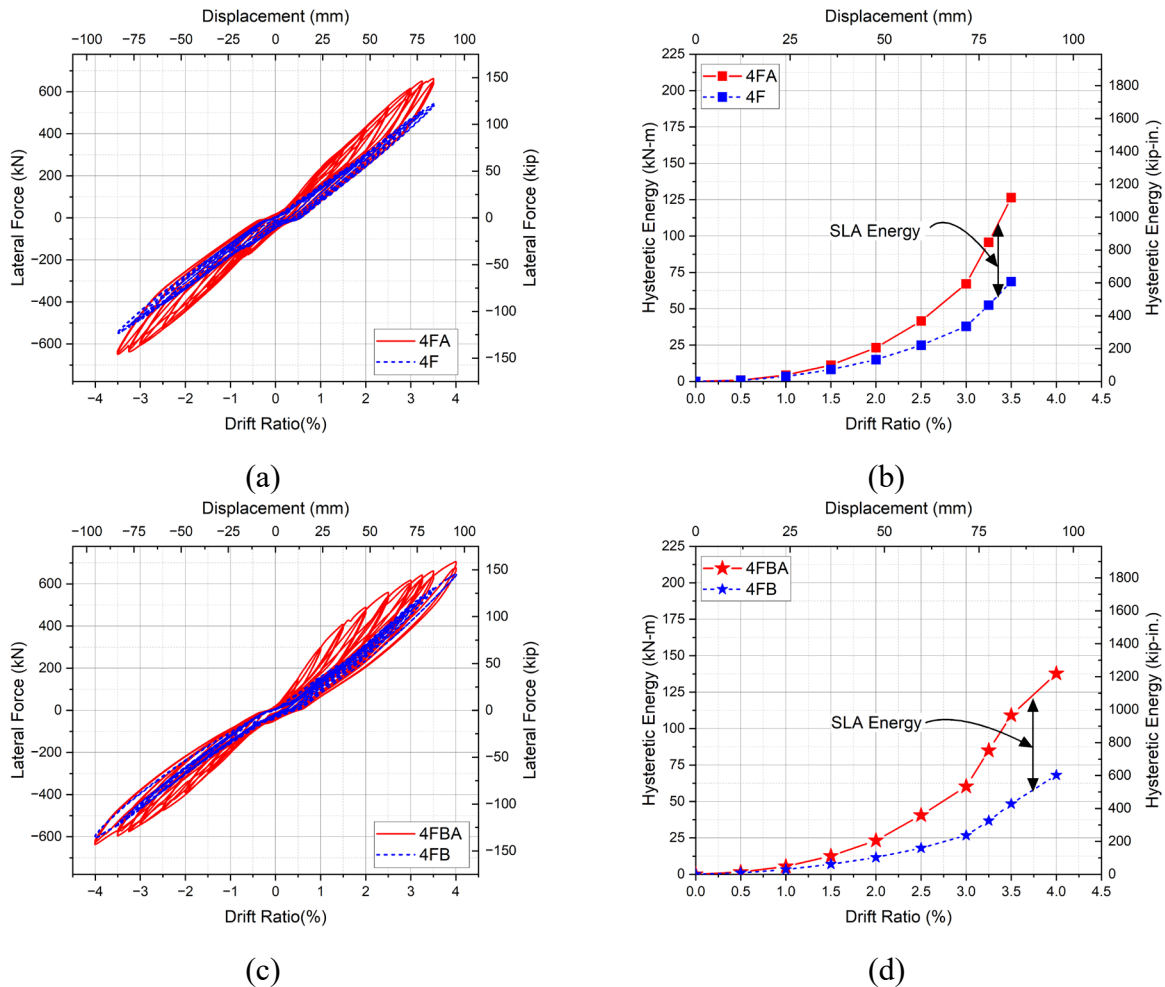


Figure 23. Hysteresis and hysteretic energy: (a, b) Bent 4FA and 4F; and (c, d) Bent 4FBA and 4FB.

with the SLAs contributing to the increased initial stiffness. **Figure 23(b)** shows that the hysteretic energy of Bent 4FA is 1.8 times that of Bent 4F, due to the energy dissipated by SLAs. **Figure 23(c)** shows that the initial stiffness of Bent 4FBA was 2.4 times that of Bent 4FB and **Figure 23(d)** shows that Bent 4FBA dissipated 2.0 times the hysteretic energy of Bent 4FB. SLAs on the extreme end yield first while the SLAs close to the neutral axis yield later causing some energy to be dissipated by the SLAs which have not yielded in subsequent cycles.

6.2 HYSTERETIC PERFORMANCE OF STRETCH LENGTH ANCHORS

Since the loading protocol, geometry, and axial load simulating the superstructure weight in the tests was the same, the hysteresis curves of the bents with no SLAs were subtracted from the hysteresis curves of the bents with SLAs; this resulted in the hysteretic response of the SLAs. The tension-only anchors require a higher displacement to elongate once they yield; this pattern is evident for both the push (first quadrant) and pull (third quadrant) directions.

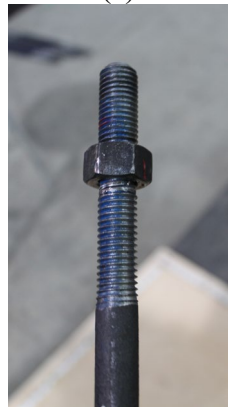
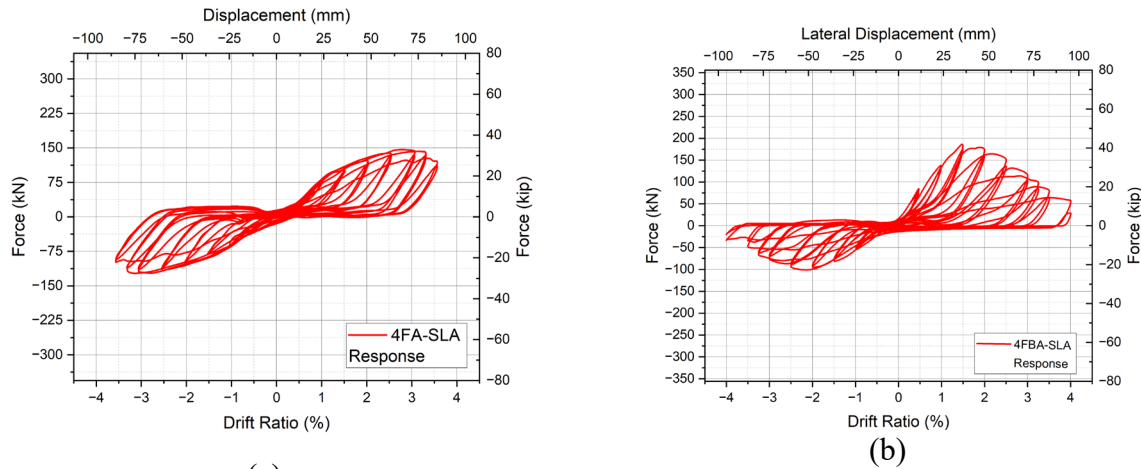


Figure 24. Hysteresis from energy dissipation mechanisms: (a) SLA hysteresis for Bent 4FA; (b) SLA hysteresis for Bent 4FBA; (c) SLA after the experiment for Bent 4FA; and (d) elongated SLAs for test 4FBA.

When drift is in the push direction (**Figure 2**), SLAs at the column bottom west face and column top east face are in tension; when drift is in the pull direction, SLAs at the column bottom east face

and column top west face are in tension. **Figure 24(a, b)** shows the hysteretic response of energy dissipating SLAs only for Bents 4FA, and 4FBA, respectively. **Figure 24(a)** shows the hysteretic response of SLAs alone for Bent 4FA. The response of SLAs in the case of Bent 4FBA, shown in **Figure 24(b)**, is not symmetric compared to SLAs in Bent 4FA since the columns of Bent 4FBA touched the shear keys when loaded in the push direction.

The hysteretic loops of the SLAs exhibit certain energy dissipation in the second cycle at each drift ratio. This behavior is attributed to the fact that some SLAs, particularly those located closer to the neutral axis of the column, yield at a later cycle. These SLAs display lower apparent stiffness and higher yield displacements compared to those positioned farther from the center. **Figure 24(c, d)** shows typical elongation of SLAs at the end of test 4FBA. The hysteric response observed in **Figure 24(a, b)** for the arrangement of SLAs in the experiment indicates the effectiveness of this configuration, exhibiting symmetric hysteric behavior and proving successful performance in both the pull and push direction.

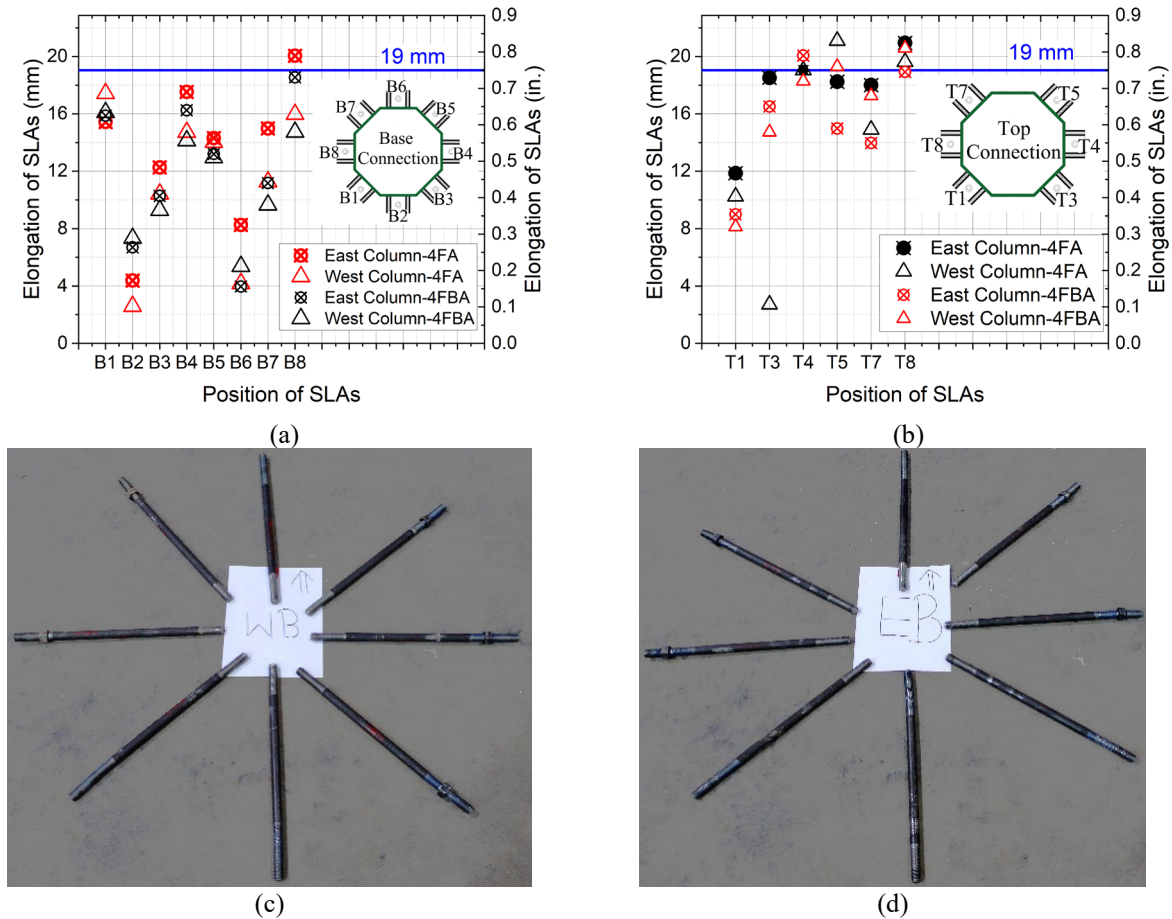


Figure 25. Elongation of 19 mm diameter SLAs at end of experiment: (a) footing SLAs; (b) cap beam SLAs; (c) SLAs attached to west footing (test 4FA); (d) SLAs attached to east footing (test 4FA); and (e) elongated SLA with nut compared to original SLA.

SLAs at the column top and bottom elongated from 2 mm to 22 mm indicating significant hysteretic energy dissipation. **Figure 25(a)** shows that for SLAs attached to the footing, only one SLA elongated more than its 19 mm diameter; **Figure 25(b)** shows that eight SLAs attached to the

cap beam elongated more than 19 mm, or the diameter of the SLAs. A greater number of anchors attached to the cap beam experience elongation exceeding 19 mm compared to those attached to the footing as there was fewer number of SLAs at the cap beam. Some SLAs which were symmetrically located did not elongate by the same amount exhibiting a maximum difference of 20% in elongation; this was because there was some out-of-plane movement of the cap beam. **Figure 25(c, d)** shows elongation of SLAs adjacent to the two footings for test 4FA.

6.3 JOINT GAP OPENING COMPARISON

The LVDT data was used to compute joint rotations; positive rotation denotes rotation during the push cycle, while negative rotation is rotation during the pull cycle. **Figure 26** illustrates the gap opening of the top and bottom joints; joint gap opening was mostly symmetric for both top and bottom joints during push and pull cycles. **Figure 26(a)** shows joint opening of bents with anchors for bottom and top joints. For bents with SLAs and four PT bars per column (Bents 4FA and 4FBA), joint rotation behavior was similar for each drift ratio as shown in **Table 7**. Bents with no SLAs were allowed to rock freely in all cases. The joint rotation of Bents 4F and 4FB with four PT bars per column was similar, as shown in **Figure 26(b)**.

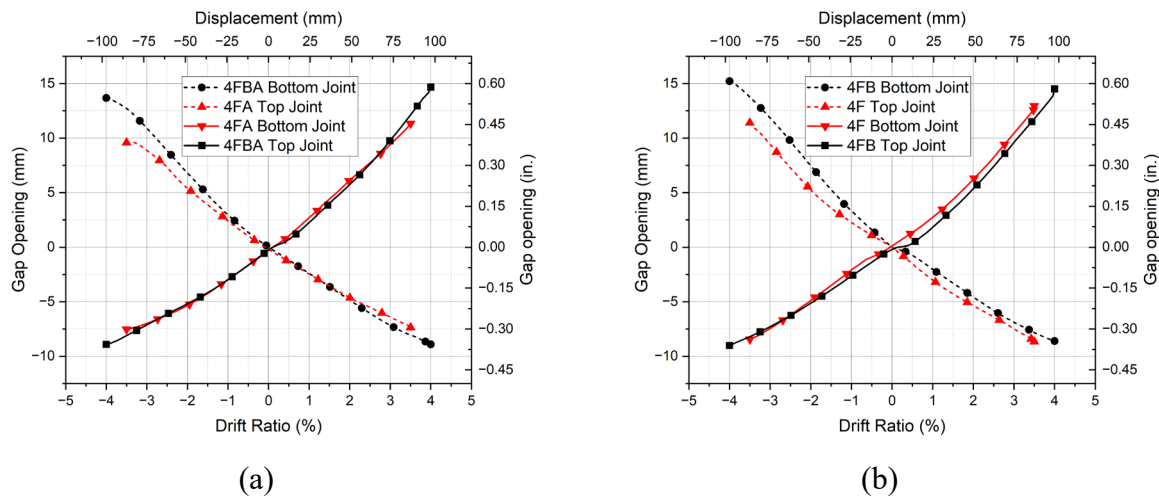


Figure 26. Maximum joint gap opening: (a) bents with SLAs; and (b) bents without SLAs.

Table 7. Maximum joint opening for specimen bents.

Specimen	Maximum Joint Opening (Top)	Maximum Joint Opening (Bottom)
	(mm)	(mm)
4FA (up to 3.5%)	10	11
4FBA	15	14
4F (up to 3.5%)	12	13
4FB	15	15

CHAPTER 7. EXPERIMENTS AND ANALYSIS OF STEEL COLLAR PLATE WITH SHEAR STUDS IN CONCRETE COLUMN STUBS UNDER ECCENTRIC LOAD

7.1 INTRODUCTION

Accelerated Bridge Construction (ABC) is a method that employs innovative materials and construction techniques to reduce construction time and traffic congestion, minimize cost, and enhance safety. One approach that can be incorporated into ABC methods, particularly in seismic regions, is the use of bridge bents with post-tensioned rocking columns. These columns can be enhanced with stretch length anchors (SLAs) to dissipate hysteretic energy. It is important to note that post-tensioned rocking columns are not inherently an ABC technique, as they can be cast-in-place. However, they are well-suited for integration into ABC schemes, typically through precast construction. When implemented as part of an ABC approach, these columns offer several advantages, including rapid on-site assembly and improved seismic performance. Accelerated bridge design increasingly integrates advanced energy dissipation technologies to enhance resilience under cyclic loading conditions. U-shaped dissipators are a prominent example of effectively maintaining structural integrity under high stress without succumbing to fatigue failure which were effective in rocking walls during the Christchurch Earthquake (Pampanin et al. 2011).

In Dissipative Controlled Rocking (DCR) connections, metallic mini-dissipators are utilized for efficient hysteretic energy dissipation. Notably, the grooved dissipator features a machined mild steel bar encased within a tube, facilitating axial yielding to absorb energy. This design is recognized for its cost-effectiveness, high strength, and ductility (White and Palermo 2016). Innovative dissipators demonstrate enhanced performance with minimal strength degradation and notable resistance to low-cycle fatigue (Mashal et al. 2019; Mashal and Palermo 2019b). Furthermore, applying shape memory alloys (SMAs) in self-centering systems influences their distinctive shape-retention properties, substantially improving resilience and self-recovery capabilities under cyclic stresses (Raza et al. 2022, 2023; Roh and Reinhorn 2010).

SLAs are assumed to be an effective measure of energy dissipation and their tension-only nature helps in maintaining self-centering (Thapa and Pantelides 2021). SLAs are specialized energy dissipation devices consisting of mild steel rods designed to yield and elongate during seismic events. These anchors rely on their material properties to provide resistance and energy dissipation, yielding in tension during column rocking and dissipating energy through plastic deformation. Typically used in pairs on opposite sides of a bridge column, SLAs ensure that at least one anchor is in tension during each half-cycle of seismic motion, enabling continuous energy dissipation. Once the SLA yields it requires a larger displacement than the yield displacement to re-engage. This configuration offers several advantages as demonstrated in quasi-static cyclic and shake table experiments (Joel E. Parks Luis Ibarra, and David H. Sanders 2018; Morano et al. 2024; Neupane and Pantelides 2024a; Parks et al. 2015, 2020; Thapa and Pantelides 2021; Trautner et al. 2017). Once SLAs yield, they require a larger displacement than the yield displacement to re-engage.

SLAs are subjected only to tensile forces during rocking of post-tensioned columns, thus they are not susceptible to buckling (Neupane and Pantelides 2024a; b; Thapa and Pantelides 2021). When the bridge is subjected to earthquakes, SLAs provide enhanced ductility; by deforming in tension, they dissipate hysteretic energy and limit damage to the column. This controlled yielding behavior contributes uniquely to the seismic performance of bridges utilizing SLAs; moreover, SLAs do not impede re-centering of post-tensioned bridge columns. The anticipated performance of SLAs in post-earthquake conditions is crucial for bridge safety. After

an earthquake, yielded SLAs would need to be inspected and likely replaced to restore the bridge's seismic capacity. The modular SLA connection system allows for straightforward replacement, unbolting damaged SLAs, and installing new ones. This is possible since SLAs are installed using couplers in the footing and cap beam (Neupane and Pantelides 2024a). This replaceability feature enhances the bridge's resilience and aligns with performance-based seismic design principles,

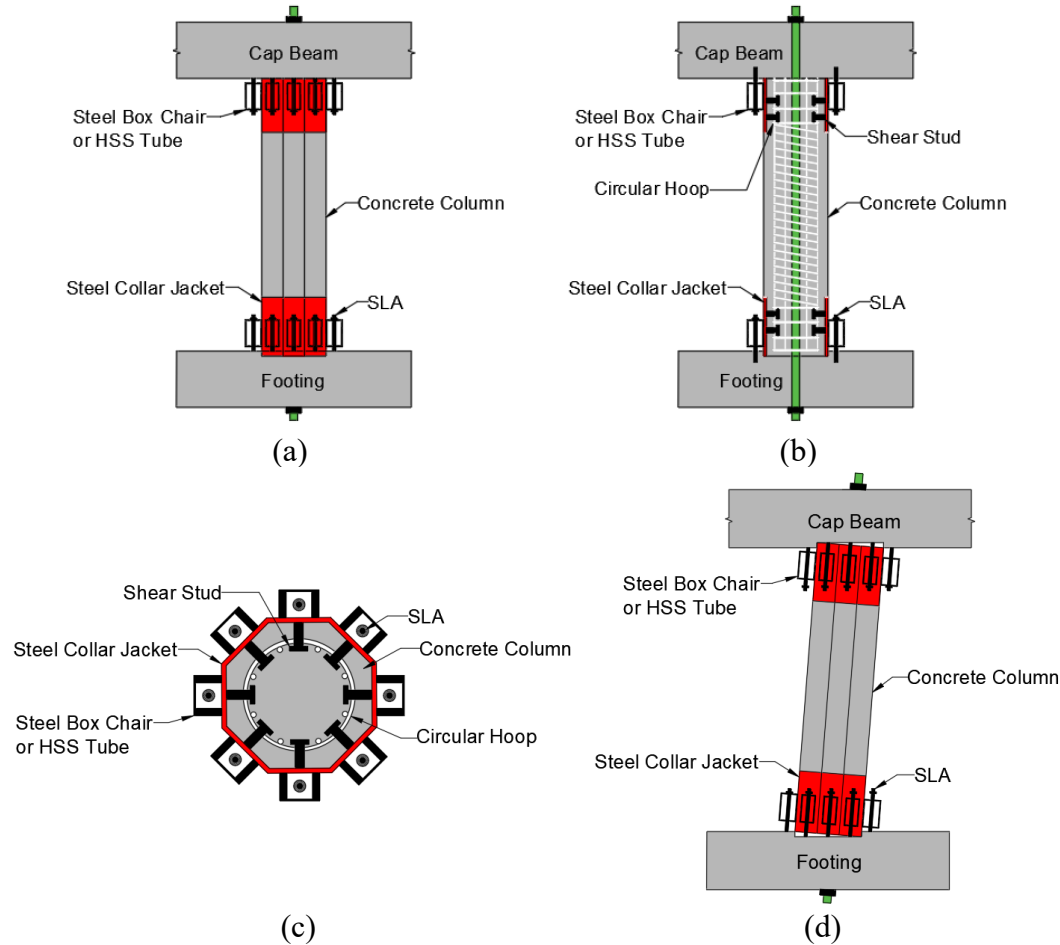


Figure 27. Bridge column with SLAs: (a) exterior; (b) interior; (c) section at SLAs; (d) rocking.

potentially reducing long-term repair costs and downtime. **Figure 27** shows SLAs attached to threaded couplers in the foundation and bolted to steel box chairs (Joel E. Parks Luis Ibarra, and David H. Sanders 2018; Parks et al. 2015) or hollow steel section (HSS) tubes (Neupane and Pantelides 2024a; b). The steel box chairs or HSS tubes are welded to a steel collar jacket composed of welded steel plates at the column ends. Shear studs are welded to the steel collar plates and are embedded in the concrete column, creating a composite member. This composite connection system is important in transferring shear forces and bending moments induced by seismic loads from SLAs to bridge columns.

Figure 27 shows a bridge column with SLAs attached at its ends. Rocking of bridge columns is one method of resisting earthquake forces (**Figure 27d**). When bridge piers resist seismic forces, rocking of the columns creates tensile forces within the SLAs. As a result, cyclic

forces due to rocking cause HSS tubes to apply reverse cyclic shear forces and bending moments to the steel collar jacket plates welded to the column. The steel collar plates, connected to the column via embedded shear studs, transfer these forces to the concrete as shown in **Figure 27(b, c)**.

When a steel beam is connected to a concrete slab, the shear stud connector may take a combination of shear and tension/compression force (Dara 2015). However, welded shear studs connecting steel collar plates to a concrete column will experience direct shear forces resulting from the lateral load transfer between the steel collar and concrete column. Additionally, bending moments are induced by the eccentricity of the shear forces and deformation of the steel collar plate, further contributing to multi-directional loading on the studs. By investigating the shear force and bending moment interaction, the design of a steel collar plate and shear stud connectors to be used in a bridge column can be determined. The design of this embedded connection system which includes steel collar plate thickness, number of shear studs, and shear stud diameter is important to ensure force transfer and structural integrity under seismic loads.

7.1.1 Previous Research

7.1.1.1 Pure Shear Loading

Shear studs are integral to composite structural members, ensuring composite action by connecting steel members to concrete and preventing slip between them. Push-out tests have confirmed that shear studs satisfy strength requirements of bridge design specifications, making them essential for static performance in composite steel bridges (Deng et al. 2024). Research on large-diameter shear studs (25 mm, 27 mm, and 30 mm) highlights their benefits for enhancing structural performance and construction efficiency. Larger studs achieve proper welding quality using current automatic welding machines, with adequate ultimate strength and ductility (Lee et al. 2005). Larger studs increase strength and fatigue capacity, allowing fewer studs to be used, accelerating construction, and simplifying deck replacement while minimizing potential damage to studs during deck removal (Badie et al. 2002). However, the fatigue strength of larger studs is slightly lower than smaller ones, necessitating conservative adjustments in fatigue design codes. Eurocode 4 supports extending the design strength to studs up to 30 mm in diameter; however, AASHTO LRFD specifications safety factors need to be increased (Lee et al. 2005).

7.1.1.2 Combined Shear and Bending Moment

Limited studies have focused on shear stud groups under combined shear and bending moment compared to pure shear. An analytical model predicts shear strength of welded shear stud connections under eccentric shear loading by considering friction and dowel action (Stanton and Calvi 2022). The model, based on the lower bound theorem, optimizes the distribution of shear and tension forces across shear stud rows, identifying a peak in shear strength at an intermediate eccentricity ratio higher than pure shear resistance. This trend aligns with test data (Cook 1989; Cook and Klingner 1992; Davaadorj et al. 2020; Hawkins et al. 1980; Stanton and Calvi 2022).

Welded shear studs transfer shear and bending forces between steel and concrete in composite construction. Experiments on partially restrained steel frames with reinforced concrete infill walls showed that reinforcement around shear studs mitigated brittle failures, but low-cycle fatigue fracture persisted as a challenge (Tong et al. 2005). Composite sections, such as steel-encased profiles in concrete shear walls, have been tested to evaluate the role of shear studs in

preventing slip between steel profiles and concrete. These tests emphasized the importance of shear stud connections in maintaining composite action under combined loading scenarios (Dan et al. 2011). Composite coupling beams were designed with embedded steel plates connected to the concrete using shear studs. This configuration enhanced the coupling beam strength and stiffness. The shear studs created an effective bond between the steel plates and concrete, resulting in improved inelastic performance of the composite beam (Lam et al. 2005). Steel-plate and concrete composite walls with shear studs connecting steel plates to concrete, resulted in increased coupling strength and stiffness under eccentric and combined loading (Epackachi et al. 2014).

7.1.1.3 Cyclic Loading

Shear stud connections in concrete-filled steel tubular columns and composite beams demonstrate a trade-off between strength and ductility under cyclic loading. Energy dissipation is a critical parameter for evaluating performance (Nie et al. 2008). Tests on steel-plate and concrete composite walls under cyclic loading showed that shear studs can bond effectively steel plates to concrete, enhancing inelastic performance and overall composite behavior (Epackachi et al. 2014). The use of shear studs in such systems underscores their importance in maintaining structural integrity during earthquakes. In bridge columns using stretch-length anchors (SLAs), shear studs present unique challenges. The intended behavior requires SLAs to yield under cyclic loading while ensuring that post-tensioned concrete bridge columns, cap-beam, and footings remain elastic without structural damage.

7.1.2 Research Objectives

While existing studies provide insight into the behavior of shear studs in various composite structures, the loading conditions associated with SLAs in rocking bridge columns require further study, due to the specific constraints and performance requirements under seismic loads. The lower and upper ends of the column need to transfer and distribute the stress caused by rocking and SLA extension into the column so that there is no damage that needs repair after a design event. The details also need to be as light as possible for cost-savings and to simplify construction. Experiments of eight column stubs constructed with a steel collar plate using welded shear studs were carried out to test different steel collar plate thicknesses as well as number and diameter of shear studs. It is important to note that the test set up does not represent the actual capacity of the column-end assembly because the 3-dimensional bracing from a complete octagonal steel collar is not included. The project team intends to use FEA to model the steel collar assembly behavior and therefore extend the test results to offer practical guidance on minimum design that achieves necessary stress distribution and column protection.

The current study focuses on the use of post-tensioned rocking columns connected to footings and cap beams with external energy dissipators. The unique aspect lies in the application of shear studs to transfer seismic forces from external energy dissipators to bridge columns, addressing the combined shear and bending moment demands. The experimental results demonstrate that increasing the shear stud diameter significantly improves shear resistance, and the findings suggest that current design values may be conservative for this specific loading condition. The goal of the research is to investigate how stud-to-steel collar connections at column ends behave under combined shear and moment. Determining the most advantageous failure mechanism and identifying the predominant failure modes under specific loading circumstances was the main goal of the study. The study also investigates the effect of steel collar thickness on

connection performance, which offers insights into design optimization. The experimental results are compared using analytical equations from the literature to verify theoretical predictions. The study proposes a 3D solid finite element model replicating the experimental findings. The 3D finite element model provides a reliable technique to replicate and predict connection behavior, which can be further used in practical engineering scenarios. This integrated approach of modeling and analytical study addresses critical gaps and promises improved design and performance assessment of structural connections. The analysis and finite element modeling methods offer a framework to generalize the findings to post-tensioned precast concrete columns of actual bridges.

The actual collar capacity versus SLA force is expected to be greater in case of an actual bridge bent design compared to that measured in this chapter because of the bracing effect from the entire collar assembly. The tests in this chapter is performed to calibrate numerical models used in characterizing the column end design details and capacity. The design goal of this chapter is to achieve a satisfactory displacement capacity through rocking and protect the column from damage for the design earthquake using the most economical design alternative.

7.2 EXPERIMENTAL METHODS AND RESULTS

7.2.1 Concrete Column Stub Specimen Details and Setup

Reinforced concrete column stubs were tested to determine the performance of a steel collar plate and shear stud connectors to be used in rocking bridge columns to support external energy dissipators such as SLAs. Eight different column stubs were tested to assess steel collar plate thickness and number and diameter of shear studs. The specimen was created to simulate a concrete column which has a steel collar jacket attached to concrete with shear stud connectors. This sub-assembly was subjected to an eccentric load to simulate the forces created by SLAs under tension.

It is important to note that the experimental setup differs from the actual polygonal collar arrangement shown in **Figure 27**. The tests were conducted on individual plates and anchors, which primarily reflect the bending component of the system strength. In contrast, the polygonal collar around a column would induce significant membrane forces, potentially reducing bending moments on the stud group and approaching a condition of pure shear. This simplification limits the direct applicability of the results to the full column system, but the test setup produces conservative results. This test arrangement was chosen as a first step to isolate and study the behavior of individual shear stud connections under combined shear and bending, which is less well understood than pure shear loading. This approach allowed a focus on the local behavior of the connection and the development of a baseline understanding of its performance.

While the fidelity of the simulation to the full column system is indeed limited, these tests provide valuable insights into the failure modes and capacity of individual connections. They serve as a foundation for future research that can incorporate the membrane effects present in the polygonal collar system. Future studies should aim to bridge the gap between these simplified tests and the actual column configuration. This could involve testing of partial or full collar assemblies to capture membrane effects, or the development of more sophisticated finite element models that account for the full system behavior. Such work would help to translate the findings to practical design guidelines for the complete collar and column system.

Figure 28 shows the test setup used for all specimens. The concrete stub column was 305 mm x 305 mm in plan with a 610 mm height. Each specimen was reinforced with a cage consisting of seven #6 (19 mm diameter) longitudinal bars, 533 mm in length, tied to ten #3 (9.5 mm diameter) closed stirrups, as shown in **Figure 28(f, g)**. The total area of the longitudinal

reinforcement was approximately 1985 mm^2 . Given the cross-sectional area of the concrete ($305 \text{ mm} \times 305 \text{ mm} = 93025 \text{ mm}^2$), the reinforcement ratio was calculated to be approximately 2.1%. **Figure 28 (c)** shows the $305 \text{ mm} \times 305 \text{ mm}$ steel collar plate for the case of a specimen with two shear studs. A setup with only one shear stud was also tested where only the top shear stud is attached. The test matrix is shown in **Table 8**. There were two steel collar plate thicknesses used, 9.5 mm and 12.7 mm, and either one or two shear studs per test. Two shear stud diameters were used, 12.7 mm and 25.4 mm per configuration. All shear studs used were 76.2 mm long. The specimens were identified based on their configuration: the first number indicates the plate thickness, the second number is the number of studs, and the third number is the shear stud diameter, as shown in the naming scheme in **Table 8**. The value of eccentricity e used in **Figure 28 (c)** was 76 mm. **Table 9** shows the properties of the materials as determined by the manufacturer.

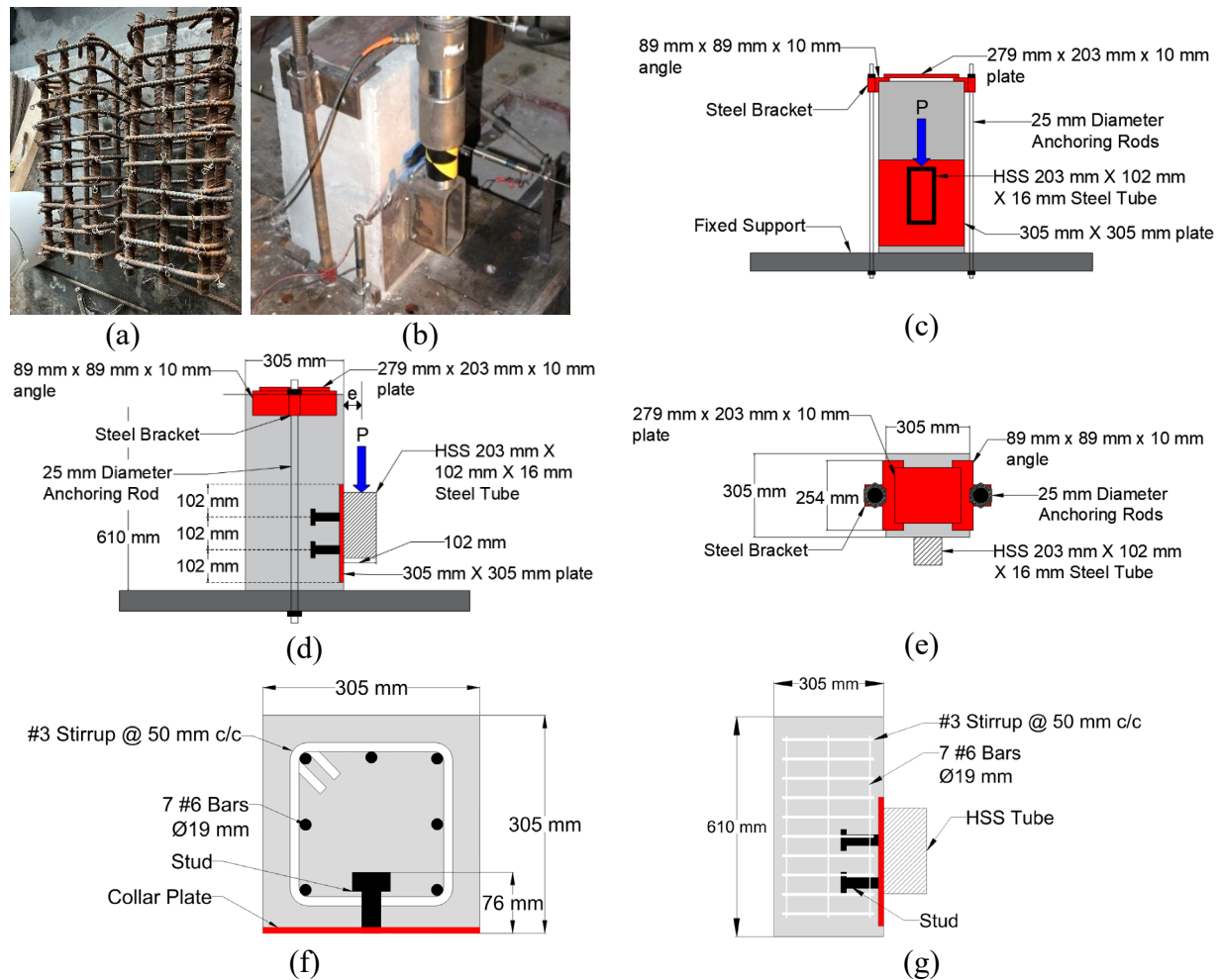


Figure 28. Specimen details: (a) column stub reinforcement cage; (b) column stub, steel collar plate, HSS tube, load cell, load and LVDTs; (c) elevation; (d) side view; (e) plan view; (f) column stub cross-section; and (g) elevation showing reinforcement.

A vertical actuator applied a downward monotonic force on the HSS steel tube that was measured with a load cell; the vertical displacement of the actuator was measured by a vertical linear variable differential transformer (LVDT). The use of a monotonic loading protocol in the

experiments provide essential insights into the initial behavior and ultimate capacity of the steel collar plate and shear stud connections, despite the primary application being in seismic zones. Monotonic tests help establish baseline performance characteristics, identify critical failure models and validate analytical models. A monotonic load was applied at a rate of 1.0 mm/min up to a displacement of 5.1 mm, after which the rate was increased to 2.0 mm/min for displacements up to 12.7 mm, and the rate increased to 2.5 mm/min until specimen failure. However, these tests do not fully capture the complexities of cyclic loading experienced during seismic events.

Future studies should include cyclic tests to evaluate connection performance under repeated load reversals and assess cumulative damage effects. This approach will enhance the design and implementation of these connections in rocking columns, ultimately improving the seismic performance of bridges utilizing external energy dissipators like stretch length anchors (SLAs). The stub column was secured using two 25.4 mm diameter high-strength steel rods, two L89 mm x 89 mm x 9.5 mm by 254 mm long steel angles and a rectangular top 279 mm x 203 mm x 9.5 mm steel collar plate. The load was applied to 203 mm x 102 mm x 15.9 mm HSS tube through a circular solid steel cylinder 76 mm in diameter and 203 mm long. Concrete cylinders, 102 mm x 203 mm were tested to determine the concrete compressive strength which on test day was 58 MPa.

Table 8. Test matrix for stub column tests

Specimen Number	Specimen Name	Plate thickness (mm)	Number of studs	Stud diameter (mm)
1	Specimen 12.7-1-12.7	12.7	1	12.7
2	Specimen 12.7-2-12.7	12.7	2	12.7
3	Specimen 9.5-1-12.7	9.5	1	12.7
4	Specimen 9.5-2-12.7	9.5	2	12.7
5	Specimen 12.7-1-25.4	12.7	1	25.4
6	Specimen 12.7-2-25.4	12.7	2	25.4
7	Specimen 9.5-1-25.4	9.5	1	25.4
8	Specimen 9.5-2-25.4	9.5	2	25.4

Location of the studs in the actual column should maximize the moment resistance by providing a greater lever arm and better resistance to bending. The experiments are also conservative in that the long tail of the collar plate in the compression region is not an issue since the steel collar plate typically is welded to the steel plate located at the bottom of the column (Neupane and Pantelides 2024b). No bending of the steel plate was observed in the present tests.

7.2.2 Test Results

Generally, a thicker steel collar plate (12.7 mm) resulted in a higher total shear force compared to a thinner one (9.5 mm); a double stud configuration resulted in higher capacity than a single stud.

Table 9. Material properties used in the experiment

Component	Material properties
Concrete (Test Day Strength)	$f'_c = 58 \text{ MPa}$
Studs	$\sigma_y = 301 \text{ MPa}$
	$\sigma_u = 426 \text{ MPa}$
Steel Plates	$\sigma_y = 345 \text{ MPa}$
	$\sigma_u = 455 \text{ MPa}$
Reinforcing Bars and Stirrups	$\sigma_y = 469 \text{ MPa}$
	$\sigma_u = 641 \text{ MPa}$
HSS Tubes	$\sigma_y = 317 \text{ MPa}$
	$\sigma_u = 400 \text{ MPa}$

7.2.2.1 Comparison of 12.7 mm steel collar plate tests (Specimen 12.7-1-12.7, Specimen 12.7-2-12.7, Specimen 12.7-1-25.4, and Specimen 12.7-2-25.4)

From **Figure 30(a)**, the 25.4 mm shear stud diameter specimens (Specimen 12.7-1-25.4 and 12.7-2-25.4) achieve a larger displacement at yield and a higher total shear force at failure compared to 12.7 mm shear stud diameter specimens (Specimen 12.7-1-12.7 and 12.7-2-12.7). Specimen 12.7-1-25.4 had a total shear force of 200 kN at failure due to shear stud shear fracture and Specimen 12.7-2-25.4 had a total shear force of 397 kN at failure due to concrete cracking and shear stud pullout, as shown in **Figure 29**. The 25.4 mm shear stud diameter specimens are able to achieve higher total shear force at larger displacements, which shows that shear stud diameter has a significant impact on performance. While all these specimens used the same 12.7 mm steel collar plate thickness, the number of studs also influenced the results. Specimen 12.7-2-25.4, with two 25.4 mm studs, achieved the highest total shear force and displacement resistance among these specimens. This comparison highlights that for a given steel collar plate thickness, both shear stud diameter and the number of studs play crucial roles in determining the connection's capacity and behavior. The shear stud diameter appears to have a more pronounced effect on total shear force and displacement resistance than the number of studs for the configurations tested.

All test specimens, regardless of the number of shear studs, show a similar initial slope in the force-displacement curves (**Figure 30a**). This may arise from uneven load distribution across multiple studs in the early stages of loading, as well as potential initial slip or settling within the connection system. However, it is noteworthy that specimens with a greater number or size of studs ultimately reached higher peak loads and demonstrated distinct failure modes, as detailed in the results section.

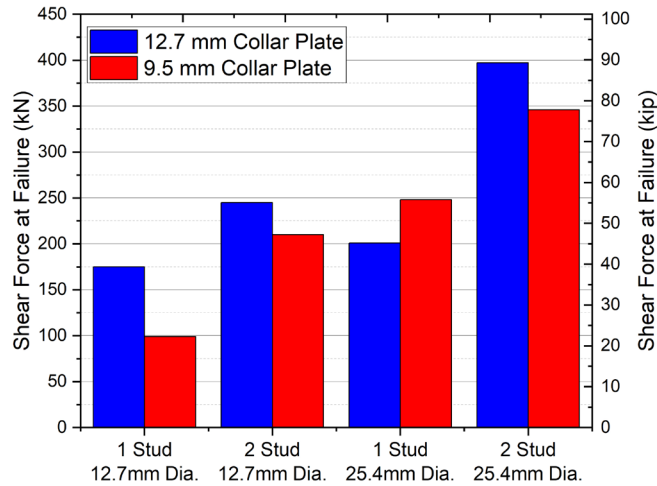


Figure 29. Shear force comparison at failure for 12.7 mm vs. 9.5 mm collar plates across varying stud numbers and diameters.

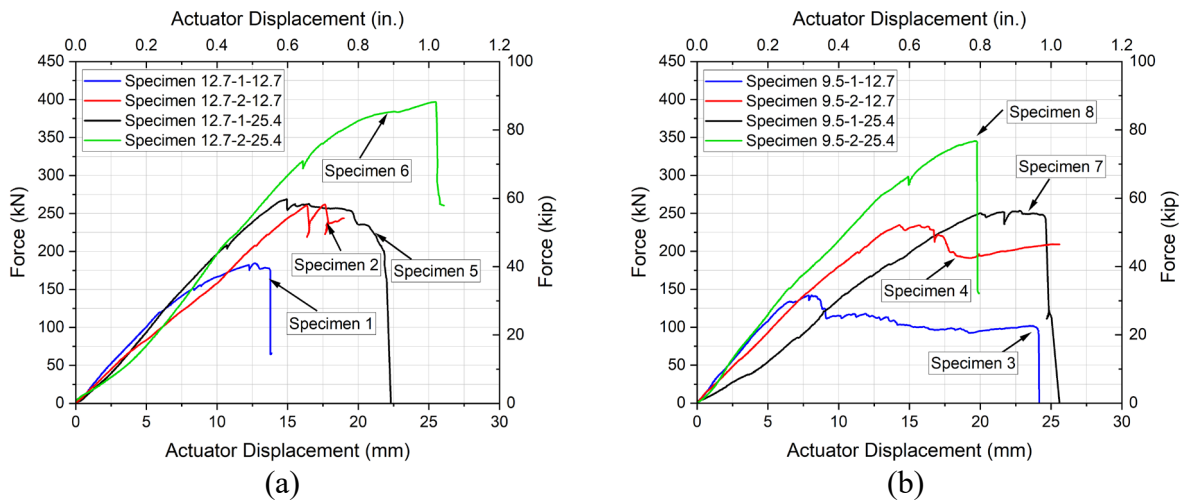


Figure 30. Total shear force versus actuator displacement comparison for: (a) 12.7 mm steel collar plate specimens (*Specimen 12.7-1-12.7*, *Specimen 12.7-2-12.7*, *Specimen 12.7-1-25.4*, and *Specimen 12.7-2-25.4*); and (b) 9.5 mm steel collar plate specimens (*Specimen 9.5-1-12.7*, *Specimen 9.5-2-12.7*, *Specimen 9.5-1-25.4*, and *Specimen 9.5-2-25.4*).

7.2.2.2 Comparison of 9.5 mm steel collar plate tests (*Specimen 9.5-1-12.7*, *Specimen 9.5-2-12.7*, *Specimen 9.5-1-25.4*, and *Specimen 9.5-2-25.4*)

From **Figure 30(b)** it can be seen that the 25.4 mm shear stud diameter specimens (*Specimen 9.5-1-25.4* and 8) achieve a higher total shear force than the 12.7 mm shear stud diameter specimens (*Specimen 9.5-1-12.7* and 4). *Specimen 9.5-1-25.4* had a total shear force of 248 kN and *Specimen 9.5-2-25.4* had a total shear force of 346 kN, as shown in **Figure 29**. *Specimen 9.5-1-25.4* failed due to shear stud shear fracture and *Specimen 9.5-2-25.4* failed due to cracking of the concrete and shear stud pullout. *Specimen 9.5-1-12.7* failed at a force of 99 kN and *Specimen 9.5-2-12.7* failed at a force of 210 kN, as shown in **Figure 29**, both due to shear stud shear fracture. When two 25.4 mm diameter shear studs are present (*Specimen 9.5-2-25.4*), the diagonal tension capacity of the concrete is reached, resulting in concrete cracking. Cracking of concrete is undesirable since

it is accompanied by shear stud pullout; the preferred failure mode is yield-pullout-tensile fracture of the shear studs which ensures that the steel components are undamaged. The analysis techniques are described in Section 7.3. The procedures used to predict the strength of the connection were conservative compared to the experimental results.

7.2.3 Failure Modes

Failure modes of shear studs observed from the experiments can be categorized into three types. Failure Mode I (yield-pullout-tensile fracture) involves the initial yielding of the shear stud, detected via strain gauge readings, followed by a gradual, partial stud pullout from the concrete, and concluding with tensile fracture at its weakest point, typically near the weld to the collar plate. In Failure Mode II (shear stud shear fracture), the stud fractures across its cross-section due to excessive shear stress without significant pullout from the concrete. Failure Mode III (concrete cracking-shear stud pullout) is marked by initial cracking in the concrete surrounding the stud, partial stud pullout as cracking begins, and crack propagation with increasing load. These failure modes were identified based on experimental evidence, including load-displacement curves that revealed changes in slope corresponding to plastic deformation and ultimate failure, visual observations of stud fracture, concrete cracking, and stud pullout during post-test inspections, and load data showing significant reduction, indicating fracture or pullout events.

7.2.3.1 Yield-pullout-tensile fracture failure mode I

Yield-pullout-tensile fracture failure mode was observed from yielding of steel studs shown by strain values obtained from strain gauges and the decrease in the load. Specimen 12.7-1-12.7, Specimen 12.7-2-12.7, Specimen 9.5-1-12.7 and Specimen 9.5-2-12.7 exhibited yield-pullout-tensile fracture failure mode I. Despite variations in the number of shear studs (single or double) and steel collar plate thickness (12.7 mm or 9.5 mm), the common factor of this failure mode across all four specimens is the 12.7 mm diameter shear stud, as shown in **Figure 31(a)** and **Figure 32(a)**. Yielding of the shear studs prior to pullout was inferred from the load-displacement curves, which showed a distinct change in slope indicating the onset of plastic deformation. This observation was corroborated by strain gauge readings collected during the experiments, providing direct evidence of stud yielding before the ultimate load was reached. Specimen 12.7-1-12.7 experienced a total shear force of 182 kN and Specimen 9.5-1-12.7 reached 142 kN. This is lower than the total shear force in Specimen 12.7-2-12.7 and Specimen 9.5-2-12.7 of 262 kN and 235 kN, respectively.

The addition of a second shear stud (Specimen 12.7-2-12.7 and Specimen 9.5-2-12.7) resulted in increased total shear force compared to the single shear stud configurations (Specimen 12.7-1-12.7 and Specimen 9.5-1-12.7). Furthermore, the thicker 12.7 mm steel collar plate (Specimen 12.7-1-12.7 and Specimen 12.7-2-12.7) provided higher total shear force compared to the 9.5 mm collar plate (Specimens Specimen 9.5-1-12.7 and Specimen 9.5-2-12.7). This increase in total shear force with plate thickness can be attributed to several factors: enhanced bending resistance crucial in eccentric loading, better load distribution across the connection interface and reduced local deformations. The thicker plate also allows for stronger weld connections between the shear studs and the collar, contributing to overall structural integrity. However, it is important to note that while steel collar plate thickness influences performance, the diameter and number of shear studs have a more pronounced effect on total shear force and displacement resistance in these configurations.

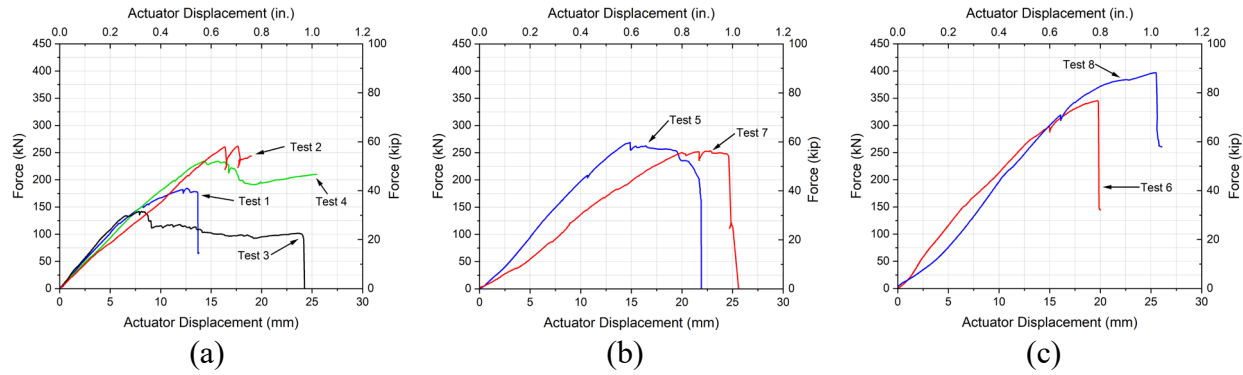


Figure 31. Total shear force versus actuator displacement: (a) 12.7 mm studs (Specimen 12.7-1-12.7, Specimen 12.7-2-12.7, Specimen 9.5-1-12.7, and Specimen 9.5-2-12.7) failure mode I; (b) 25.4 mm diameter studs (Specimen 12.7-1-25.4 and Specimen 9.5-1-25.4) failure mode II; and (c) 25.4 mm diameter studs (Specimen 12.7-2-25.4 and Specimen 9.5-2-25.4) failure mode III.

While the observed trend of increased strength with larger stud diameters, more studs, and thicker plates aligns with expectations, it is crucial to compare these results to design values to provide meaningful insights. The design values were calculated using the American Institute of Steel Construction (AISC) methodology for shear stud connectors and compared to the experimental results: The design shear strength per AISC is 65.8 kN for 12.7 mm studs, where the experimental results yielded 142–262 kN (216–398% of the design value).

7.2.3.2 Shear stud shear fracture failure mode II

Shear stud shear fracture was characterized by a significant load drop. Fracture of the shear stud occurred in Specimens 5 and 7, when there was a single 25.4 mm diameter shear stud welded to a 12.7 mm steel collar plate and a 9.5 mm steel collar plate, respectively. From **Figure 31(b)**, Specimen 12.7-1-25.4 achieved a total shear force equal to 267 kN and Specimen 9.5-1-25.4 equal to 254 kN. The specimens achieved a displacement of 25 mm for the 9.5 mm steel collar plate specimen and a displacement of 22 mm for the 12.7 mm steel collar plate specimen. The shear stud shear fracture failure mode II can be seen in **Figure 32(b)**. The design shear strength per AISC is 145.2 kN for single 25.4 mm studs, whereas the experimental results were 254–267 kN (175–184% of the design value).

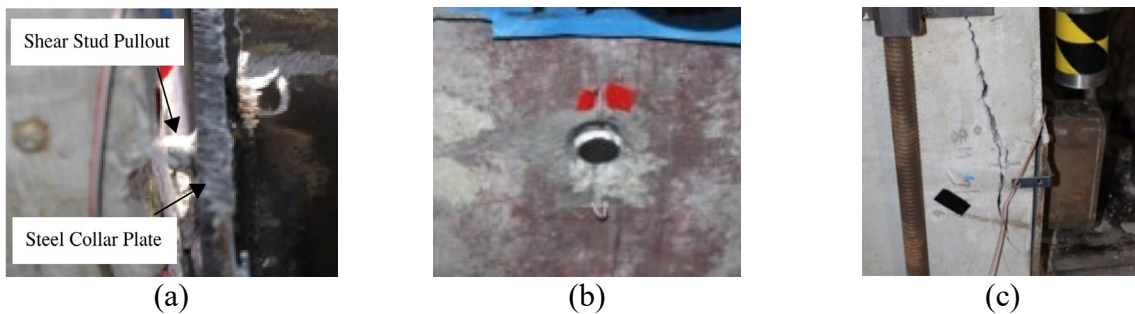


Figure 32. Failure modes: (a) yield-pullout-tensile fracture mode I; (b) shear stud shear fracture mode II; and (c) concrete cracking-shear stud pullout failure mode III.

7.2.3.3 Concrete cracking-shear stud pullout failure mode III

Concrete cracking-shear stud pullout failure was indicated by crack initiation and propagation in the concrete, identified by stress localization in tensile regions. Cracking of concrete due to diagonal tension and shear stud pullout occurred in Specimen 12.7-2-25.4 and Specimen 9.5-2-25.4. **Figure 31(c)** shows that these specimens achieved higher total shear forces than the remaining specimens. Specimen 12.7-2-25.4 achieved 397 kN while Specimen 9.5-2-25.4 achieved 346 kN. Since these specimens had two 25.4 mm diameter shear studs, they exhibited a higher resistance. Specimen 12.7-2-25.4 reached a displacement of 26 mm while Specimen 9.5-2-25.4 reached a displacement of 20 mm at failure. This shows that the two 25.4 mm diameter shear studs with 12.7 mm steel collar plate (Specimen 12.7-2-25.4) had the highest total shear and displacement resistance. The presence of transverse reinforcement influenced the observed behavior by providing confinement to the concrete around the shear studs, potentially enhancing pullout resistance and overall capacity (Lee et al. 2005). Additionally, the transverse reinforcement contributed to the distribution of internal forces and control of crack propagation, affecting the failure mode and ultimate load. In Specimen 12.7-2-25.4 and Specimen 9.5-2-25.4, the stirrups delayed the onset of concrete cracking and increased the load at which shear stud pullout occurred. Failure mode III is shown in **Figure 32(c)**. The design shear strength per AISC is 290.4 kN for a group of two 25.4 mm studs, whereas the experimental results were 346–397 kN (119–137% of the design value).

A summary of test results is shown in **Table 10**. Three failure modes are identified: (I) yield-pullout-tensile fracture of the shear stud; (II) shear stud shear fracture; and (III) concrete cracking followed by shear stud pullout failure. The specimens with 12.7 mm diameter shear studs (Specimen 12.7-1-12.7, Specimen 12.7-2-12.7, Specimen 9.5-1-12.7, and Specimen 9.5-2-12.7), with either single or double shear studs, exhibited yield-pullout-tensile fracture of the top shear stud (mode I). In Specimen 12.7-1-12.7 and Specimen 12.7-2-12.7, with a 12.7 mm steel collar plate, the total shear forces at stud fracture were 182 and 262 kN, respectively. For Specimen 9.5-1-12.7 and Specimen 9.5-2-12.7 with a 9.5 mm steel collar plate, the total shear forces at stud

Table 10. Experimental results

Test number	Number of studs	Failure mode	Shear force at failure (kN)	Failure disp. (mm)	Shear force at stud yield (kN)	Shear force at stud yield / SLA tensile strength
Specimen 12.7-1-12.7	1	I	175	14	155	1.2
Specimen 12.7-2-12.7	2	I	245	19	261	2.1
Specimen 9.5-1-12.7	1	I	99	25	142	1.1
Specimen 9.5-2-12.7	2	I	210	26	235	1.9
Specimen 12.7-1-25.4	1	II	201	22	267	2.2
Specimen 12.7-2-25.4	2	III	397	26	315	2.5
Specimen 9.5-1-25.4	1	II	248	25	254	2.0
Specimen 9.5-2-25.4	2	III	346	20	299	2.4

Note: Failure Mode I = Yield-Pullout-Tensile Fracture Failure, Failure Mode II = Weld-Shear Fracture Failure, Failure Mode III = Concrete Cracking-Shear Stud Pullout Failure.

fracture were 142 and 235 kN, respectively. The specimens with single 25.4 mm diameter shear studs (Specimen 12.7-1-25.4 and Specimen 9.5-1-25.4) failed due to shear stud shear fracture at approximately a total shear force of 200 and 245 kN, respectively (mode II). The specimens with two 25.4 mm diameter shear studs (Specimen 12.7-2-25.4 and Specimen 9.5-2-25.4) achieved the highest total shear forces of 397 and 346 kN, respectively, and experienced concrete cracking failure and stud pullout (mode III).

Comparisons between tests revealed that shear stud diameter has a greater influence on total shear resistance than steel collar plate thickness. For a single shear stud, increasing the stud diameter from 12.7 to 25.4 mm improved shear resistance by up to 80%, whereas increasing steel collar plate thickness from 9.5 to 12.7 mm provided a gain of about 15%. Thus, increasing the number of shear studs led to higher total shear and displacement resistance. Comparing the single versus double shear stud specimens for both the 12.7 mm and 25.4 mm shear stud diameter shows that using two shear studs allows the system to achieve 20-30% higher total shear resistance. These comparisons reveal that the experimental results consistently exceeded design values, with the most significant overstrength observed for the smaller diameter studs (failure mode I). The larger diameter studs (failure modes II and III) showed less overstrength but still exceeded design values by a considerable margin. These findings suggest that current design values are conservative for the specific loading conditions and configurations tested in this study. However, it is important to note that design values incorporate safety factors and are intended to cover a wide range of conditions. The observed overstrength provides an additional margin of safety for the specific application of shear studs in rocking bridge columns with external energy dissipators (SLAs).

A comparison of the total shear force to SLA tensile strength is made. The ratio of total shear force at stud yield to SLA tensile strength is an important parameter that indicates the relative capacity of the shear stud connection compared to SLA tensile strength. This ratio helps ensure that the shear stud connection remains stronger than the SLA, allowing the SLA to yield and dissipate energy as intended during a seismic event, while the connection between the steel collar plate and concrete column remains intact. The tensile strength of a 19 mm SLA with an ultimate tensile stress of 442 MPa is 126 kN. A ratio greater than 1.0 indicates that the shear stud connection has a higher capacity than the SLA tensile strength, which is desirable for the intended performance of the system. **Table 10** shows that the ratio between total shear force at stud yield to SLA tensile strength for one shear stud ranges from 1.1 to 2.2 and for two shear studs from 1.9 to 2.5. The range of ratios observed in the experiments suggests that the shear stud connections have sufficient capacity to transfer the forces from yielding SLAs to the concrete column without premature failure of the connection.

The tests demonstrate the desired yield-pullout-tensile fracture failure mode I for the 12.7 mm diameter shear studs, as observed in Specimen 12.7-1-12.7, Specimen 12.7-2-12.7, Specimen 9.5-1-12.7, and Specimen 9.5-2-12.7. This mode, characterized by yielding of shear studs, ensures that the bridge column remains intact and undamaged during a seismic event. By designing the connection system to exhibit this preferred failure mechanism structural integrity of the column is maintained with no damage to the column.

7.3 ANALYSIS TECHNIQUES

Analytical techniques are used to match key characteristics observed in the physical tests and provide assessment of the experimental results using simplified closed-form solutions. Detailed finite element models can further validate connection behavior. Integration of these techniques can assist in design of full-scale columns with shear stud connection systems.

Analytical methods were used to supplement the experimental results. Schematic diagrams (**Figure 33**) are provided to visually illustrate failure patterns observed during testing. **Figure 33 (a)** shows the yielding pullout-tensile fracture failure mode I, **Figure 33 (b)** shows the shear stud shear fracture failure mode II, and **Figure 33 (c)** shows the concrete cracking-shear stud pullout failure mode III. For the yielding pullout-tensile fracture failure mode I, the Whitney stress block method was used to determine the total tensile force in the studs. For the shear stud shear fracture failure mode II, equations from the literature were utilized that account for the connection geometry, material properties, and frictional effects to find the total shear resistance (Stanton and Calvi 2022). The shear stud nominal shear strength was also evaluated using code equations and compared to the experimental results. For the concrete cracking-shear stud pullout failure mode III of **Figure 33 (c)**, a finite element model was used to predict total shear resistance.

7.3.1 Yield-pullout-tensile fracture failure mode I

In this method, the Whitney stress block is used to obtain the total tensile force in the studs; a rectangular compressive stress distribution is assumed for the concrete, with a magnitude of $0.85f'_c$, where f'_c is the 28-day concrete compressive strength. Using this stress distribution, the compressive force in the concrete, C , and total tensile force, T , in the shear stud connectors can be calculated as:

$$C = T = 0.85f'_c ab \quad (7.1)$$

where a is the depth of the Whitney stress block and b is the width of the concrete block or steel plate (**Figure 28 (b)**). The external bending moment, M_{ext} , acting on the shear stud is determined as:

$$M_{ext} = Pe = V_{tot}e \quad (7.2)$$

$$M_{int} = T(jd) \quad (7.3)$$

where P is the applied load, which equals the total shear force V_{tot} , and e is the eccentricity. Setting M_{ext} from Eq. (7.2) equal to the internal bending moment, M_{int} in Eq. (7.3), the tensile force in the single shear stud case, T , is obtained; the lever arm, jd , was found iteratively by enforcing equilibrium as 203 mm. . For the case of two shear studs, strain compatibility was used to determine the tensile force in each stud. As shown in **Table 11**, the tensile force in the top shear stud ranged from 61 kN to 67 kN.

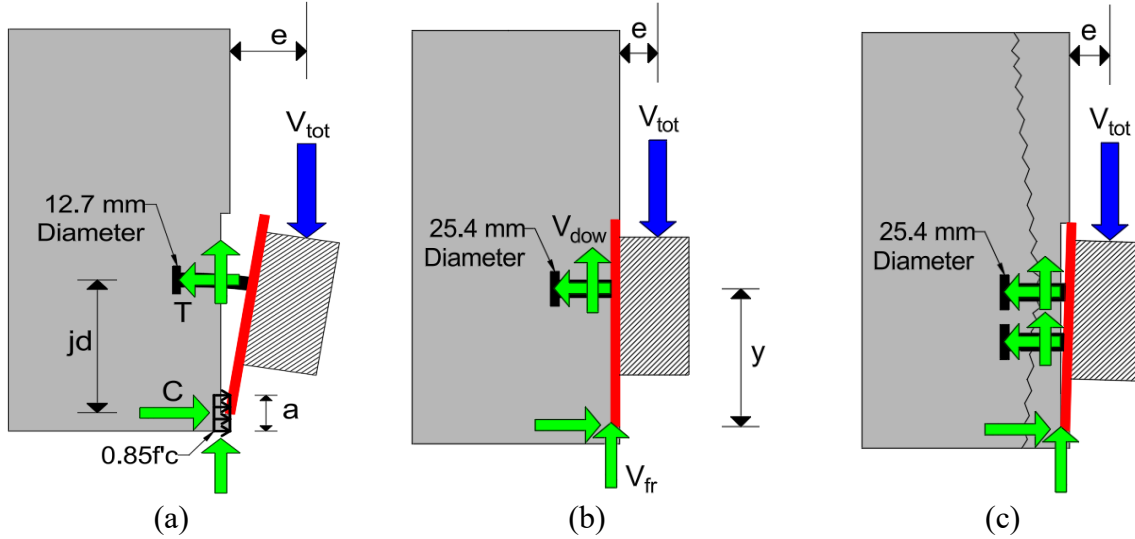


Figure 33. Schematic of experimental failure modes: (a) yield-pullout-tensile fracture mode I; (b) shear stud shear fracture mode II; and (c) concrete cracking-shear stud pullout failure mode III.

7.3.2 Weld-shear stud fracture mode II

7.3.2.1 *Von Mises Failure Criterion*

For the shear stud shear fracture failure mode, analytical equations that account for connection geometry, material properties and frictional effects at the steel-concrete interface are used to determine total shear force resistance (Stanton and Calvi 2022). The equation is part of a model that predicts the behavior of stud groups subjected to combined shear and moment loading. It relates the shear and tension stresses in the studs to the eccentricity of the applied load, which helps determine the shear capacity for a given eccentricity. The tangent of the failure angle, θ , based on the Von Mises failure criterion is evaluated as:

$$\tan\theta = \frac{\lambda}{\frac{y}{e} - \mu} \quad (7.4)$$

Table 11. Experimental tensile force in shear studs at stud fracture

Specimen number	Number of studs	Total tensile force (T) (kN)	Tensile force in top stud (kN)
1	1	66	66
2	2	121	67
3	1	61	61
4	2	113	63

where λ is a geometric parameter based on the von Mises failure criteria (0.5774), e is the eccentricity (76 mm), y is the connection arm from the bottom of the steel collar plate to the center of the shear stud (203 mm), as shown in **Figure 33(b)** and μ is the coefficient of friction between

steel and concrete assumed as 0.9 (AISC 1986). Solving Eq. (7.4) for θ , the total shear force, V_{tot} , acting on the connection is determined as:

$$V_{tot} = (A_s \sigma_u) \frac{y}{e} \sin \theta \quad (7.5)$$

where A_s is the shear stud cross-sectional area, and σ_u is the shear stud ultimate strength. From the analytical equations developed in the literature (Stanton and Calvi 2022), a shear force versus load eccentricity plot was generated to predict the expected shear force acting on the connection at a given load eccentricity. Based on the test setup, the loading point was located approximately 76 mm from the concrete surface which is the value of the eccentricity, e . Using this eccentricity in the model, the predicted total shear force at shear stud shear fracture was determined as 178 kN for one stud. This prediction was found to be conservative when compared to the experimental results. The physical tests achieved a total shear force of 201 kN (Specimen 12.7-1-25.4) and 248 kN (Specimen 9.5-1-25.4) for shear stud shear fracture failure (**Table 10**). This difference suggests that the analytical equations, while providing a good estimate, are conservative for this configuration compared with the actual shear demand on the connection under the given loading conditions and geometry.

7.3.2.2 *Shear Strength of One Stud from Code Predictions*

The stud shear strength equations in the 9th and 10th editions of the AASHTO Specifications were used to compare with the experimental results. The shear strength of one stud from the 9th edition of AASHTO (AASHTO 2020) and the 10th edition of AASHTO (AASHTO 2021) are respectively:

$$Q_{n1} = 0.5A_{sc}\sqrt{f'_c E_c} \leq A_{sc}F_u \quad (7.6)$$

$$Q_{n2} = 0.7A_{sc}F_u \quad (7.7)$$

where Q_{n1} , Q_{n2} = stud nominal shear strength; A_{sc} = cross-sectional area of stud; f'_c = compressive strength of concrete; E_c = modulus of elasticity of concrete; and F_u = tensile strength of stud. The shear strength of one stud in Eurocode 4 is given as follows (Eurocode 2004):

$$Q_{n3} = 0.37A_{sc}\sqrt{f'_c E_c} \leq 0.8A_{sc}F_u \quad (7.8)$$

where Q_{n3} = stud nominal shear strength; A_{sc} = cross-sectional area of stud; f'_c = compressive strength of concrete; E_c = modulus of elasticity of concrete; and F_u = tensile strength of stud. A comparison of the experimental results for Specimen 12.7-1-25.4 and Specimen 9.5-1-25.4 and the code predictions is summarized in **Table 12**. When comparing the experiments to code predictions it can be seen that Eq. (7.6) provides the largest value for stud shear strength (216 kN), which is still conservative compared to the experimental results of 267 and 254 kN for Specimen 12.7-1-25.4 and 7, respectively.

Table 12. Comparison of experimental result to code predictions

Specimen Number	Shear force at stud yield (kN)	Shear stud strength from Eq. 7.6 (AASHTO 2020) (kN)	Shear stud strength from Eq. 7.7 (AASHTO 2021) (kN)	Shear stud strength from Eq. 7.8 (Eurocode 2004) (kN)
5	267	216	151	173
7	254			

To further support capacity protection, the authors recommend increasing the number of studs once the tensile force in the SLAs (multiplied by a 1.5 safety factor) approaches yielding levels in studs or plates. Under extreme seismic loads, slight yielding in secondary components, such as the shear studs, can act as a controlled “fail-safe” mechanism, allowing for limited ductility to prevent brittle failure and protect the main structural elements. This approach ensures that even under high-intensity loading, any yielding remains minor, protecting the structural integrity and facilitating post-event repair if needed.

7.4 NUMERICAL FINITE ELEMENT ANALYSIS

Finite element modeling is essential for capturing initial stiffness, force-displacement response, and total shear force and displacement resistance for composite connections with shear studs. Building on prior research (Bursi et al. 2005; Epackachi et al. 2014; Qi et al. 2017), a detailed 3D finite element model was used to investigate the performance of the connections. The finite element model uses geometric details of the specimens, including the steel collar plate, shear studs, HSS tube, concrete block, and reinforcing steel (**Figure 34(a)**). The material properties, contact interactions, boundary conditions, and loading protocol were selected to match the experiment. **Figure 34(b)** illustrates the complete boundary condition implemented.

7.4.1 Element type and mesh density

The shear studs used to anchor the steel collar plate to the concrete were modeled as solid homogeneous elements, rather than using discrete fastener elements from ABAQUS (Smith 2009). This approach allowed the nonlinear load-slip behavior of shear stud-to-concrete to be captured directly through material modeling rather than by relying on specialized fastener elements. Shear studs were modeled using an 8-node linear brick element with reduced integration and hourglass control (C3D8R element). The reduced integration scheme helps the model run faster since it requires fewer integration points compared to full integration. The hourglass control feature was utilized to limit excessive distortion that can occur with reduced integration of brick elements. The C3D8R element was also used for modeling the steel collar plate, HSS tube, and concrete block in the finite element model.

For the vertical steel reinforcing bars and stirrups embedded in the concrete, a different element type was selected. Since these were modeled as thin wire-like members, a 2-node linear 3D truss element, denoted as T3D2 was used for representing the axial force-only behavior of reinforcing steel bar components. The mesh size was tailored based on the size and geometry of the component; no mesh element exceeded 25.4 mm in size. A mesh sensitivity analysis was performed to ensure the mesh refinement was sufficient across all model components. Specifically, the concrete block was modeled using 25.4 x 25.4 x 25.4 mm cubic elements, the HSS tube utilized

25.4 x 25.4 x 12.7 mm brick elements, and the steel collar plate was discretized with 25.4 x 25.4 mm shell elements, as shown in **Figure 34(a)**.

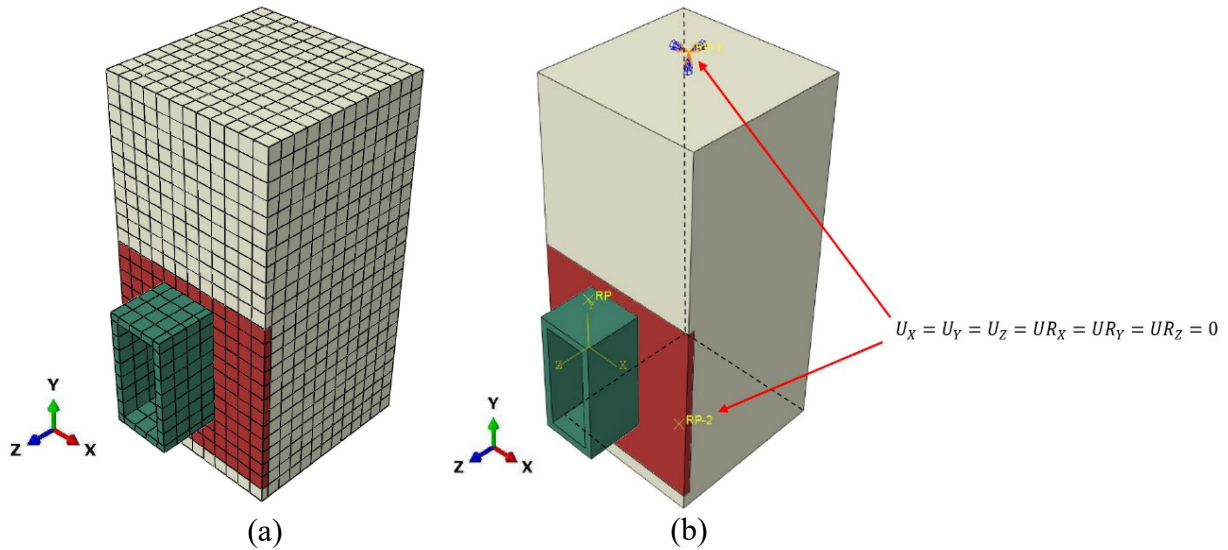


Figure 34. Finite element model used in analysis: (a) mesh density of the specimen; and (b) encastre boundary conditions applied to top and bottom of the specimen.

7.4.2 Material modeling and interaction properties

Material properties and contact interactions were critical in the development of the finite element model. For the concrete material, the concrete damage plasticity (CDP) constitutive model was utilized to capture the nonlinear stress-strain behavior under compression. The CDP model parameters, including the dilation angle, flow potential eccentricity, compressive strength, tensile strength, and viscosity parameter were calibrated based on concrete properties. **Table 13** provides the set of CDP model parameters used. The material properties for the shear studs and reinforcing bars were also precisely determined by using the yield strength, ultimate strength, and strain hardening characteristics of the specific steel grades used in the experiments.

Establishing appropriate contact interactions between various model components is another important consideration. To prevent penetration or excessive deformation at the interfaces, a hard contact was selected in the normal direction using a surface-to-surface contact formulation. In the tangential direction, a friction coefficient of 0.9 was assigned, based on typical values for steel-to-concrete interfaces, utilizing a penalty-based friction model. The shear studs were embedded within the concrete volume and fully tied to the steel collar plate. The finite element model in ABAQUS uses the Johnson-Cook ductile damage criterion to model failure mechanisms in steel studs (Johnson and Cook 1985). Damage initiation was determined by equivalent plastic strain, which depends on stress triaxiality and strain rate. For the steel studs used in the experiments the critical plastic strain at fracture ranges from 0.10 to 0.25 for a triaxiality level of 0.33 to 1.0 (Bao and Wierzbicki 2004).

The damage evolution was characterized using a fracture energy-based approach with linear stiffness degradation, ensuring realistic material behavior during failure. A uniform fracture energy value was applied across all simulations. An element removal technique was employed to enhance computational reliability and reduce mesh dependency. The model was validated by comparing its load-displacement responses and observed failure patterns to experimental data. The simulation successfully captured the key behavior of steel studs, including yielding and tensile fracture. The HSS tube was also rigidly tied to the steel collar plate. The vertical steel reinforcing bars and stirrups were embedded directly within the concrete block elements, ensuring monolithic behavior between steel and concrete.

Table 13. Concrete damage plasticity values used in finite element model

Dilation Angle (deg)	Eccentricity	f_{b0}/f_{c0}	K	Viscosity Parameter
30	0.1	1.16	0.667	0.03

7.4.3 Boundary and loading conditions

Boundary conditions were applied to the finite element model to simulate the test setup. To restrain out-of-plane displacements and model the fixed support conditions of the concrete block its top and bottom faces were fully fixed using the "encastre" boundary condition. This prevented any translational or rotational degrees of freedom at those surfaces simulating the fixed support provided by the test frame, as shown in **Figure 34(b)**. A load couple, which couples the motion of a collection of nodes on a surface to the motion of a reference node, was applied to the top surface of the HSS tube at the location where the vertical load was applied in the tests. This load couple introduces an eccentric load into the model since the applied load was offset from the centroid of the HSS tube cross-section. Complementing the load couple on the HSS tube, a couple restraint support, constraining a group of coupling nodes to the rigid body motion of a single node, was applied to the top and bottom surfaces of the concrete block which prevented any rotational degrees of freedom at those locations.

The loading applied to the finite element model was selected to replicate the displacement-controlled test protocol. Vertical downward displacements were prescribed on the top surface of the HSS tube up to a maximum displacement of 25.4 mm. This displacement-controlled approach captured the full nonlinear response of the connection. The combination of appropriate boundary conditions and realistic loading enabled the finite element model to predict the experimental behavior across the various failure modes.

7.4.4 Model validation

Dynamic implicit analyses were carried out to compare the finite element model results with the experiments. The comparison shows very good agreement between the finite element model and experimental data for the three failure modes; moreover, the finite element models illustrate the failure limit states of stud yielding and concrete damage.

Figure 35(a) presents the force-displacement comparison for Specimen 12.7-1-12.7 with the yield-pullout-tensile fracture failure mode I. The results are nearly identical, with the total shear force occurring at the same displacement and the stiffness of the two curves in close alignment. Similar comparisons for the remaining yield-pullout-tensile fracture failure mode specimens

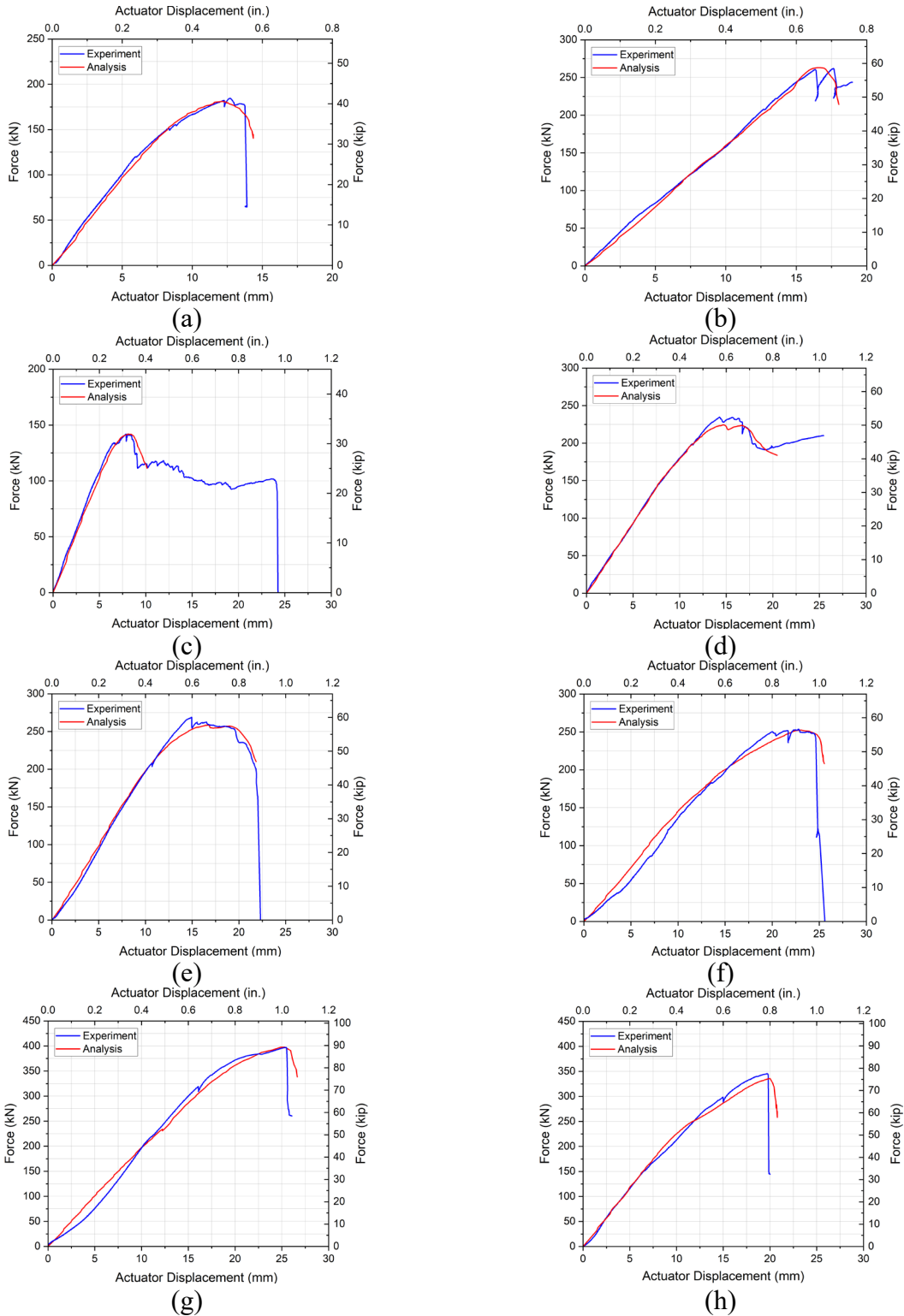


Figure 35. Comparison between experiment and finite element model results for total shear force versus actuator displacement: (a) Test 1; (b) Test 2; (c) Test 3; (d) Test 4; (e) Test 5; (f) Test 7; (g) Test 6; and (h) Test 8.

(Specimen 12.7-2-12.7, Specimen 9.5-1-12.7, Specimen 9.5-2-12.7 in **Figure 35(b)**, **Figure 35 (c)** and **Figure 35(d)**, respectively) demonstrate that the finite element results closely matched the experimental total shear forces and displacements. **Figure 35(e)** shows the force-displacement comparison for the shear stud shear fracture failure mode II (Specimen 12.7-1-25.4); experimental and finite element model results exhibited nearly identical total shear forces. Likewise, the comparison for the other shear stud shear fracture specimen (Specimen 9.5-1-25.4), presented in **Figure 35 (f)** indicates that the finite element model overpredicted the initial stiffness but still captured the total shear force adequately.

The comparison for the concrete cracking-shear stud pullout failure mode III (Specimen 12.7-2-25.4), shown in **Figure 35(g)**, revealed differences between the model and experiments. The model initially over-predicted stiffness since it did not fully capture the initial rotation of the specimen; as the total shear force increased, the experimental curve flattened out, surpassing the finite element prediction, before both failing at the same total shear force. The finite element model for Specimen 9.5-2-25.4 in **Figure 35(h)** showed excellent agreement with the experimental force-displacement response.

To achieve a closer match between model predictions and experimental data, adjustments were made to select model parameters. The elastic moduli assigned to the steel collar plate, HSS tube, and shear studs were modified from their nominal values due to bond slip observed in the experiments; they were assumed to be lower than the actual values to account for bond slip effects of studs and steel collar plate, and this reduction is similar to that used to account for bond slip effects of mild steel reinforcing bars in reinforced concrete columns (Neupane et al. 2023). Calibration of stiffness properties enabled finite element simulations to capture the experimental initial force-displacement. An offset of the vertical loading point from the HSS tube center in the range of 2.5 to 25 mm was applied for the loading eccentricity which improved the correlation between finite element model and experimental results. Through these modifications, the finite element model was able to replicate the nonlinear force-displacement response, total shear force, and deformation.

The finite element model can simulate complex nonlinear behavior and failure mechanisms of the shear stud connection, including the yield-pullout-tensile fracture, and concrete cracking-shear stud pullout failure. By calibrating geometric and material properties, the finite element model can be used to explore a wider design space and identify configurations that maximize strength and ductility of steel-concrete composite connections. This allows engineers to refine the design of interface details leading to efficient solutions for full-scale columns in bridges.

7.5 CONCLUSIONS FROM SMALL SCALE SUBASSEMBLIES AND PARAMETRIC STUDY

This research investigated the performance of shear stud and steel collar plate connections in bridge columns with stretch length anchors (SLAs) through a combination of experiments, analysis, and finite element model simulations. These findings offer guidance for estimating the capacity of steel-concrete interface details in bridge rocking columns. This will be used to explore practical design details that include additional capacity offered by steel collar assembly and/or other stress transfer mechanisms such as shear rims or stiffener plates.

1. Three primary failure modes were observed in the experiments: yield-pullout-tensile fracture, shear stud shear fracture, and concrete cracking-shear stud pullout. The yield-pullout-tensile fracture mode is desirable since it preserves concrete column integrity.

2. The experiments with one 12.7 mm diameter shear stud demonstrated the ability to achieve the desired yield-pullout-tensile fracture behavior for both a 9.5 mm and a 12.7 mm steel collar plate thickness. Specimens with two 12.7 mm diameter shear studs had the same failure mode and achieved 1.5 to 1.7 times the total shear force resistance of a single shear stud. Analysis using the Whitney stress block confirmed that one shear stud could reliably transfer tensile forces from the SLA anchor to the column without damaging the concrete.
3. The single 25.4 mm diameter shear stud specimens experienced shear fracture of the shear stud for both a 9.5 mm and a 12.7 mm steel collar plate thickness. Analytical equations from the literature which included connection geometry, material properties and frictional effects at the steel-concrete interface with a Von Mises failure criterion produced conservative total shear force predictions for this failure mode.
4. Specimens with two 25.4 mm diameter shear studs failed due to concrete cracking and shear stud pullout caused by diagonal tension in the concrete. The specimens with two studs achieved 1.3 to 1.5 times the total shear force resistance of the case with a single 25.4 mm shear stud.
5. This research emphasizes the importance of the diameter and number of studs as well as the steel collar plate thickness to achieve the desired yield-pullout-tensile fracture failure mode while maximizing the total shear force.
6. The stud shear strength was compared to the AASHTO 9th and 10th editions and to Eurocode 4, which were found to be conservative. The experimental stud shear strength was found to be 1.21 times the AASHTO 9th edition, 1.73 times the AASHTO 10th edition, and 1.51 times the Eurocode 4 values. The AASHTO and Eurocode predictions are based on shear alone and this implies that these shear strength factors are lower bounds.
7. The finite element method model demonstrated excellent agreement with experimental results for all three failure modes. The model accurately captured total shear force, displacement, and initial stiffness. The finite element model can be extended to predict the total shear force and displacement resistance of larger columns.

CHAPTER 8. CAPACITY CALCULATION USING FINITE ELEMENT METHOD

8.1 FINITE ELEMENT MODEL OF BENT 4FA AND 4F

A numerical analysis was conducted on the 4FA bridge bent test. Static monotonic pushover curves were computed for bent configuration and then compared with the outcomes of the physical tests. The subsequent sections describe the details of the numerical model and its correlation with the experimental findings.

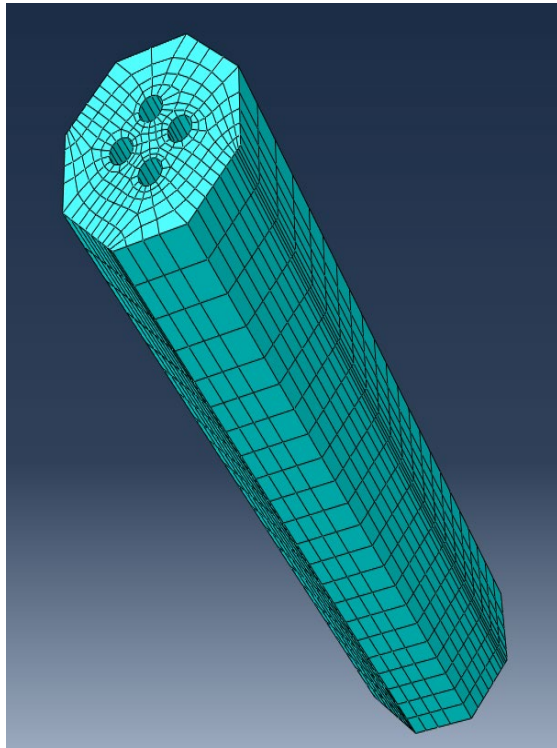
8.1.1 Model Layout

The concrete was represented with properties corresponding to the measured 14 ksi compressive concrete compressive strength. To represent concrete characteristics, the concrete damage plasticity (CDP) model was used. Columns were modeled using solid brick elements which used C3D8R element type. As in the real test specimen, there are a total of 4 holes passing throughout each column. In a similar manner, the footings and cap-beam were modeled as solid brick elements. The footings contained a shear key which was modeled by lowering the concrete surface; a finer mesh size was used to model the area where there was a shear key (**Figure 36(c)**).

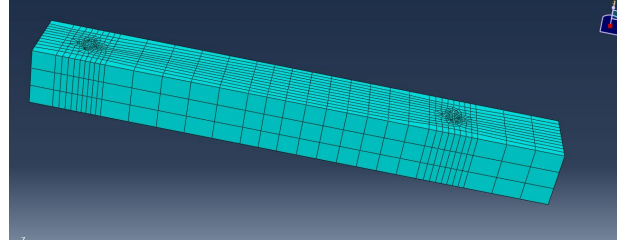
Post-tensioning bars were replicated using truss wire elements. The steel collar is simulated using material properties consistent with ASTM A709 Grade 59. A steel plate measuring ½ in. in thickness was used, coupled with 1-in. studs interconnecting the steel collar's plates. The meshed structures are shown in the **Figure 36(a-d)**. The steel collars were modeled to replicate the experimental setup. At the footing end, the collar included a welded steel plate, simulating a closed steel collar configuration that enabled steel-to-concrete interaction with the footing.

In contrast, the top face of the octagonal steel collar was left open to allow concrete-to-concrete interaction with the column. A tie contact was assigned between the concrete surface and the steel collar to simulate the effect of shear studs. Static and kinematic friction coefficients are used to establish interactions for both concrete-to-concrete and concrete-to-steel connections. To simplify numerical representation, the freely moving steel plate is disregarded, and instead, a general contact condition is established between the steel and concrete surfaces. Lateral pushover and axial loads are applied using reference nodes linked to the cap-beam's surface to replicate the experimental loading. The numerical response of the structure is simulated using explicit dynamic analysis. Reinforcing bars are embedded into the concrete surface of the column to simulate the bond between the concrete and reinforcement.

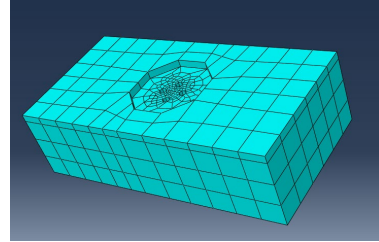
Steel chairs were modeled as solid brick elements and holes were provided to incorporate the free stretching of the SLAs. SLAs were modeled as wired truss elements made with Grade 36 steel material. SLAs were embedded to the nut on the top of steel chairs, while the parts inside the footing and column were modelled as embedded inside the concrete surface. **Figure 37** shows the schematic of the prepared FEM model in ABAQUS with the applied lateral loading. **Table 14** and **Table 15** show the bridge bent components with the element type used in ABAQUS and the respective contact properties.



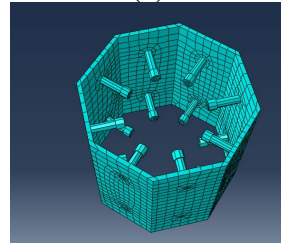
(a)



(b)










(c)



(d)

Figure 36. Meshed structures: (a) Column; (b) Cap beam; (c) Footing; and (d) Steel collar and studs

Table 14. Parts with their respective elements

Parts	Element Type	Element View
Column	Solid Element (C3D8R)	
Footing	Solid Element (C3D8R)	
Steel-chair	Solid Element (C3D8R)	
PT-nut & collar	Solid Element (C3D8R)	
SLA-nut	Solid Element (C3D8R)	
PT-Bar	Truss Element (T3D2)	
SLA	Truss Element (T3D2)	

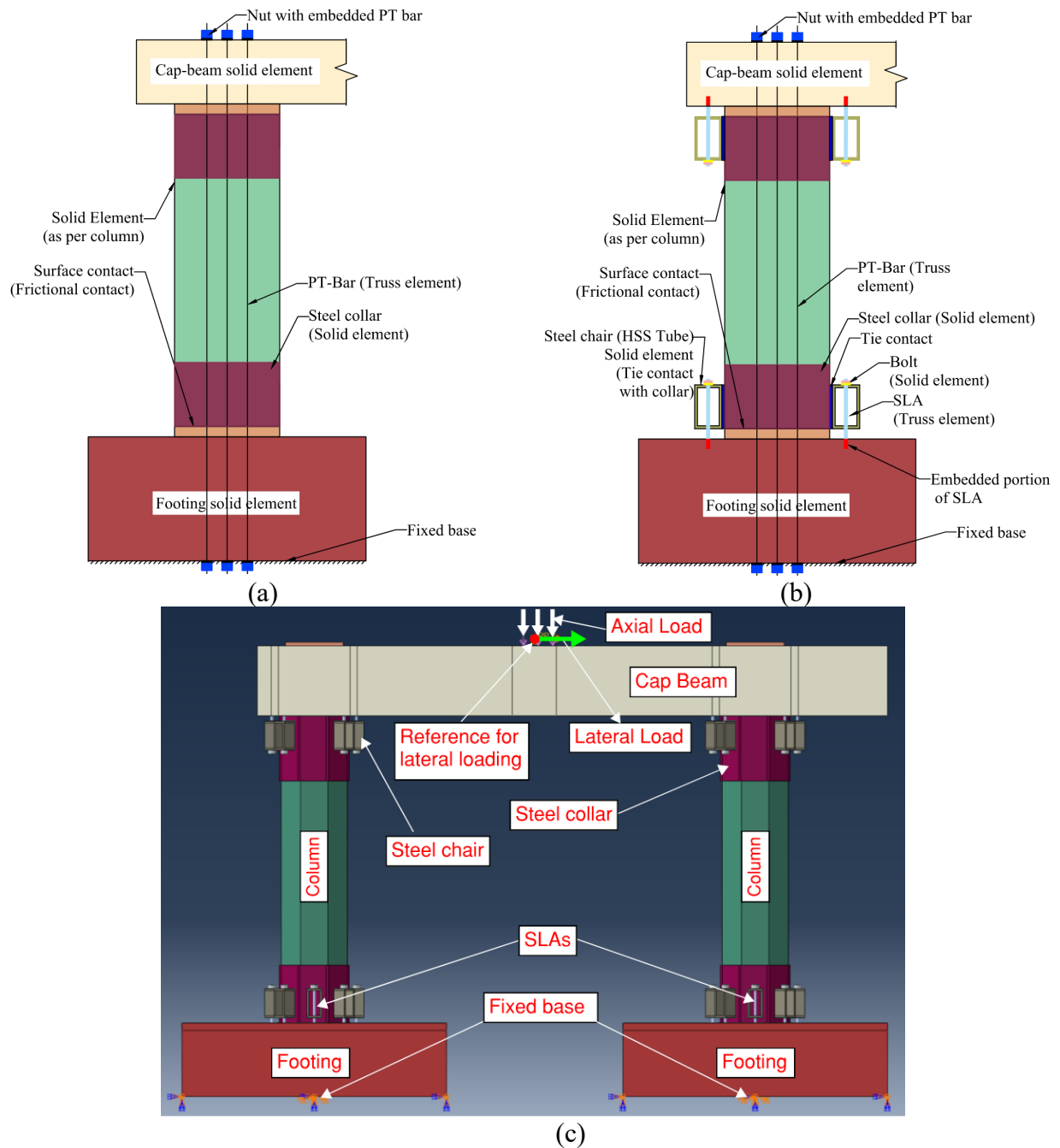






Figure 37. Schematic of the FEM model: (a) 4F; (b) 4FA; and (c) Whole bent as represented by ABAQUS

Table 15. Parts and their respective contact properties

Parts	Contact Property	Color Representation	Coef. of friction used
Column-to-footing	Surface-to-surface friction		0.5
PT-nut to surface column/footing	Surface-to-surface friction		0.35
SLA-nut to surface Steel-chair	Surface-to-surface friction		0.35
SLA-to-footing/cap-beam	Embedment in footing		N/A (bonded to concrete)
PT-to-nut	Embedment in nut		N/A (bonded to nut)
SLA-to-nut	Embedment in nut		N/A (bonded to nut)

8.1.2 FEM Results and Comparison with Experiments

A preliminary numerical analysis was conducted, and the outcomes from ABAQUS were compared with the cyclic response obtained from the experimental study for the Bent 4FA

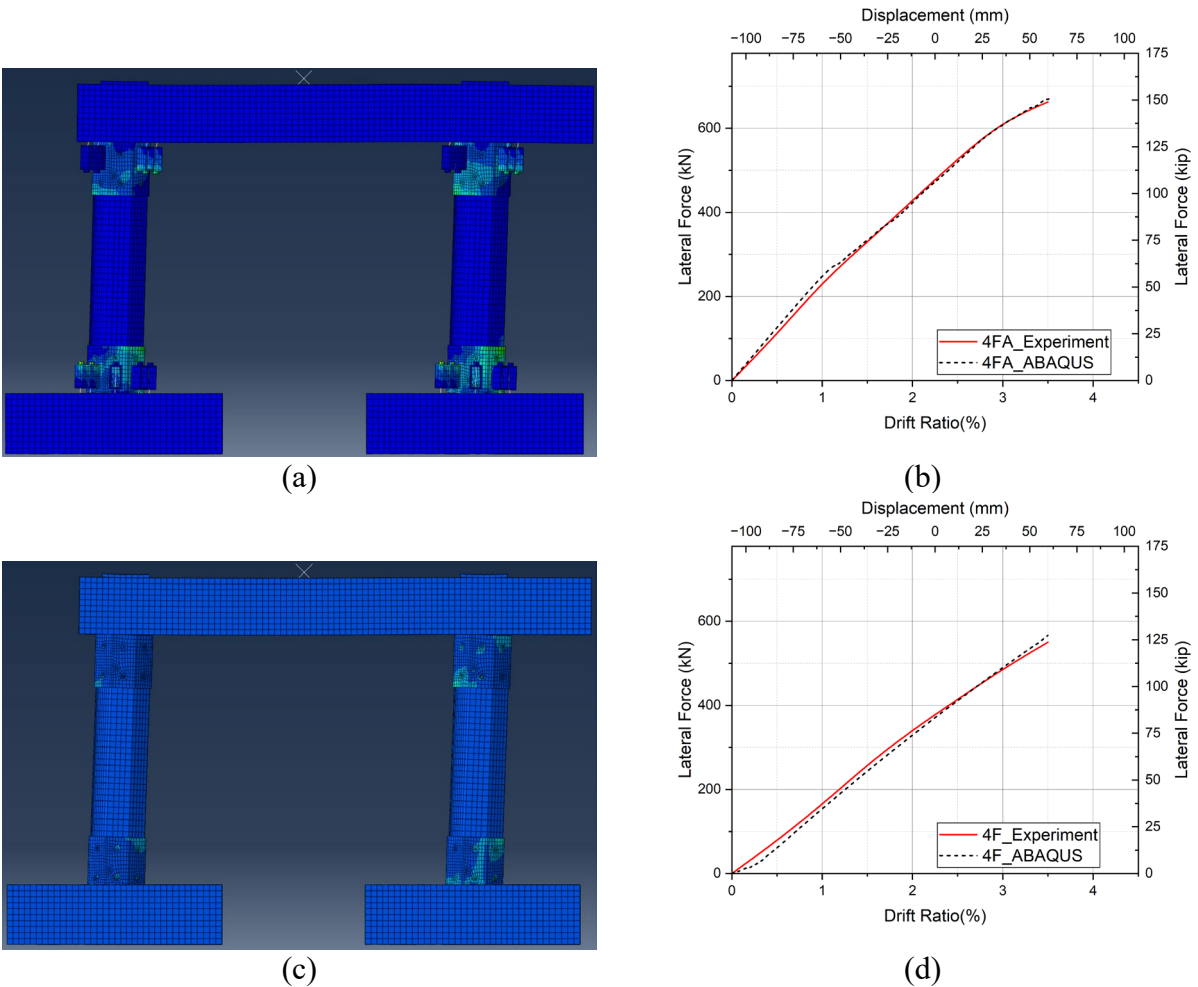


Figure 38. FEM Results: (a) Deflected shape; (b) Hysteresis vs Pushover test 4F; (c) Deflected shape test 4FA; and (d) Hysteresis vs Pushover test 4FA.

specimen. Due to the higher computational demands, only a monotonic static nonlinear pushover analysis was performed. The deflected shape of the bridge bent is represented (**Figure 38(a, c)**), showing the maximum lateral displacement at a 3.5% drift ratio, scaled by a factor of 5 for clear visualization of deformations. This illustration indicates that the adopted modeling methodology can effectively forecast the rocking behavior of the bridge bent. Additionally, a comparison was made between the results obtained from the numerical analysis and the experimental hysteresis envelope (**Figure 38 (b, d)**). Notably, the pushover curve closely aligns with the cyclic envelope from the experimental study, effectively forecasting both the peak lateral load and the stiffness of the bent with minimal deviation, thus indicating the effectiveness of the modeling approach. Once the hysteretic response was computed within a reasonable range parametric study of the same bridge bent was done with the shear rims; the alternative solution of the studs was studied, and recommendations were based on numerical results. **Figure 39** shows the FEM model results for the specimen 4FBA and 4FB and the experimental cyclic envelope was compared with the FEM model. This shows that the FEM model can predict pushover response.

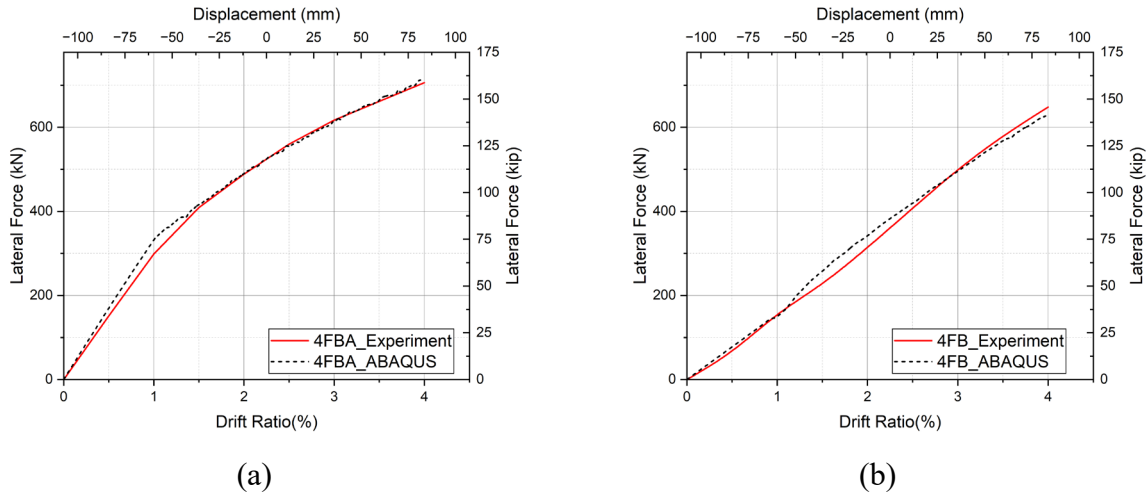


Figure 39. Experimental cyclic envelope vs pushover response from FEM model: (a) bent 4FBA; and (b) bent 4FB.

8.2 PARAMETRIC STUDY WITH STUDS AND RIMS

Once the working numerical model was obtained the performance was studied in terms of concrete crushing strengths and it was seen that the bent with SLAs did not have any concrete damage caused due to stress concentrations and no pullout of the studs was seen. Similarly, a model where studs were replaced by using rims was used and it was found that concrete crushing was initiated just above steel collar and caused higher stresses in the steel collar. This suggested that the specimen model with two stud could distribute eccentric load transferred from the SLAs through the chair and steel collar without any damage. In addition, during experimental study 3 studs were welded to each face of steel collar. However, FEM study suggests that two studs are enough to dissipate required force developed due to elongation of SLAs. **Figure 40(a)** and **Figure 40(b)** show the FEM results and the concrete damage initiation in a high stress concentration region. The compressive strain damage analysis for the specimen with a shear rim was terminated at a 2.75%

drift ratio, since a significant drop in lateral load was observed following the onset of concrete crushing. Beyond this point, the accuracy of the numerical model predictions became less reliable.

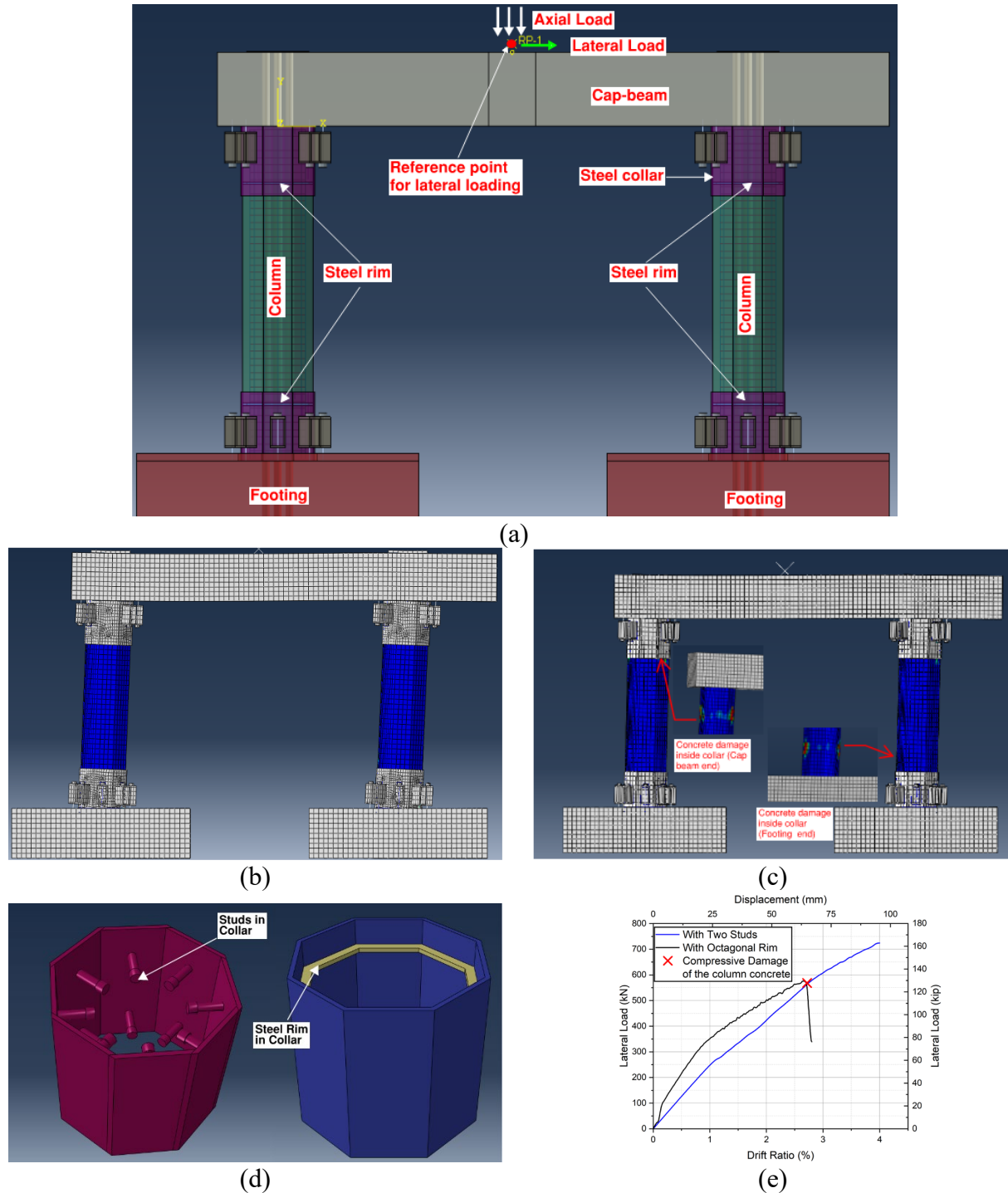


Figure 40. Parametric study of bent specimen with rims: (a) FEM model layout, (b) Deflected shape showing concrete damage with studs (4.0% drift ratio), (c) Deflected shape with rims (2.75% drift ratio), (d) Steel collar detail with rims and studs, and (e) Pushover response comparison of studs vs. rims.

Compressive damage was observed in the bridge bent specimen FEM model with shear rims but not in the specimen with shear studs, as revealed by the FEM analysis results, due to differences in load distribution and stress concentration. In the shear rim configuration, modeled as a continuous steel plate around the column, localized stresses developed near the steel collar, initiating concrete crushing at a 2.75% drift ratio, as shown in **Figure 40(c)** and **Figure 41(c)**. This suggests that shear rims remain a viable design option for structures where displacement demands are limited to approximately 2.75% drift, as they effectively transfer loads up to this threshold without compromising structural integrity. However, for higher seismic regions where drift demands may exceed this level, the FEM results indicate that shear studs, using two studs per face of the steel collar, better distribute the eccentric loads from the SLAs. This distribution prevents stress concentrations, allowing the stud-equipped specimen to sustain up to a 4.0% drift ratio without concrete damage, as shown in **Figure 40 (b)** and validated by experimental results.

Both shear rims and studs can be effectively utilized in bridge bent design, with the choice depending on the seismic demand of the region. For moderate seismic zones with drift ratios around 2.75%, shear rims provide a practical solution, while studs are recommended for high-seismic zones requiring resilience beyond 4.0% drift. The FEM analysis underscores the importance of tailoring the design to specific displacement demands for optimal performance. While shear rims offer practical benefits for moderate drift scenarios, further experimental and numerical studies are recommended to optimize their performance in high-seismic regions to ensure robustness under high displacement demands.

8.3 CONCRETE DAMAGE PROPAGATION

A finite element (FEM) numerical model was developed to investigate damage propagation in bridge bents equipped with shear rims and those with shear studs. The model was primarily used to evaluate strain distribution, which serves as an indicator of damage initiation and progression. Results showed that the specimen with shear rims began approaching a critical strain threshold at approximately a 2.5% drift ratio, whereas the specimen with shear studs exhibited no signs of damage up to 4.0% drift ratio. **Figure 41(a-c)** illustrates the progression of concrete compressive damage at various drift levels. Specifically, **Figure 41(c)** captures the state just before the onset of concrete compressive damage—no damage was observed until this stage. Once compressive damage occurred in the rim region near the steel collar, a noticeable drop in lateral load capacity was observed, as shown in **Figure 40(e)**. Importantly, this degradation occurred only beyond the 2.5% drift ratio, suggesting that shear rims may be suitable for use in regions where displacement demands remain below this threshold. **Figure 41(d)** shows the concrete strain values at different drift ratios, highlighting the influence of shear studs and rims on strain development. For the specimen with a shear rim, strain localization initiates in a small region, and as the drift increases, most of the mesh elements approach their peak crushing strain around a 2.75% drift ratio. Beyond this point, a significant reduction in lateral load capacity is observed, indicating the onset of substantial concrete damage, which was not seen in the specimen with shear studs.

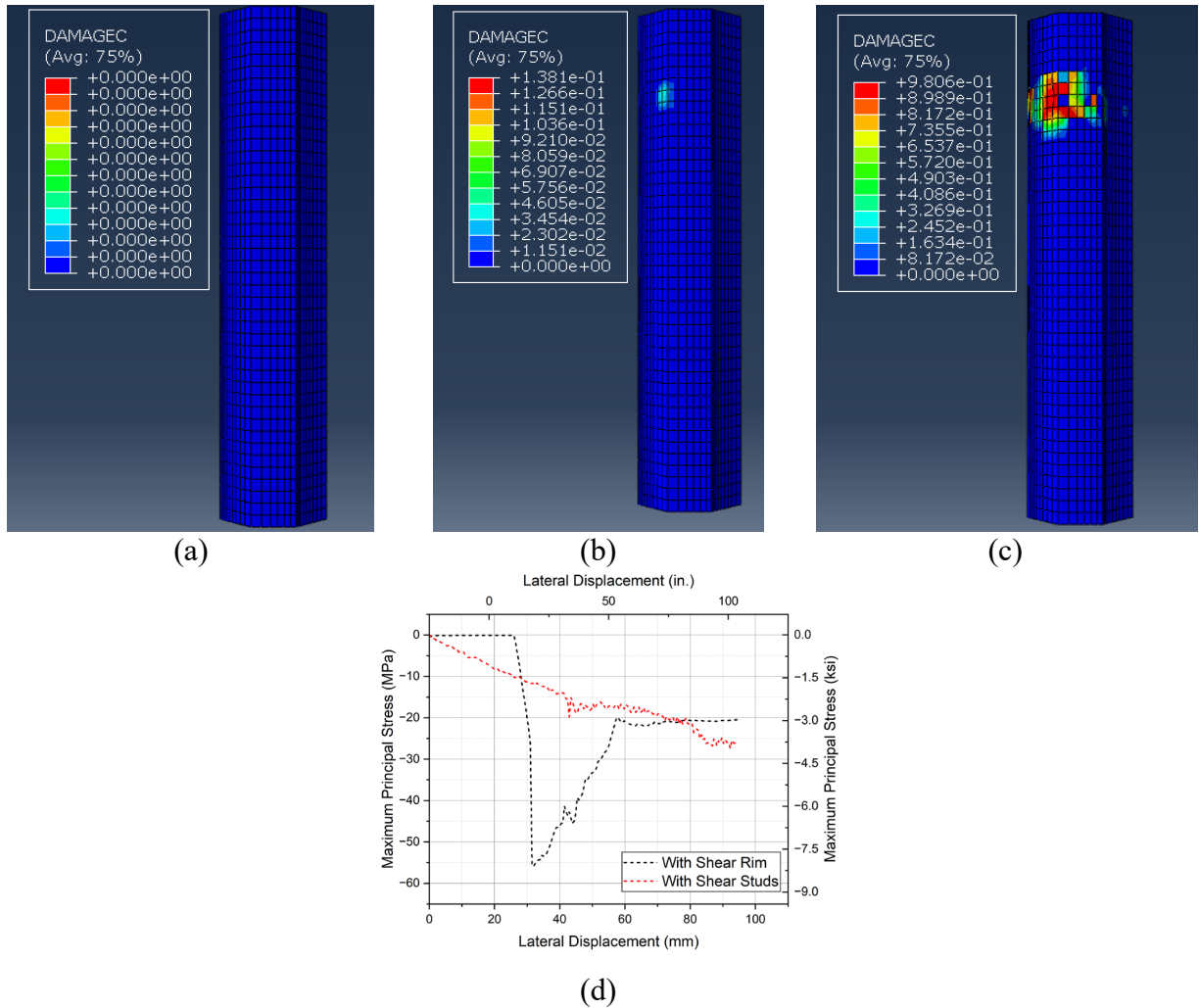


Figure 41. Concrete compressive damage propagation at different lateral displacement for column with shear rim: (a) Initial state; (b) 1.5 % drift ratio; (c) 2.5% drift ratio; and (d) Concrete compressive strain distribution inside the steel collar.

8.4 DESIGN OF SHEAR RIMS

The thickness of the shear rim can be calculated based on the ultimate load capacity of the SLAs ($F_{u,SLA}$). Once the ultimate load capacity is known, it can be used to calculate the total moment that needs to be distributed, and that moment and section modulus can be used to calculate the thickness (t) of the shear rim plate. The geometrical detail for shear rim load distribution calculations is shown in **Figure 42**. The shear-rim needs to be designed in such a way that the width (w) of the shear-rim does not touch the spirals, thus the width (w) should be assumed less than the clear concrete cover, while breadth (b) is equal to the width of the concrete column octagon side.

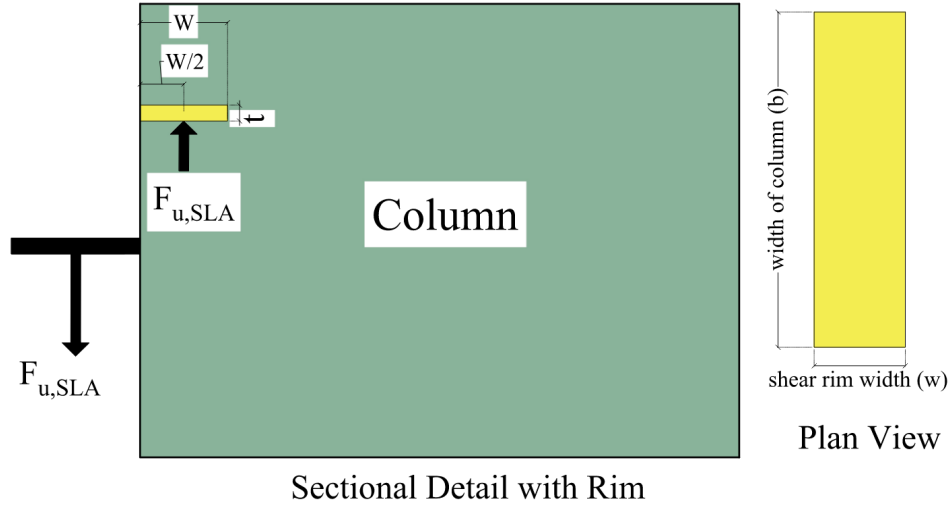


Figure 42. Schematic of shear rim force distribution at 4.0% drift ratio.

The total resisting moment produced due to reaction on the shear rim can be calculated as:

$$M = F_{u,SLA} * \frac{w}{2} \quad (8.1)$$

Once, this moment is known, for a given ultimate strength (f_u) of the shear rim steel plate, the section modulus (S) can be determined as:

$$S = \frac{M}{f_u} \text{ and } S = \frac{bt^2}{6} \text{ (rectangular section)} \quad (8.2)$$

Using equations (8.1) and (8.2), the thickness required for the shear rim can be calculated. The thickness of the Grade 36 shear rim was found to be 12 mm when Grade 36 SLAs were used for the specimen bent construction.

8.5 CONCLUSIONS BASED ON FEM STUDY

The Finite Element Method (FEM) model was developed to predict the cyclic response of specimen bents, achieving remarkable accuracy in replicating the experimental cyclic envelope, thus establishing its reliability for future structural design applications. This validated FEM model was further extended to conduct a comparative analysis of bents equipped with shear studs versus those with shear rims, focusing on key performance metrics such as initial stiffness, drift capacity, and resistance to damage under seismic loading. The results revealed that shear rims offer a marginally higher initial stiffness and perform effectively up to a 2.5% drift ratio, beyond which concrete compression damage was observed in the column. In contrast, shear studs demonstrated superior resilience, maintaining structural integrity without column damage up to a 4.0% drift ratio, making them a more robust choice for applications requiring higher drift capacities. A comprehensive parametric study using FEM models showed the value of shear studs at higher drift levels while confirming that shear rims remain a viable, lightweight, and constructible alternative for designs limited to a 2.5% drift ratio. This dual approach highlights the versatility of the FEM model in addressing diverse design requirements.

Building on these findings, the proposed FEM-based methodology facilitated the development of an innovative shear rim-based design, which, although not yet tested experimentally, optimizes moment transfer into the column while adhering to critical design objectives: maintaining essentially elastic material behavior, minimizing steel weight, and enhancing constructability by eliminating the need for studs through the steel cage. This design solution, derived from FEM simulations, complements the experimental validation of shear studs, which exceeded the design drift ratio limit, effectively protecting the column and ensuring efficient force transfer from SLAs. The methodology also provides a practical framework for calculating the initial thickness of shear rims, streamlining the design process. To further enhance confidence in these findings, additional experimental studies on shear rim-equipped specimens are recommended to validate FEM predictions and refine design parameters. Collectively, the FEM analysis, supported by experimental and analytical results, establishes a robust framework for designing specimen bents with either shear studs or shear rims, ensuring reliable column end protection and force distribution under seismic loading conditions.

CHAPTER 9. PUSHOVER CAPACITY ESTIMATION OF ROCKING BRIDGE BENT USING ANALYSIS METHOD

A theoretical model for rocking bridge bents was proposed in which the columns are assumed to remain rigid without any local yielding deformations (Mander and Cheng 1997). However, in experiments it has been observed that compressive deformations exist, and the rigid body assumption is not sufficient (Guerrini et al. 2015a; Mashal and Palermo 2019a). The region of compressive deformations must be included for determining the neutral axis depth based on rocking column behavior. The presence of shear keys enables the column rocking without sliding. There are two deformation stages for a rocking column under lateral load: (1) pre-rocking or decompression stage, and (2) rocking stage.

9.1 PRE-ROCKING OR DECOMPRESSION STAGE

Before rocking starts bridge, columns are vertical and assumed fixed at both ends. **Figure 43** shows a two-column bridge bent at the pre-rocking or decompression stage. The flexural stiffness of the system is provided by the columns and is calculated using fixed conditions as (Han et al. 2019):

$$K_c = n_c \left(\frac{12EI_{eff}}{H_c^3} \right) \quad (9.1)$$

where, K_c is the flexural stiffness of the fixed column before rocking, n_c is the number of columns, E is the modulus of elasticity of concrete, I_{eff} is the effective moment of inertia of the column cross-section ($0.7I_g$ for post-tensioned columns), I_g is the gross moment of inertia of the column section, H_c is the column height, and L_c is the height from the footing surface to the centerline of the lateral load in the cap beam, as shown in **Figure 43**.

During the decompression stage, the gap at the column ends is closed and the materials are within the elastic region. A total constant axial gravity load of 640 kN is assumed as used in the experimental study. The decompression moment (M_{dec}) can be computed from basic elastic section analysis as (Guerrini et al. 2015a; b):

$$M_{dec} = n_c \left(\frac{W}{n_c} + n_{PT} F_{PT,i} \right) \left(\frac{S_c}{A_c} \right) \quad (9.2)$$

where n_c is the number of the columns, $\frac{W}{n_c}$ is the axial gravity load on each column, $F_{PT,i}$ is the initial PT force in the columns and n_{PT} number of PT bars on each column. The column section is octagonal, but it is modified into a circular section of equivalent area; hence D is the diameter of the equivalent section; A_c is the cross-sectional area of the column, and S_c is calculated as:

$$S_c = 2 \frac{I_{eff}}{D} \quad (9.3)$$

Once the decompression moment is known the lateral force required to overcome this moment can be obtained using equation 8.4(a) and once the decompression lateral load is obtained the displacement is obtained assuming the bent as a portal frame with stiff column using equation 8.4(b).

$$F_{dec} = \frac{2M_{dec}}{H_c} \quad 9.4(a)$$

$$\Delta_{dec} = \frac{F_{dec}L_c^3}{24E_cI_{eff}} \quad 9.4(b)$$

After the lateral force at decompression is computed, it is added to the lateral force computed in the rocking analysis, since the column must pass the decompression stage before it starts rocking.

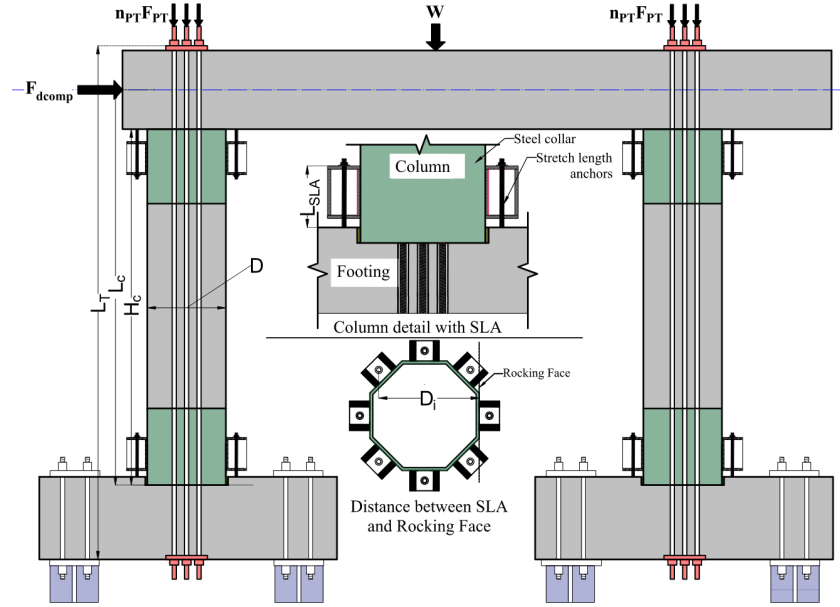


Figure 43. Two-column bridge bent at decompression stage with or without SLAs.

9.2 ROCKING STAGE

Once the decompression moment is exceeded at a joint, a gap forms that opens and a rocking mechanism develops. **Figure 44** illustrates the rocking stage of a two-column bridge bent. The neutral axis depth (c) must be found to compute the post-tensioning forces and the lateral force during rocking. The column cross-section is such that the post-tensioning bars are symmetric about both sides of the centroidal axis; moreover, it is assumed that each PT bar experiences an equal force which was verified experimentally (Neupane and Pantelides 2024a). Once the neutral axis depth is known, the tensile force F_{PT} in the PT bars at a given drift ratio is (Han et al. 2019):

$$F_{PT} = \begin{cases} F_{PT,i} & \text{for } c > \frac{D}{2} \\ E_{PT}A_{PT} \left[\frac{(\frac{D}{2}-c)\theta}{L_T} + \varepsilon_0 \right] & \text{for } c \leq \frac{D}{2} \end{cases} \quad (9.5)$$

where A_{PT} and E_s are the area and modulus of elasticity of the PT bars, θ is the total joint rotation, L_T is the total unbonded length of the PT bars, and ε_0 is the initial strain due to initial post-tensioning:

$$\theta = \frac{\Delta_{\text{rot}}}{H_c} \quad (9.6)$$

$$\Delta_{rot} = (DR) L_c \quad (9.7)$$

$$\varepsilon_0 = \frac{f_{PT,i}}{E_s}, F_{PT,i} = f_{PT,i} A_{PT} \quad (9.8)$$

where DR is the drift ratio expressed as a percentage, $f_{PT,i}$ is initial post tensioning stress. From bending moment equilibrium about the rocking toe (point O in **Figure 44**) and the number of columns, the lateral force due to rocking (F_{rot}) can be calculated from the number of PT bars (n_{PT}) and the total gravity load (W) as:

$$F_{rot} H_c = n_c \left(n_{PT} F_{PT} + \frac{W}{n_c} \right) (D - c - \Delta_{rot}) \quad (9.9)$$

Eq. (8.9) can be used to compute the pushover response of the bent without SLAs i.e. PT-only bent during rocking using the PT-force distribution and the gravity load for given drift ratio.

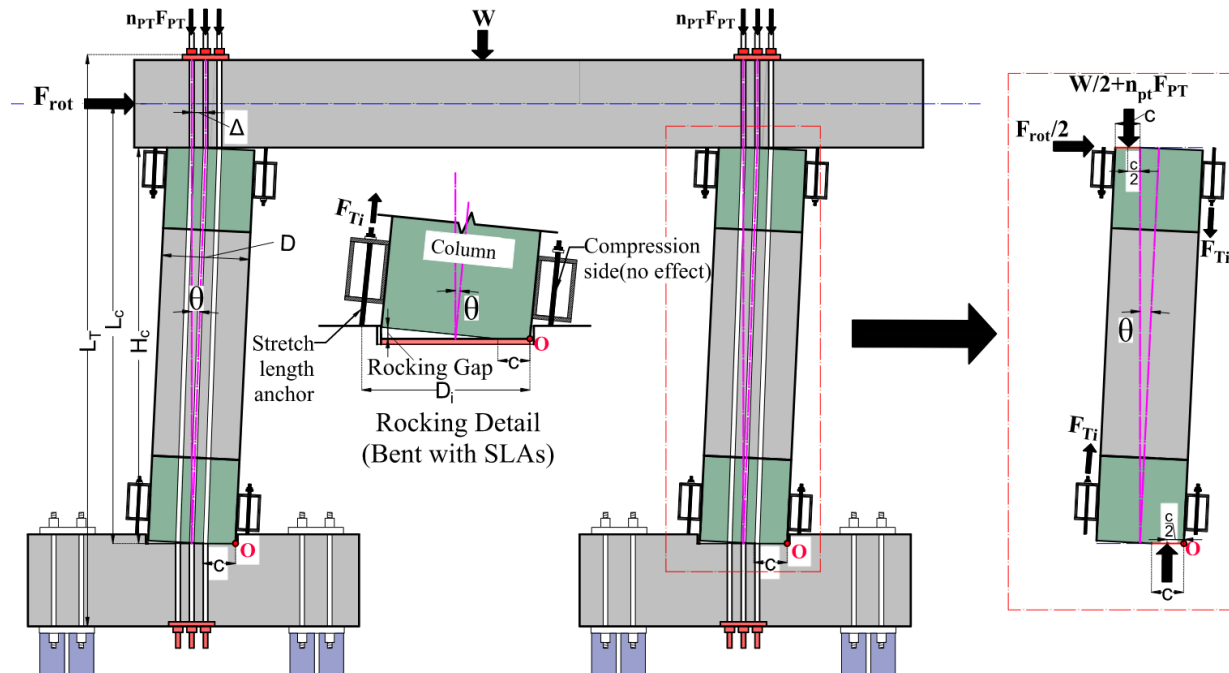


Figure 44. Two-column bridge bent at rocking stage with SLAs.

9.2.1 Rocking bridge bent with post-tensioning and external energy dissipators

When external energy dissipators (SLAs) are used they undergo tension by design; as shown in rocking detail in **Figure 44**, SLAs are secured at the top of the steel chair with a nut and washer; they experience tensile forces on the tension side of the column with no effect on the compression side, i.e. the SLAs are tension-only elements. The presence of SLAs is incorporated in the analysis to predict the behavior. The tensile strain in the SLAs at any location can be calculated as:

$$\begin{aligned}\varepsilon_{SLA} &= \theta \left(\frac{(D_i - c)}{L_{SLA}} \right); \text{ for } (D_i - c) \geq 0 \\ \varepsilon_{SLA} &= 0; \text{ for } (D_i - c) < 0\end{aligned}\tag{9.10}$$

where D_i is the distance of the SLA from the extreme compressive fiber (**Figure 44**), and L_{SLA} is the SLA stretch length, calculated as the free length of the anchor, as shown in **Figure 43**. Once, the tensile strain is found, the corresponding tensile stress ($\sigma_{T,i}$) and tensile force ($F_{T,i}$) in the SLA can be obtained from the stress-strain curve at each drift ratio as:

$$F_{T,i} = A_{SLA} \sigma_{T,i}\tag{9.11}$$

Once the force in each SLA is computed, the bending moment equilibrium at the rocking toe (point O in **Figure 44**) gives:

$$F_{rot} H_c = n_c \left\{ \left(n_{PT} F_{PT} + \frac{W}{n_c} \right) (D - c - \Delta_{rot}) + \sum_{n=1}^{n_{SLA}} F_{T,i} D_i \right\}\tag{9.12}$$

where n_{SLA} is the number of SLAs in tension for each column.

Once, the F_{rot} is obtained from equations (9.9) and (9.12), the net horizontal force needs to be calculated as the elongation of PT bars and the angle made by PT bars during rocking with vertical surface has a horizontal component that acts in the direction of F_{rot} . The lateral load contribution due to PT bars in rocking system is calculated as:

$$F_{PT, horizontal} = n_c n_{PT} F_{PT} \sin(\theta)\tag{9.14}$$

As, $F_{PT, horizontal}$ acts against the F_{rot} , the total lateral load can be computed as,

$$F_{tot} = F_{rot} + F_{PT, horizontal}\tag{9.15}$$

The total lateral displacement is the sum of Δ_{rot} due to column rocking and elastic displacement ($\Delta_{elastic}$) caused by application of the lateral load. Thus, the total lateral displacement can be calculated as:

$$\Delta_{Tot} = \Delta_{rot} + \Delta_{elastic}\tag{9.16}$$

where, $\Delta_{elastic}$ can be calculated as,

$$\Delta_{elastic} = \frac{F_{tot} L_c^3}{24 E_c I_{eff}}\tag{9.17}$$

where F_{tot} is based on the bridge bent configuration. Equation (9.9) and (9.15) should be used for a bent with only PT bars in the columns and Eq. (9.12) and (9.15) for a bent with PT bars in the columns and SLAs. The final drift ratio is computed based on the total lateral displacement using equation (9.18).

$$\text{Final Drift Ratio } (DR_T) = \frac{\Delta_{Tot}}{L_c} * 100\% \quad (9.18)$$

9.3 COMPUTATION OF NEUTRAL AXIS DEPTH (c)

At the end of decompression stage, which begins the start of rocking stage. At this point decompression force needs to be equal to the rocking force at $\Delta_{rot} = 0$. Thus, decompression force and rocking force at $\Delta_{rot} = 0$ should be equal which results in:

$$\frac{2}{H_c} * n_c \left(\frac{W}{n_c} + n_{PT} F_{PT,i} \right) \left(\frac{S_c}{A_c} \right) = \frac{n_c}{H_c} \left\{ \left(n_{PT} F_{PT} + \frac{W}{n_c} \right) (D - c - \Delta_{rot}) + \sum_{n=1}^{n_{SLA}} F_{T,i} D_i \right\} \quad (9.19)$$

At this point Δ_{rot} and SLA force is equal to zero,

$$\frac{2}{H_c} * n_c \left(\frac{W}{n_c} + n_{PT} F_{PT,i} \right) \left(\frac{S_c}{A_c} \right) = \frac{n_c}{H_c} \left\{ \left(n_{PT} F_{PT} + \frac{W}{n_c} \right) (D - c) \right\} \text{ i.e. } 2 * \left(\frac{S_c}{A_c} \right) = (D - c)$$

The value of S_c/A_c is computed to be, $\frac{\frac{2I_{eff}}{D}}{\frac{\pi D^2}{4}} = \frac{2 * 0.7 * \frac{\pi D^4}{64}}{\frac{\pi D^3}{4}} = \mathbf{0.0875D}$

Substituting value of S_c/A_c gives, $2 * 0.0875D = D - c$, i.e., $\frac{c}{D} = \mathbf{0.825}$ at the end of decompression stage.

The neutral axis depth is required for determining the capacity of a bridge bent. Using Eq. (9.15) the neutral axis depth (c) is calculated based on the lateral force obtained from the experiment for bent 4FB. The neutral axis depth is then normalized by the diameter of the equivalent section (D), and the resulting values are obtained as a function of rotational drift ratio expressed as a percentage (DR). The resulting curve fits a second-order polynomial (Eq. 9.20) with an R^2 value of 0.998. response from the theoretical study closely matched the cyclic envelope observed in the experimental study (**Figure 45a**).

$$\frac{c}{D} = \begin{cases} 0.825, & \text{if } DR = 0.0\% \\ 574.86 (DR)^2 - 35.96(DR) + 0.825, & \text{if } 0.0\% < DR \leq 3.25\% \text{ (Rocking Stage)} \\ 0.26, & \text{if } 3.25\% < DR \leq 4.0\% \text{ (Rocking Stage)} \end{cases} \quad (9.20)$$

9.4 VALIDATION OF ANALYSIS METHOD RESULTS

Figure 45(a) illustrates the normalized neutral axis depth values obtained from the experiment study of specimen 4FB and the curve derived from a fitted polynomial equation for specimen 4FB (**Figure 45a**). Comparing the pushover capacity obtained from the analysis method and the polynomial equation to compute the normalized neutral axis depth revealed close agreement, supporting the proposed technique for calculating the neutral axis depth. Once the (c/D) value was determined from the polynomial equation, this same (c/D) value was applied to specimen 4FA, 4F and 4FBA, and the pushover curve was obtained (**Figure 45b-e**); the predicted response from the analysis method was within permissible limits. Same (c/D) equation obtained for specimen 4FB was used for all other specimens 4FA, 4F and 4FBA. Specimen 4FBA exhibited an

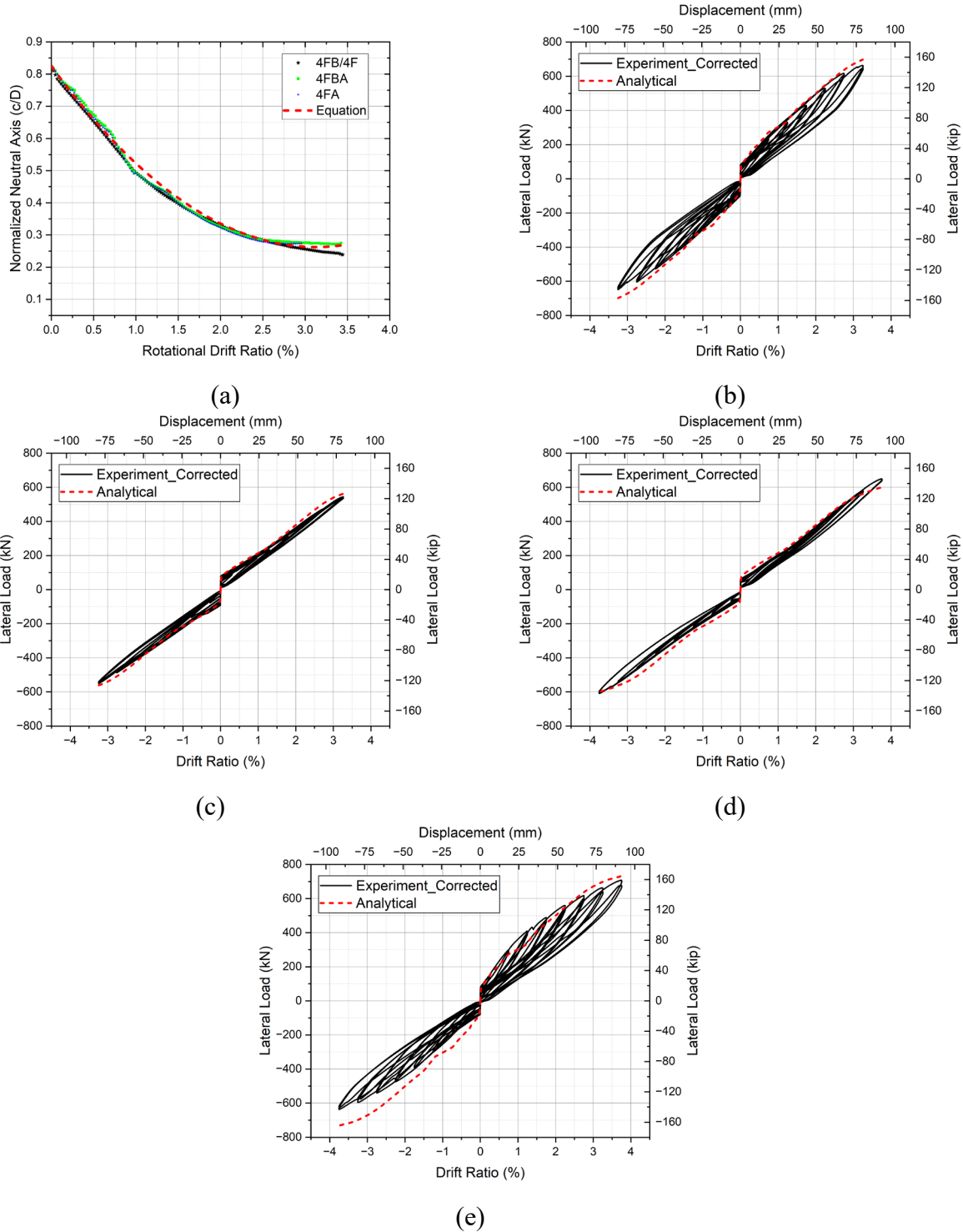


Figure 45. Comparison of analysis method to experiments: (a) normalized neutral axis depth for 4F and 4FA; (b) pushover capacity for bent 4FA (c) pushover capacity for bent 4F; (d) pushover capacity for bent 4FB; and (e) pushover capacity for bent 4FBA.

asymmetric response during the experiment, leading to discrepancies between the observed and analytical responses. In the previous section, experimental results for the specimens revealed some

play in the actuator connection, which introduced sliding displacements. This issue was addressed by correcting the experimental data, resulting in updated hysteretic response curves. The corrected curves, not featured in earlier sections, are used exclusively in the analytical study. The correction was implemented to reflect the anticipated experimental response, eliminating the initial play in the actuator, and to ensure alignment with the proposed analytical predictions.

The results obtained from analysis method incorporated sum of lateral load effects contributing of effects of decompression lateral force, contribution of PT bars, contribution of SLAs. **Figure 46** shows the contribution of each component in total lateral force capacity.

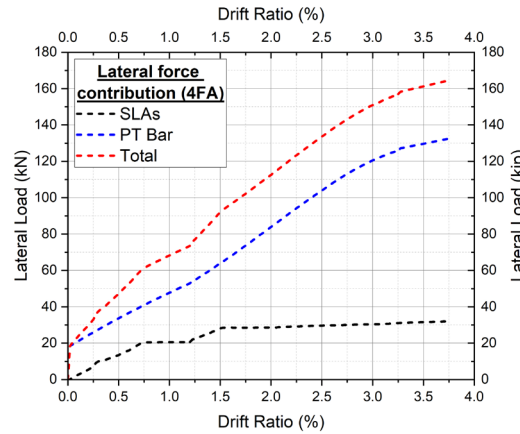


Figure 46. Contribution of PT bars and SLAs in Lateral Load capacity.

9.5 DESIGN STEPS

9.5.1 Initial Design

1. Calculate the initial geometric dimensions based on the monolithic bridge design.
2. Compute the equivalent circular diameter (D) of the column based on the gross area of the column.
3. Calculate ultimate tensile strength provided by the mild steel reinforcing bars when they are present in the case of monolithic or cast-in-place bridge design.

$$T_{ult} = \rho_{long} A_g f_u$$

where, T_{ult} is the total ultimate tensile strength contribution of mild steel longitudinal bars when present, ρ_{long} longitudinal reinforcement ratio generally 1.0% to 2.0% of gross area (A_g) and f_u is ultimate tensile strength of longitudinal reinforcing bars.

This T_{ult} must be distributed to the PT-bars and SLAs for a rocking bridge bent, as these are the primary components which pass through the interface of column to footing or column to cap-beam.

4. Assume the initial diameter of PT bars (D_{PT}) and calculate the area of PT bars (A_{PT}) and number of PT bars in each column (n_{PT}). The maximum PT force needs to be limited to the yield strength ($f_{PT,y}$) of the PT bars which ensures PT bars do not yield and maintain self-centering.

Calculate the contribution of PT bars ($F_{PT,y}$) to substitute ultimate tensile strength contributed by mild steel bars in the case of cast-in-place bridge bent as:

$$\mathbf{F}_{PT,y} = n_{PT} A_{PT} f_{PT,y}$$

5. The force that SLAs (F_{SLA}) need to distribute can be found as:

$$\mathbf{T}_{ult} = \mathbf{F}_{PT,y} + \mathbf{F}_{SLA} \text{ i.e. } \mathbf{F}_{SLA} = \mathbf{T}_{ult} - \mathbf{F}_{PT,y}$$

Assuming the number and area of SLAs (A_{SLA}) and grade of SLAs to be used ($f_{SLA,y}$), the number of SLAs required in each column can be computed (n_{SLA}).

$$n_{SLA} = \frac{F_{SLA}}{A_{SLA} f_{SLA,y}}$$

Since, only half of the SLAs go in tension while the other half remain in compression, the total number of SLAs that should be provided is $2n_{SLA}$.

6. Select initial PT force ($F_{PT,i}$) based on the rigid body analogy calculation.
7. Check for energy dissipation coefficient (Λ_D) and self-centering coefficient (Λ_C):

$$\Lambda_D = \frac{F_{SLA,u}}{P_u + F_{PT,i} + F_{SLA,u}}, \text{ where } F_{u,SLA} = f_{SLA,u} A_{SLA} n_{SLA}, P_u \text{ is the total axial gravity load and } f_{SLA,u} \text{ is the ultimate strength of SLAs.}$$

Check if Λ_D is from 0.1 to 0.6, if not go to step 4 and 5 and change the values of n_{PT} and n_{SLA} .

Also, verify that the self-centering conditions are satisfied,

$$\Lambda_C = \frac{F_{u,SLA}}{P_u + F_{PT,i}} \leq 1.0$$

8. Calculate the height of the steel collar (h_s):

The unfactored height (h_s^*) of the steel collar is calculated by using the equation given by (Shen et al. 2023).

$$h_s^* = 0.5\sqrt{D^2 - c^2} + 2D\sqrt{D^2 - c^2}, \text{ where } c \text{ is the neutral axis depth for maximum design drift ratio.}$$

This initial unfactored height is multiplied by a factor of safety (λ_s). This value was assumed to be equal to an overstrength factor of 1.2 used in the capacity design procedure (AASHTO 2015).

$$h_s = \lambda_s h_s^*$$

9. Collar thickness (t_s) is calculated based on the depth-to-thickness ratio as suggested by (Guerrini et al. 2015a).

$$\frac{D}{t_s} \leq 100$$

10. The number of studs can be calculated based on the shear strength of one stud using AASHTO 9th edition guidelines.

$$Q_{n1} = 0.5A_{sc}\sqrt{f'_c E_c} \leq A_{sc}f_{sc,u} \text{ where } Q_{n1} \text{ is the shear strength of one stud, } A_{sc} \text{ is the area of a shear stud, } f'_c \text{ is the concrete compressive strength, } E_c \text{ is the modulus of elasticity of the concrete and } f_{sc,u} \text{ is the ultimate strength of stud.}$$

$$\text{The number of studs } (n_{sc}) \text{ provided must be } n_{sc} \geq \frac{F_{SLA,u}}{Q_{n1}}.$$

Figure 47, shows the flow chart for initial sizing of the individual elements of the rocking bridge bent with SLAs.

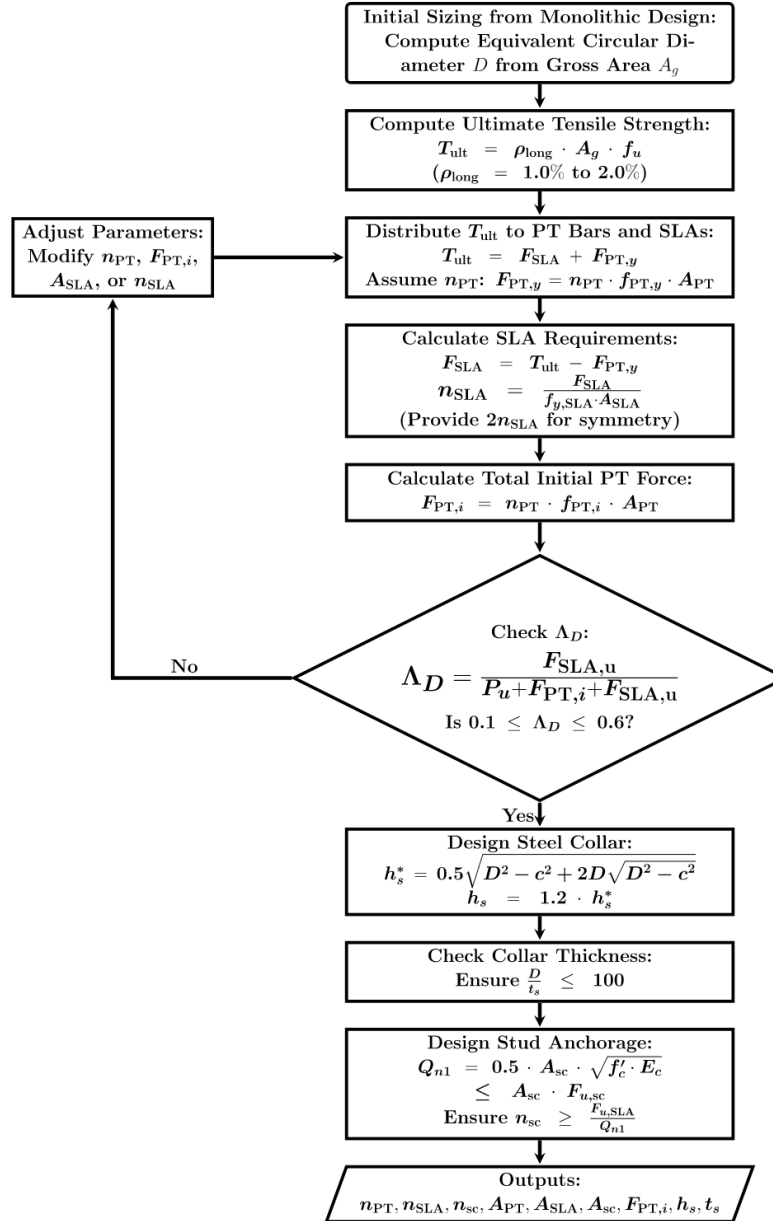


Figure 47. Flow chart for initial design.

9.5.2 Selection of initial PT force (Rigid body analogy with neutral axis depth)

1. Based on the geometry measure the length of PT bars (L_T), height of column (H_c), height from top of footing to mid-height of cap beam (L_c).
2. The rotation during rocking is calculated for each drift ratio using, $\theta = \frac{\Delta_{rot}}{H_c}$.
3. Δ_{rot} for a given drift ratio (DR) is calculated using, $\Delta_{rot} = (DR)L_c$.
4. Initial strain(ε_0) for an assumed initial PT force $F_{PT,i}$ is calculated as,

$\varepsilon_0 = \frac{f_{PT,i}}{E_{PT}}$, $f_{PT,i} = \frac{F_{PT,i}}{A_{PT}}$ where $f_{PT,i}$ is initial PT stress, A_{PT} is area of PT bar, E_{PT} is modulus of elasticity of PT bar.

5. Calculate neutral axis depth:

$$\frac{c}{D} = 0.825 \text{ for } DR = 0\% \text{ (Decompression stage)}$$

$$\frac{c}{D} = 574.86 (DR)^2 - 35.96(DR) + 0.825 \text{ for } 0\% \leq DR \leq 3.25\% \text{ (Rocking Stage)}$$

$$\frac{c}{D} = 0.26 \text{ for } 3.25\% \leq DR \leq 4.0\% \text{ (Rocking Stage)}$$

6. The PT force for a given drift ratio can be obtained,

$$F_{PT} = E_{PT} A_{PT} * \left[\frac{(\frac{D}{2} - c)\theta}{L_T} + \varepsilon_0 \right] \text{ and } F_{PT} = F_{PT,i} \text{ for } c > \frac{D}{2}$$

It should be noted that until c reaches $D/2$ there is no change in PT forces.

Figure 48 shows the flow chart for PT force distribution.

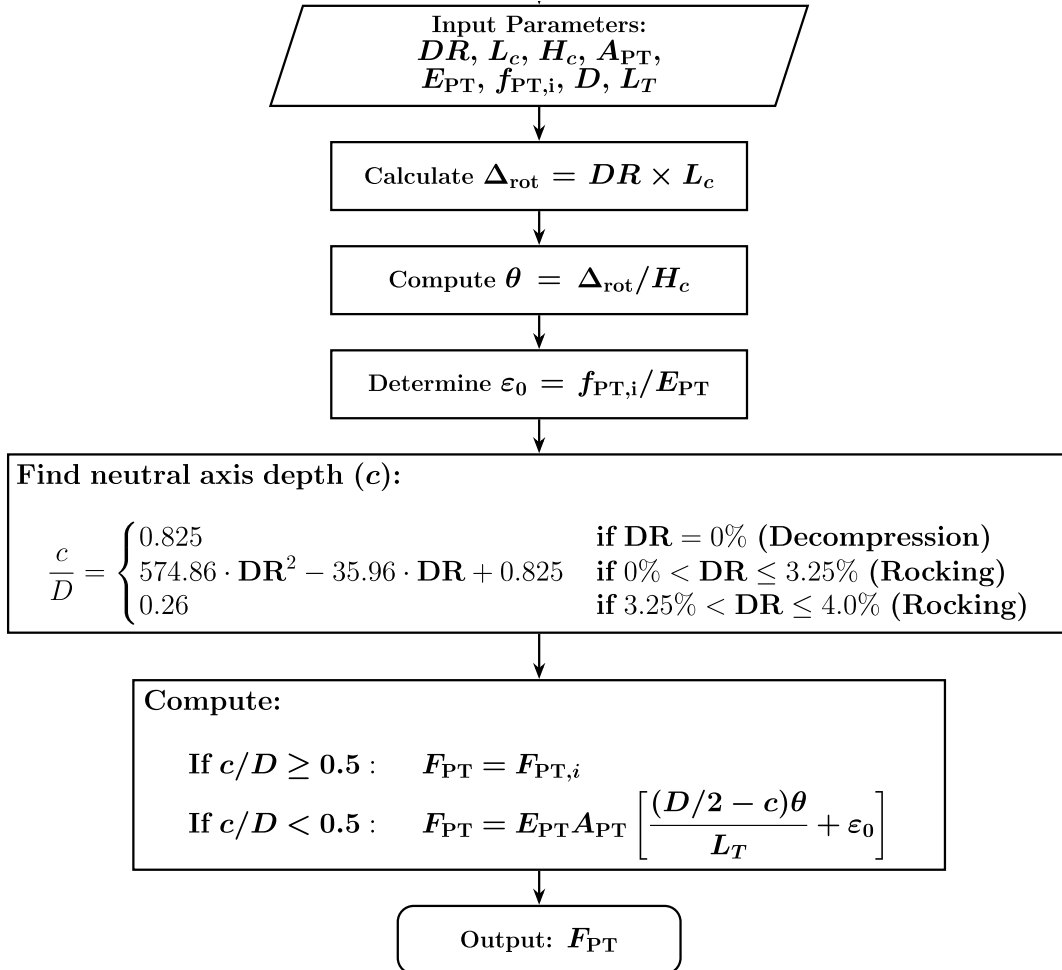


Figure 48. Flow chart for PT force distribution.

9.5.3 Pushover capacity prediction

Decompression Stage

1. Calculate stiffness of the system (K_c) assuming fixed conditions.

$$K_c = n_c \left(\frac{12EI_{eff}}{H_c^3} \right)$$

where, K_c is the flexural stiffness of the fixed column before rocking, n_c is the number of columns, E is the modulus of elasticity of concrete, I_{eff} is the effective moment of inertia of the column cross-section ($0.7I_g$ for post-tensioned columns), I_g is the gross moment of inertia of the column section, H_c is the column height, and L_c is the height from the footing surface to the centerline of the lateral load in the cap beam.

2. Calculate decompression moment (M_{dec})

$$M_{dec} = n_c \left(\frac{W}{n_c} + n_{PT} F_{PT,i} \right) \left(\frac{S_c}{A_c} \right)$$

where n_c is the number of the columns, $\frac{W}{n_c}$ is the axial gravity load on each column, $F_{PT,i}$ is the initial PT force in the columns and n_{PT} number of PT bars on each column

$$S_c = 2 \frac{I_{eff}}{D}$$

3. Calculate decompression force (F_{dec}) and decompression displacement (Δ_{dec})

$$F_{dec} = \frac{2M_{dec}}{H_c} \text{ (decompression force)}$$

$$\Delta_{dec} = \frac{F_{dec}}{K_c} \text{ (decompression displacement)}$$

Rocking Stage:

4. Calculate Lateral Force for PT-Only Bent (No SLAs):

Use moment equilibrium to calculate lateral force due to rocking (F_{rot}) for PT-only bent

$$F_{rot} H_c = n_c \left(n_{PT} F_{PT} + \frac{W}{n_c} \right) (D - c - \Delta_{rot})$$

5. For each SLA, compute the tensile strain, ϵ_{SLA} , based on its position relative to the neutral axis:

$$\epsilon_{SLA} = \theta \left(\frac{(D_i - c)}{L_{SLA}} \right); \text{ for } (D_i - c) \geq 0$$

$$\epsilon_{SLA} = 0; \text{ for } (D_i - c) < 0$$

Note: SLAs are tension-only elements and contribute no force on the compression side.

6. Determine Tensile Force in SLAs

Using the stress-strain curve for the SLAs, find the tensile stress, $\sigma_{T,i}$, corresponding to ϵ_{SLA} .

$$\text{Tensile force in each SLA } F_{T,i} = A_{SLA} \sigma_{T,i}$$

7. Calculate Lateral Force for PT-Only Bent (No SLAs):

Modify the bending moment equilibrium to include the contribution of SLAs:

$$F_{rot} H_c = n_c \left\{ \left(n_{PT} F_{PT} + \frac{W}{n_c} \right) (D - c - \Delta_{rot}) + \sum_{n=1}^{n_{SLA}} F_{T,i} D_i \right\}$$

Sum the forces $F_{T,i}$ only for SLAs in tension (i.e., where $\epsilon_{SLA} > 0$)

8. Account for Horizontal Component of PT Force

$$F_{PT, horizontal} = n_c n_{PT} F_{PT} \sin(\theta)$$

9. Compute total lateral force (F_{Tot})

$$F_{Tot} = F_{rot} + F_{PT, horizontal}$$

F_{rot} from step 4 for PT-only bent and F_{rot} from step 7 for PT-SLA bent.

10. Calculate total lateral displacement (Δ_{Tot})

$$\Delta_{Tot} = \Delta_{rot} + \Delta_{elastic}$$

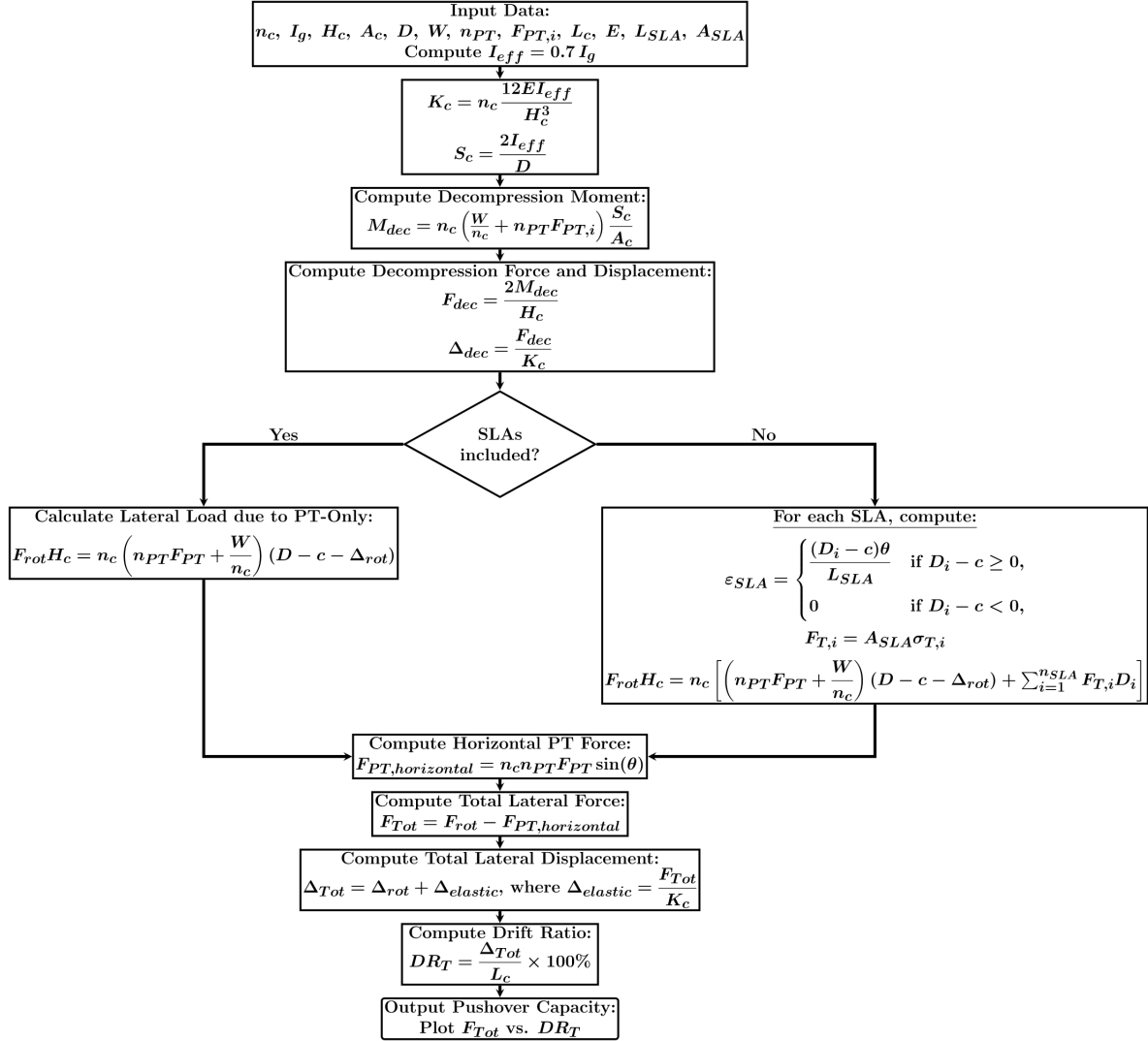


Figure 49. Flowchart for pushover capacity.

where, $\Delta_{elastic}$ is elastic deformation due to F_{Tot} can be calculated as,

$$\Delta_{elastic} = \frac{F_{tot}}{K_c}$$

11. Compute final drift ratio

$$Final\ Drift\ Ratio\ (DR_T) = \frac{\Delta_{Tot}}{L_c} * 100\%$$

12. Iterate the values for different drift ratio and plot F_{Tot} vs DR_T curve to obtain pushover capacity of the system.

Figure 49 shows the flow chart for pushover capacity calculation.

9.5.4 Additional recommendations:

1. Additional vertical reinforcing bent steel bars (135° hooks at one end and 90° hooks at the other) need to be provided near the beam-column surface which resembles the requirement as if a conventional ductile column extends into the cap-beam. Similar reinforcement needs to be designed comparable to the seismic design provisions that prevent punching shear. Also, spirals of the same size as those in the column need to be provided to confine vertical bent steel bars.
2. Additional vertical reinforcing bent steel bars (135° hooks at one end and 90° hooks at the other) need to be provided near the footing-column surface in the footing which resembles the requirement as if a conventional ductile column extends into the footing. Similar reinforcement needs to be designed comparable to the seismic design provisions that prevent punching shear. Also, spirals of the same size of those in the column need to be provided to confine vertical bent steel bars.
3. The steel chair base should have a sufficient gap with the footing top surface or with the cap-beam bottom surface, so there will not be any interaction of the chair base with the surface of the concrete. This gap needs to be calculated based on the size of the steel chair and its position due to rotation of the column based on the design drift ratio.
4. PT bar anchorage at the ends of the footing and column needs to be designed to resist bearing stress on both ends of the PT bars.
5. Washers at the SLAs should be made sufficiently thick and at least equal to the thickness of the steel collar so that they can transfer ultimate SLAs strength to the steel chair.
6. SLAs should have a minimum stretch length of eight times the diameter of SLA bars ($8d_b$).

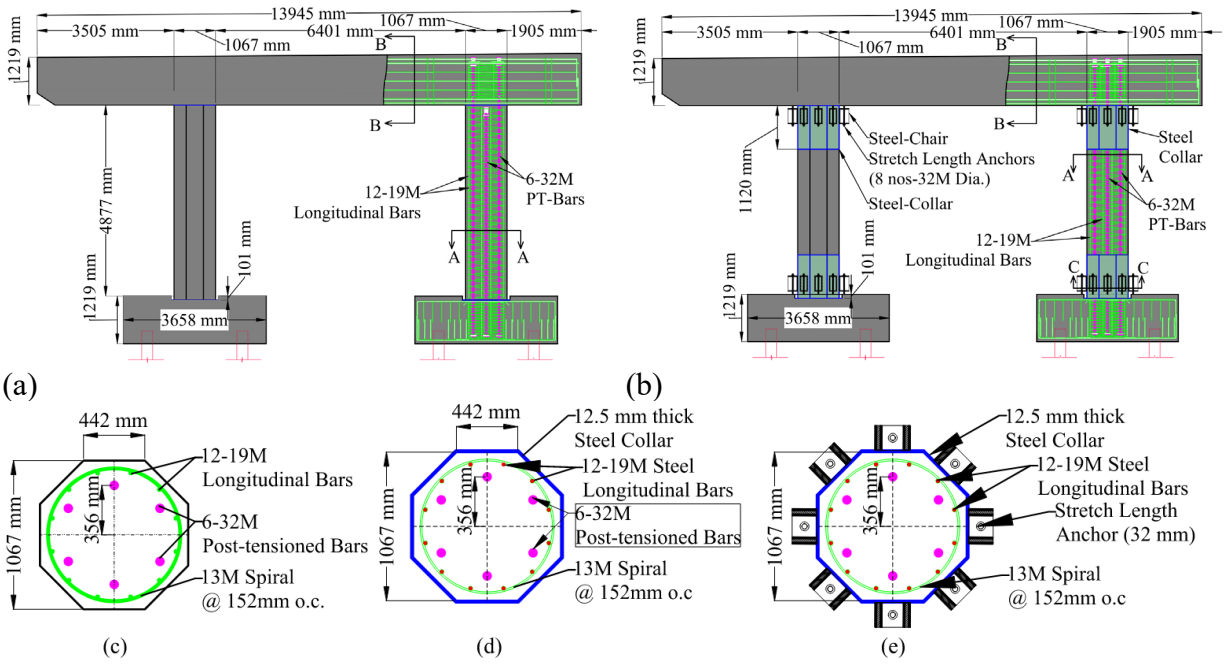
CHAPTER 10. PUSHOVER CAPACITY ESTIMATION OF EXISTING AND MODIFIED RIVERDALE BRIDGE BENT USING ANALYSIS METHOD

The Riverdale Bridge bents were built with ABC methods using precast concrete columns and cap beams. The bridge has two main spans, two approach spans, and is supported by three rows of piers, each with four two-column bridge bents. The existing bridge bent consists of a precast concrete cap beam, precast concrete columns, and footings, with 4877 mm long octagonal columns, a 1067 mm-wide cross-section and six 32 mm-diameter PT bars around the perimeter, as shown in **Figure 50(a, c)**. The PT bars are high-strength steel with 1034 MPa tensile strength and an initial post-tensioning stress of 620 MPa. The PT bars connect the cap beam to the columns and footings and are grouted inside 54 mm galvanized steel ducts for their whole length. The bridge bent is constructed without any additional lateral force resisting reinforcement, since the longitudinal mild steel bars do not extend across the column-to-footing or column-to-cap beam interfaces. The footings include 101 mm deep octagonal shear keys to distribute shear forces and prevent column sliding; there are no shear keys present in the cap beam.

The column ends in a rocking bridge bent must be protected. PT-only bridge bents are not able to dissipate high hysteretic energy; thus, external hysteretic energy dissipation devices such as SLAs can be used to improve hysteretic energy dissipation, as shown in **Figure 50(b)**. The existing bridge bent had 620 MPa initial post-tensioning stress in the column PT bars; based on Eq. (9.5) this value of initial post-tensioning stress causes yielding of the PT bars after a 2.0% drift ratio. Based on the analysis method (**Figure 51**), the initial post-tensioning stress was reduced to 440 MPa to delay yielding of PT bars after 3.0% drift ratio. To protect concrete in the column end regions from spalling, steel collars are assumed to exist at the top and bottom ends of the columns, as shown in **Figure 50(d)** which applies to section C-C without SLAs; when external SLAs are provided for hysteretic energy dissipation **Figure 50(e)** applies to section C-C. The footing reinforcing details are shown in **Figure 50(f)** and the cap beam details are shown in **Figure 50(g)**. Parametric studies are performed for three configurations: (i) existing bridge bent with 620 MPa initial post-tensioning stress; (ii) modified bridge bent with column end protection using steel collars and initial post-tensioning stress of 440 MPa; and (iii) modified bridge bent similar to configuration (ii) with replaceable SLAs. **Table 16** shows a description of the three configurations.

Table 16. Details of the existing and modified Riverdale Bridge bents.

Properties	Existing Riverdale	Modified Riverdale (PT-only)	Modified Riverdale (PT and SLAs)
PT- bars	6 - 32M dia.	6 - 32M dia.	6 - 32M dia.
Initial post-tensioning stress	620 MPa	440 MPa	440 MPa
Column end protection	N/A	Steel collar (1120 mm) 12.5 mm thick	Steel collar (1120 mm) 12.5 mm thick
Longitudinal steel bars	12 – 19M dia.	12 – 19M dia.	12 – 19M dia.
SLAs	N/A	N/A	16 SLAs each column (32M dia.)
Expected performance improvement	Control	Postpone PT bar yielding	Postpone PT bar yielding and increase energy dissipation



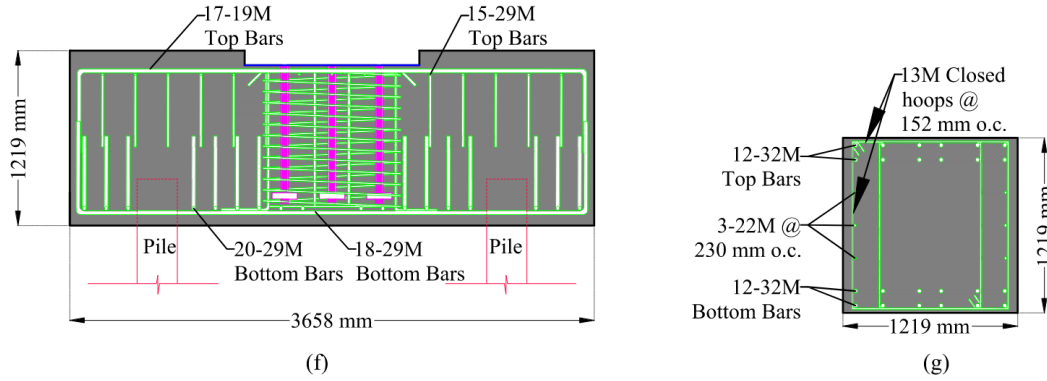


Figure 50. Existing and modified Riverdale Bridge bents: (a) existing bent; (b) modified bent; (c) section A-A; (d) section C-C without SLAs; (e) section C-C with SLAs; (f) footing details; and (g) cap beam details.

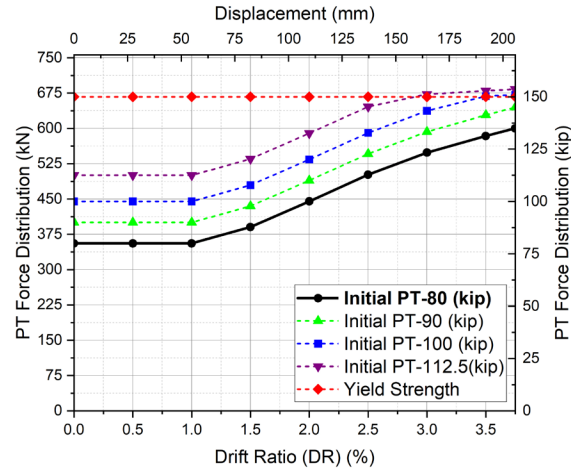


Figure 51. Post-tensioning force at various drift ratios for different initial post-tensioning stress.

10.1 PUSHOVER CAPACITY OF EXISTING AND MODIFIED RIVERDALE BRIDGE BENTS

The analytical method discussed in section 3 was used to find the pushover capacity of an existing bridge bent from the Riverdale Bridge with an initial post-tensioning stress of 620 MPa in each PT bar to simulate existing conditions. Concrete damage is assessed based on the maximum strain from concrete confinement. For design purposes, the depth of the neutral axis can be used to calculate the maximum concrete strain based on the assumption that during column rocking, the extreme compressive fiber shortens by an amount equal to the product of the total joint rotation (θ) times the neutral axis depth (c) (Restrepo and Rahman 2007). Moreover, the extreme compressive strain at the outer shell is equal to the joint rotation (Guerrini et al. 2015a). This relationship is expressed as:

$$\varepsilon_{cu} = \theta \quad (10.1)$$

Eq. (9.5) was used to compute the post-tensioning force distribution for various initial post-tensioning stress values, including the value used in the existing bridge of 620 MPa, as shown in

Figure 51. The existing Riverdale Bridge was originally designed with an initial PT stress of 620 MPa. However, **Figure 51** shows that the PT bars start to yield around 2.0% drift ratio. To postpone yielding of the PT bars above 3.0% drift ratio, the initial PT stress was reduced from 620 MPa to 414 MPa. The pushover capacity indicates that the PT bars yield early when the initial post-tensioning stress is high. **Figure 52** shows the response of the existing bridge bent with six 32M PT bars initially post-tensioned to 620 MPa using the analysis method; concrete spalling occurs at 1.0% drift ratio since there is no steel collar present to protect the plastic hinge region; the PT bars start yielding around 2.0% drift ratio.

When the column of the existing Riverdale Bridge bent starts rocking, the column toe experiences high stress and must be protected otherwise there is a good chance of concrete spalling or concrete crushing. To protect high stress concentration regions at the end of the column, a steel collar must be provided. From Eq. (10.1), the maximum strain in the concrete at 1.0% drift ratio is approximately 0.01 mm/mm. At the column toe, which lacks protection from a steel collar in the case of the existing Riverdale Bridge bent, the strain is expected to increase significantly leading to elevated stress and potential concrete damage. Therefore, a 1.0% drift ratio is assumed as the onset of concrete spalling for this case.

The modified bridge bent with similar geometry, but different initial post-tensioning stress and column end zones protected using a steel collar was also analyzed; in this case, the PT bars yield after 3.0% drift ratio as shown in **Figure 51** and **Figure 52**. For the third configuration of the modified Riverdale Bridge bent, a number of external energy dissipators (SLAs) are added to dissipate hysteretic energy. When SLAs are present and the column undergoes rocking, they elongate in tension and dissipate hysteretic energy, while also resisting part of the lateral force. This leads to an increase in lateral base shear compared to specimens without SLAs. The contribution of SLAs to base shear can be evaluated using Eq. (9.12). The number and size of SLAs is determined in the next section.

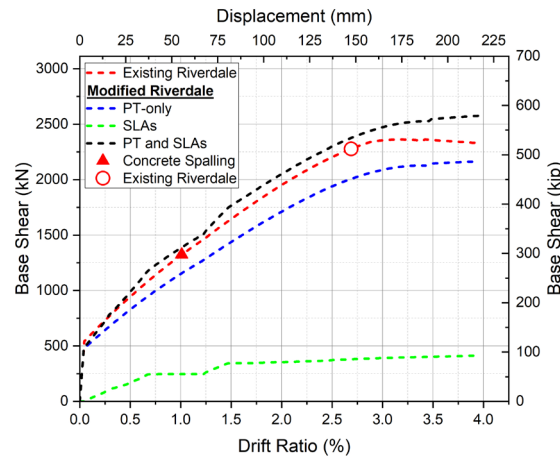


Figure 52. Analytical pushover capacity for existing and modified Riverdale bridge bent with and without SLAs.

10.2 CALCULATION OF NUMBER OF SLAS

For each bridge column, the total ultimate tensile force at the rocking joint is determined using a longitudinal mild steel reinforcing ratio from 1.0 to 2.0% (Guerrini et al. 2015b). The ultimate tensile force (T_{ult}) is:

$$T_{ult} = 0.01 A_c f_u \quad (10.2)$$

where f_u is the ultimate strength of mild steel longitudinal bars; and A_c is the gross area of the octagonal column. This value of T_{ult} is distributed to the SLAs and PT bars; at the design drift ratio, the maximum post-tensioning force in the PT bars should not reach the yield stress ($f_{y,PT}$) limit. The maximum tensile force contribution from the PT bars is given as:

$$F_{PT} = A_{PT} f_{y,PT} \quad (10.3)$$

The balance of the tensile force up to T_{ult} is contributed by the SLAs:

$$F_{SLA} = T_{ult} - F_{PT} \quad (10.4)$$

From this value of tensile force (F_{SLA}), the number of SLAs (n_{SLA}) can be computed by assuming a cross-sectional area (A_{SLA}) and yield strength ($f_{y,SLA}$) as follows:

$$n_{SLA} = \frac{F_{SLA}}{f_{y,SLA} A_{SLA}} \quad (10.5)$$

Assuming 32M diameter SLAs with a yield strength of 276 MPa (Grade 36) the number of SLAs required is ten. One SLA is provided on each of the eight sides of the octagonal columns at both the footings and the cap-beam.

Self-centering of the rocking system can be verified using the energy dissipation coefficient (Λ_D), which should be in the range of 0.1 to 0.6 to ensure self-centering and efficient energy dissipation. The energy dissipation coefficient is calculated as (Guerrini et al. 2015a; b):

$$\Lambda_D = \frac{F_{u,SLA}}{P_u + F_{PT,i} + F_{u,SLA}} \quad (10.6)$$

where P_u is the gravity load and $F_{PT,i}$ is the initial post-tensioning force in all PT bars. The column gravity load (P_u) is calculated based on deck weight, girder weight, and self-weight; a conservative value of 10% of the column axial compression capacity is used here. The energy dissipation coefficient Λ_D was found to be equal to 0.36, which is within the desired range indicating good self-centering performance of the modified Riverdale Bridge bent with SLAs.

The number of PT bars and SLAs is calculated such that the value of Λ_D remains within the threshold limit of 0.1 to 0.6. Also, self-centering coefficient (Λ_D) was calculated and was found to be 0.54 which is less than 1, suggesting good self-centering performance. An initial number of PT bars is assumed for a selected initial PT force and the number of SLAs is calculated and the value of Λ_D is computed; if it is inside the acceptable limit, the assumed values for the number of PT bars and number of SLAs are used or else the process is repeated again for a different number of PT bars until the acceptable limit of Λ_D is achieved. Once the number of SLAs is computed and the initial post-tensioning stress is determined based on rigid body analogy (Pampanin et al. 2010) as 440 MPa and six number of PT bars were found to be enough to maintain Λ_D within selected limit; this value is equal to $f_{PT,i}$ that can be used in Eq. (9.12) of the analysis method to obtain the pushover capacity of the modified Riverdale Bridge bent with SLAs, as shown in **Figure 52**. The

comparison shows that the Riverdale Bridge bent with SLAs reaches a lateral load capacity approximately 1.25 times that of the modified Riverdale Bridge bent without SLAs; moreover, the PT bars are elastic until 3.25% drift ratio which demonstrates that self-centering is within an acceptable range.

10.3 CALCULATION OF STEEL COLLAR THICKNESS (t_s) AND HEIGHT (h_s)

In rocking bridge bents, the column toe is prone to crushing in the non-linear compression region. The pier must be protected in the nonlinear stress zone where there is a chance of concrete damage during rocking; to prevent concrete damage, a steel collar is provided to increase concrete confinement and concrete crushing resistance. The height of the steel collar (h_s^*) in the nonlinear stress zone is calculated using the half-space model (Johnson 1985) described by Roh and Reinhorn (2009) (Roh and Reinhorn 2009) as a relationship between the equivalent column diameter and neutral axis depth (c) at the rocking interface (Shen et al. 2023) as:

$$h_s^* = 0.5 \sqrt{D^2 - c^2 + 2D\sqrt{D^2 - c^2}} \quad (10.7)$$

For the Riverdale bridge bent, assuming a maximum drift ratio of 4.0%, the value of h_s^* was calculated using the c value obtained from Eq (9.20) and was found as 945 mm. Hewes and Priestley (2002) suggest using a factor of safety (λ_s) to incorporate the higher pier strength to account for material property variations (Hewes and Priestley 2002). This value was assumed to be equal to an overstrength factor of 1.2 used in the capacity design procedure (AASHTO 2015). Thus, the final height of the steel (h_s) collar required to protect the nonlinear stress zone is computed as:

$$h_s = \lambda_s \cdot h_s^* \quad (10.8)$$

Using Eq. (9.8) the total height of the steel collar was computed as 1145 mm; this height of steel collar was proposed for the modified Riverdale bridge bents.

The thickness of the steel tube (t_s) was designed following the guidelines provided by Guerrini et al. (2015a) (Guerrini et al. 2015a). Equation (10.9) ensures that the steel collar provides adequate confinement and effective composite action with the surrounding concrete:

$$\frac{D}{t_s} \leq 100 \quad (10.9)$$

Direct contact between the mortar bed and steel collar during pier rocking could result in crushing the mortar bed (Dangol et al. 2022; Shen et al. 2021; Zhong et al. 2022) or local buckling of the steel tube (Jeong et al. 2008). To mitigate these risks, a free-moving steel plate is placed on top of the footing to protect the concrete against crushing. A steel plate welded to the steel collar should be installed at the base of the column to safeguard against potential concrete damage. A 12.5 mm thick steel collar was used in the modified Riverdale bent resulting in a D/t_s ratio of 88.

CHAPTER 11. CAPACITY ESTIMATION USING CONVENTIONAL STRUCTURAL MODELING IN SAP 2000

A refined numerical model was developed in SAP 2000 to predict the nonlinear behavior of the specimen bent, building on preliminary analytical studies (Wilson and Habibullah, 1997). The model replicates the geometry of the experimental specimen and Riverdale Bridge bent, incorporating line elements, rotational springs, and post-tensioning (PT) bars. Cross-sectional properties for the column, cap-beam, and footing were explicitly determined in SAP2000's Section Designer to match the as-built experimental specimen, ensuring fidelity to the original design.

11.1 NUMERICAL MODEL DETAILS FOR SPECIMEN BENT

11.1.1 Material and Element Properties

- **Tendons:** Modeled as tendon elements using A722 Grade 150 high-strength steel (ultimate tensile capacity: 150 ksi) to replicate the threaded PT bars.
- **Concrete:** Assigned both *confined* (core column regions) and *unconfined* (cover concrete) properties, with a nominal compressive strength f'_c of 41.4 MPa (6 ksi) for Riverdale Bridge bent while 97 MPa (14.1 ksi) for specimen bents.
- **Structural Elements:**
 - *Cap-beam and Footings:* Modeled as linear elastic elements to reflect their rigid behavior under service loads.
 - *Footings:* Assigned fixed supports to simulate full fixity at the base.

11.1.2 Boundary Conditions and Loading

- Axial gravity loads were applied at the cap-beam midspan (**Figure 53**).
- An initial load case combined gravity loads and PT pre-tensioning forces.
- A subsequent pushover analysis was performed, incrementally applying lateral displacement to the cap-beam to generate the capacity curve.

11.1.3 Modeling Approach

Rotational Spring Implementation:

- **Connection Behavior:** Columns and cap-beams were connected via two-node link elements acting as rotational springs in the lateral direction. These springs distributed vertical/horizontal loads while enabling nonlinear rotational behavior.
- **Tri-Linear Moment-Rotation Properties:**
 - *Initial Moment (M_{joint}):* Moment at a joint is derived based on analytical solution techniques. It was calculated as the total moment in each joint based on the lateral load (F_{tot}) at given drift ratio.

$$M_{joint} = \frac{(F_{tot} * L_c)}{4} \quad (11.1)$$

Where L_c is the distance to the rocking point.

- **Rotation Limits:** Tri-linear curve slopes were established at drift ratios at the end of decompression, 2.5%, and 4.0%, corresponding to key inflection points in the analytical force-displacement response (**Table 17**).

Rotation Calculation: Joint rotation is calculated based on the drift ratio and lateral displacement for a given drift ratio.

$$Rotation (\theta) = \tan^{-1} \left(\frac{Lateral\ displacement (\Delta_{lat})}{Height\ of\ the\ Column (H_c)} \right) \quad (11.2)$$

11.1.4 Calibration and Validation

- **Rotational Spring Adjustment:** The model was calibrated by scaling rotational spring stiffness and incorporating initial PT forces to replicate analytical and experimental moment-rotation behavior.
- **Calibration:** During the rocking stage, experiments showed that the bridge bent exhibited higher joint rotation compared to the analytical model. This indicates that for a given bending moment (M_{joint}) value, a larger joint rotation (θ) occurred in the experiments compared to the model. This suggests that the analytical model may be underestimating rotations due to factors such as deformation of the cap beam, which is assumed to be rigid (Eq. 11.1 and 11.2), and relative deformation of the PT bars inside the joints. To replicate this effect in the analytical model, the M_{joint} value was reduced to correspond to the lower observed joint rotation θ . This suggests that the analytical model may be underestimating rotations due to factors such as deformation of the cap beam, which is assumed to be rigid, and relative deformation of the PT bars inside the joints. The assumptions made in the numerical model, such as deformation of the cap beam that is assumed to be rigid and relative deformation of the PT bars inside the joints, influenced the joint rotation. Iterative adjustments revealed that using $0.6M_{joint}$ provided optimal alignment with experimental and analytical pushover curves. Different adjustment values were checked for M_{joint} and response obtained from sap while using adjustment of $0.5M_{joint}$, $0.6M_{joint}$, and $0.7M_{joint}$

Table 17. Rotational Spring Properties

Drift Ratio (%)	Lateral Displacement (mm)	Rotation (rad)	Analytical Lateral Force (kN)	M_{joint} (kN-m)	$(0.6)M_{joint}$ (kN-m)
0	0	0.0000	0	0	0
0.02	0.5	0.0002	82	50	30
1	24	0.0114	304	185	111
1.5	37	0.0171	409	249	150
2	49	0.0229	501	305	183
2.5	61	0.0286	594	362	217
3	73	0.0343	672	409	246
3.5	85	0.0400	717	437	262
3.75	91	0.0428	734	447	268

Note: M_{joint} values derived from analytical force-displacement curves. Final calibrated moments = $0.6M_{joint}$.

is shown in **Figure 54**. From the response it is clear that $0.6M_{joint}$ gives the close solution and it is used in SAP model.

- **Pushover Analysis:** After applying gravity and initial PT pre-stress, lateral displacement was incrementally imposed. The resulting capacity curve closely matched the experimental and analytical predictions for the specimen bent, validating the model's accuracy.

11.1.5 Results

- **Figure 53** illustrates the SAP 2000 model geometry, boundary conditions, and load application points.
- **Figure 55** compares the pushover response of the SAP 2000 model with experimental data and analytical solutions, demonstrating strong agreement across all phases (elastic, yield, and post-peak).
- **Table 17** summarizes the calibrated rotational spring properties, including drift ratios, rotations, and moments at critical stages.

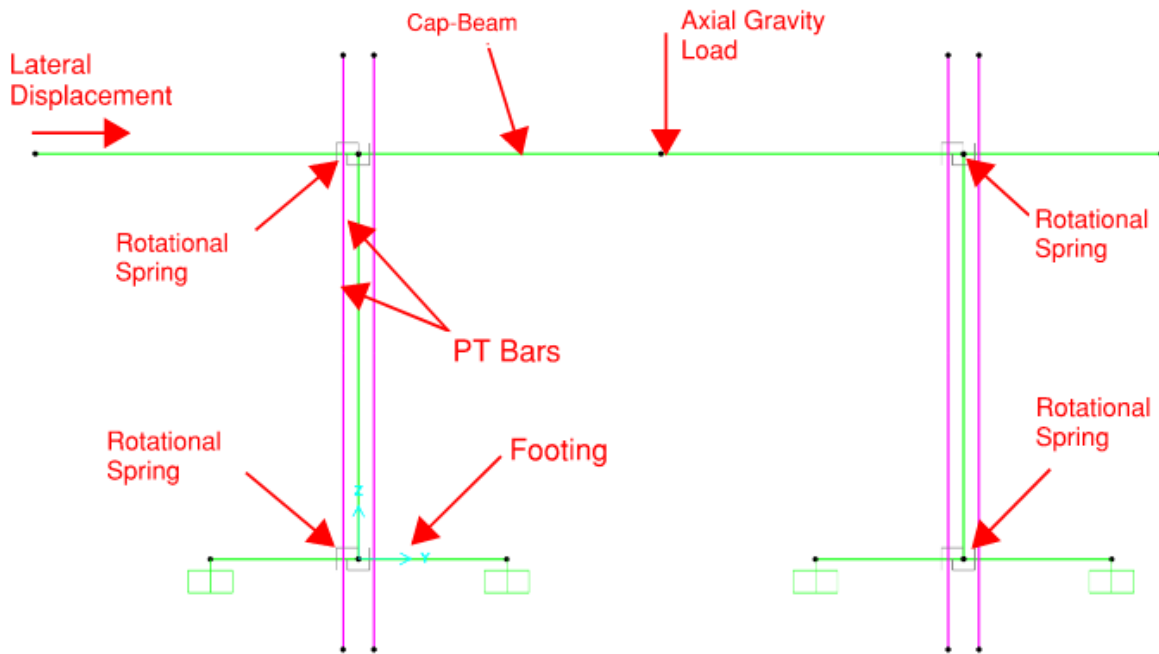


Figure 53. Schematic of Specimen Bent SAP 2000 model.

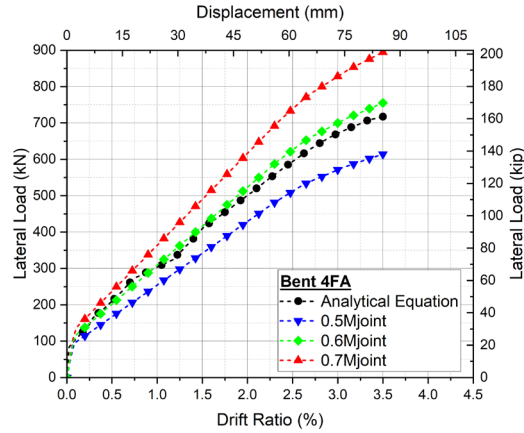


Figure 54. Pushover response obtained from SAP 2000 while using various values of M_{joint} and comparison with analytical equation.

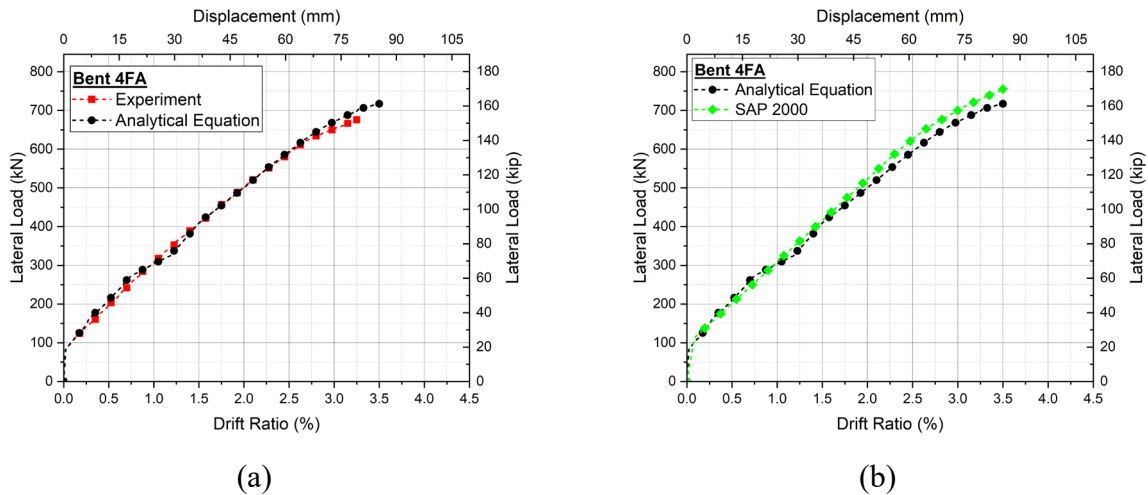


Figure 55. Pushover Response Comparison for Bent 4FA: (a) Experimental vs Analytical Equations; and (b) Experimental vs SAP 2000.

11.2 NUMERICAL MODEL DETAILS FOR RIVERDALE BRIDGE

Once the response of the specimen bent was obtained, the SAP 2000 model was extended to model the Riverdale Bridge bent and the whole Riverdale Bridge with the girder and connect that with the abutment. The detailed model of the whole bent is shown in **Figure 56**.

11.2.1 Simplified model of the Riverdale Bridge Bent:

The SAP2000 model of the specimen bent was designed to simulate the Riverdale Bridge bent with several modifications, including variations in geometry, cross-sectional properties, the number of post-tensioning (PT) bars, the cross-sectional area of the PT bars, and the initial PT force. These adjustments were necessary to replicate the existing geometry and structural characteristics of the Riverdale Bridge.

Before modeling the entire bridge, a simplified model of the Riverdale Bridge bent was created to analyze its response using the schematic of the numerical model as shown in

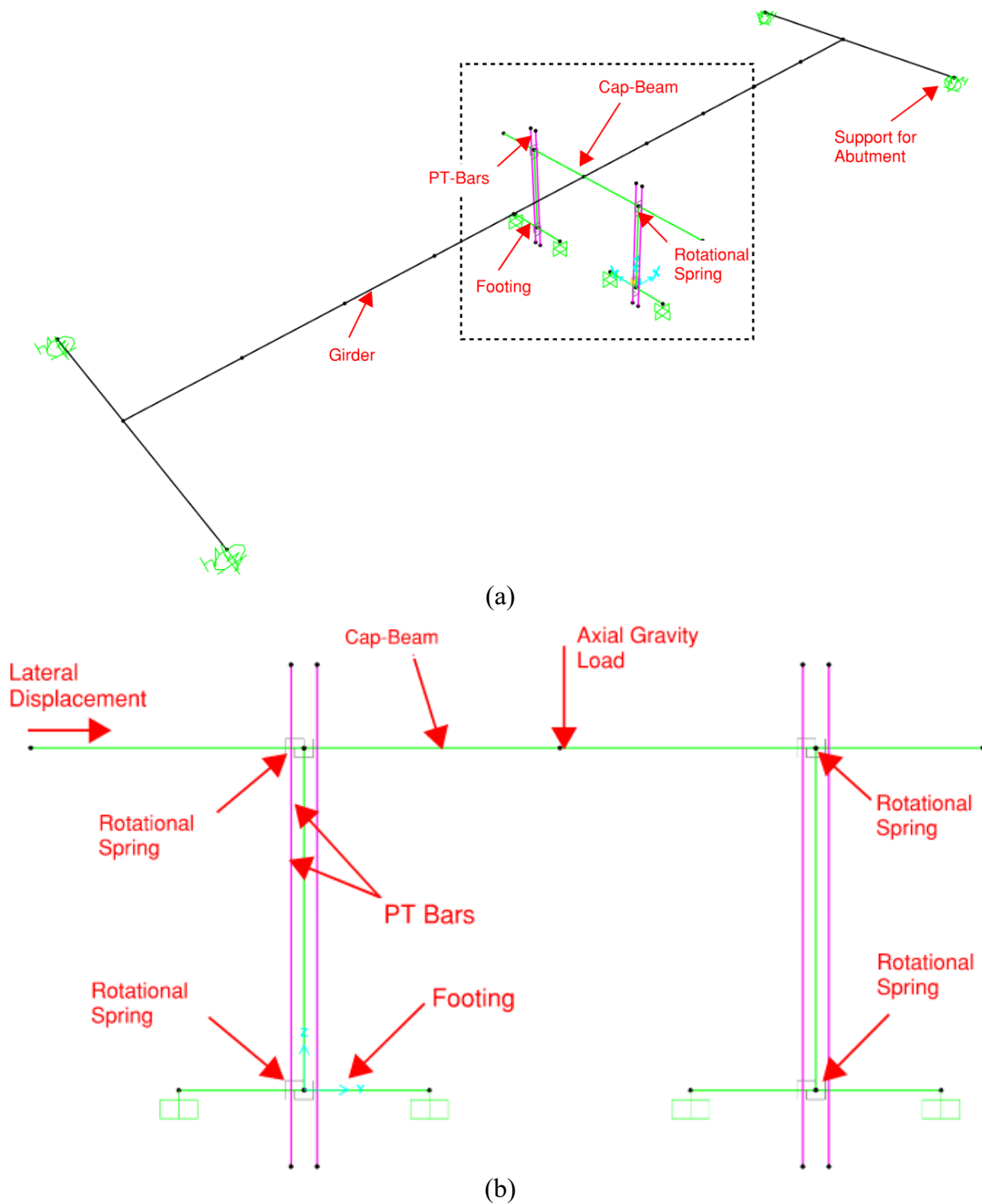


Figure 56. Schematic of SAP 2000 model: (a) 3D model of the Riverdale Bent; and (b) 2D model of bent in consideration.

Figure 56(b). The response of this bent model was compared with the analytical solution, incorporating SLAs as external energy dissipators. The axial load index for the bent was maintained at 10%, consistent with the value used in the analytical calculations.

To model the bent in SAP2000, rotational springs were established based on the method described in the previous section for the specimen bent modelling. These springs were calibrated using moment-rotation values, as presented in **Table 18**, to ensure accurate representation of the Riverdale bent's behavior. During the calibration process, the pushover response was refined by adjusting the parameter M_{joint} , and it was determined that $0.6 * M_{joint}$ closely matched the analytical solution as observed for the specimen bent. **Figure 57(a)** shows the rotational spring properties used in the SAP 2000 for Riverdale Bridge bent (2D-model) and **Figure 57(b)** shows the pushover response comparison for bent from analytical equation and the SAP 2000 model. The numerical model of SAP 2000 showed a period of 0.19 sec for the Riverdale Bridge bent model (2D model) as shown in **Figure 58**.

Table 18. Calculation of Rotational Spring Properties for Riverdale Bridge bent

Drift Ratio (%)	Lateral Displacement (mm)	Rotation (rad)	Analytical Lateral Force (kN)	M_{joint} (kN-m)	$0.6M_{joint}$ (kN-m)
0.00	0	0.0000	0	0	0
0.04	1	0.0002	475	651	391
1.00	55	0.0112	1378	1889	1134
1.50	82	0.0169	1763	2418	1451
2.00	110	0.0225	2048	2809	1686
2.50	137	0.0281	2295	3148	1889
3.00	165	0.0337	2474	3394	2036
3.50	192	0.0394	2549	3496	2098
4.00	218	0.0447	2576	3533	2120

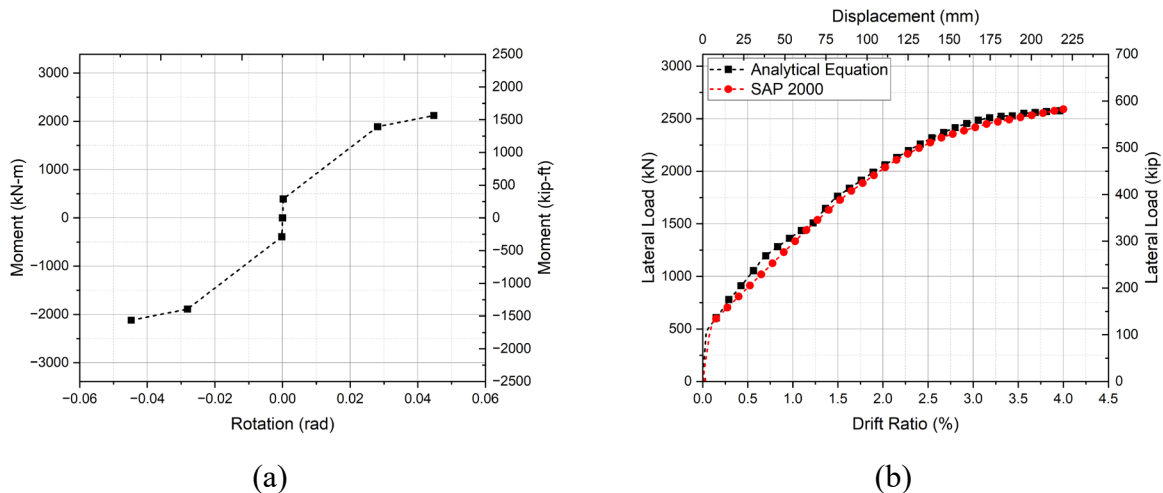


Figure 57. Riverdale Bridge bent Model SAP 2000: (a) Rotational Spring used in SAP 2000; and (b) Pushover response comparison analytical equation vs SAP 2000.

The pushover response obtained from the SAP 2000 numerical model was in close agreement with the response obtained from the analytical equation. This close representation further can be

used to numerically model the response of the whole bridge including girder and the abutment properties together with the same tri-linear rotational spring used for the Riverdale Bridge bent.

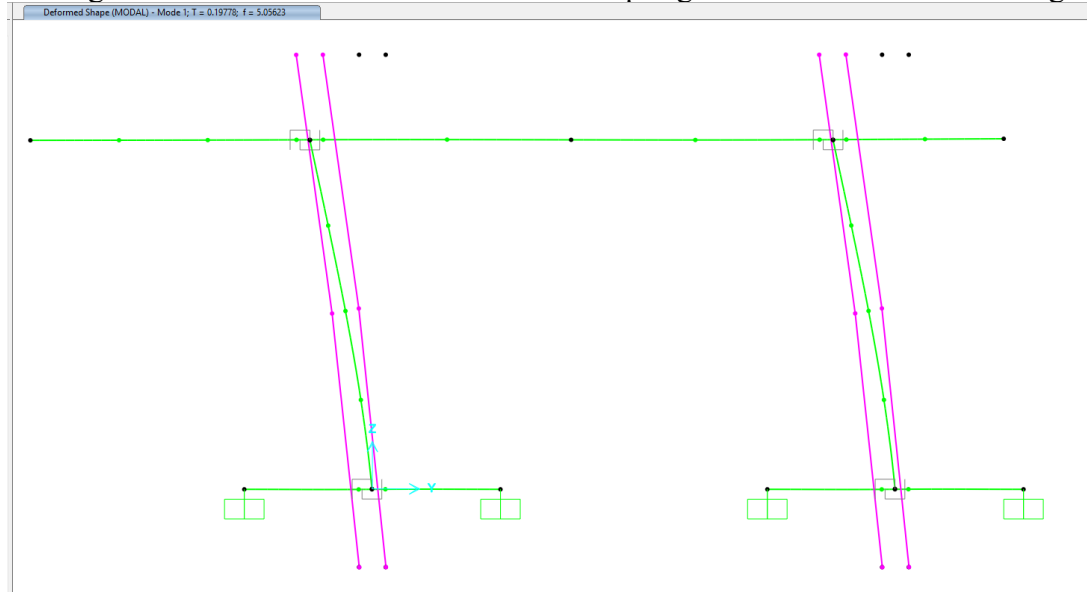


Figure 58. Mode shape of the 2D-model in SAP 2000.

11.2.2 Simplified Model of the Riverdale Bridge (3D-model):

The pushover response of the Riverdale Bridge bent from the numerical model exhibited strong agreement with the analytical solution of the 2D Riverdale Bridge bent, validating the reliability of the numerical approach. This consistency confirms the applicability of the calibrated rotational spring parameters for extending the methodology to the full bridge system. By using the spring properties, the model accounts for coupled nonlinear behavior of the superstructure, girders, and abutments under seismic demand, enabling complete assessment of the global response. The calibrated tri-linear rotational spring properties, originally derived from the 2D bridge bent model, were directly implemented in the 3D numerical model. As shown in **Figure 56(a)** and **Figure 59** the full 3D bridge model incorporated elastic girder elements discretized into five segments to enhance computational precision. Axial loads from the bridge deck were distributed uniformly across six nodal points along the girder to replicate a realistic load transfer mechanism. A constant damping ratio of 5.0% is used for numerical study in SAP 2000, however extensive study in damping ratio needs to be calculated and studied.

To simulate soil-structure interaction (SSI), longitudinal and transverse soil springs were incorporated at the abutments, combined with vertical roller supports to represent vertical restraint. Soil spring stiffness was calculated according to the Caltrans method using a soil pressure coefficient of 115 MPa. The resulting longitudinal and transverse stiffness values—715 kN/m and 298 kN/m, respectively—were assigned as elastic spring properties in the model. **Figure 59** shows the orientation and application of the transverse and longitudinal spring stiffness parallel and perpendicular to the abutment.

The validated numerical framework ensures robust replication of the bridge's real-world behavior under different loading conditions, leveraging calibrated parameters to predict nonlinear structural response. Following the development of the full 3D bridge model, a pushover analysis was conducted to evaluate the global capacity response of the system by applying lateral displacement

at node “a” (**Figure 60a**). To verify consistency between subsystem and system-level behavior, the bridge bent response was isolated from the full bridge model and compared against the standalone 2D Riverdale Bridge bent analysis; this was done by calculating foundation shear forces, i.e. reactions at nodes “b”, “c”, “d”, and “e” in the direction of lateral displacement as shown in **Figure 59**. **Figure 60b** demonstrates close agreement between the foundation shear force and the original 2D bent capacity curve calculated from the analytical method, confirming that the 3D framework preserves the validated behavior of critical components while accounting for system-level interactions.

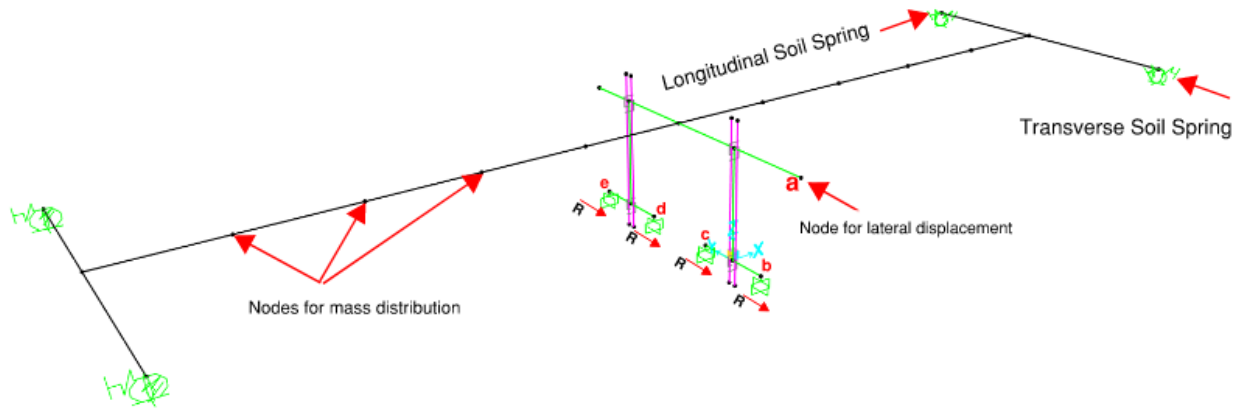


Figure 59. 3D SAP 2000 model of the bent showing soil springs.

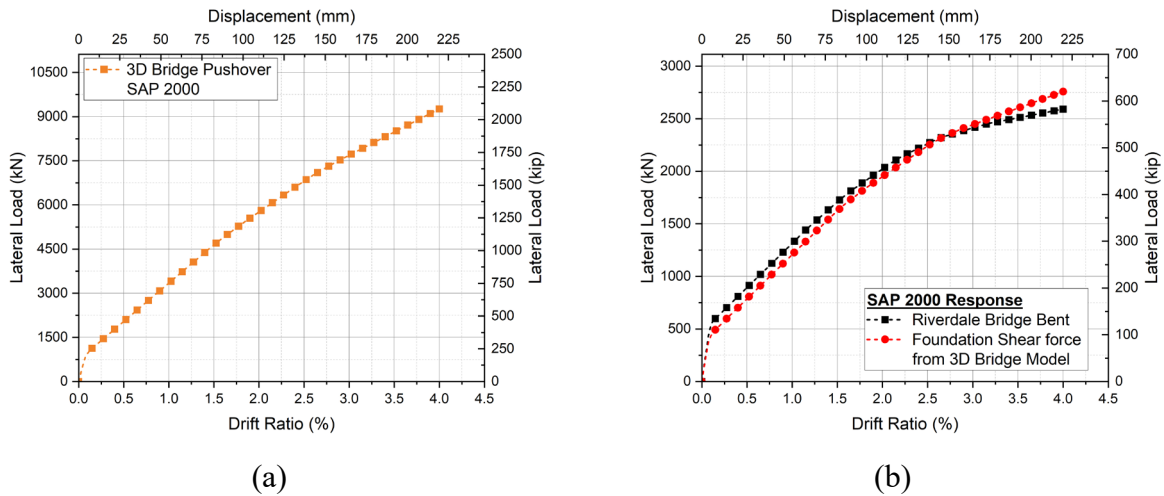
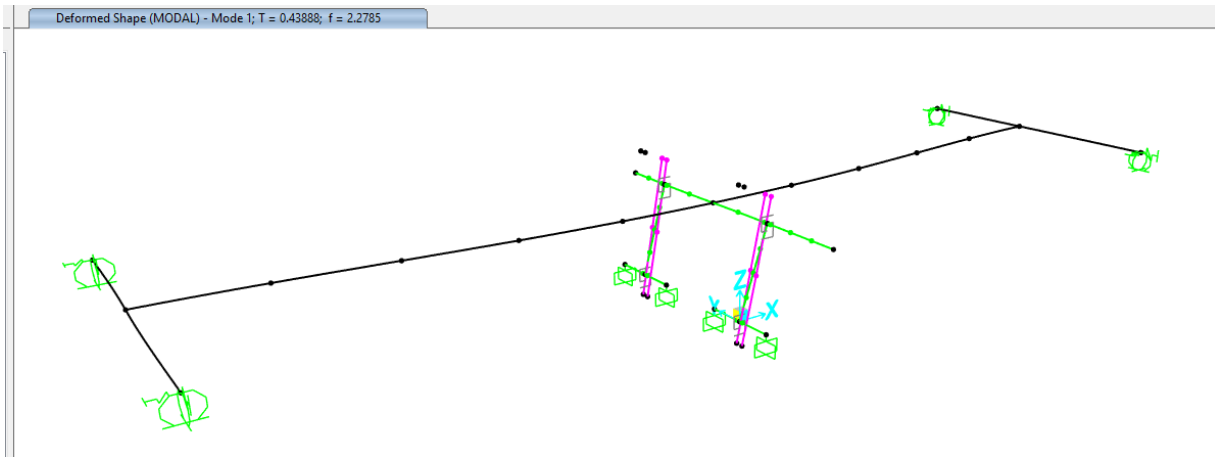


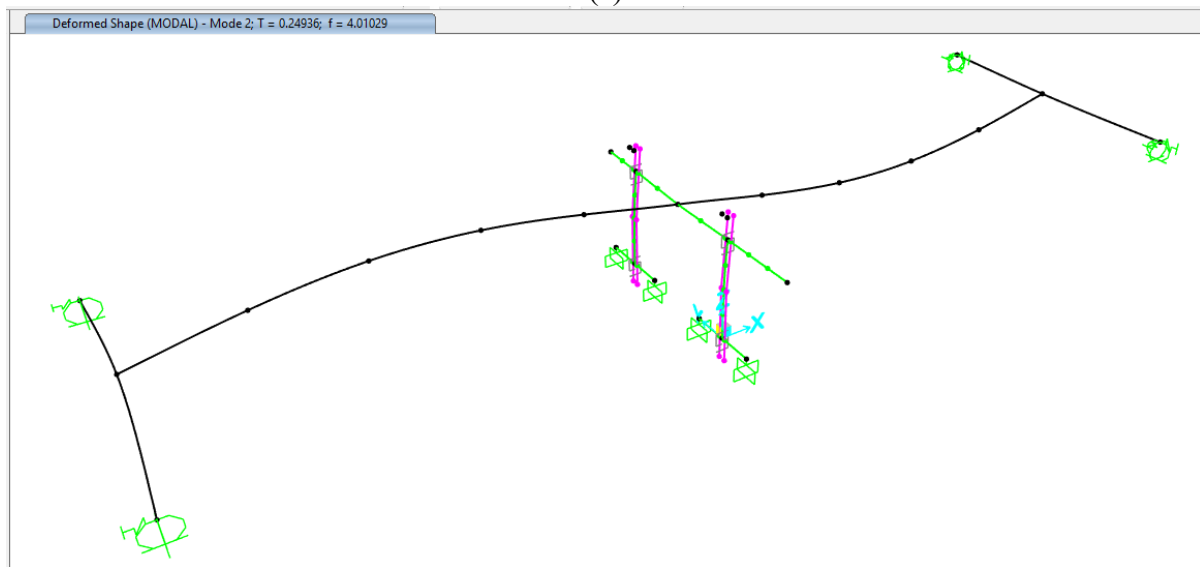
Figure 60. Pushover Response from 3D model: (a)Whole Riverdale Bridge; and (b) Riverdale bent only (2D-model) and response of the bent only from Riverdale Bridge (3D-model)

Modal analysis of the 3D bridge model had a fundamental and second period calculated as 0.44 s and 0.25 s, respectively (**Figure 61**). The comparison between subsystem (2D bent) and global (3D bridge) response highlights the performance evaluation by preserving component

adherence while capturing system-level interactions—such as girder-abutment constraints and soil-structure interaction effects.



(a)



(b)

Figure 61. Mode shapes; (a) 1st mode response; and (b) 2nd mode response.

CHAPTER 12. CONVENTIONAL STRUCTURAL DEMAND ANALYSIS IN SAP2000

The numerical model of the bridge bent was prepared in SAP 2000 and validated in the previous chapter. Once the numerical model was developed, the seismic demand on the structure was determined using a response spectrum analysis. Since the response spectrum analysis uses elastic stiffness, in order to capture the nonlinear effects, the secant stiffness of the trilinear rotational springs was used for the demand calculation using an iterative process. Effective stiffness response was compared with the seismic capacity of the bridge obtained using analytical calculations and with the simplified numerical model in SAP2000.

12.1 SELECTION OF RESPONSE SPECTRA

The Design Basis Earthquake (DBE) response spectrum, corresponding to a 10% probability of exceedance in 50 years, was utilized for the analysis. This assumed of the structure being in Berkeley, California, which has a Site Class D soil profile. The seismic hazard in this location is higher compared to Salt Lake City, making it suitable for evaluating higher demand conditions. After obtaining the DBE response spectrum, the seismic demand on the bent was further analyzed using the Maximum Considered Earthquake (MCE) response spectrum. The MCE corresponds to a 2% probability of exceedance in 50 years, representing the most severe expected ground shaking for the site. Both DBE and MCE response spectra were used to calculate the demands on the bent, providing a comprehensive understanding of the structure's performance under varying levels of seismic hazard. **Figure 62** shows the DBE and MCE response spectra used in the demand calculations.

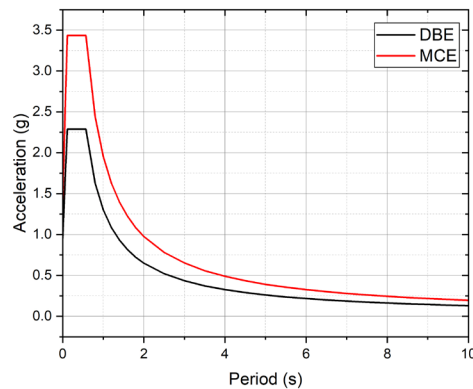


Figure 62. Design base and maximum credible response spectra used for demand calculation.

Figure 63 shows the flowchart that can be used to compute the seismic demand of the system using the secant stiffness procedure. For the demand calculation and to select effective rotational stiffness of the system iterative process must be followed. The process began with the selection of the initial stiffness based on the first slope of the tri-linear rotational spring curve. Using this initial linear stiffness, a response spectrum analysis was conducted in SAP 2000. The maximum rotation values at the rotational springs were extracted from the SAP 2000 analysis, with a maximum rotation of 0.00167 rad observed for this case. It was verified that this rotation value lies outside

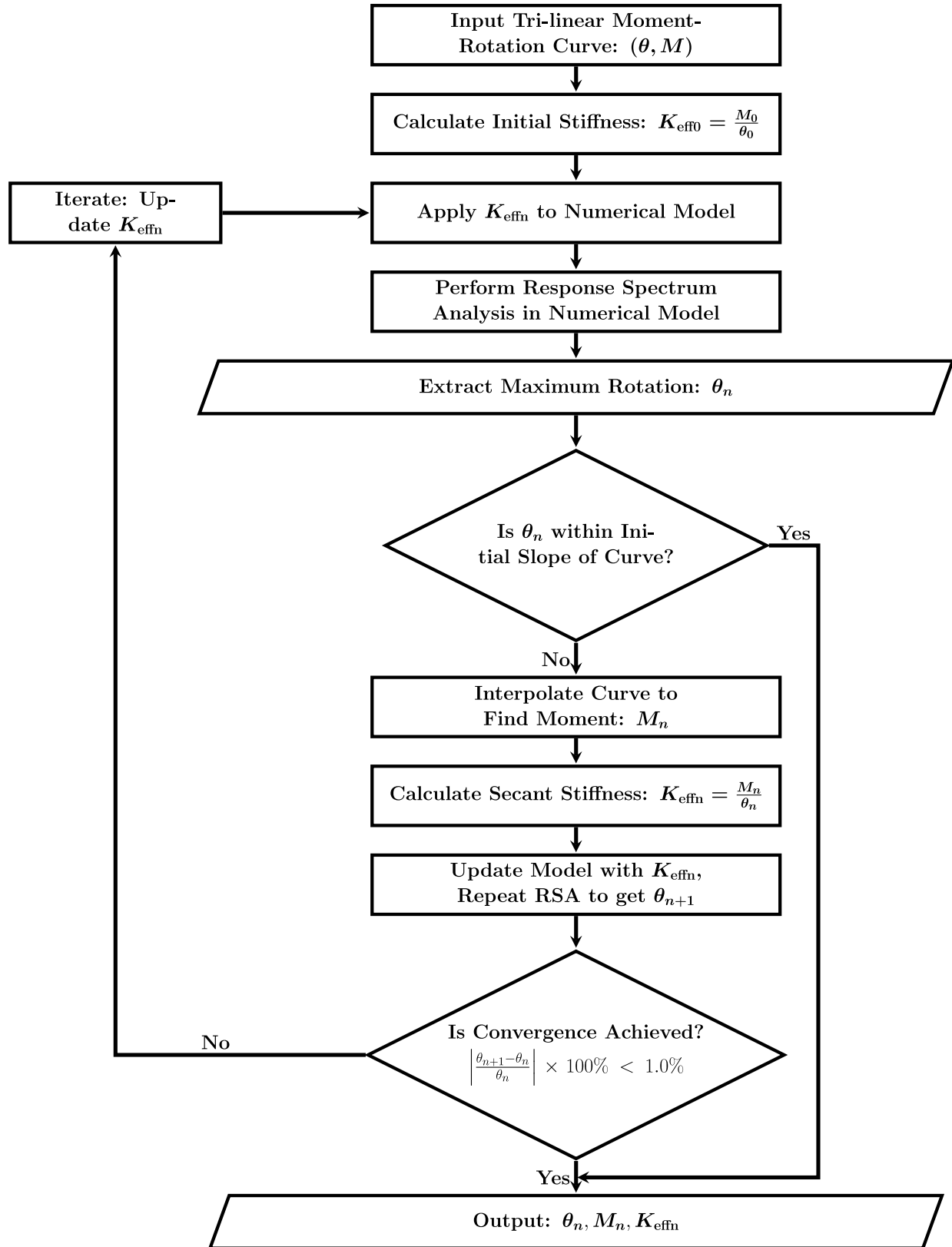


Figure 63. Flow chart showing the seismic demand calculation procedure once the trilinear curve is determined.

the initial slope of the tri-linear curve. To determine the corresponding moment, interpolation was performed on the tri-linear curve for the obtained rotation, resulting in a moment of 457 kNm.

With the moment value calculated, the linear stiffness for the first iteration was determined as the ratio of the obtained moment to the maximum rotation at the rotational spring. This updated linear stiffness was then applied to the model, and the response spectrum analysis was repeated. The process involved recalculating the maximum rotation at the rotational spring, obtaining the corresponding moment using the tri-linear curve, and updating the stiffness. These steps were iterated until the maximum rotation at the rotational spring converged, with an error below 1.0%.

Once convergence was achieved, the maximum displacement demand was obtained from SAP 2000. The tri-linear spring behavior, along with the iterative process of updating linear stiffness and displacement demands for the MCE-level response spectrum, is illustrated in **Figure 64(a)** and **Figure 64(b)**. **Figure 64(a)** also shows the zoomed in iterative effective linear rotational stiffness calculation procedure followed for the Riverdale Bridge.

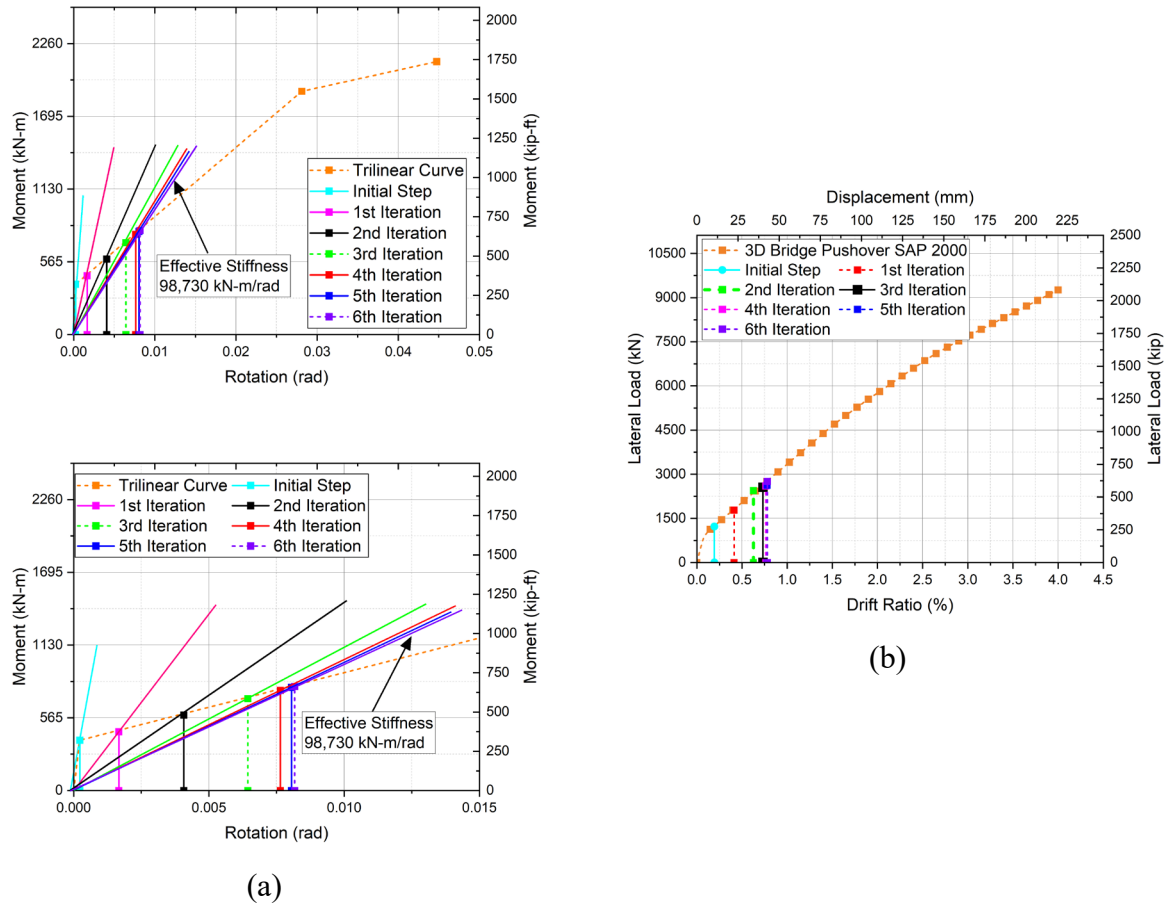


Figure 64. Demand Calculation: (a) Effective stiffness calculation; and (b) Demand obtained from the tri-linear and linear responses for a Riverdale Bent only from Riverdale Bridge Model.

The drift ratio at maximum displacement demand (D_d) was found to be 0.78%, which is well below the displacement capacity (D_c) of 3.5%, the threshold at which the PT bars yield; suggesting

that the maximum demand is below the expected capacity of the Riverdale Bridge, which is expected as per AASHTO seismic guide specification (2023).

CHAPTER 13. CONCLUSIONS

This project has demonstrated effective methods for residual drift mitigation and minimal intervention repair strategies for bridges in seismically active regions, contributing to improved seismic resilience. Post-tensioned hybrid bridge bents with external stretch length anchors (SLAs) as energy dissipators were evaluated through quasi-static cyclic testing and numerical analysis. Four unbonded post-tensioned bridge bents were assessed under cyclic loading conditions; two bridge bents were equipped with SLAs. Key design parameters—including the number of post-tensioning (PT) bars, initial PT force, shear key configurations, and column-to-footing and column-to-cap beam interfaces—were studied to understand their influence on the seismic performance of these bents. The key findings from experimental and analytical studies are as follows:

1. **Energy Dissipation and Self-Centering:** Bridge bents with SLAs demonstrated substantial hysteretic energy dissipation and effective self-centering maintaining a residual drift below 0.5% at 4.0% drift ratio. Hysteretic energy dissipation in SLA-equipped bents was 1.8 to 3.2 times greater than those without SLAs.
2. **Damage Prevention and Free Rocking Mechanism:** Bents with four PT bars per column and corresponding SLAs prevented yielding in longitudinal steel bars and showed no damage, underscoring the importance of design aspects such as the gap between steel chairs and footing or cap beam to allow free column rocking and prevent concrete damage. Steel collars with adequate thickness, height, and secure anchorage helped protect concrete while facilitating SLA attachment.
3. **Elastic Response in Bents Without SLAs:** Bridge bents exhibited linear elastic behavior with minimal energy dissipation. All configurations achieved residual displacements below 0.5% drift at an imposed 4.0% drift ratio, indicating adequate self-centering capability.
4. **Lateral Force Capacity:** SLA-equipped bents exhibited greater lateral force capacity than those without SLAs, which remained unaffected by shear key location (footings only or both footings and cap beam) or surface interactions at the column ends.
5. **Steel Chair and Collar Design Efficiency:** Steel collars successfully supported steel chairs without yielding, with the use of HSS tube segments in steel chairs proving effective in reducing construction time and cost. The vertical gap between HSS tube and concrete surface allowed unrestricted column rocking, avoiding interaction between steel chairs and concrete surfaces.
6. **SLA Design Based on Engineering Principles:** SLA dimensions and quantities were determined using engineering design principles for reinforced concrete columns, performing well as external energy dissipators under cyclic loading.
7. **Validated Analysis Method for Design:** An analysis method based on the normalized neutral axis was validated against experimental results, enabling pushover analysis of bridge bents with PT bars and SLAs. This method and rigid body analogy to estimate PT force evolution ensure that PT bars can withstand high drift ratios without yielding, which applies to columns with different geometry.
8. **Design Procedure Application:** The procedure for determining the number of PT bars and SLAs can be applied to seismic design of similar full-scale rocking bridge bents, establishing a foundation for further design applications.
9. **Parametric Study:** The same analytical design procedure was used to predict the pushover response of the full-scale existing Riverdale Bridge bent and a Modified

Riverdale Bridge bent, and the response obtained from the analysis method showed that the reduction of initial PT force postpones PT bar yielding and helps in maintaining the self-centering capability of the bridge bent.

The analytical and numerical models successfully matched the experimental results from prior studies for octagonal bridge bent columns and comparable rectangular columns. However, further research, including full-scale cyclic and shake table testing, is recommended to verify the applicability of these methods and models for full-scale structures. Additional studies should explore variations in column dimensions, SLA number and size, PT bar count, and initial post-tensioning levels to refine and optimize seismic design strategies for bridge resilience in earthquake-prone areas.

CHAPTER 14. REFERENCES

- AASHTO. 2021. *AASHTO LRFD Bridge Design Specification, 10th Edition*. Washington, DC: AASHTO.
- AASHTO. 2023. *AASHTO Guide Specifications for Seismic Bridge Design, 3rd Edition*. Washington, DC: AASHTO.
- ACI (American Concrete Institute). 2019. Building code requirements for structural concrete and commentary. ACI 318-19. Farmington Hills, MI: ACI
- AISC (American Institute of Steel Construction). 1986. Load and Resistance Factor Design Specification for Structural Steel Buildings. AISC
- Ameli, M. J., and C. P. Pantelides. 2017. "Seismic Analysis of Precast Concrete Bridge Columns Connected with Grouted Splice Sleeve Connectors." *J. Struct. Eng.*, 143 (2): 04016176. [https://doi.org/10.1061/\(asce\)st.1943-541x.0001678](https://doi.org/10.1061/(asce)st.1943-541x.0001678).
- ASTM. 2018. *Standard specification for anchor bolts, steel, 36, 55, and 105-ksi yield strength*. ASTM F1554-18. West Conshohocken, PA: ASTM.
- Badie, S. S., M. K. Tadros, H. F. Kakish, D. L. Splittgerber, and M. C. Baishya. 2002. "Large shear studs for composite action in steel bridge girders." *J. Bridge Eng.* 7 (3): 195–203. [https://doi.org/10.1061/\(ASCE\)1084-0702\(2002\)7:3\(195\)](https://doi.org/10.1061/(ASCE)1084-0702(2002)7:3(195)).
- Barton, R. D., M. J. Ameli, and C. P. Pantelides. 2022. "Precast Concrete Bridge Column-Footing Connections with Recessed Grouted Splice Sleeve Connectors." *ACI Struct. J.*, (1). <https://doi.org/10.14359/51734218>.
- Bu, Z.-Y., Y.-C. Ou, J.-W. Song, N.-S. Zhang, and G. C. Lee. 2016a. "Cyclic loading test of unbonded and bonded posttensioned precast segmental bridge columns with circular section." *J. Bridge Eng.* 21 (2): 04015043. [https://doi.org/10.1061/\(asce\)be.1943-5592.0000807](https://doi.org/10.1061/(asce)be.1943-5592.0000807)
- Bu, Z., J. Guo, R. Zheng, J. Song, and G. C. Lee. 2016b. "Cyclic performance and simplified pushover analyses of precast segmental concrete bridge columns with circular section." *Earthq. Eng. Eng. Vib.*, 15 (2): 297–312. <https://doi.org/10.1007/s11803-016-0323-3>.
- Bursi, O. S., F.-F. Sun, and S. Postal. 2005. "Non-linear analysis of steel–concrete composite frames with full and partial shear connection subjected to seismic loads." *J. Constr. Steel Res.* 61 (1): 67–92. <https://doi.org/10.1016/j.jcsr.2004.06.002>
- Chopra, A. K. 2007. *Dynamics of Structures, Theory and Application to Earthquake Engineering*. Upper Saddle River, NJ: Pearson and Prentice Hall.
- Cook, R. A., and R. E. Klingner. 1989. *Behavior and design of ductile multiple-anchor steel-to-concrete connections*. Research Rep. No. 1126-3. Austin, TX: Texas Department of Highways and Public Transportation.
- Cook, R. A., and R. E. Klingner. 1992. "Ductile multiple-anchor steel-to-concrete connections." *J. Struct. Eng.* 118 (6): 1645–1665. [https://doi.org/10.1061/\(ASCE\)0733-9445\(1992\)118:6\(1645\)](https://doi.org/10.1061/(ASCE)0733-9445(1992)118:6(1645)).
- Culmo, M. P. 2011. *Accelerated bridge construction: Experience in design, fabrication and erection of prefabricated bridge elements and systems*. FHWA-HIF-12-013. McLean, VA: FHWA, Office of Bridge Technology, HIBT-10.
- Dan, D., A. Fabian, and V. Stoian. 2011. "Theoretical and experimental study on composite steel–concrete shear walls with vertical steel encased profiles." *J. Constr. Steel Res.* 67 (5): 800–813. <https://doi.org/10.1016/j.jcsr.2010.12.013>.

- Dangol, I., and C. P. Pantelides. 2022. "Resilient Posttensioned Bridge Bent with Buckling Restrained Brace." *J. Bridg. Eng.*, 27 (2): 1–17. [https://doi.org/10.1061/\(asce\)be.1943-5592.0001823](https://doi.org/10.1061/(asce)be.1943-5592.0001823).
- Dangol, I., D. Thapa, and C. P. Pantelides. 2022. "Experimental evaluation of post-tensioned bridge bent under cyclic loads and comparison to hybrid bridge bents." *Eng. Struct.*, 256: 113962. Elsevier Ltd. <https://doi.org/10.1016/j.engstruct.2022.113962>.
- Dara, S. 2015. "Behavior of the shear studs in composite beams at elevated temperatures." Ph.D., Dept. of Civil, Architectural, and Environmental Engineering, Univ. of Texas at Austin
- Davaadorj, O., P. M. Calvi, and J. F. Stanton. 2020. "Experimental response of headed stud connections subjected to combined shear and bending actions." *PCI J.*, 65 (5): 38–50. <https://doi.org/10.15554/pcij65.5-02>.
- Deng, X., M. Engelhardt, T. Helwig, E. Williamson, L. Wan, and Y. Alp. 2024. "Static Push-Out Tests on 29 mm Diameter Shear Studs." *J. Bridg. Eng.*, 29 (6): 4024038. American Society of Civil Engineers. <https://doi.org/10.1061/JBENF2.BEENG-6668>.
- ElGawady, M. A., and A. Sha'lan. 2011. "Seismic behavior of self-centering precast segmental bridge bents." *J. Bridge Eng.* 16 (3): 328–339. [https://doi.org/10.1061/\(ASCE\)BE.1943-5592.0000174](https://doi.org/10.1061/(ASCE)BE.1943-5592.0000174).
- Epackachi, S., N. H. Nguyen, E. G. Kurt, A. S. Whittaker, and A. H. Varma. 2014. "In-plane seismic behavior of rectangular steel-plate composite wall piers." *J. Struct. Eng.* 141 (7): 04014176. [https://doi.org/10.1061/\(ASCE\)ST.1943-541X.0001148](https://doi.org/10.1061/(ASCE)ST.1943-541X.0001148).
- Eurocode C. 4: *design of composite steel and concrete structures. Part 1.1: general rules and rules for buildings*. London, UK: British Standards Institution; 2004.
- FHWA (Federal Highway Administration). 2011. *Accelerated bridge construction: Experience in design, fabrication and erection of prefabricated elements and systems*. Washington, DC: FHWA.
- Guerrini, G., J. I. Restrepo, A. Vervelidis, and M. Massari. 2015a. *Selfcentering precast concrete dual-steel-shell columns for accelerated bridge construction: Seismic performance, analysis, and design*. PEER Report 2015/13. Berkley, CA: Univ. of California.
- Guerrini, G., J. I. Restrepo, M. Massari, and A. Vervelidis. 2015b. "Seismic Behavior of Posttensioned Self-Centering Precast Concrete Dual-Shell Steel Columns." *J. Struct. Eng.*, 141 (4): 04014115. [https://doi.org/10.1061/\(asce\)st.1943-541x.0001054](https://doi.org/10.1061/(asce)st.1943-541x.0001054).
- Han, Q., Z. Jia, K. Xu, Y. Zhou, and X. Du. 2019. "Hysteretic behavior investigation of self-centering double-column rocking piers for seismic resilience." *Eng. Struct.*, 188 (March): 218–232. Elsevier. <https://doi.org/10.1016/j.engstruct.2019.03.024>.
- Hawkins, N. M., D. Mitchell, and C. W. Roeder. 1980. "Moment resisting connections for mixed construction." *Eng. J.*, 17 (1): 1–10.
- Hewes, J. T. 2007. "Seismic tests on precast segmental concrete columns with unbonded tendons." *Bridg. Struct.*, 3 (3, 4): 215–227. IOS Press. <https://doi.org/10.1080/15732480701520352>.
- Hewes, J. T., and M. J. N. Priestley. 2002. *Seismic design and performance of precast concrete segmental bridge column*. Rep. No. SSRP-2001/25. San Diego: Univ. of California.
- Jeong, H. I., J. Sakai, and S. A. Mahin. 2008. *Shaking table tests and numerical investigation of self-centering reinforced concrete bridge columns*. Washington, DC: Pacific Earthquake Engineering Research Center.
- Joel E. Parks Luis Ibarra, and David H. Sanders, C. P. P. 2018. "Stretch Length Anchor Bolts under Combined Tension and Shear." *ACI Struct. J.*, 115 (5): 1317–1328. <https://doi.org/10.14359/51702236>.

- Johnson, K. L. 1985. *Contact mechanics*. UK: Cambridge university press.
- Kawashima, K. 1997. "Japanese seismic design specifications of highwaybridges and the performance based design." In *Proc., Seismic Design Methodologies for the Next Generation of Codes*, edited by P. Fajfar and H. Krawinkler. Rotterdam, Netherlands: A. A. Balkema
- Lam, W. Y., R. K. L. Su, and H. J. Pam. 2005. "Experimental study on embedded steel plate composite coupling beams." *J. Struct. Eng.* 131 (8): 1294–1302. [https://doi.org/10.1061/\(ASCE\)0733-9445\(2005\)131:8\(1294\)](https://doi.org/10.1061/(ASCE)0733-9445(2005)131:8(1294)).
- Lee, P. G., C. S. Shim, and S. P. Chang. 2005. "Static and fatigue behavior of large stud shear connectors for steel-concrete composite bridges." *J. Constr. Steel Res.*, 61 (9): 1270–1285. <https://doi.org/10.1016/j.jcsr.2005.01.007>.
- Mander, J. B., and C. T. Cheng. 1997. *Seismic resistance of bridge piers based on damage avoidance design*. Rep. No. NCEER-97-0014. Buffalo, NY: Univ. at Buffalo
- Marriott, D., S. Pampanin, and A. Palermo. 2009. "Quasi-static and pseudo-dynamic testing of unbonded post-tensioned rocking bridge piers with external replaceable dissipaters." *Earthquake Eng. Struct. Dyn.* 38 (3): 331–354. <https://doi.org/10.1002/eqe.857>.
- Marsh, M. L., M. Wernly, B. E. Garrett, J. F. Stanton, M. O. Eberhard, and M. D. Weinert. 2011. *Application of accelerated bridge construction connections in moderate-to-high seismic regions*. NCHRP Rep. No.698. Washington, DC: National Cooperative Highway Research Program.
- Mashal, M., and A. Palermo. 2019a. "Low-Damage Seismic Design for Accelerated Bridge Construction." *J. Bridg. Eng.*, 24 (7): 04019066. [https://doi.org/10.1061/\(asce\)be.1943-5592.0001406](https://doi.org/10.1061/(asce)be.1943-5592.0001406).
- Mashal, M., and A. Palermo. 2019b. "Emulative seismic resistant technology for Accelerated Bridge Construction." *Soil Dyn. Earthquake Eng.* 124 (December 2018): 197–211. <https://doi.org/10.1016/j.soildyn.2018.12.016>.
- Mashal, M., A. Palermo, and G. Keats. 2019. "Innovative metallic dissipaters for earthquake protection of structural and non-structural components." *Soil Dyn. Earthquake Eng.* 116: 31–42. <https://doi.org/10.1016/j.soildyn.2018.10.002>.
- Morano, M., J. Liu, E. Williamson, T. C. Hutchinson, C. P. Pantelides, R. Piccinin, and J. Silva. 2024. "Rotationally compliant column baseplates to improve the seismic response of a 3-story steel building." *WCEE*, 1–12.
- Neupane, S., M. J. Ameli, and C. P. Pantelides. 2023. "Numerical Modeling of Column Piers with Recessed Spliced Sleeves and Intentional Debonding for Accelerated Bridge Construction." *J. Struct. Eng.*, 149 (3): 1–18. <https://doi.org/10.1061/jsendh.steng-11769>.
- Neupane, S., and C. P. Pantelides. 2024a. "Experiments and Numerical Analysis of Seismically Resilient Bridge Bent with Stretch Length Anchors as Energy Dissipaters." *J. Bridg. Eng.* <https://doi.org/10.1061/JBENF2/BEENG-6453>.
- Neupane, S., and C. P. Pantelides. 2024b. "Hybrid bridge bent using stretch length anchors with post-tensioning and shear key alternatives." *Eng. Struct.*, 310 (May): 118144. Elsevier Ltd. <https://doi.org/10.1016/j.engstruct.2024.118144>.
- Nie, J., K. Qin, and C. S. Cai. 2008. "Seismic behavior of connections composed of CFSSTCs and steel-concrete composite beams—experimental study." *J. Constr. Steel Res.*, 64 (10): 1178–1191. Elsevier.

- Ou, Y.-C., M.-S. Tsai, K.-C. Chang, and G. C. Lee. 2010. "Cyclic behavior of precast segmental concrete bridge columns with high performance or conventional steel reinforcing bars as energy dissipation bars." *Earthq. Eng. Struct. Dyn.*, 39: 1181–1198. <https://doi.org/10.1002/eqe>.
- Pampanin, S., Kam, W., Haverland, G., and Gardiner, S. (2011). "Expectation meets reality: Seismic performance of post-tensioned precast concrete southern cross endoscopy building during the 22nd Feb 2011 Christchurch earthquake." *NZ Concrete Industry Conf.*, New Zealand Concrete Society, Auckland, New Zealand.
- Pampanin, S., D. Marriott, and A. Palermo. 2010. *PRESSSdesign handbook*. Auckland, New Zealand: New Zealand Concrete Society.
- Parks, J. E., C. P. Pantelides, L. Ibarra, and D. Sanders. 2015. "Seismic anchorage of dry storage casks." SMIRT 23, 23rd Conf. Struct. Mech. in Reactor Technology. Paper ID 247.
- Parks, J. E., C. P. Pantelides, L. Ibarra, and D. H. Sanders. 2018. "Stretch length anchor bolts under combined tension and shear." *ACI Struct. J.*, 115 (5): 1317–1328. American Concrete Institute. <https://doi.org/10.14359/51702236>.
- Parks, J. E., C. P. Pantelides, L. Ibarra, and D. H. Sanders. 2020. "Cyclic Tests and Modeling of Stretch Length Anchor Bolt Assemblies for Dry Storage Casks." *ACI Struct. J.*, 117 (6): 225–236. <https://doi.org/https://doi.org/10.14359>.
- Qi, Y., Q. Gu, G. Sun, and B. Zhao. 2017. "Shear force demand on headed stud for the design of composite steel plate shear wall." *Eng. Struct.*, 148: 780–792. Elsevier.
- Raza, S., B. Shafei, M. S. Saiidi, M. Motavalli, and M. Shahverdi. 2022. "Shape memory alloy reinforcement for strengthening and self-centering of concrete structures—State of the art." *Constr. Build. Mater.* 324 (Mar):126628. <https://doi.org/10.1016/j.conbuildmat.2022.-126628>.
- Raza, S., R. Widmann, J. Michels, M. Saiid Saiidi, M. Motavalli, and M. Shahverdi. 2023. "Self-centering technique for existing concrete bridge columns using prestressed iron-based shape memory alloy reinforcement." *Eng. Struct.*, 294 (August): 116799. Elsevier Ltd. <https://doi.org/10.1016/j.engstruct.2023.116799>.
- Restrepo, J. I., and A. Rahman. 2007. "Seismic Performance of Self-Centering Structural Walls Incorporating Energy Dissipators." *J. Struct. Eng.*, 133 (11): 1560–1570. [https://doi.org/10.1061/\(asce\)0733-9445\(2007\)133:11\(1560\)](https://doi.org/10.1061/(asce)0733-9445(2007)133:11(1560)).
- Roh, H., and A. M. Reinhorn. 2009. "Analytical modeling of rocking elements." *Eng. Struct.*, 31 (5): 1179–1189. Elsevier Ltd. <https://doi.org/10.1016/j.engstruct.2009.01.014>.
- Roh, H., and A. M. Reinhorn. 2010. "Hysteretic behavior of precast segmental bridge piers with superelastic shape memory alloy bars." *Eng. Struct.* 33 (10): 3394–3403. <https://doi.org/10.1016/j.engstruct.2010.07.013>.
- Routledge, P., B. McHaffie, M. Cowan, and A. Palermo. 2020. "Wigram–Magdala Link Bridge: Low-Damage Details for a More Efficient Seismic Design Philosophy." *Struct. Eng. Int.*, 30 (2): 177–184. <https://doi.org/10.1080/10168664.2019.1679696>.
- Shen, Y., F. Freddi, Y. Li, and J. Li. 2022. "Parametric experimental investigation of unbonded post-tensioned reinforced concrete bridge piers under cyclic loading." *Earthq. Eng. Struct. Dyn.*, 51 (15): 3479–3504. <https://doi.org/10.1002/eqe.3732>.
- Shen, Y., F. Freddi, Y. Li, and J. Li. 2023. "Enhanced Strategies for Seismic Resilient Posttensioned Reinforced Concrete Bridge Piers: Experimental Tests and Numerical Simulations." *J. Struct. Eng.*, 149 (3): 1–17. <https://doi.org/10.1061/jsendh.steng-11831>.

- Shen, Y., X. Liu, Y. Li, and J. Li. 2021. "Cyclic tests of precast post-tensioned concrete filled steel tubular (PCFT) columns with internal energy-dissipating bars." *Eng. Struct.*, 229 (October 2020): 111651. Elsevier Ltd. <https://doi.org/10.1016/j.engstruct.2020.111651>.
- Shi, X., L. L. Song, T. Guo, and Z. H. Pan. 2022. "Seismic design of self-centering bridge piers considering soil-structure interaction." *Structures*, 43 (August): 1819–1833. Elsevier Ltd. <https://doi.org/10.1016/j.istruc.2022.07.055>.
- Sideris, P. 2012. "Seismic analysis and design of precast concrete segmental bridges." Ph.D. thesis, Dept. of Civil, Structural, and Environmental Engineering, Univ. at Buffalo.
- Sideris, P., A. J. Aref, and A. Filiatrault. 2014. "Quasi-static cyclic testing of a large-scale hybrid sliding-rocking segmental column with slip-dominant joints." *J. Bridge Eng.* 19 (10): 04014036. [https://doi.org/10.1061/\(ASCE\)BE.1943-5592.0000605](https://doi.org/10.1061/(ASCE)BE.1943-5592.0000605).
- Smith, M. 2009. *ABAQUS/Standard User's Manual, Version 6.9*. Providence, RI: Dassault Systèmes Simulia Corp.
- Soules, J. G., R. E. Bachman, and J. F. Silva. 2016. *Chile earthquake of 2010: Assessment of industrial facilities around conception*. Reston, VA: ASCE/SEI.
- Stanton, J. F., and P. M. Calvi. 2022. "A model for stud groups subjected to shear and moment." *Eng. Struct.*, 260 (November 2021): 114182. Elsevier Ltd. <https://doi.org/10.1016/j.engstruct.2022.114182>.
- Thapa, D., and C. P. Pantelides. 2021. "Self-Centering Bridge Bent with Stretch Length Anchors as a Tension-Only Hysteretic Hybrid System." *J. Struct. Eng.*, 147 (10): 04021163. [https://doi.org/10.1061/\(asce\)st.1943-541x.0003146](https://doi.org/10.1061/(asce)st.1943-541x.0003146).
- Thonstad, T., I. M. Mantawy, J. F. Stanton, M. O. Eberhard, and D. H. Sanders. 2016. "Shaking Table Performance of a New Bridge System with Pretensioned Rocking Columns." *J. Bridge Eng.*, 21 (4): 04015079. [https://doi.org/10.1061/\(asce\)be.1943-5592.0000867](https://doi.org/10.1061/(asce)be.1943-5592.0000867).
- Tong, X., J. F. Hajjar, A. E. Schultz, and C. K. Shield. 2005. "Cyclic behavior of steel frame structures with composite reinforced concrete infillwalls and partially-restrained connections." *J. Constr. Steel Res.* 61 (4): 531–552. <https://doi.org/10.1016/j.jcsr.2004.10.002>.
- Trautner, C., T. Hutchinson, M. Copellini, P. Grosser, R. Bachman, and J. Silva. 2017. "Developing ductility using concrete anchorage." *ACI Struct. J.*, 114 (1): 101–112. <https://doi.org/10.14359/51689152>.
- Trono, W., G. Jen, M. Panagiotou, M. Schoettler, and C. P. Ostertag. 2015. "Seismic Response of a Damage-Resistant Recentering Posttensioned-HYFRC Bridge Column." *J. Bridge Eng.*, 20 (7): 04014096. [https://doi.org/10.1061/\(asce\)be.1943-5592.0000692](https://doi.org/10.1061/(asce)be.1943-5592.0000692).
- Upadhyay, A., C. P. Pantelides, and L. Ibarra. 2019. "Residual drift mitigation for bridges retrofitted with buckling restrained braces or self centering energy dissipation devices." *Eng. Struct.*, 199 (September): 109663. Elsevier. <https://doi.org/10.1016/j.engstruct.2019.109663>.
- Wang, Z., J. Q. Wang, Y. C. Tang, T. X. Liu, Y. F. Gao, and J. Zhang. 2018. "Seismic behavior of precast segmental UHPC bridge columns with replaceable external cover plates and internal dissipaters." *Eng. Struct.*, 177 (September 2017): 540–555. Elsevier. <https://doi.org/10.1016/j.engstruct.2018.10.012>.
- Wang, Z., J. Wang, G. Zhao, and J. Zhang. 2019. "Design criterion for the self-centering capacity of precast segmental UHPC bridge columns with unbonded post-tensioning tendons." *Eng. Struct.*, 200 (February): 109706. Elsevier. <https://doi.org/10.1016/j.engstruct.2019.109706>.

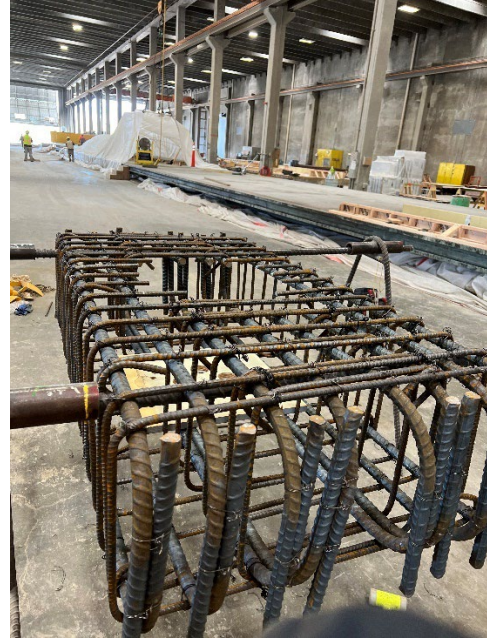
- White, S., and A. Palermo. 2016. "Quasi-static testing of posttensioned nonemulative column-footing connections for bridge piers." *J. Bridge Eng.* 21 (6): 04016025. [https://doi.org/10.1061/\(ASCE\)BE.1943-5592.0000872](https://doi.org/10.1061/(ASCE)BE.1943-5592.0000872).
- Wilson EL, Habibullah A. SAP2000, integrated finite element analysis and design of structures graphic user interface manual. Berkley, California, USA: Computers and Structures, Inc.; 1997.
- Xue, D., K. Bi, H. Dong, H. Qin, Q. Han, and X. Du. 2021. "Development of a novel self-centering slip friction brace for enhancing the cyclic behaviors of RC double-column bridge bents." *Eng. Struct.*, 232 (January): 111838. Elsevier Ltd. <https://doi.org/10.1016/j.engstruct.2020.111838>.
- Zhang, D., N. Li, Z. X. Li, and L. Xie. 2020. "Seismic performance of bridge with unbonded posttensioned self-centering segmented concrete-filled steel-tube columns: An underwater shaking table test." *Soil Dyn. Earthq. Eng.*, 138 (July): 106350. Elsevier Ltd. <https://doi.org/10.1016/j.soildyn.2020.106350>.
- Zhong, X., Y. Li, J. Li, Y. Shen, and Z. Bao. 2022. "Seismic Performance of Self-Centering Bridge Piers with Rocking Mechanical Hinges." *J. Bridg. Eng.*, 27 (12): 1–15. [https://doi.org/10.1061/\(asce\)be.1943-5592.0001961](https://doi.org/10.1061/(asce)be.1943-5592.0001961).

CHAPTER 15. APPENDIX

15.1 EXPERIMENTAL CONSTRUCTION HIGHLIGHTS



Reinforcing steel cage below shear key



Footing steel reinforcement cage



Footing steel reinforcement cage inside the formwork



Column steel reinforcing cage



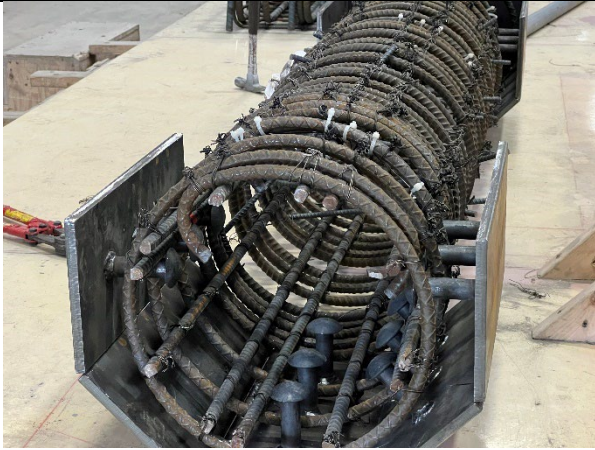
Column steel reinforcing cage with PVC pipes for PT bars



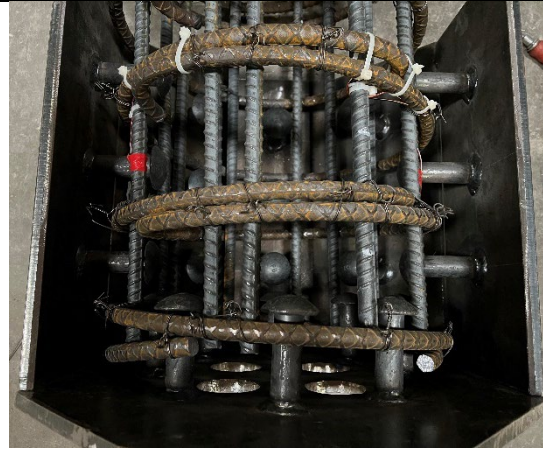
Steel collar with studs



Half collar placement in column rebar cage



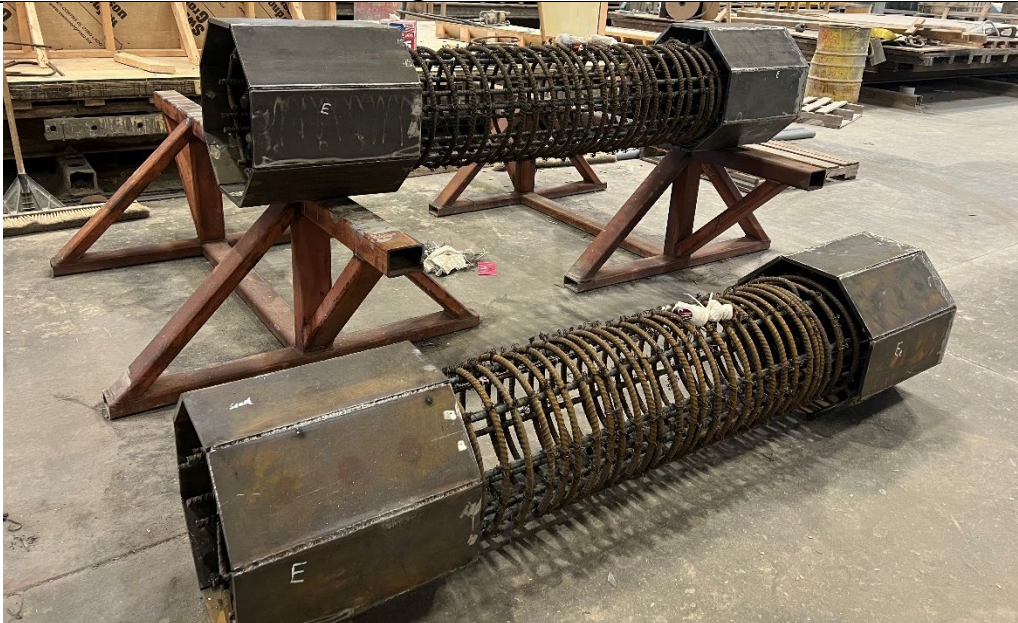
Collar and rebar cage details



Stud orientation in rebar cage



Column rebar cage with steel collar on both-sides



Column rebar cage with steel collar on both-sides



Column rebar cage inside the formwork



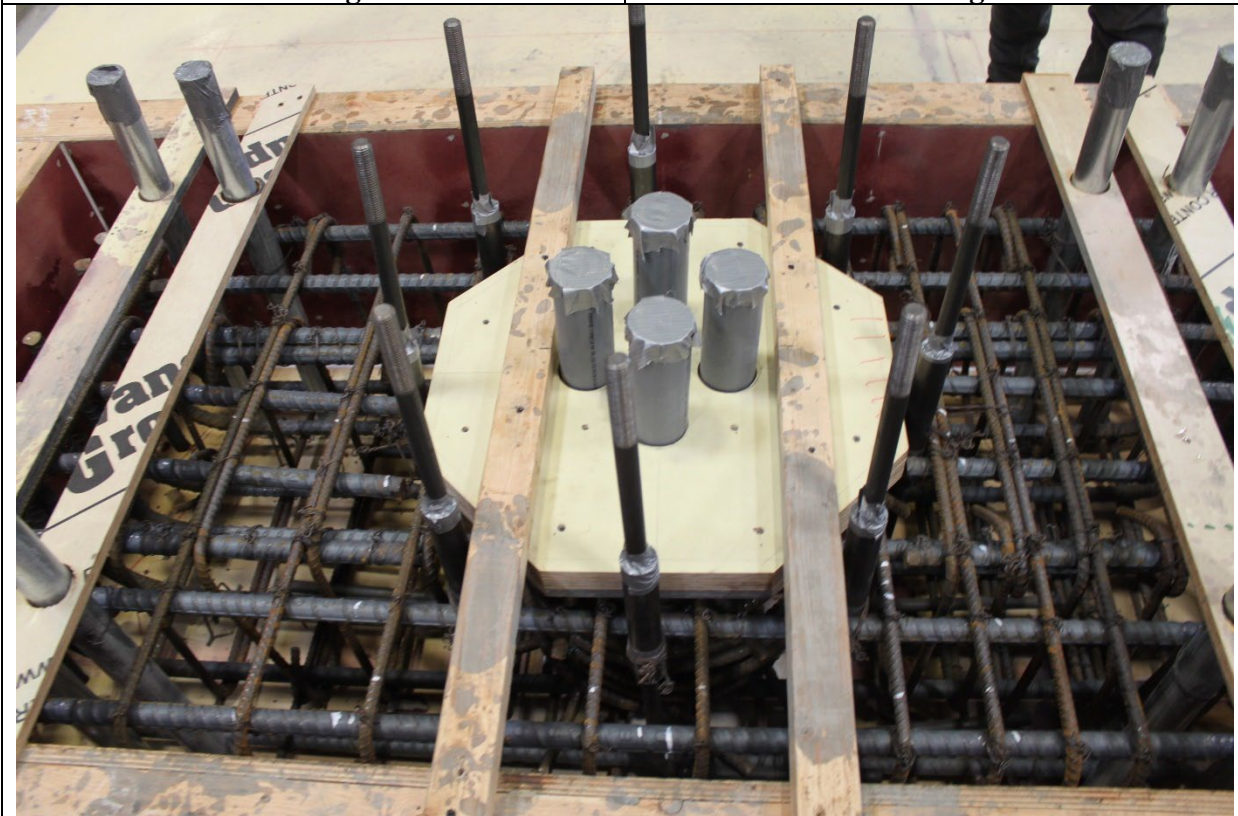
Column reinforcement inside the formwork with opening in collar



Footing rebar cage inside formwork before casting



Column rebar cage inside formwork before casting



Footing detail with shear key, steel couplers, SLAs and footing anchorage pipes



Column rebar cage inside formwork with eyes to lift the column after casting



Footing after casting



Column after casting



Column after 28 days



Footing after 28 days



Steel reinforcing cage for cap-beam



Formwork for cap-beam

15.2 CAP-BEAM MODIFICATION



Cap-beam after addition of shear keys

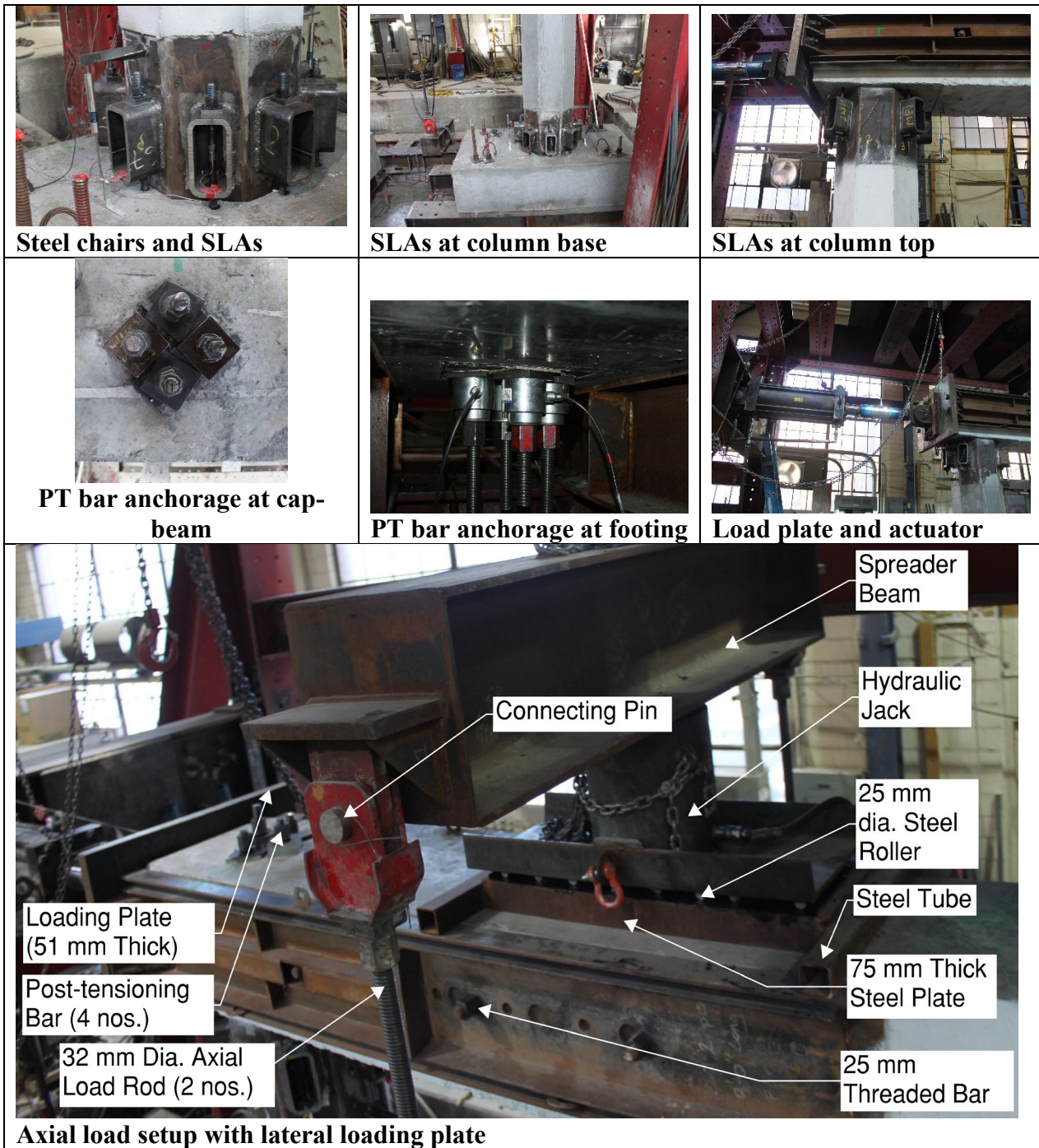


Shear-key details with steel plates and anchors



Shear-key details with steel plates and anchors

15.3 SPECIMEN SET UP AND INSTRUMENTATION





LVDT at footing



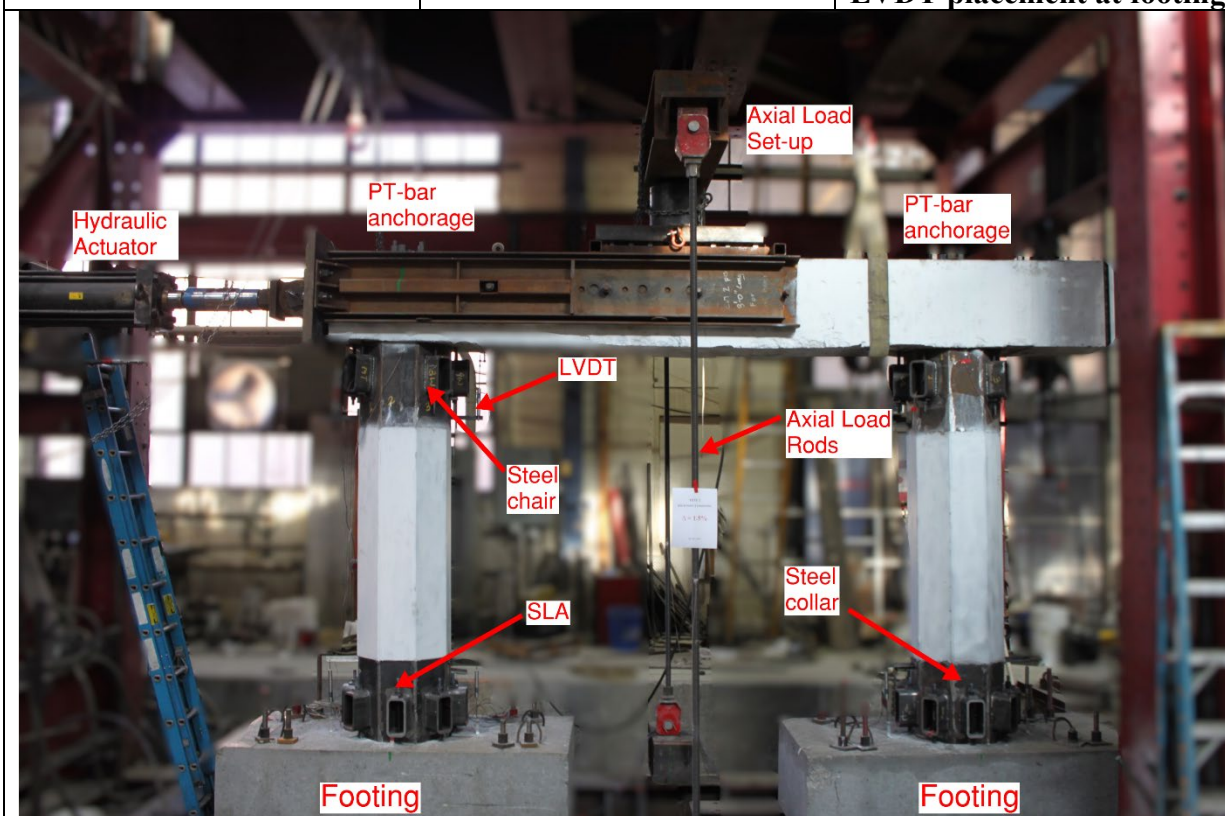
LVDT at cap-beam



LVDT placement at cap-beam



LVDT placement at footing



Experimental set-up and details



Loading channels attached to cap-beam



Load cells to measure PT bar forces



Strain gauges attached to column reinforcement cage

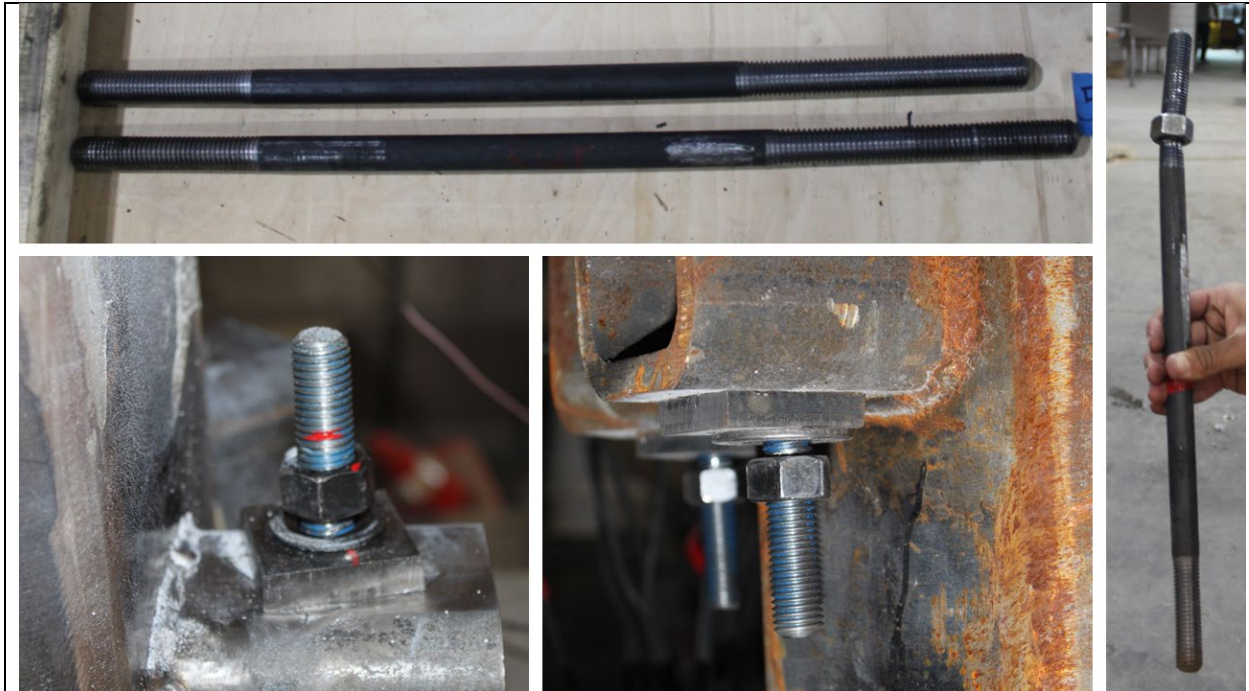
15.4 EXPERIMENTAL RESULTS



Typical deflected shape of bridge bent at 3.5% drift ratio (pull)



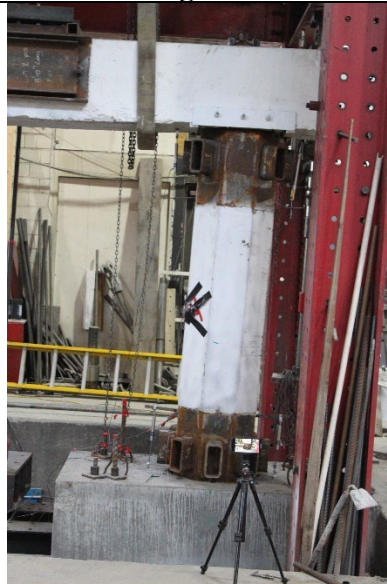
Typical deflected shape of bridge bent at 4.0% drift ratio (push)



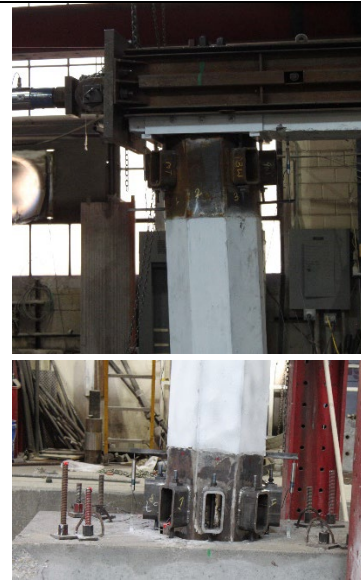
SLAs elongation details



Rocking column (pull)



Rocking column (push)



Detail of column rocking



SLA elongation (cap-beam)



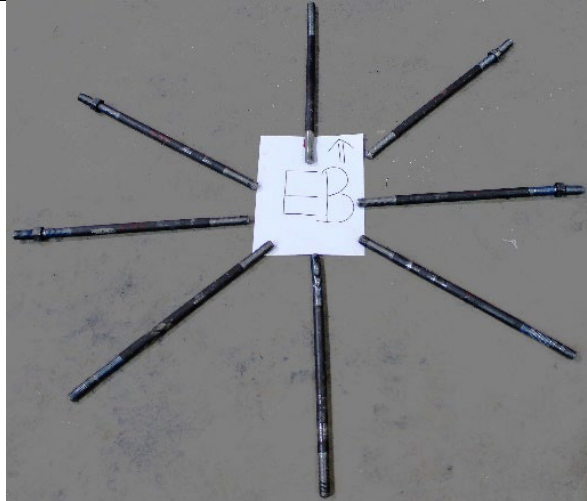
SLA elongation (footing)



SLA elongation details



SLAs after test (West column footing SLAs)



SLAs after test (East column footing SLAs)

15.5 STEP BY STEP ANALYSIS PROCEDURE FOR SPECIMEN BENT

Initial Design:

Column width **19.00 in.**
each side of octagonal (a) **7.87 in.**

$$A_g = 2(1 + \sqrt{2}) * a^2$$

Gross column area (A_g) **299.06 in.²**
compressive strength (f'_c) **14.10 ksi**
Modulus of concrete (E_c) **6768.37 ksi**

Equivalent diameter of circular section (D) **19.51 in.**

Longitudinal bar properties

Yield strength (f_y) **60.00 ksi**
Ultimate Strength (f_u) **87.50 ksi**
numbers of longitudinal bars **12.00 nos**

PT bar properties

Yield strength (f_{PT,y}) **120.00 ksi**
Ultimate Strength (f_{PT,u}) **150.00 ksi**

SLAs properties

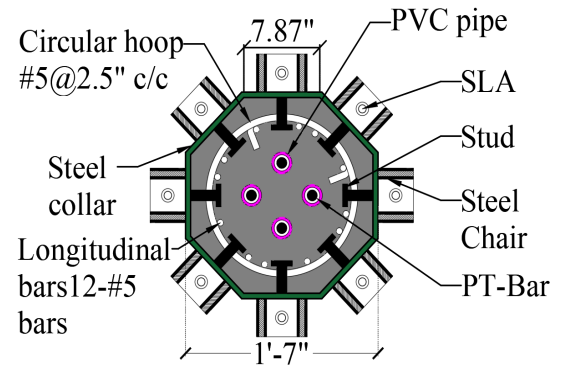
Yield strength (f_{SLA,y}) **40.00 ksi**
Ultimate Strength (f_{SLA,u}) **60.00 ksi**

Stud Properties

Yield strength (f_{STUD,y}) **44.00 ksi**
Ultimate Strength (f_{STUD,u}) **62.00 ksi**

Design of PT bars and SLAs

Assumed longitudinal bar % **2.00 %**



Rocking bridge bent won't have any rebars passing through and the force that will be transferred by rebars in case of monolithic must be transferred by SLAs and PT bars in the case of rocking

$$T_{ult} = \text{Longitudinal Rebar Percentage} * A_g * f_u$$

Ultimate tensile strength (T_{ult})	523.36	kip
---	--------	-----

Assume number of PT bars per column (n_{PT})	4.00	nos
--	------	-----

Assume diameter of PT bars (D_{PT})	1.00	in.
---	------	-----

Area of PT bars (A_{PT})	0.85	in. ²
------------------------------	------	------------------

Since, PT bars should not yield for the given drift ratio. Maximum force is assumed to be equal to yielding force of PT bars

$$\text{Maximum allowed PT force for each column}(F_{PT,y}) = n_{PT} * A_{PT} * f_{PT,y}$$

Maximum force by PT bars each column ($F_{PT,y}$)	408.00	kip
---	--------	-----

Since there is nothing connecting the column to the footing except for the PT bars and SLAs. The total ultimate tensile force dissipated by longitudinal bar in case of CIP must be dissipated by the combination of PT bars and SLAs

$$T_{ult} = F_{PT,y} + F_{SLA}$$

Certain force will be dissipated by PT bars and remaining force must be dissipated by SLAs.

$$F_{SLA} = T_{ult} - F_{PT,y}$$

Maximum force by SLAs (F_{SLA})	116.00	kip
-------------------------------------	--------	-----

Assume diameter of SLAs (D_{SLA})	0.75	in.
---------------------------------------	------	-----

Area of each SLA (A_{SLA})	0.44	in. ²
--------------------------------	------	------------------

$$\text{No of SLAs} = \frac{F_{SLA}}{f_{ySLA} * A_{SLA}}$$

Number of SLAs	8.00	nos
----------------	------	-----

Minimum Stretch Length	6.00	in.
------------------------	------	-----

Minimum $8d_b$ (d_b is diameter of SLA)

This means 8 SLAs should be in tension for each column (total from top and bottom). Since SLAs are provided on all sides of the octagonal base of the footing, only 6 SLAs are provided on the top. Only 5 are in tension at the bottom, and 3 go in tension on top, summing up to 8 (the required number of SLAs). Thus 8 SLAs on the bottom connected to the footing and 6 SLAs connected to the column should be provided. Making total 14 SLAs for each column.

Total number of SLAs **14.00 nos**

Computation of Initial PT force

Initial PT force is computed based on the rigid body analogy and the initial PT force which does not let PT bars yield up to design drift ratio must be selected

Initial PT force ($F_{PT,i}$) **40.00 kip**

Axial Gravity load

6% axial load index (ALI) should be considered as the axial load in the column, and this is the total gravity load coming from bridge deck and other superstructure load

Gravity load applied in the experiment (P_u) **72 kip**

$$\Lambda_D = \frac{F_{u,SLA}}{P_u + F_{PT,i} + F_{u,SLA}}$$

Energy dissipation coefficient (Λ_D) **0.48 OK $0.1 \geq \Lambda_D \leq 0.6$**

$$F_{u,SLA} = f_{u,SLA} * A_{SLA} * n_{SLA}$$

If energy dissipation coefficient is not within the limit of 0.1 to 0.6, the number of PT bars and the initial PT force must be changed in order to get it within the limit by optimizing number of SLAs and on yielding PT bars-- however for a bridge bent with SLAs which do not impede self-centering following calculations can be done for energy dissipation and self-centering:

$$\Lambda_C = \frac{F_{u,SLA}}{P_u + F_{PT,i}} \leq 1.0$$

$F_{u,SLA}$ is ultimate strength of all energy dissipators
 P_u is total gravity load

Self-centering coefficient (Λ_C) **0.91 OK $\Lambda_C \leq 1$**
 $F_{PT,i}$ is total initial PT force, after losses

Energy dissipation is validated using energy dissipation coefficient

$$\Lambda_D = \frac{F_{u,SLA}}{P_u + F_{PT,i} + F_{u,SLA}} \geq 0.1$$

Energy dissipation coefficient (Λ_D)	0.48	OK	0.1 > Λ_D
---	------	----	-------------------

Steel collar Design

Steel collar was designed based on the neutral axis depth at 4.0% drift ratio 2 times the design drift ratio of 2.0%

Maximum assumed drift ratio **4.00%**

$$\frac{c}{D} = 0.825 \text{ for } DR = 0\% \text{ and } \frac{c}{D} = 520(DR)^2 - 37.76(DR) + 0.79 \text{ for } DR > 0\%$$

Neutra axis at 4.0% drift (c) **2.30 in.**

$$h_s^* = 0.5 \sqrt{D^2 - c^2 + 2D \sqrt{D^2 - c^2}}$$

Unfactored height of collar (h_s^*) **16.82 in.**

Factor of Safety (λ_s) **1.2**

Height of steel collar (h_s) **19.30 in.**

Provided height of steel collar **19.50 in.**

Assuming thickness of plate (t_s) **0.50 in.**

$$\frac{D}{t_s} \leq 100$$

Check **39.03 OK**

Stud Design

Yield Strength (f_y) **44.00 ksi**

Ultimate Strength (f_u) **62.00 ksi**

Maximum expected load from SLAs **27.00 kip** (assuming ultimate load of SLAs)

Assume Factor of Safety for SLA load **2.00**

Maximum factored SLA load **54 kip**

assume number of studs **2.00 nos**

Diameter of Studs (D_{stud}) **1.00 in.**

Area of stud (A_{sc}) **0.79 in²**

Ultimate SLA force is assumed to be acting on the steel chair and must be distributed by Studs-- factor of safety is used to increase SLA load for conservative design

Shear strength of One Stud from

Codal Predictions

$$Q_{n1} = 0.5A_{sc}\sqrt{f'_cE_c} \leq A_{sc}F_u$$

Q_{n1} 97.39 kip

OK

AASHTO 9th
edition

Summary			
Item	Qty	Units	Grade
Initial PT Force	40.00	kip	120 ksi PT bar
Number of PT bar	4.00	nos	
Diameter of PT bar	1.00	in.	
Number of SLAs	14.00	nos	Grade 36
Diameter of SLAs	0.75	in.	
Height of steel Collar	19.50	in.	Grade 50
Thickness of Steel Collar	0.50	in.	
Number of Studs	2.00	nos	Grade 50
Diameter of Studs	1.00	in.	

PT force Distribution

Calculation sheet for Initial PT Selection

Length of PT Bars (L_T)	123.00	in.
Column Height (H_c)	86.00	in.
Loading Point (L_c)	96.00	in.
Initial Axial Gravity Load (P_u)	72.00	kip
Elastic Modulus of PT bar (E_s)	29000.00	ksi
Equivalent Circular Diameter of Column (D)	19.51	in.
compressive strength (f'_c)	14.10	ksi
Modulus of concrete (E_c)	6768.37	ksi
number of PT (n_{PT})	4.00	
number of column (n_c)	2.00	
yield strain of PT bars	0.004138	in./in.

Initial PT forces:

FPTi,1	40	kip
FPTi,2	50	kip
FPTi,3	60	kip
FPTi,4	70	kip

The PT force distribution is calculated based on the rotation(θ), deflection(Δ_{rot}) and neutral axis depth (c).

The rotation during rocking is calculated for each drift ratio using, $\theta = \frac{\Delta_{rot}}{H_c}$

Δ is calculated for a given drift ratio (DR) is calculated using, $\Delta = (DR)L_c$

where L_c is length upto loading point from footing surface.

Initial strain(ε_0) for a assumed initial PT force $F_{PT,i}$ is calculated as,

$$\varepsilon_0 = \frac{f_{PT,i}}{E_{PT}}, f_{PT,i} = \frac{F_{PT,i}}{A_{PT}}$$

where $f_{PT,i}$ is initial PT stress, A_{PT} is area of PT bar, E_{PT} is modulus of elasticity of PT bar.

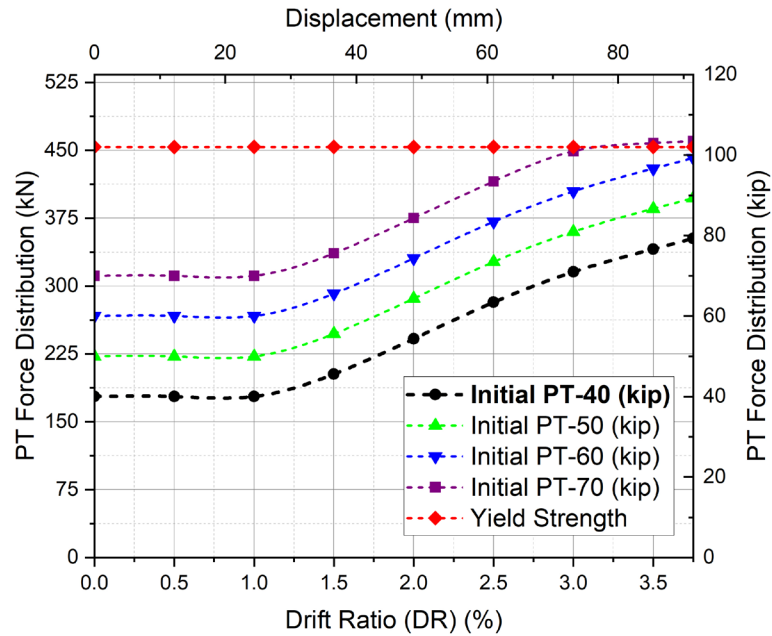
The PT force for a given drift ratio is obtained,

$$F_{PT} = E_{PT}A_{PT} * \left[\frac{\left(\frac{D}{2}-c\right)\theta}{L_T} + \varepsilon_0 \right] \text{ i.e. Until } c \text{ reaches } D/2 \text{ there is no change in PT forces.}$$

Table shows the PT force calculated for different initial PT force:

Table 19. Analytical calculation for PT force distribution for specimen bent

Drift Ratio (DR) (%)	Displacement (Δ) (in.)	Theta (θ) (rad)	c/D	c (in.)	PT Force for Initial PT-70 (kip)	PT Force for Initial PT-40 (kip)	PT Force for Initial PT-50 (kip)	PT Force for Initial PT-60 (kip)	PT Yield (kip)
0.00%	0.00	0.0000	1.00	19.51	70.00	40.00	50.00	60.00	102.00
0.50%	0.48	0.0056	0.66	12.87	70.00	40.00	50.00	60.00	102.00
1.00%	0.96	0.0112	0.52	10.20	70.00	40.00	50.00	60.00	102.00
1.50%	1.44	0.0167	0.41	8.10	75.57	45.57	55.57	65.57	102.00
2.00%	1.92	0.0223	0.34	6.55	84.34	54.34	64.34	74.34	102.00
2.50%	2.40	0.0279	0.29	5.57	93.43	63.43	73.43	83.43	102.00
3.00%	2.88	0.0335	0.26	5.14	100.96	70.96	80.96	90.96	102.00
3.50%	3.36	0.0390	0.26	5.07	102.96	76.65	86.65	96.65	102.00
3.75%	3.60	0.0418	0.26	5.07	103.50	79.27	89.27	99.27	102.00



Analytical calculation for PT force distribution for specimen bent

Pushover Calculation:

Calculation sheet for Pushover

Length of PT Bars (L_{PT})	123.00	in.	
Length of SLA (L_{SLA})	13.00	in.	(Used for the experiment)
Column Height (H_C)	86.00	in.	
Loading Point (L_C)	96.00	in.	
Initial PT Force ($F_{PT,i}$)	40.00	kip	
Initial Axial Gravity Load each column (P_u)	72.00	kip	
Elastic Modulus of PT bar (E_{PT})	29000.00	ksi	
Initial Strain in PT bars (ϵ_{PT})	0.0016227	in./in.	
Equivalent Circular Diameter of Column (D)	19.51	in.	
yield strain of PT bars	0.004138	in./in.	
compressive strength (f'_c)	14.10	ksi	
Modulus of concrete (E_c)	6768.37	ksi	
number of PT each column (n_{PT})	4.00		
number of column (n_c)	2.00		
Gross Moment of inertia of concrete column (I_g)	7117.27	in. ⁴	
Effective moment of Inertia (I_{eff})	4982.09	in. ⁴	
Total Gravity load (W)	144.00	kip	

$$S_C = 2 * \frac{I_{eff}}{D}$$

$$S_c = 510.63 \text{ in}^3$$

$$M_{dec} = n_c \left(\frac{W}{n_c} + n_{PT} F_{PT,i} \right) * \frac{S_C}{A_g}$$

$$M_{dec} = 792.25 \text{ kip-in.}$$

$$F_{decomp} = \frac{2 * M_{dec}}{H_C}$$

$$F_{decomp} = 18.42 \text{ kip}$$

There is a small elastic deflection (Δ_{dcomp}) of the bent up to a decompression region. This deflection is calculated assuming bent as a portal frame and F_{dcomp} as a lateral load causing deflection.

$$\Delta_{dcomp} = \frac{F_{dcomp} L_c^3}{24 * E_c * I_{eff}} \quad \mathbf{0.02 \quad in. \quad 0.02 \quad \%}$$

$$\frac{c}{D} = 1 \text{ for } DR = 0\% \text{ and } \frac{c}{D} = 451.3 (DR)^2 - 37.17(DR) + 0.94 \text{ for } DR > 0\%$$

$$\varepsilon_{SLA} = \theta \left(\frac{(D_i - c)}{L_{SLA}} \right); \text{ for } (D_i - c) \geq 0 \text{ and } \varepsilon_{SLA} = 0; \text{ for } (D_i - c) < 0$$

$$F_{T,i} = A_{SLA} \sigma_{T,i} \quad \sigma_{T,i} \text{ is stress corresponding to } \varepsilon_{SLA} \text{ from stress strain relationship for SLAs}$$

$$F_{rot} H_c = n_c \left(n_{PT} F_{PT} + \frac{W}{n_c} \right) (D - c - \Delta_{rot}) + \sum F_{T,i}(D_i)$$

Due to lateral load during rotation there is some elastic displacement, and it can be calculated as:

$$\Delta_{elastic} = \frac{F_{rot} L^3}{24 E_c I_{eff}}$$

The final drift ratio can be calculated as:

$$\text{Final Drift Ratio} = \frac{\Delta_{elastic} + \Delta_{rot}}{L_c}$$

$$F_{tot} = F_{rot} + F_{PT_horizontal}$$

Table 20. Analytical response for specimen bent 4FA and 4FBA.

Drift Ratio (DR) (%)	Delta _{rot}	Theta (rad)	c/D	c (in.)	PT force each PT bar (kip)	PT force Vertical (kip)	Axial Gravity Load	Strain of SLAs			Force in each SLA (kip)			Horizontal PT force (kip)	Frot kip	Delta _{sl} in.	Total Disp (in.)	Total Drift ratio (%)
	in.							e1	e2	e3	F1	F2	F3					
0.00	0.00	0.00	1.00	19.51	40.00	40.00	72.00	0.0000	0.0000	0.0000	0.00	0.00	0.00	0.00	0.00	0.00	0.00	0.00
0.03	0.00	0.00	0.83	16.10	40.00	40.00	72.04	0.0000	0.0000	0.0000	0.00	0.00	0.00	0.00	18.43	0.02	0.02	0.02
0.05	0.03	0.00	0.82	15.91	40.00	40.00	72.07	0.0001	0.0000	0.0000	2.52	0.00	0.00	0.10	20.65	0.02	0.05	0.05
0.08	0.05	0.00	0.81	15.75	40.00	40.00	72.11	0.0002	0.0000	0.0000	3.78	0.00	0.00	0.18	22.13	0.02	0.07	0.08
0.10	0.07	0.00	0.80	15.59	40.00	40.00	72.14	0.0004	0.0000	0.0000	5.34	0.00	0.00	0.26	23.73	0.03	0.10	0.10
0.13	0.09	0.00	0.79	15.44	40.00	40.00	72.17	0.0005	0.0000	0.0000	6.51	0.00	0.00	0.34	25.12	0.03	0.12	0.13
0.15	0.11	0.00	0.78	15.28	40.00	40.00	72.20	0.0006	0.0000	0.0000	8.18	0.00	0.00	0.43	26.78	0.03	0.14	0.15
0.18	0.14	0.00	0.77	15.12	40.00	40.00	72.21	0.0008	0.0000	0.0000	9.29	0.00	0.00	0.51	28.16	0.03	0.17	0.18
0.20	0.16	0.00	0.77	14.96	40.00	40.00	72.21	0.0009	0.0000	0.0000	10.84	0.00	0.00	0.60	29.74	0.03	0.19	0.20
0.23	0.18	0.00	0.76	14.80	40.00	40.00	72.22	0.0011	0.0000	0.0000	12.33	0.00	0.00	0.68	31.30	0.03	0.22	0.23
0.25	0.21	0.00	0.75	14.65	40.00	40.00	72.26	0.0013	0.0000	0.0000	14.02	0.00	0.00	0.76	32.94	0.03	0.24	0.25
0.28	0.23	0.00	0.74	14.49	40.00	40.00	72.29	0.0014	0.0000	0.0000	15.76	1.81	0.00	0.85	35.84	0.04	0.26	0.28
0.30	0.25	0.00	0.73	14.34	40.00	40.00	72.33	0.0016	0.0001	0.0000	17.31	1.95	0.00	0.93	37.51	0.04	0.29	0.30
0.33	0.27	0.00	0.73	14.19	40.00	40.00	72.37	0.0018	0.0001	0.0000	17.34	2.52	0.00	1.02	38.70	0.04	0.31	0.33
0.35	0.30	0.00	0.72	14.04	40.00	40.00	72.40	0.0020	0.0002	0.0000	17.34	3.16	0.00	1.10	39.92	0.04	0.34	0.35
0.38	0.32	0.00	0.71	13.90	40.00	40.00	72.61	0.0022	0.0002	0.0000	17.34	3.21	0.00	1.18	40.71	0.04	0.36	0.38
0.40	0.34	0.00	0.70	13.75	40.00	40.00	72.83	0.0024	0.0003	0.0000	17.32	4.14	0.00	1.27	42.13	0.04	0.38	0.40
0.43	0.36	0.00	0.70	13.60	40.00	40.00	72.97	0.0026	0.0003	0.0000	17.28	4.67	0.00	1.35	43.25	0.04	0.41	0.43
0.45	0.39	0.00	0.69	13.45	40.00	40.00	73.10	0.0028	0.0004	0.0000	17.26	5.49	0.00	1.44	44.56	0.05	0.43	0.45
0.48	0.41	0.00	0.68	13.31	40.00	40.00	73.23	0.0030	0.0005	0.0000	17.25	6.44	0.00	1.52	45.96	0.05	0.46	0.48
0.50	0.43	0.01	0.68	13.17	40.00	40.00	73.36	0.0032	0.0006	0.0000	17.23	7.10	0.00	1.60	47.13	0.05	0.48	0.50
0.53	0.45	0.01	0.67	13.03	40.00	40.00	73.51	0.0034	0.0007	0.0000	17.23	8.18	0.00	1.69	48.61	0.05	0.50	0.53
0.55	0.48	0.01	0.66	12.89	40.00	40.00	73.67	0.0037	0.0007	0.0000	17.23	9.19	0.00	1.77	50.05	0.05	0.53	0.55
0.58	0.50	0.01	0.65	12.75	40.00	40.00	73.83	0.0039	0.0008	0.0000	17.23	10.07	0.00	1.86	51.39	0.05	0.55	0.58
0.60	0.52	0.01	0.65	12.61	40.00	40.00	74.03	0.0042	0.0009	0.0000	17.24	10.84	0.00	1.94	52.66	0.05	0.58	0.60
0.63	0.54	0.01	0.64	12.48	40.00	40.00	74.22	0.0044	0.0010	0.0000	17.26	11.86	0.00	2.02	54.07	0.06	0.60	0.63
0.65	0.57	0.01	0.63	12.35	40.00	40.00	74.42	0.0046	0.0012	0.0000	17.27	13.41	0.00	2.11	55.86	0.06	0.62	0.65
0.68	0.59	0.01	0.63	12.21	40.00	40.00	74.62	0.0049	0.0013	0.0000	17.28	14.45	0.00	2.19	57.30	0.06	0.65	0.68
0.70	0.61	0.01	0.62	12.08	40.00	40.00	74.81	0.0052	0.0014	0.0000	17.29	15.62	0.00	2.28	58.82	0.06	0.67	0.70
0.73	0.64	0.01	0.61	11.95	40.00	40.00	75.01	0.0054	0.0015	0.0000	17.30	16.78	0.00	2.36	60.33	0.06	0.70	0.73
0.75	0.66	0.01	0.61	11.82	40.00	40.00	75.20	0.0057	0.0017	0.0000	17.31	17.34	0.00	2.44	61.39	0.06	0.72	0.75
0.78	0.68	0.01	0.60	11.69	40.00	40.00	75.40	0.0060	0.0018	0.0000	17.32	17.34	0.00	2.53	62.09	0.06	0.74	0.78
0.80	0.70	0.01	0.59	11.56	40.00	40.00	75.59	0.0063	0.0019	0.0000	17.32	17.33	0.00	2.61	62.79	0.07	0.77	0.80
0.83	0.73	0.01	0.59	11.44	40.00	40.00	75.79	0.0065	0.0021	0.0000	17.35	17.34	0.00	2.70	63.50	0.07	0.79	0.83
0.85	0.75	0.01	0.58	11.31	40.00	40.00	75.99	0.0068	0.0022	0.0000	17.36	17.34	0.00	2.78	64.19	0.07	0.82	0.85
0.88	0.77	0.01	0.57	11.19	40.00	40.00	76.21	0.0071	0.0024	0.0000	17.40	17.32	0.00	2.87	64.85	0.07	0.84	0.88
0.90	0.79	0.01	0.57	11.07	40.00	40.00	76.43	0.0074	0.0025	0.0000	17.46	17.30	0.00	2.95	65.54	0.07	0.86	0.90
0.93	0.82	0.01	0.56	10.94	40.00	40.00	76.64	0.0077	0.0027	0.0000	17.52	17.27	0.00	3.04	66.23	0.07	0.89	0.93
0.95	0.84	0.01	0.55	10.82	40.00	40.00	76.86	0.0080	0.0029	0.0000	17.56	17.26	0.00	3.12	66.91	0.07	0.91	0.95
0.98	0.86	0.01	0.55	10.70	40.00	40.00	77.19	0.0083	0.0030	0.0000	17.59	17.25	0.00	3.21	67.59	0.07	0.94	0.98
1.00	0.88	0.01	0.54	10.59	40.00	40.00	77.53	0.0086	0.0032	0.0000	17.60	17.23	0.00	3.29	68.25	0.08	0.96	1.00

Table 21. Analytical response for specimen bent 4F and 4FB.

Drift Ratio (DR) (%)	Delta _{rot} in.	Theta (rad)	c/D	c (in.)	PT force each PT bar (kip)	PT force Vertical (kip)	Axial Gravity Load each	Horizontal PT force (kip)	F _{rot} kip	Delta _{elastic} in.	Total Disp (in.)	Total Drift ratio
0.000	0.00	0.00	1.00	19.51	40.00	40.00	72.01	0.00	0.00	0.00	0.00	0.00
0.025	0.000	0.00	0.83	16.10	40.00	40.00	72.04	0.00	18.43	0.02	0.02	0.02
0.050	0.03	0.00	0.82	15.91	40.00	40.00	72.07	0.10	19.42	0.02	0.05	0.05
0.075	0.05	0.00	0.81	15.74	40.00	40.00	72.11	0.18	20.26	0.02	0.07	0.08
0.100	0.07	0.00	0.80	15.58	40.00	40.00	72.14	0.27	21.10	0.02	0.10	0.10
0.125	0.09	0.00	0.79	15.42	40.00	40.00	72.17	0.35	21.95	0.03	0.12	0.13
0.150	0.12	0.00	0.78	15.26	40.00	40.00	72.20	0.44	22.80	0.03	0.14	0.15
0.175	0.14	0.00	0.77	15.09	40.00	40.00	72.21	0.52	23.64	0.03	0.17	0.18
0.200	0.16	0.00	0.77	14.93	40.00	40.00	72.21	0.61	24.46	0.03	0.19	0.20
0.225	0.19	0.00	0.76	14.77	40.00	40.00	72.22	0.70	25.29	0.03	0.22	0.23
0.250	0.21	0.00	0.75	14.61	40.00	40.00	72.26	0.78	26.11	0.03	0.24	0.25
0.275	0.23	0.00	0.74	14.46	40.00	40.00	72.29	0.87	26.93	0.03	0.26	0.28
0.300	0.26	0.00	0.73	14.30	40.00	40.00	72.33	0.96	27.74	0.03	0.29	0.30
0.325	0.28	0.00	0.72	14.15	40.00	40.00	72.37	1.04	28.54	0.03	0.31	0.33
0.350	0.30	0.00	0.72	13.99	40.00	40.00	72.40	1.13	29.33	0.03	0.34	0.35
0.375	0.33	0.00	0.71	13.84	40.00	40.00	72.61	1.22	30.13	0.03	0.36	0.38
0.400	0.35	0.00	0.70	13.69	40.00	40.00	72.83	1.30	30.94	0.03	0.38	0.40
0.425	0.37	0.00	0.69	13.54	40.00	40.00	72.97	1.39	31.72	0.03	0.41	0.43
0.450	0.40	0.00	0.69	13.39	40.00	40.00	73.10	1.47	32.50	0.04	0.43	0.45
0.475	0.42	0.00	0.68	13.25	40.00	40.00	73.23	1.56	33.28	0.04	0.46	0.48
0.500	0.44	0.01	0.67	13.10	40.00	40.00	73.36	1.65	34.04	0.04	0.48	0.50
0.525	0.47	0.01	0.66	12.96	40.00	40.00	73.51	1.73	34.81	0.04	0.50	0.53
0.550	0.49	0.01	0.66	12.82	40.00	40.00	73.67	1.82	35.56	0.04	0.53	0.55
0.575	0.51	0.01	0.65	12.67	40.00	40.00	73.83	1.91	36.31	0.04	0.55	0.58
0.600	0.54	0.01	0.64	12.53	40.00	40.00	74.03	1.99	37.06	0.04	0.58	0.60
0.625	0.56	0.01	0.64	12.40	40.00	40.00	74.22	2.08	37.81	0.04	0.60	0.63
0.650	0.58	0.01	0.63	12.26	40.00	40.00	74.42	2.16	38.55	0.04	0.62	0.65
0.675	0.60	0.01	0.62	12.12	40.00	40.00	74.62	2.25	39.28	0.04	0.65	0.68
0.700	0.63	0.01	0.61	11.99	40.00	40.00	74.81	2.34	40.00	0.04	0.67	0.70
0.725	0.65	0.01	0.61	11.85	40.00	40.00	75.01	2.42	40.72	0.04	0.70	0.73
0.750	0.67	0.01	0.60	11.72	40.00	40.00	75.20	2.51	41.43	0.05	0.72	0.75
0.775	0.70	0.01	0.59	11.59	40.00	40.00	75.40	2.60	42.14	0.05	0.74	0.78
0.800	0.72	0.01	0.59	11.46	40.00	40.00	75.59	2.68	42.84	0.05	0.77	0.80
0.825	0.74	0.01	0.58	11.34	40.00	40.00	75.79	2.77	43.53	0.05	0.79	0.83
0.850	0.77	0.01	0.57	11.21	40.00	40.00	75.99	2.85	44.22	0.05	0.82	0.85
0.875	0.79	0.01	0.57	11.08	40.00	40.00	76.21	2.94	44.91	0.05	0.84	0.88
0.900	0.81	0.01	0.56	10.96	40.00	40.00	76.43	3.03	45.58	0.05	0.86	0.90
0.925	0.84	0.01	0.56	10.84	40.00	40.00	76.64	3.11	46.26	0.05	0.89	0.93
0.950	0.86	0.01	0.55	10.72	40.00	40.00	76.86	3.20	46.92	0.05	0.91	0.95
0.975	0.88	0.01	0.54	10.60	40.00	40.00	77.19	3.28	47.60	0.05	0.94	0.98
1.000	0.91	0.01	0.54	10.48	40.00	40.00	77.53	3.37	48.28	0.05	0.96	1.00

15.6 STEP BY STEP ANALYSIS PROCEDURE FOR RIVERDALE BRIDGE BENT

Design of Riverdale Bridge Bent

Column width **42.00 in.**
 each side of octagonal (a) **17.40 in.**

$$A_g = 2(1 + \sqrt{2}) * a^2$$

Gross column area (A_g) **1461.35 in²**
 compressive strength (f'_c) **6.00 ksi**

Modulus of concrete (E_c) **4415.20 ksi**

Equivalent diameter of circular section (D) **43.14 in.**

Longitudinal bar properties

Yield strength (f_y) **60.00 ksi**
 Ultimate Strength (f_u) **90.00 ksi**
 numbers of longitudinal bars **12.00 nos**

PT bar properties

Yield strength (f_{PT,y}) **120.00 ksi**
 Ultimate Strength (f_{PT,u}) **150.00 ksi**

SLAs properties

Yield strength (f_{SLA,y}) **40.00 ksi**
 Ultimate Strength (f_{SLA,u}) **60.00 ksi**

Stud Properties

Yield strength (f_{STUD,y}) **44.00 ksi**
 Ultimate Strength (f_{STUD,u}) **62.00 ksi**

Design of PT bars and SLAs

Assumed longitudinal bar % **1.00 %**

Rocking bridge bent won't have any rebars passing through and the force that will be transferred by rebars in case of monolithic must be transferred by SLAs and PT bars in the case of rocking

$$T_{ult} = \text{Longitudinal Rebar Percentage} * A_g * f_u$$

Ultimate tensile strength (T_{ult})	1315.21	kip
---	---------	-----

Assume number of PT bars per column (n_{PT})	6.00	nos
--	------	-----

Assume diameter of PT bars (D_{PT})	1.25	in.
---	------	-----

Area of PT bars (A_{PT})	1.25	in. ²
------------------------------	------	------------------

Since, PT bars should not yield for the given drift ratio. Maximum force is assumed to be equal to yielding force of PT bars

$$\text{Maximum allowed PT force for each column}(F_{PT,y}) = n_{PT} * A_{PT} * f_{PT,y}$$

Maximum force by PT bars each column($F_{PT,y}$)	900.00	kip
--	--------	-----

Since there is nothing connecting the column to the footing except for the PT bars and SLAs. The total ultimate tensile force dissipated by longitudinal bar in case of CIP must be dissipated by the combination of PT bars and SLAs

$$T_{ult} = F_{PT,y} + F_{SLA}$$

Certain force will be dissipated by PT bars and remaining force must be dissipated by SLAs.

$$F_{SLA} = T_{ult} - F_{PT,y}$$

Maximum force by SLAs (F_{SLA})	416.00	kip
-------------------------------------	--------	-----

Assume diameter of SLAs (D_{SLA})	1.25	in.
---------------------------------------	------	-----

Area of each SLA (A_{SLA})	1.23	in. ²
--------------------------------	------	------------------

$$\text{No of SLAs} = \frac{F_{SLA}}{f_{ySLA} * A_{SLA}}$$

Number of SLAs	10.00	nos
----------------	-------	-----

Minimum Stretch Length	10.00	in.	Minimum $8d_b$ (d_b is diameter of SLA)
------------------------	-------	-----	--

This means 10 SLAs should be in tension for each column (total from top and bottom). Since SLAs are provided on all sides of the octagonal base of the footing, and cap beam. Only 5 are in tension at the bottom, and 5 go in tension on top, summing up to 10 (the required number of SLAs). Thus 8 SLAs on the bottom connected to the footing and 8 SLAs connected to the column should be provided. Making a total of 16 SLAs for each column.

Total number of SLAs	16.00	nos
----------------------	-------	-----

Computation of Initial PT force

Initial PT force is computed based on the rigid body analogy and the initial PT force which does not let PT bars yield up to design drift ratio must be selected

Initial PT force ($F_{PT,i}$) **80.00 kip**

Axial Gravity load

6%-10% axial load index (ALI) should be considered as the axial load in the column and this is the total gravity load coming from bridge deck and other superstructure load

Gravity load applied in the experiment (P_u) **876.8073 kip**

$$\Lambda_D = \frac{F_{u,SLA}}{P_u + F_{PT,i} + F_{u,SLA}}$$

Energy dissipation coefficient (Λ_D) **0.36** **OK** **$0.1 \geq \Lambda_D \leq 0.6$**

$$F_{u,SLA} = f_{u,SLA} * A_{SLA} * n_{SLA}$$

If energy dissipation coefficient is not within the limit of 0.1 to 0.6, the number of PT bars and the initial PT force must be changed in order to get it within the limit by optimizing number of SLAs and on yielding PT bars-- however for a bridge bent with SLAs which do not impede self-centering following calculations can be done for energy dissipation and self-centering:

$$\Lambda_C = \frac{F_{u,SLA}}{P_u + F_{PT,i}} \leq 1.0$$

$F_{u,SLA}$ is ultimate strength of all energy dissipators

P_u is total gravity load

$F_{PT,i}$ is total initial PT force, after losses

Self-centering coefficient (Λ_C) **0.54** **OK** **$\Lambda_C \leq 1$**

Energy dissipation is validated using energy dissipation coefficient

$$\Lambda_D = \frac{F_{u,SLA}}{P_u + F_{PT,i} + F_{u,SLA}} \geq 0.1$$

Energy dissipation coefficient (Λ_D) **0.36** **OK** **$0.1 \geq \Lambda_D$**

Steel collar Design

Steel collar was designed based on the neutral axis depth at 4.0% drift ratio 2 times the design drift ratio of 2.0%

Maximum assumed drift ratio **4.00%**

$$\frac{c}{D} = 0.825 \text{ for } DR = 0\% \text{ and } \frac{c}{D} = 520(DR)^2 - 37.76(DR) + 0.79 \text{ for } DR > 0\%$$

Neutra axis at 4.0% drift (c) 5.08 in.

$$h_s^* = 0.5\sqrt{D^2 - c^2 + 2D\sqrt{D^2 - c^2}}$$

Unfactored height of collar (h_s^{*}) 37.18 in.

Factor of Safety (λ_s) 1.2

Height of steel collar (h_s) 44.62 in.

Provided height of steel collar 45.00 in.

Assuming thickness of plate (t_s) 0.50 in.

$$\frac{D}{t_s} \leq 100$$

Check 86.27 OK

Stud Design

Yield Strength (f_y) 44.00 ksi

Ultimate Strength (f_u) 62.00 ksi

Maximum expected load from SLAs 74.00 kip (assuming ultimate load of SLAs)

Assume Factor of Safety for SLA load 1.50

Maximum factored SLA load 111 kip

assume number of studs 3.00 nos

Diameter of Studs (D_{stud}) 1.00 in.

Area of stud (A_{sc}) 0.79 in.²

Ultimate SLA force is assumed to be acting on the steel chair and must be distributed by Studs-- factor of safety is used to increase SLA load for conservative design

Shear strength of One Stud from Codal Predictions $Q_{n1} = 0.5A_{sc}\sqrt{f'_c E_c} \leq A_{sc}F_u$

Q_{n1} 146.08 kip

OK

AASHTO 9th
edition

Summary			
Item	Qty	Units	Grade
Initial PT Force	80.00	kip	120 ksi PT bar
Number of PT bar	6.00	nos	
Diameter of PT bar	1.25	in.	
Number of SLAs	16.00	nos	Grade 36
Diameter of SLAs	1.25	in.	

Height of steel Collar	45.00	in.	Grade 50
Thickness of Steel Collar	0.50	in.	
Number of Studs	3.00	nos	Grade 50
Diameter of Studs	1.00	in.	

PT force Distribution

Calculation sheet for Initial PT Selection

Length of PT Bars (L_T)	288.00	in.
Column Height (H_c)	192.00	in.
Loading Point (L_c)	216.00	in.
Initial Axial Gravity Load (P_u)	72.00	kip
Elastic Modulus of PT bar (E_s)	29000.00	ksi
Equivalent Circular Diameter of Column (D)	43.14	in.
compressive strength (f'_c)	6.00	ksi
Modulus of concrete (E_c)	4415.20	ksi
number of PT (n_{PT})	6.00	
number of column (n_c)	2.00	
yield strain of PT bars	0.004138	in./in.
Initial PT forces:		
$F_{PT,1}$	80	kip
$F_{PT,2}$	90	kip
$F_{PT,3}$	100	kip
$F_{PT,4}$	112.5	kip

The PT force distribution is calculated based on the rotation(θ), deflection(Δ_{rot}) and neutral axis depth (c).

The rotation during rocking is calculated for each drift ratio using, $\theta = \frac{\Delta_{rot}}{H_c}$

Δ is calculated for a given drift ratio (DR) is calculated using, $\Delta = (DR)L_c$

where L_c is length upto loading point from footing surface.

Initial strain(ϵ_0) for a assumed initial PT force $F_{PT,i}$ is calculated as,

$$\epsilon_0 = \frac{f_{PT,i}}{E_{PT}}, f_{PT,i} = \frac{F_{PT,i}}{A_{PT}}$$

where $f_{PT,i}$ is initial PT stress, A_{PT} is area of PT bar, E_{PT} is modulus of elasticity of PT bar.

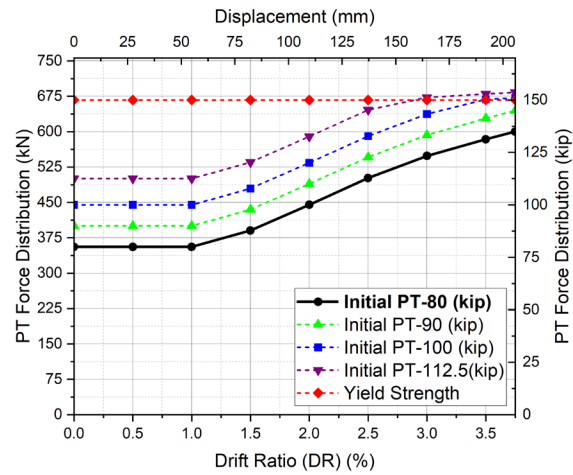
The PT force for a given drift ratio is obtained,

$$F_{PT} = E_{PT}A_{PT} * \left[\frac{\left(\frac{D}{2}-c\right)\theta}{L_T} + \varepsilon_0 \right] \text{ i.e. Until } c \text{ reaches } D/2 \text{ there is no change in PT forces.}$$

Table shows the PT force calculated for different initial PT force:

Table 22. Analytical calculation for PT force distribution for Riverdale bent

Drift Ratio (DR) (%)	Displacement (Δ) (in.)	Theta (θ) (rad)	c/D	c (in.)	PT Force for Initial PT-80 (kip)	PT Force for Initial PT-90 (kip)	PT Force for Initial PT-100 (kip)	PT Force for Initial PT-112.5 (kip)	PT Yield (kip)
0.00%	0.00	0.0000	1.00	43.14	80.00	90.00	100.00	112.50	150.00
0.50%	1.08	0.0056	0.66	28.45	80.00	90.00	100.00	112.50	150.00
1.00%	2.16	0.0112	0.52	22.55	80.00	90.00	100.00	112.50	150.00
1.50%	3.24	0.0169	0.41	17.90	87.79	97.79	107.79	120.29	150.00
2.00%	4.32	0.0225	0.34	14.48	100.07	110.07	120.07	132.57	150.00
2.50%	5.40	0.0281	0.29	12.30	112.79	122.79	132.79	145.29	150.00
3.00%	6.48	0.0337	0.26	11.37	123.32	133.32	143.32	151.20	150.00
3.50%	7.56	0.0394	0.26	11.22	131.28	141.28	150.26	152.85	150.00
3.75%	8.10	0.0422	0.26	11.22	134.94	144.94	151.02	153.61	150.00



Analytical calculation for PT force distribution for Riverdale bent

Pushover Calculation:

Calculation sheet for Pushover		
Length of PT Bars (L_{PT})	288.00	in.
Length of SLA (L_{SLA})	20.00	in.
Area of PT bars	1.25	in. ²
Column Height (H_C)	192.00	in.
Loading Point (L_C)	216.00	in.
Initial PT Force ($F_{PT,i}$)	80.00	kip
Initial Axial Gravity Load each column (P_u)	876.80	kip
Elastic Modulus of PT bar (E_{PT})	29000.00	ksi
Initial Strain in PT bars (ϵ_{PT})	0.0022069	in./in.
Equivalent Circular Diameter of Column (D)	43.14	in.
yield strain of PT bars	0.004138	in./in.
compressive strength (f'_c)	6.0	ksi
Modulus of concrete (E_c)	4415.20	ksi
number of PT each column (n_{PT})	6.00	
number of column (n_c)	2.00	
Gross Moment of inertia of concrete column (I_g)	169940.12	in. ⁴
Effective moment of Inertia (I_{eff})	118958.08	in. ⁴
Total Gravity load (W)	1753.61	kip
$S_C = 2 * \frac{I_{eff}}{D}$		
S_c	5515.60	in. ³
$M_{dec} = n_c \left(\frac{W}{n_c} + n_{PT} F_{PT,i} \right) * \frac{S_C}{A_g}$		
M_{dec}	10242.07	kip-in.
$F_{decomp} = \frac{2 * M_{dec}}{H_c}$		
F_{decomp}	106.69	kip

Should exceed the minimum requirement of length and a gap should be provided so that the chair base does not touch the surface of the footing

There is a small elastic deflection (Δ_{dcomp}) of the bent up to a decompression region. This deflection is calculated assuming bent as a portal frame and F_{dcomp} as a lateral load causing deflection.

$$\Delta_{dcomp} = \frac{F_{decomp} L_c^3}{24 * E_c * I_{eff}} \quad 0.09 \quad \text{in.} \quad 0.04 \quad \%$$

$$\frac{c}{D} = 1 \text{ for } DR = 0\% \text{ and } \frac{c}{D} = 451.3 (DR)^2 - 37.17(DR) + 0.94 \text{ for } DR > 0\%$$

$$\varepsilon_{SLA} = \theta \left(\frac{(D_i - c)}{L_{SLA}} \right); \text{ for } (D_i - c) \geq 0 \text{ and } \varepsilon_{SLA} = 0; \text{ for } (D_i - c) < 0$$

$$F_{T,i} = A_{SLA} \sigma_{T,i} \quad \sigma_{T,i} \text{ is stress corresponding to } \varepsilon_{SLA} \text{ from stress strain relationship for SLAs}$$

$$F_{rot} H_c = n_c \left(n_{PT} F_{PT} + \frac{W}{n_c} \right) (D - c - \Delta_{rot}) + \sum F_{T,i}(D_i)$$

Due to lateral load during rotation there is some elastic displacement, and it can be calculated as:

$$\Delta_{elastic} = \frac{F_{rot} L^3}{24 E_c I_{eff}}$$

The final drift ratio can be calculated as:

$$\text{Final Drift Ratio} = \frac{\Delta_{elastic} + \Delta_{rot}}{L_c}$$

$$F_{tot} = F_{rot} + F_{PT_horizontal}$$

Table 23. Analytical pushover response calculation for Modified Riverdale with SLAs.

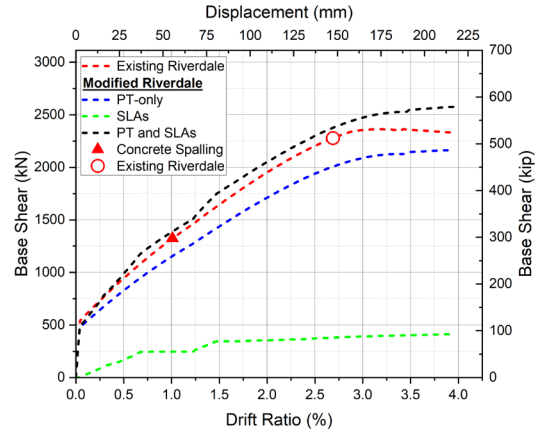
Drift Ratio (DR) (%)	Delta _{rot} in.	Theta (rad)	c/D	c (in.)	PT force each PT bar (kip)	PT force Vertical (kip)	Axial Gravity Load	Strain of SLAs			Force in each SLA (kip)			Horizontal PT force (kip)	F _{rot} kip	Delta _{el} in.	Total Disp (in.)	Total Drift ratio (%)	Final Force (kip)
								e1	e2	e3	F1	F2	F3						
0.000	0.00	0.00	0.83	35.59	80.00	80.00	876.81	0.0000	0.0000	0.0000	0.00	0.00	0.00	0.00	106.69	0.09	0.09	0.00	0.00
0.025	0.05	0.00	0.82	35.20	80.00	80.00	876.81	0.0001	0.0000	0.0000	7.92	0.00	0.00	0.27	115.38	0.09	0.15	0.04	106.69
0.050	0.11	0.00	0.81	34.82	80.00	80.00	876.81	0.0003	0.0000	0.0000	12.00	0.00	0.00	0.54	122.22	0.10	0.21	0.07	115.38
0.075	0.16	0.00	0.80	34.44	80.00	80.00	876.81	0.0005	0.0000	0.0000	16.59	0.00	0.00	0.81	129.25	0.10	0.27	0.10	122.22
0.100	0.22	0.00	0.79	34.06	80.00	80.00	876.81	0.0006	0.0000	0.0000	21.49	0.00	0.00	1.08	136.39	0.11	0.33	0.12	129.25
0.125	0.27	0.00	0.78	33.69	80.00	80.00	876.81	0.0008	0.0000	0.0000	26.90	0.00	0.00	1.35	143.72	0.11	0.38	0.15	136.39
0.150	0.32	0.00	0.77	33.32	80.00	80.00	876.81	0.0010	0.0000	0.0000	31.57	0.00	0.00	1.62	150.67	0.12	0.44	0.18	143.72
0.175	0.38	0.00	0.76	32.95	80.00	80.00	876.81	0.0012	0.0000	0.0000	37.26	0.00	0.00	1.89	158.05	0.13	0.50	0.21	150.67
0.200	0.43	0.00	0.76	32.58	80.00	80.00	876.81	0.0014	0.0000	0.0000	43.38	0.00	0.00	2.16	165.58	0.13	0.56	0.23	158.05
0.225	0.49	0.00	0.75	32.22	80.00	80.00	876.81	0.0016	0.0000	0.0000	48.16	4.17	0.00	2.43	175.25	0.14	0.63	0.26	165.58
0.250	0.54	0.00	0.74	31.86	80.00	80.00	876.81	0.0019	0.0001	0.0000	48.15	5.41	0.00	2.70	180.66	0.14	0.68	0.29	175.25
0.275	0.59	0.00	0.73	31.51	80.00	80.00	876.81	0.0021	0.0001	0.0000	48.17	7.01	0.00	2.97	186.27	0.15	0.74	0.32	180.66
0.300	0.65	0.00	0.72	31.16	80.00	80.00	876.81	0.0024	0.0002	0.0000	48.12	8.92	0.00	3.24	192.02	0.15	0.80	0.34	186.27
0.325	0.70	0.00	0.71	30.81	80.00	80.00	876.81	0.0026	0.0003	0.0000	48.01	11.65	0.00	3.51	198.24	0.16	0.86	0.37	192.02
0.350	0.76	0.00	0.71	30.46	80.00	80.00	876.81	0.0029	0.0004	0.0000	47.95	14.84	0.00	3.78	204.77	0.16	0.92	0.40	198.24
0.375	0.81	0.00	0.70	30.12	80.00	80.00	876.81	0.0032	0.0005	0.0000	47.87	16.59	0.00	4.05	210.26	0.17	0.98	0.43	204.77
0.400	0.86	0.00	0.69	29.78	80.00	80.00	876.81	0.0035	0.0006	0.0000	47.86	19.73	0.00	4.32	216.68	0.17	1.04	0.45	210.26
0.425	0.92	0.00	0.68	29.44	80.00	80.00	876.81	0.0038	0.0007	0.0000	47.86	24.07	0.00	4.59	223.87	0.18	1.10	0.48	216.68
0.450	0.97	0.01	0.67	29.11	80.00	80.00	876.81	0.0041	0.0008	0.0000	47.90	27.97	0.00	4.86	230.73	0.18	1.16	0.51	223.87
0.475	1.03	0.01	0.67	28.78	80.00	80.00	876.81	0.0044	0.0010	0.0000	47.93	31.31	0.00	5.13	237.18	0.19	1.22	0.54	230.73
0.500	1.08	0.01	0.66	28.45	80.00	80.00	876.81	0.0047	0.0011	0.0000	47.97	34.25	0.00	5.40	243.31	0.19	1.27	0.56	237.18

Table 24. Analytical pushover response calculation for Modified Riverdale with PT bars only.

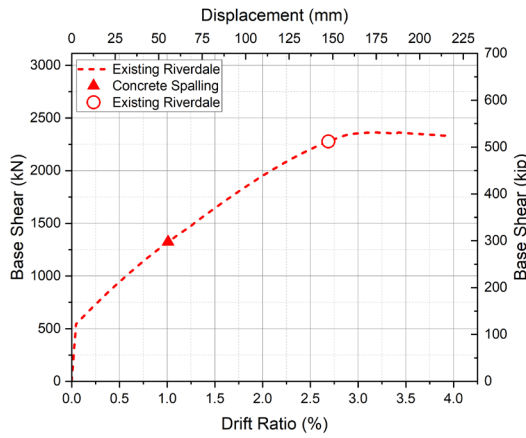
Drift Ratio (DR) (%)	Delta _{rot} in.	Theta (rad)	c/D	c (in.)	PT force each PT bar (kip)	PT force Vertical (kip)	Axial Gravity Load each column(Pu) (kip)	Horizontal PT force (kip)	Frot kip	Delta _{elastic} in.	Total Disp (in.)	Total Drift ratio	Final Force (kip)
0.000	0.00	0.00	0.83	35.59	80.00	80.00	876.81	0.00	106.69	0.09	0.09	0.00	0.00
0.025	0.05	0.00	0.82	35.20	80.00	80.00	876.81	0.27	111.65	0.09	0.14	0.04	106.69
0.050	0.11	0.00	0.81	34.82	80.00	80.00	876.81	0.54	116.58	0.09	0.20	0.07	111.65
0.075	0.16	0.00	0.80	34.44	80.00	80.00	876.81	0.81	121.45	0.10	0.26	0.09	116.58
0.100	0.22	0.00	0.79	34.06	80.00	80.00	876.81	1.08	126.29	0.10	0.32	0.12	121.45
0.125	0.27	0.00	0.78	33.69	80.00	80.00	876.81	1.35	131.08	0.10	0.37	0.15	126.29
0.150	0.32	0.00	0.77	33.32	80.00	80.00	876.81	1.62	135.82	0.11	0.43	0.17	131.08
0.175	0.38	0.00	0.76	32.95	80.00	80.00	876.81	1.89	140.53	0.11	0.49	0.20	135.82
0.200	0.43	0.00	0.76	32.58	80.00	80.00	876.81	2.16	145.19	0.12	0.55	0.23	140.53
0.225	0.49	0.00	0.75	32.22	80.00	80.00	876.81	2.43	149.80	0.12	0.61	0.25	145.19
0.250	0.54	0.00	0.74	31.86	80.00	80.00	876.81	2.70	154.37	0.12	0.66	0.28	149.80
0.275	0.59	0.00	0.73	31.51	80.00	80.00	876.81	2.97	158.90	0.13	0.72	0.31	154.37
0.300	0.65	0.00	0.72	31.16	80.00	80.00	876.81	3.24	163.38	0.13	0.78	0.33	158.90
0.325	0.70	0.00	0.71	30.81	80.00	80.00	876.81	3.51	167.82	0.13	0.84	0.36	163.38
0.350	0.76	0.00	0.71	30.46	80.00	80.00	876.81	3.78	172.22	0.14	0.89	0.39	167.82
0.375	0.81	0.00	0.70	30.12	80.00	80.00	876.81	4.05	176.57	0.14	0.95	0.41	172.22
0.400	0.86	0.00	0.69	29.78	80.00	80.00	876.81	4.32	180.88	0.14	1.01	0.44	176.57
0.425	0.92	0.00	0.68	29.44	80.00	80.00	876.81	4.59	185.15	0.15	1.07	0.47	180.88
0.450	0.97	0.01	0.67	29.11	80.00	80.00	876.81	4.86	189.37	0.15	1.12	0.49	185.15
0.475	1.03	0.01	0.67	28.78	80.00	80.00	876.81	5.13	193.54	0.15	1.18	0.52	189.37
0.500	1.08	0.01	0.66	28.45	80.00	80.00	876.81	5.40	197.68	0.16	1.24	0.55	193.54

Table 25. Analytical pushover response calculation for Existing Riverdale with PT bars only.

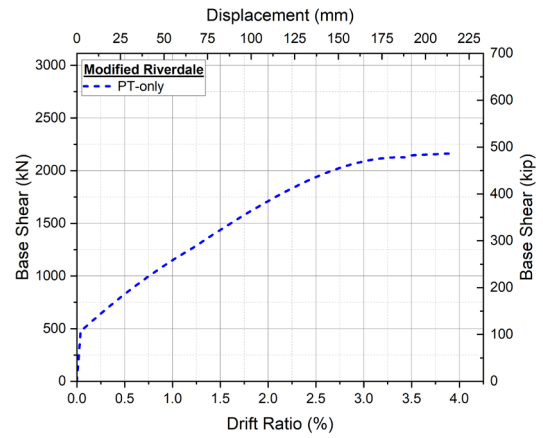
Drift Ratio (DR) (%)	Delta _{rot} in.	Theta (rad)	c/D	c (in.)	PT force each PT bar (kip)	PT force Vertical (kip)	Axial Gravity Load each column(Pu) (kip)	Horizontal PT force (kip)	Frot kip	Delta _{elastic} in.	Total Disp (in.)	Total Drift ratio	Final Force (kip)
0.000	0.00	0.00	0.83	35.59	112.50	112.50	876.81	0.00	122.02	0.10	0.10	0.00	0.00
0.025	0.05	0.00	0.82	35.20	112.50	112.50	876.81	0.38	127.77	0.10	0.16	0.05	122.02
0.050	0.11	0.00	0.81	34.82	112.50	112.50	876.81	0.76	133.47	0.11	0.21	0.07	127.77
0.075	0.16	0.00	0.80	34.44	112.50	112.50	876.81	1.14	139.12	0.11	0.27	0.10	133.47
0.100	0.22	0.00	0.79	34.06	112.50	112.50	876.81	1.52	144.72	0.12	0.33	0.13	139.12
0.125	0.27	0.00	0.78	33.69	112.50	112.50	876.81	1.90	150.27	0.12	0.39	0.15	144.72
0.150	0.32	0.00	0.77	33.32	112.50	112.50	876.81	2.28	155.77	0.12	0.45	0.18	150.27
0.175	0.38	0.00	0.76	32.95	112.50	112.50	876.81	2.66	161.22	0.13	0.51	0.21	155.77
0.200	0.43	0.00	0.76	32.58	112.50	112.50	876.81	3.04	166.62	0.13	0.57	0.23	161.22
0.225	0.49	0.00	0.75	32.22	112.50	112.50	876.81	3.42	171.97	0.14	0.62	0.26	166.62
0.250	0.54	0.00	0.74	31.86	112.50	112.50	876.81	3.80	177.27	0.14	0.68	0.29	171.97
0.275	0.59	0.00	0.73	31.51	112.50	112.50	876.81	4.18	182.52	0.15	0.74	0.32	177.27
0.300	0.65	0.00	0.72	31.16	112.50	112.50	876.81	4.56	187.72	0.15	0.80	0.34	182.52
0.325	0.70	0.00	0.71	30.81	112.50	112.50	876.81	4.94	192.86	0.15	0.86	0.37	187.72
0.350	0.76	0.00	0.71	30.46	112.50	112.50	876.81	5.32	197.96	0.16	0.91	0.40	192.86
0.375	0.81	0.00	0.70	30.12	112.50	112.50	876.81	5.70	203.01	0.16	0.97	0.42	197.96
0.400	0.86	0.00	0.69	29.78	112.50	112.50	876.81	6.07	208.01	0.17	1.03	0.45	203.01
0.425	0.92	0.00	0.68	29.44	112.50	112.50	876.81	6.45	212.96	0.17	1.09	0.48	208.01
0.450	0.97	0.01	0.67	29.11	112.50	112.50	876.81	6.83	217.86	0.17	1.15	0.50	212.96
0.475	1.03	0.01	0.67	28.78	112.50	112.50	876.81	7.21	222.71	0.18	1.20	0.53	217.86
0.500	1.08	0.01	0.66	28.45	112.50	112.50	876.81	7.59	227.50	0.18	1.26	0.56	222.71



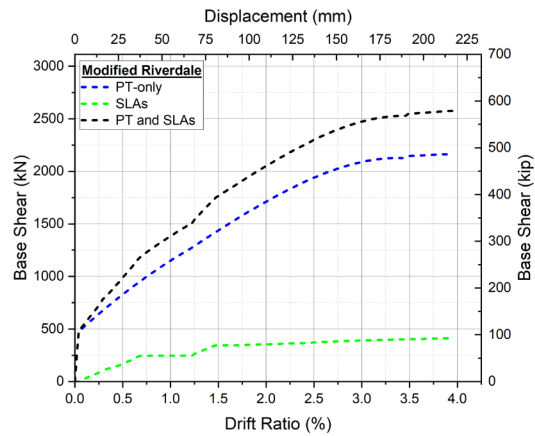
Analytical pushover response comparison for Existing and Modified Riverdale with and without SLAs.



(a)



(b)



(c)

Pushover response and contribution of each components: (a) Existing Riverdale; (b) Modified Riverdale (PT-only); and (c) Modified Riverdale with PT bars and SLAs.